Max-Planck-Institut für Kolloid- und Grenzflächenforschung

C_xN_y-Materials from Supramolecular Precursors for "All-Carbon" Composite Materials

Dissertation

zur Erlangung des akademischen Grades
Doktor der Naturwissenschaften (Dr. rer. nat.)
in der Wissenschaftsdisziplin „Kolloidchemie“

eingereicht an der
Mathematisch-Naturwissenschaftlichen Fakultät
der Universität Potsdam

von

Thomas Jordan

Potsdam-Golm, im Februar 2017

Acknowledgement

First of all, I would like to thank Prof. Dr. Markus Antonietti, for giving me the opportunity to work in this Institute on this interesting topic, and for his helpful support throughout my PhD.

A lot of thanks go to my supervisors Dr. Nina Fechler and Dr. Menny Shalom. Thanks for the scientific discussions, the constant support, their patience and the very nice atmosphere in these groups. I learned a lot during my PhD, about science, but also about life as a scientist in general.

I would like thank Prof. Dr. Andreas Taubert and Prof. Dr. Bernd Smarsly for agreeing to review this thesis.

A lot of people contributed by their lab work to the results presented in this thesis. I thank Rona Pitschke for the supercritical CO_2 drying and for TEM measurements, Antje Völkel for thermogravimetric analysis, Sylvia Pirok for elemental analysis and Regina Rothe for general support in the lab. I especially would like to thank Dr. Oleksandr Savatieiev for introducing me to the photocatalytic water splitting setup.

I also thank Dr. Thomas Brenner from the University of Potsdam for the photoluminescence lifetime measurements and Matthias Trunk from TU Berlin for the solid state ^{13}C NMR measurements.

Furthermore, I would like to thank Prof. Dr. Bernd Smarsly from the University of Gießen for the opportunity to perform electrospinning-experiments in his lab. Here, I especially would like to thank Pascal Vöpel and Dr. Christian Suchomski.

A lot of thanks go to my colleagues and friends Berti and Chris, for the very nice atmosphere in the lab and in the office and for the numerous discussions on science and life in general. Thanks a lot for helping with the salt-templating experiments and thanks to Berti for doing the CO_2 adsorption measurements and helping with the dye adsorption experiments. I also thank Zhilong Yu for his precious contributions to the chitosan experiments.

Furthermore, I would like to thank the many interesting people I met here in MPI and had a wonderful time with: Jonas, Marc, Christian, Max, Micaela, Afroditi, Jochen, Noah, Baris, Steffen, Max, Tim, Martin, Remi, Valerio, Jesus, Martina, Claudio, Caro, and the ones I possibly forgot to mention.

And finally, I deeply would like to thank my family, my friends and my girlfriend Marie for their constant support and motivation.

Outline

1 Introduction

The high standard of living in our modern society goes along with a high need for energy. From 2000 to 2014, the global energy demand increased by 30 %.[1] And this trend will continue, as economies around the world are emerging and the global population is rising: In 2040, the world population will increase from today's 7.2 billion to 9 billion.[2] According to estimations made by the U.S. Energy Information Administration, in 2040 the energy consumption will increase by another 48 %.[1] But where does this energy come from? The main sources are fossil fuels. According to the International Energy Agency, 81 % of the global energy consumption in 2014 were based on fossil fuels like coal, oil and natural gas.[3] However, the consumption of these resources leads to the emission of the greenhouse gas CO_2, which is one major contribution towards global warming. Furthermore, fossil fuels are not endlessly available.

Considering this, it becomes apparent that sooner or later we have to overcome our dependence on fossil fuels as major energy source. Alternative energy sources are available- be it in the form of wind power, water power, geothermal energy, biofuels, solar light, etc.; however, the challenge still lies in the efficient transfer into that form of energy on which our energy-infrastructure is built on: Electricity. The preference to still take the tremendous efforts to extract fossil fuels for today's energy demands, already indicates that the energy transfer from alternative sources is still accompanied by technological difficulties and high costs. To change this, contributions can be made by chemists and material scientists in developing new materials with desired electronic properties, best in an affordable and sustainable manner.

An important source of energy is solar light. The amount of solar energy which reaches the earth per year, is estimated to be up to $49.8 \cdot 10^{18}$ J per year.[4] Basic principle for the transfer of light into electricity is the intrinsic photoelectric effect, which describes the interaction of light with a semiconductor. A semiconductor is characterized by its electronic structure, in which a band of occupied electronic states (the valence band, VB) is separated from an energetically higher unoccupied band (the conduction band, CB) by a zone, in which no electronic states are available (the band gap with the energy E_g, see **Scheme 1**). If light with a wavelength of higher energy than the band gap energy is absorbed by the semiconductor, electrons (e^- in **Scheme 1**) are excited into the conduction band, leaving behind positively charged holes (h^+ in **Scheme 1**). The photogenerated electrons and holes are charge carriers, which can be used directly as photoelectric current in photovoltaics. In photocatalysis, the charge carriers take part as redoxactive species in chemical reactions. An important application of this principle is the production of hydrogen for fuel cells by the photocatalytic splitting of water.

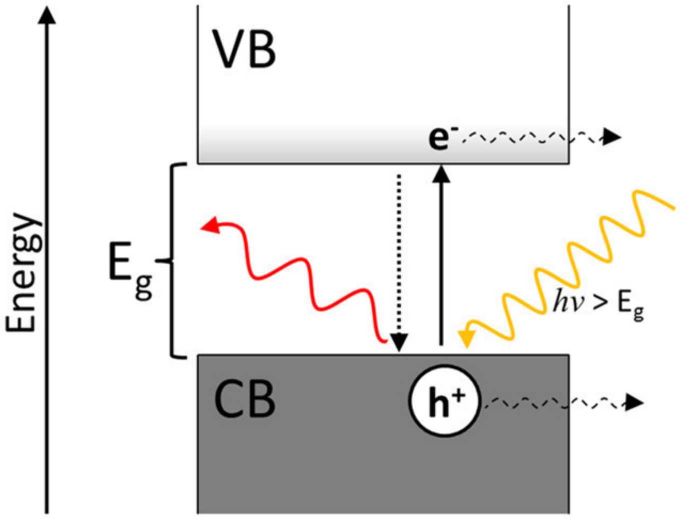

Scheme 1. Photoexcitation of a semiconductor. If light with an energy *hv* exceeding the band gap energy E_g is absorbed by the semiconductor, electrons (e^-) are excited from the conduction band (CB) into the valence band (VB), leaving behind a positive charged hole (h^+). The charge carriers can then re-combine (dotted arrow) under energy-loss, e.g. photoluminescence (red arrow), or migrate to the surface (dashed arrows) and take part in redox-reactions.

However, one of the major challenges in controlling photoelectric processes is it to prevent the photogenerated charge carriers from their re-combination, which would result in complete loss of their energy, e.g. by photoluminescence (see **Scheme 1**). A way to inhibit this unwanted process is bringing the photoactive material into a heterojunction contact. In general, a heterojunction is the interface between two solid-state materials with different electronic properties. This leads to new electronic phenomena at the interface region. If two semiconductors with different band structures are in contact, crossing the interface for the photogenerated charge carriers is accompanied by changes in their energy. This facilitates the spatial separation of photogenerated electrons and holes and thus prevents their recombination.

Apart from the field of organic photovoltaics,[5,6] the vast majority of materials for heterojunctions in photovoltaics and in photocatalysis are based on inorganic semiconductors. The highest efficiency for solar cells is achieved with GaAs,[7] and commercial solar cells are made of silicon or CdTe. The most active materials in photocatalysis are transition metal oxides, –sulfides, or -nitrides.[8-11] However, these materials can have serious disadvantages: The production of silicon photovoltaics requires environmentally destructive compounds, and the transition metal based semiconductors are very often expensive, toxic and environmentally harmful.

A class of materials which combines wide availability, non-toxicity and environmentally friendliness with a broad range of possibilities to tune their electronic and catalytic properties, are carbon-based solid state materials. Among them, carbon/nitrogen compounds are of special interest, as it is possible to tune their electronic structure with their nitrogen content: Depending on the carbon/nitrogen ratio, conducting as well as semiconducting materials with different band gaps can be obtained, ranging from semiconducting and photoactive high nitrogen content carbon nitride, to electrically conducting nitrogen-doped carbons. This potentially allows for preparing an "all-carbon" heterojunction, where the interface is built between carbon materials of different nitrogen content and thus different electronic properties. Besides the advantages of carbon/nitrogen compounds as non-toxic, "green" materials, a particular benefit of this concept lies in making a heterojunction composite between two components constituted by the same elements, however with different properties: This way, the performance lowering contact resistance which occurs at the interface due to a certain lattice mismatch between the heterojunction components, can be minimized. In a broader sense, this concept might be even extended towards a carbon/nitrogen material with local variations in the nitrogen content, introducing local variations of the electronic structure and thus multiple heterojunctions in one material. This can be realized in a gradient material with a spatial gradient regarding the nitrogen content, or in a material with regular spatial doping patterns.

However, be it the heterojunction between two components or the vision of the material with local composition inhomogeneities on a small scale: Such an "all-carbon" composite requires synthetic strategies to obtain carbon/nitrogen compounds with tailored electronic properties and morphologies.

Carbon materials are usually prepared by carbonization processes, i.e. the thermal treatment of organic precursors. However, carbonization reactions are still some sort of "black box" processes, where most of the occurring reactions are not yet understood and thus not easy to control.

An approach to gain more control over the carbonization process is the attempt to pre-organize desired patterns of the final carbon material already on the stage of the presursor.

This can be done in the form of supramolecular organized precursor complexes, where specially arranged molecular patterns already give a guide-line towards desired reaction pathways during carbonization.[12] These supramolecular complexes can be formed between precursor molecules by non-covalent interactions like hydrogen bonding, π-π-, van der Waals- or ionic interactions.[13] By carbonizing these pre-organized complexes, in an ideal case the rather randomly carbonization process is replaced by the controlled condensation of neighbored molecular entities.

In this work, strategies are shown to synthesize carbon/nitrogen materials with desired properties by applying pre-organized supramolecular complexes as precursor, as well as approaches towards combining them to an “all-carbon” composite.

2 Background

2.1 Carbon and carbon/nitrogen compounds

2.1.1 The element carbon

Among all 118 elements known so far to humanity, carbon can claim- without any doubt- being the “master” of diversity and complexity. Carbon is the basic building block of the most complex system on earth, which slowly developed in a process of billions of years: Life. A whole part of chemistry, organic chemistry, is dedicated to the combination of this element with only a few others. Furthermore, one should not forget the huge impact of carbon materials on technology and modern materials chemistry. But why is carbon such a versatile element?

The answer might be found in the versatility of electronic states and bonding patterns carbon is capable of. Hybridization of carbon’s orbitals allows for at least three stable bonding schemes (sp, sp^2 and sp^3), each with their own bonding multiplicity and geometry. Furthermore, carbon can be present in all oxidation states from –IV (e.g. in methane) to +IV (e.g. in CCl_4). And finally, carbon can form covalent bonds with a lot of other elements, like H, B, N, O, S, halogens, and more.

However, the chemical versatility is not restricted to the molecular compounds, which make up the organic world or the chemistry of life. Also in the field of solid-state materials, carbon is probably the element with the biggest flexibility. This begins with elemental carbon, whose electrical properties, color or hardness can vary between different extremes for the different modifications. Carbon can exist as insulator, conductor or semiconductor, depending on the hybridization and structure. In the colorless and insulating diamond, the hardest naturally occurring material, sp^3 hybridized carbon is arranged in a cubic crystal structure (**Figure 2.1** (a)). Opposing properties exhibits the black and conducting graphite, which is a very soft material. Here, sp^2 hybridized carbon atoms arrange in hexagonal layers by σ- and π-bonding. A monolayer of such arranged carbon atoms is known as graphene (**Figure 2.1** (b)). Due to delocalized π-molecular orbitals, graphene is conductive, as well as graphite in the direction of the graphene layers. Structural homologue to graphite is the family of the fullerenes (carbon nanotubes and fullerenes). Carbon nanotubes (CNTs) are single- (SWCNTs) or multi-walled (MWCNTs) tubes with the structure of graphene, which can display conductive and semiconductive behavior (**Figure 2.1** (c)). When replacing some

C6-rings in the graphene structure by C5-rings, fullerenes in form of hollow spheres can be obtained (buckyball clusters). The smallest isolated spherical fullerene is the Buckminster-Fullerene C_{60} (**Figure 2.1** (d)).

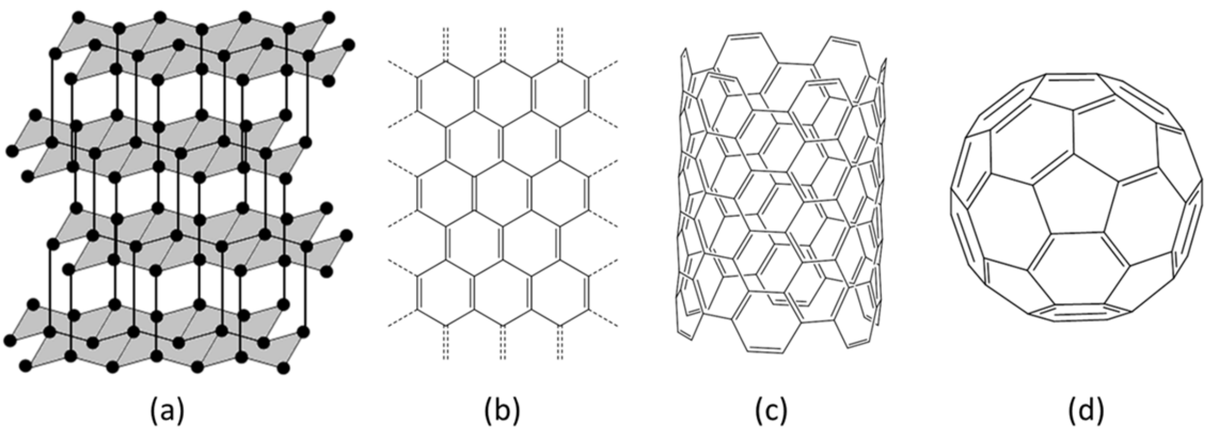

Figure 2.1. The allotropes of carbon. (a) Cubic diamond. (b) Structure of graphene. (c) (6,6)-armchair carbon nanotube and (d) the Buckminster-Fullerene C_{60}.

Because of this versatility in structure and electronic properties, the allotropes of elemental carbon are very interesting for a broad field of technological applications. This ranges from the use of diamond as hard material for technological and medicinal applications, to the use of graphite in electrical engineering (e.g. as electrode or heating resistor material) or as corrosion resistant material.[14]

Due to their unique structure and high chemical stability when compared to inorganics, the nanostructured elemental carbon modifications like graphene or fullerenes are especially interesting in modern materials chemistry, physics or medicine research. Graphene, which is referred to as a two-dimensional (2D) material, has unique physical and chemical properties like a fast charged carrier mobility ($\sim 200\,000\ \text{cm}^2\ \text{V}^{-1}$)[15], high thermal conductivity (~ 5000 W/mK)[15], high surface area (2630 m^2/g)[16], a strong Young's modulus (~ 1 TPa)[17] and a high chemical stability. This makes graphene a promising material in alternative-energy related applications like supercapacitors, batteries and fuel cells.[18]

2.1.2 Carbon/nitrogen compounds

As can be seen by the above introduced well-known carbon allotropes, already materials constituted by only carbon can exhibit a very broad range of properties. These characteristics can be further tuned by the introduction of heteroatoms like boron,[19] nitrogen,[20] sulfur,[21] phosphor,[22] etc. into the carbon lattice (which however should not be confused with post-functionalization). This can greatly affect their physical and chemical properties, potentially leading to a significantly increased catalytic or electrochemical performance. However, among all classes of heteroatom containing solid-state carbon materials, it is the group of carbon/nitrogen compounds, which is target of the most active research.

This is due to certain unique properties of this materials class:

I) Nitrogen can be included in a wide range of percentage into the carbon lattice, resulting in stable compounds with different structures and properties. This is because nitrogen “fits in” to the carbon lattice, with bonding schemes that allow chemical incorporation in different oxidative states and bonding multiplicities. And furthermore, nitrogen and carbon reveal not too much difference in their atomic radius, which allows incorporation without large structural disruptions.

II) As nitrogen contains one more valence electron than carbon, the electronic properties of carbon/nitrogen compounds are greatly affected by their nitrogen content and can range from an increased conductivity to the behavior of semiconductors. This makes carbon/nitrogen compounds especially interesting for energy related applications.

III) And finally, one of the reasons for the focus on carbon/nitrogen compounds especially in the field of alternative energy applications, is simply their facile synthesis and wide abundance: Compared to the carbon nanostructures like carbon nanotubes or fullerenes, whose synthesis is difficult and expensive, some carbon/nitrogen compounds with comparable properties can be derived from natural precursors (e.g. biomass, nitrogen/carbon containing compounds like nucleobases, urea, etc.) by simple carbonization processes.

Depending on their nitrogen content, two classes of carbon/nitrogen compounds are distinguished in general: Nitrogen-rich carbons, with an elemental N/C ratio ≥ 1, and nitrogen-doped carbons (NDCs), with an elemental N/C ratio < 1.[23] Nitrogen-rich carbons can contain up to 61 wt%, however, also a compound with higher nitrogen contents and an estimated compositions of C_3N_5 has been reported.[24] In these nitrogen-rich carbons, new molecular units are formed, which goes along with entirely new properties with respect to the pristine carbon. They are usually semiconductors. Examples for nitrogen-rich carbons are modifications of carbon nitride, C_3N_4. In general, nitrogen-rich carbons are prepared by the thermal condensation of appropriate nitrogen-rich precursors with an elemental N/C ratio ≥ 1 at intermediate temperatures (ca. 550 °C). At higher temperatures, these structures usually decompose.

Nitrogen-doped carbon

In nitrogen-doped carbons, single carbon atoms in the graphitic lattice are replaced by nitrogen atoms. Hence, the graphitic structure is retained in large parts of the material. Here, properties of the corresponding bulk carbon materials (like conductivity,[25] basicity,[26] oxidative stability[23] or catalytic activity[25]) do not change completely, but are further improved by the nitrogen doping. Nitrogen-doped carbons are usually synthesized by carbonization of nitrogen containing precursors (with an elemental N/C ratio < 1) or via post-treatment of carbon materials with reactive nitrogen containing reagents (NH_3, CH_3CN). There are interesting routes towards nitrogen-doped carbons by applying simple procedures and starting from naturally abundant precursors, like from nitrogen-rich biomass,[27] lignin,[28] or by the carbonization of ionic liquids (ILs)[23,29-31] and polyionic liquids (PILs),[32] which in turn as well can be potentially derived from natural precursors.[33]

The possible configurations of nitrogen atoms incorporated in the graphitic lattice, are shown in **Figure 2.2**.[34] The two most stable incorporations are quaternary N (graphitic N), where nitrogen substitutes sp^2 carbon in the hexagonal ring, and pyridinic N, where sp^2 carbons at the edges of the structure are substituted (occurring at edges or defects). Less stable incorporations are the sp^2 hybridized pyrazinic N in opposite positions at isolated hexagonal rings, and sp^3 hybridized pyrrolic N. Also, pyridinic nitrogen oxides are observed in NDCs.[35]

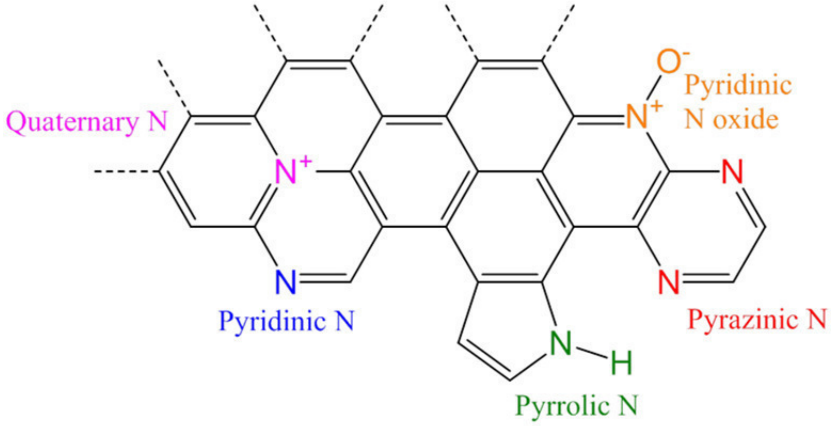

Figure 2.2. Bonding configurations of nitrogen in the graphitic lattice.

Among all bonding configurations, quaternary nitrogen is by far the most stable, which means that the relative amount of quaternary nitrogen usually increases with increasing carbonization temperature.[36] However, since quaternary nitrogens replace single carbon atoms in the graphitic lattice, there is an upper limit for the amount of incorporated nitrogen while maintaining the graphitic structure. As calculations by Watanabe et al. revelaed, a graphitic nitrogen content above 16 wt% is energetically not favoured.[36]

On the atomic level, the incorporation of nitrogen atoms into the carbon lattice primarily leads to three effects. First, the basicity of the carbon framework increases.[37] This is due to the additional valence electron brought in by the nitrogen, which contributes to the delocalized π electron system. This also leads to local positively charged carbon atoms neighbored to the electron-withdrawing nitrogen atoms.[38] Due to the additional valence electron, nitrogen can be seen as n-dopant. This leads to the second effect, i.e. the formation of localized electron donor states near the Fermi level, resulting in a significantly increased conductivity of nitrogen doped carbons.[39] Finally, incorporated nitrogen to a certain degree disrupts the graphitic structure and this way induces defects.[36] This however is desired for some catalytic applications, as defects are known to be the active sites in heterogenous catalysis.[40,41]

As stated above, nitrogen-doped carbons are conducting materials. This makes them promising materials as metal-free electrodes for the electrochemical water splitting. The major challenge for electrochemical water splitting are the sluggish kinetics for the oxygen-involving half reaction (the oxygen evolution reaction, OER).[42] So far, the best electrode materials for the OER are based on noble metals, like Iridium- and Ruthenium.[43] However, to replace the expensive noble metals, the search for metal-free OER electrodes is subject of intensive research. Here, nitrogen-doped carbon has been revealed as a material with a nearly comparable activity.[37,44] It is still disputed why exactly nitrogen doping significantly increases the OER activity, but theoretical and experimental studies suggest the following contributions: Due to the higher electronegativity of nitrogen, adjacent carbon atoms obtain a lower electron density, which might favour the adsorption of OH^- ions for OER.[44] And additionally, as stated above, nitrogen incorporation induces defects in the carbon lattice, which are known as the active sites in catalytic processes.[40,41] However, too high nitrogen contents are counterproductive to the OER activity, as they come along with semiconductive behavior and thus decreased electrical conductivity.

Carbon nitride and the photocatalytic splitting of water

A nitrogen-rich compound with a defined structure is graphitic carbon nitride, g-C_3N_4. However, the empirical formula C_3N_4 summarizes several carbon nitride allotropes. In 1989, Liu et al. and Cohen et al. predicted the existence of sp^3-bonded C_3N_4 carbon nitride, with the same structure like ß-Si_3N_4 and an extremely high bulk modulus and hardness, being comparable or even exceeding that of diamond.[45,46] Since then, several reports claimed the observation of this[47] and further C_3N_4 allotropes (α-C_3N_4, pseudocubic or rhombohedral C_3N_4 and new phases with unknown structures).[48] However, several critical reviews on those reports conclude that a definite evidence for the existence of the mentioned C_3N_4 phases has not been presented yet.[49,50]

There is only one allotrope of C_3N_4 which structure has been confirmed by several techniques like wide-angle X-ray diffraction (WAX), electron microscopy or neutron diffraction: Graphitic carbon nitride, g-C_3N_4.[51-55] This allotrope has the structure of N-bridged tri-s-triazine units ("poly(tri-s-triazine", with structural holes between three connected tri-s-triazine units), which form planar, π-conjugated 2D layers, which are stacked in the bulk material (**Figure 2.3**). Because of the structural analogues to graphite, this allotrope is denoted as "graphitic" carbon nitride. From diffraction patterns, a stacking distance between the layers of 0.326 nm can be determined experimentally, which is slightly smaller than in graphite (0.335 nm).[56] This indicates a stronger binding between the layers for g-C_3N_4, which is due to the nitrogen substitution. However, it should be noted that after tempering g-C_3N_4 at 600 °C, the interlayer distance is decreased to only 0.319 nm, indicating a more perfect packing. This interlayer distance is among the smallest values ever determined for the packing of aromatic units.[48]

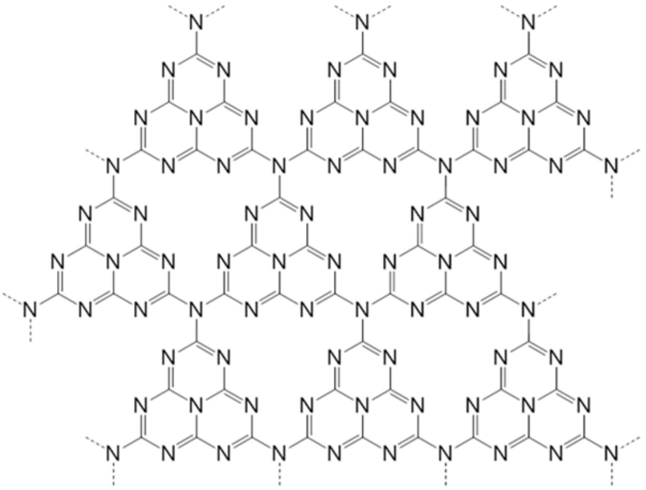

Figure 2.3. The tri-s-triazine structure of g-C_3N_4.

However, elucidating the structure of g-C_3N_4 has been a long story with a lot of speculations. A derivative of this compound was already known in 1834 by the name polymeric melon, initially prepared and described by Berzelius and Liebig by the thermolysis of mercury(II) thiocyanate.[57] Beginning with Franklin in 1922, structural investigations on "polymeric melon" were undertaken, finally coming to the agreement that this compound is a mixture of several polymeric condensation products of melamine, like melam, melem, melon and their condensation products (see **Scheme 2.1**).[58] "Polymeric melon" was then forgotten until the 1990s, when the quest for the superhard ß-C_3N_4 (like predicted by Liu et al. and Cohen et al., see above) began. From then on, many compounds with a composition close to C_3N_4 were prepared.[48] However, as the preparation of single crystalline carbon nitride with an exact C_3N_4 composition has not been successful yet, structural investigations are still challenging. Two structures were proposed: The above described tri-s-triazine structure (see **Figure 2.3**) and a triazine-based structure (depicted as structure (10) in **Scheme 2.1**). Only the tri-s-triazine structure could be confirmed yet. Nevertheless, g-C_3N_4 still has to be considered as a theoretical compound, as the preparation of defect- and hydrogen free C_3N_4 and its complete structural resolution still has to be done.

The degree of condensation, crystallinity and composition of the g-C_3N_4 greatly depends on the applied precursors. Up to now, a lot of different precursor systems have been applied. Most of them are based on cyanamide, melamine, cyanurchloride or other triazines.[48] Also urea has been applied for the synthesis g-C_3N_4.[59] In this work, g-C_3N_4 will be synthesized from melamine-based precursor complexes. A pathway for the condensation of cyanamide or melamine towards g-C_3N_4, based on DFT-calculations and the detection of intermediates by thermoanalytical methods (TGA, DSC) combined with XRD, is shown in **Scheme 2.1**.[48]

Starting from cyanamide ((1) in **Scheme 2.1**), dimerization to dicyanamide ((2) in **Scheme 2.1**) and further reaction to melamine ((3) in **Scheme 2.1**) occurs when heating. Around 390 °C melamine can condensate to melem (triamino-s-triazine, (4) in **Scheme 2.1**), accompanied by the elimination of ammonia. Melem can be regarded as the single unit in the polymeric tri-s-triazine network of g-C_3N_4. This polymerization occurs around 520 °C, certainly via dimerization to di-melem ((5) in **Scheme 2.1**), further oligomerization to the linear chain melon ((6) in **Scheme 2.1**), and finally fusion of the melon chains into the g-C_3N_4 network ((7) in **Scheme 2.1**). However, starting from melamine, the reaction theoretically could also occur via the formation of melam ((8) in **Scheme 2.1**), a dimer of melamine, followed by further oligomerization into a melamine chain ((9) in **Scheme 2.1**) This route would finally result in the formation of a C_3N_4 structure based on triazine units ((10) in **Scheme 2.1**). However, as described above, structural investigations on obtained C_3N_4 samples revealed them to be composed of tri-s-triazine units. Indeed, experiments and DFT calculations showed that melam (the melamine-dimer leading to the triazine-route) is metastable and thus that the formation of melem (tri-s-triazine-route) is favoured.[60]

Graphitic carbon nitride is stable only up to a certain temperature (until ≈ 650 °C, depending on the degree of condensation).[48] Above that limit, the material decomposes completely into nitrogen and cyano fragments.

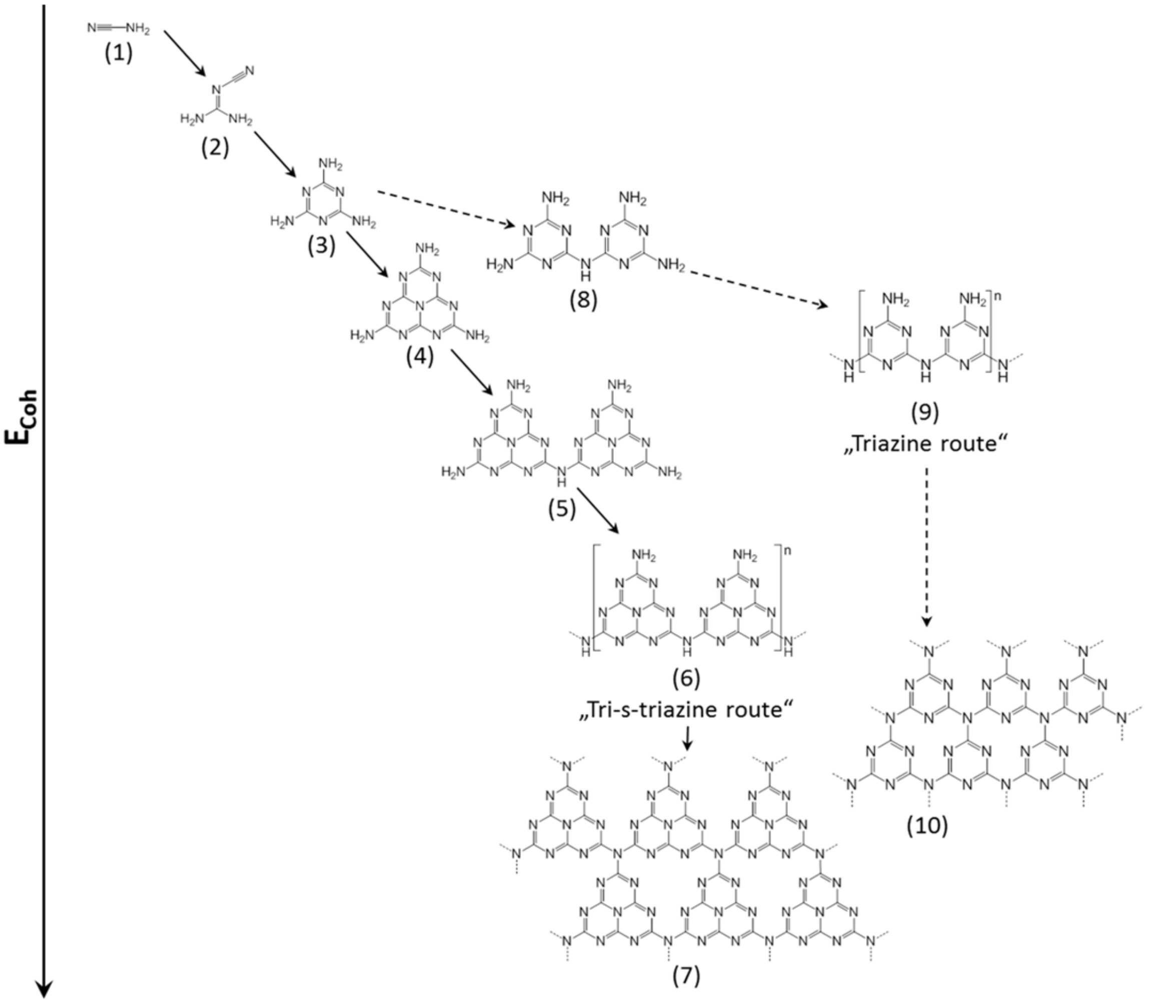

Scheme 2.1. Increase of cohesive energy E_{coh} per mass unit along the condensation of cyanamide (1) into g-C_3N_4 (7), with the intermediates dicyanamide (2), melamine (3), melem (4), di-melem (5) and melon (6) ("tris-s-triazine route") and with the side products melam (8), melamine-chains (9) and triazine-based C_3N_4 (10, "triazine route", dashed lines). The relative contents of E_{coh} are depicted according to ref.48.

Due to their fully conjugated π-electron structures, graphene (and N-doped graphene with quaternary nitrogens) have a vanishingly small band gap and are conducting materials.[61] Contrary to that, the holey tri-s-triazine structure of g-C_3N_4 leads to the opening of a band gap of ≈ 2.7 eV (depending on the degree of condensation), which makes g-C_3N_4 a semiconductor.[56] Basically, semiconducting materials can be capable of photocatalytic reactions, e.g. photocatalytic water splitting or photocatalytic dye degradation. Using the example of g-C_3N_4 for photocatalytic water splitting, the basic principles of semiconductor photocatalysis are shown in **Scheme 2.2**. When light (sunlight or an illuminating light source) with an energy matching or exceeding the band gap energy of the semiconductor is absorbed by this semiconductor, electrons are excited from the valence- (VB) to the conduction band (CB). The semiconductor is now in a "photo-excited" state, with the excited electrons (e^-) in the conduction band leaving behind positively charged holes (h^+). An electron/hole pair is called exciton. Its lifetime depends on the applied material, and is usually in the order of nanoseconds. The photogenerated charge carriers (electrons and holes) can then either recombine (accompanied by the loss of energy as photoluminescence or phonon-vibration), or migrate to the semiconductor surface (dashed arrows in **Scheme 2.2**). Here, at the interface between the surface and the surrounding solution, electrons and holes can take part in redox-reactions. The electron then acts as reducing agent, whereas the holes take part in oxidation reactions.

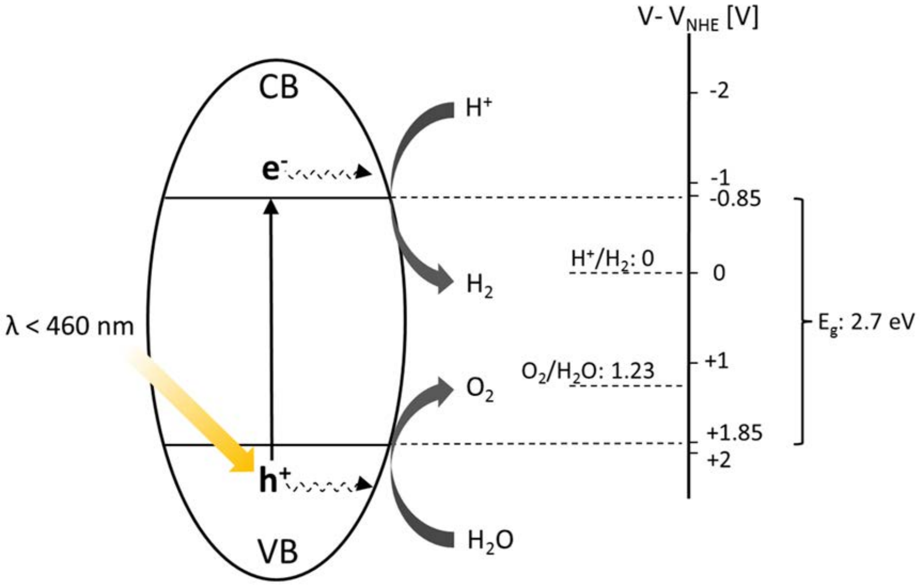

Scheme 2.2. Basic principles of photocatalytic water splitting with a semiconductor, with the positions of the reduction potential of H^+/H_2 (0 V vs. NHE), the oxidation potential of O_2/H_2O (1.23 V vs. NHE) and the potentials for the valence band- (1.85 V vs. NHE) and conduction band edge (-0.85 V vs. NHE) of g-C_3N_4 according to ref. 62.

In photocatalytic water splitting, photogenerated electrons reduce H^+ to hydrogen and holes oxidize OH^- to oxygen. The overall process is endergonic, a standard Gibbs free energy of $\Delta G^0 = 237$ KJ/mol is needed (**Equation 1**).

$$H_2O \rightarrow \frac{1}{2}O_2 + H_2;\ \Delta G^0 = +\,237\ \text{KJ/mol} \qquad \textbf{(Eq.1)}$$

This energy corresponds to a band gap energy of 1.23 eV or light with a wavelength of 1000 nm. However, not only the size of the band gap is important, but also the positions of the valence- and conduction band. The bottom level of the conduction band has to be more negative than the reduction potential of H^+/H_2 (0 V vs. normal hydrogen electrode (NHE)), whereas the top level of the valence band has to be more positive than the oxidation potential of O_2/H_2O (1.23 V vs. NHE).

All these requirements are matched by g-C_3N_4: With an energy of ≈ 2.7 eV (corresponding to a light wavelength of ≈ 460 nm), the band gap is sufficiently large and the band structure is suitable for both water reduction and oxidation.[56] In **Scheme 2.2**, the positions of the valence band edge (1.85 V vs. NHE) and the conduction band edge (-0.85 V vs. NHE) of g-C_3N_4 relative to the reduction potential of H^+/H_2 (0 V vs. NHE) and the oxidation potential of O_2/H_2O (1.23 V vs. NHE) are shown:[62] It can be seen, that the reduction and oxidation potential of water are located within the band gap of g-C_3N_4. Furthermore, g-C_3N_4 is insoluble in water, stable in acidic and basic solution and widely stable against oxidation and photocorrosion.[63] Indeed, the first report of light-driven water splitting with polymeric carbon nitride as photocatalyst, was given in 2008 by Wang et al.[56] However, for applying carbon nitride as a photocatalyst, still certain challenges have to be faced:

I) The overall quantum efficiency for the photocatalytic process is low, which is due to a high recombination rate of the photogenerated charge carriers. In photocatalysis experiments, the recombination rate can be decreased by adding platinum as co-catalyst.[64] However, even if this is done in very low amounts (≈ 0.5 wt%), it basically makes it a not metal-free system anymore.

II) Second, with a band gap of 2.7 eV (which corresponds to absorbing light with $\lambda > 460$ nm), the absorption-coefficient in the visible light part of the spectrum is low, which limits the use of solar light.[56]

III) And third, the activity for oxygen evolution is very low. In photocatalysis experiments, this problem can be bypassed by adding triethanolamine (TEOA) as a sacrificial electron donor to accelerate the oxidation side.[56]

Hence, to apply carbon nitride as completely metal free photocatalyst for the production of hydrogen with solar light, these problems have to be overcome.

It should be noted, that photocatalysis is not limited to the splitting of water. Another important application is the photodegradation of organic molecules, which can be used for removing pollutants from water. The degradation of organic molecules can occur either directly by oxidation with photogenerated holes, or indirect by the reaction with solvent radicals (e.g. $^\bullet$OH-radicals in water) created at the photocatalyst surface.[65] As model compound for organic molecules, usually organic dyes are applied, as here the degradation process can be monitored by UV/Vis-spectroscopy. Carbon nitride has been revealed as an active compound for the photodegradation of several organic dyes (including methylene blue,[66] methyl orange,[67] Rhodamin B (RhB)[68]).

C_2N carbon

Besides graphitic carbon nitride, recently another nitrogen-rich carbon compound with a defined structure was described. A first report on that was given by Fechler et al. in 2015, who prepared a carbon material with an unusually high nitrogen content (36 wt% when prepared at 500 °C) from a eutectic precursor mixture of hexaketocyclohexane octahydrate and urea (**Scheme 2.3**).[69]

For this compound, a composition of "$C_{0.6}N_{0.4}$" was determined by elemental combustion analysis. Powder x-ray diffractommetry (PXRD) analysis indicated a structure of conjugated layers, which are stacked in a graphite-like manner. According to x-ray photoelectron spectroscopy (XPS) measurements, the nitrogen in this material is predominantly bound in pyridinic/ pyrazinic- (67 % of the total nitrogen) and pyrrollic positions (23 %). Only a minor amount of nitrogen is bound in graphitic positions (8 %). The high overall nitrogen content could be retained up to high carbonization temperatures: The material obtained at 800 °C still revealed a nitrogen content of 28 wt%, with still 46 % of the nitrogen bound in pyridinic/ pyrazinic positions and 23 % in pyrrollic positions. The amount of quaternary graphitic nitrogen, which usually increases with increasing carbonization temperature,[36] was then at a still relatively low level of 18 %.

For a carbon/nitrogen compound, these findings were quite surprising and raised the question for structural explanations. The low amount of quaternary nitrogen excludes the formation of N-doped graphite, whereas the overall high nitrogen content at high temperatures excludes the formation of g-C_3N_4. As the only possible way to incorporate pyrazinic nitrogen in a regular fashion and without C-H bonds into a conjugated carbon network, the structural motif which is highlighted in red for structure (2) in **Scheme 2.3** (a) was proposed. This structural element consists of repeating units with a C_2N composition, in which benzene rings are connected with pyrazine units into a conjugated 12-membered ring system (**Scheme 2.3** (b)). However, due to the relatively high amount of pyrrolic nitrogen, a defect-rich structure and absence of long-range order was assumed. The defective C_2N structure was also confirmed by ^{15}N- and ^{13}C-solid state NMR spectroscopy and by electron energy loss spectroscopy (EELS).

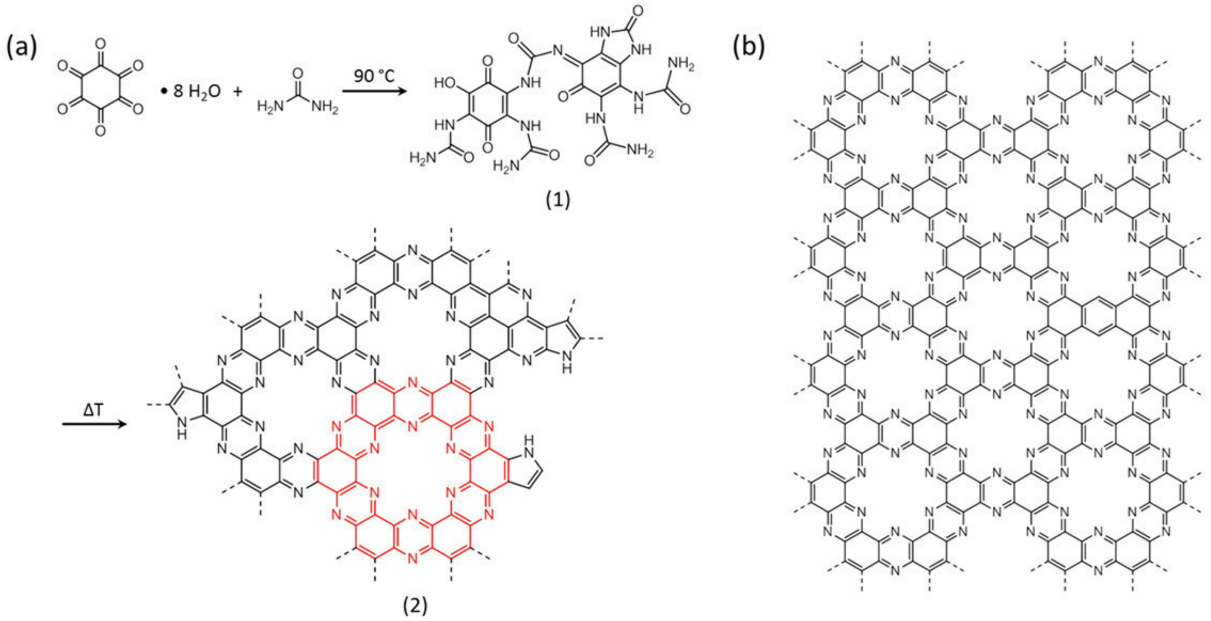

Scheme 2.3. (a) Preparation of C_2N from a eutectic precursor mixture of hexaketocyclohexane octahydrate and urea. According to ref. 69, a representative structure for the intermediate obtained at 90 °C is shown as structure (1), a representative structure for the obtained defective C_2N carbon is shown as structure (2), with the C_2N structural motif highlighted in red. (b) Idealized C_2N structure.

As the hexaketocyclohexane octahydrate/urea precursor system will be applied in this work, the processes occurring during the condensation of the precursor molecules into C_2N will be introduced in more detail.

The condensation process between hexaketocyclohexane octahydrate and urea occurs in several steps. A mixture of hexaketocyclohexane octahydrate and urea in the molar ratio 1:3 forms a deep eutectic, which melts at 68 °C (below the melting points of the respective components). At 90 °C, the color of the molten mixture turns from beige to deep orange, the viscosity increases and the evaporation of H_2O can be observed. As can be seen by optical microscopy of the supercooled 90 °C melt, in the early stages the eutectic melt shows liquid crystalline behavior. With fourier-transformed infrared spectroscopy (FT-IR) and ^{1}H solution state NMR spectroscopy, it could be seen that the eutectic in the early stages is formed due to an extended hydrogen bonding network between the precursor molecules. After the water evaporation, covalent amine linkages are formed, and aromatization sets in. The formation of stacked aromatic networks can be observed with PXRD and is supported by characteristic ^1H solution state NMR signals. Furthermore, the formation of covalent amide linkages can be observed with FT-IR. These findings indicate an intermediate like depicted as structure (1) in **Scheme 2.3** for the late stages of the melt at 90 °C. To obtain C_2N, the 90 °C melt is cooled to room temperature, resulting in a dark red resin, and then carbonized at temperatures above 500 °C under nitrogen atmosphere. During the carbonization process, with increasing temperature the formation of larger stacked aromatic networks can be observed, where nitrogen is incorporated in pyrazinic units, finally condensating into the C_2N structure (structure (2) in **Scheme 2.3**).

It should be noted that it is the special geometry of the precursor complex, which directs the condensation process towards the formation of the C_2N structure. The high order of the liquid-crystalline hydrogen bonded precursor complex aligns molecular entities in positions, which allow for the directed condensation into the C_2N network. During the condensation, the nitrogen atoms are incorporated in stable aromatic position, which leads to their retention during the carbonization process, resulting in the high nitrogen content and high yields. The concept of pre-organizing desired motifs of the carbon material already on the stage of the precursor, will be pursued in this work and is explained in more detail in the next chapter.

Interestingly, the C_2N structure as depicted in **Scheme 2.3** was reported very shortly after also by Baek et al., who used a precursor system also based on hexaketocyclohexane octahydrate.[70,71] Here, hexaketocyclohexane octahydrate was reacted with hexaaminobenzene trihydrochloride in N-Methyl-2-pyrrolidon (NMP) catalyzed by sulfuric acid, resulting in a graphite-like dark black solid. Elemental combustion analysis, XPS, SEM- and TEM- EDS suggested an overall composition of $C_6H_2N_3O$. With XPS, mainly pyrazinic bound, sp^2 hybridized nitrogen was confirmed. After succeeding to deposit this material on a Cu(111)-substrate, the C_2N-structure, could be confirmed with scanning tunneling microscopy (STM). This revealed a holey structure with an interhole-distance of approximately 8 Å. With that findings, Baek et al. denoted the observed C_2N structure as “C_2N-h2D” (here, “h2D” stands for holey and two-dimensional).

Compared to the fully conjugated structures of graphene and nitrogen doped graphene, significantly altered electronic properties can be expected for the C_2N structure with its structural holes. The material synthesized by Fechler et al. from hexaketocyclohexane and urea at 500 °C, possess a pronounced metallic gloss, which is very unusual for such low carbonization temperatures.[69] Conductivity measurements revealed a conductivity of 2 S cm^{-1} at 423 K for the material prepared at 800 °C, Seebeck measurements indicated a mainly n-character for the charge transport. With UV/Vis spectroscopy, for the material synthesized by Baek et al. from hexaketocyclohexane octahydrate and hexaaminobenzene a band gap of 1.96 eV was determined and further confirmed by cyclic voltammogramm (CV) measurements and DFT calculations.[70,71] This makes C_2N a medium band gap semiconductor, with a band gap smaller than that of g-C_3N_4 (≈ 2.7 eV). A further interesting finding for the material prepared by Baek et al., was that the as-prepared C_2N-h2D crystals (before annealing) showed semi-metallic behavior in a field-effect transistor with a high electron- (13.5 $cm^2V^{-1}s^{-1}$) and hole- (13.5 $cm^2V^{-1}s^{-1}$) mobility.[70,71] The authors attributed this to doping effects of residual impurities and/ or adsorbed gases.

The findings that C_2N is a material with a medium band gap and at the same time can reveal good electronic conductivity and high mobility for charge carriers (upon doping or with the introduction of defects), make this material a promising compound with regard to electronic applications.

2.2 “All-carbon”-heterojunction materials

2.2.1 The physics of heterojunctions

In the previous chapter, it was described how the electronic properties of carbon/nitrogen compounds can be tuned by their nitrogen content. Whereas carbon and nitrogen-doped carbons are electrical conductors with a vanishingly small band gap, the carbon nitrides g-C_3N_4 and C_2N are semiconductors with band gaps of ≈ 2.7 eV and ≈ 1.96 eV, respectively.[56,70,71]

This in principle makes it possible to fabricate an “all-carbon” heterojunction, i.e. bringing carbon materials with different electronic properties in contact. The interface between a semiconductor and a material with different electronic properties, i.e. between a conductor and a semiconductor, between two semiconductors with different band structures or between differently doped semiconductors (n-doped and p-doped semiconductor) is referred to as a heterojunction. At a heterojunction, electronic phenomena are occurring, which are the basis for important semiconductor applications like solar cells, transistors or photocatalysis. The reason for the observed electronic phenomena at the heterojunction is a bending of the semiconductor band structure towards the interface. The characteristics of the band bending depend on the applied electronic system, i.e. if it is a metal/ semiconductor or a semiconductor/ semiconductor interface. As in this work the semiconductors g-C_3N_4 and C_2N are used, a heterojunction between two semiconductors will be described in more detail.

To describe the band bending at the interface region between two semiconductors, certain characteristics of the respective components have to be considered: These are the energy positions of the valence band edge (E_{VB}, the highest electronic state in the valence band), the conduction band edge (E_{CB}, the lowest electronic state in the conduction band) and the Fermi level (E_f). The energy of the Fermi level correlates to the chemical potential of the electrons in the semiconductor and is the (hypothetical) energy level which is occupied with an electron by the probability of 50 %. The separation between the valence band edge and the conduction band edge is the band gap (E_g, see **Scheme 2.4**). Depending on the differences ΔE_{VB} and ΔE_{CB} between the respective E_{VB} and E_{CB} values of two semiconductors, three types of semiconductor-heterojunctions are distinguished (**Scheme 2.4** (a)):

I) Type I (“straddling gap”): Here, the band gap of one component is included in the band gap of the other one.

II) Type II ("staggered gap"): The band gap overlaps, but the E_{VB} and E_{CB} values of one component are of lower energy than for the other component.

III) Type III ("broken gap"): Like for type II, the E_{VB} and E_{CB} values of one component are of lower energy than for the other component, but the band gaps do not overlap.

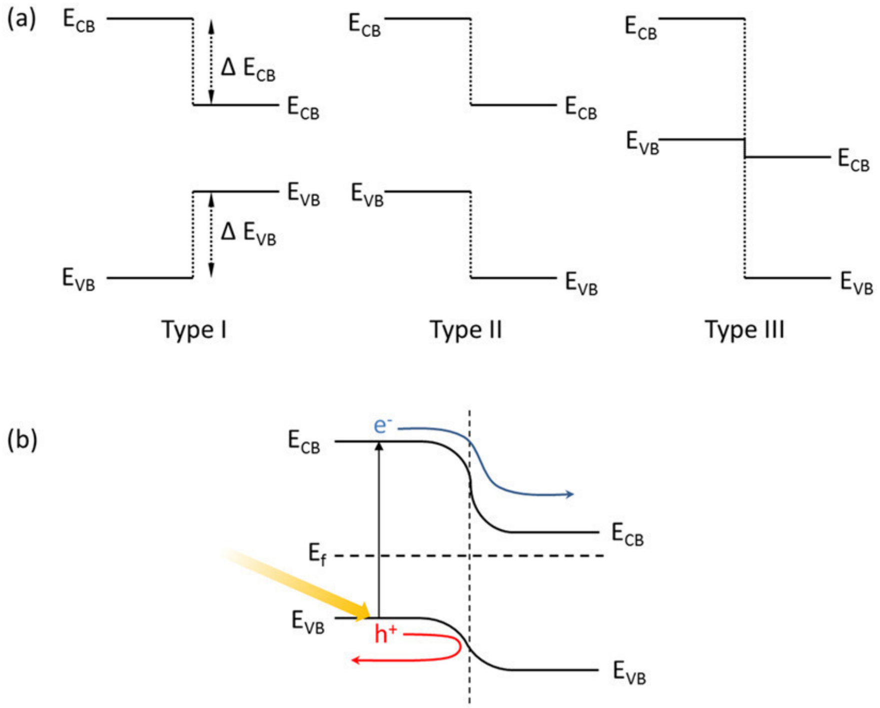

Scheme 2.4. (a) Different types of semiconductor heterojunctions. (b) Band-alignment and separation of photogenerated charge carriers for a type II heterojunction. Blue arrow indicates the transfer of photoexcited electrons (e^-) across the interface, while the transfer across the interface for the photogenerated holes (h^+) is energetically not favored (red arrow).

If the two semiconductor materials are brought into contact, differences in the chemical potential of the electrons (i.e. different Fermi-Levels on both sides) will result in the flow of charge carriers from one side to the other, until thermodynamic equilibrium is reached. This leads to a bending of the band edges towards the heterojunction and a space-charge region around the interface. The bendings of the band structures at a heterojunction are depicted in **Scheme 2.4** (b), applying the example of a type II heterojunction.

Band structure bending affects the flow of charge carriers across the semiconductor/ semiconductor interface, as the drop or increase of the conduction- or valence band edge means an altered energy level of the charge carriers: Hence, the flow of the charge carriers in certain directions would be an energetic uphill process, and for that reason will not take part. The energetically favored direction of the charge carrier flow depend on the type of the heterojunction: In Type I heterojunctions, migration of charge carriers from the large band gap to the small band gap material is accompanied by a gain of energy, whereas the other way round additional energy is required. Thus, type I heterojunction devices are capable of trapping the charge carriers in one material. In a type II heterojunction, migration of the electrons from the material with a higher conduction band edge across the interface is energetically favoured, whereas the migration of holes is favored in the other direction (see **Scheme 2.4** (b)). The same effect applies for type III heterojunctions, but even more pronounced. Hence, type II and type III heterojunctions facilitate the separation of charge carriers.

This is of great importance for certain applications, e.g. in photocatalysis: One of the major challenges for photocatalysts, is it to decrease the rate of charge carrier recombination. This can be achieved by making a type II heterojunction between the photocatalyst and another semiconductor as co-catalyst: When excitating near the interface region, photogenerated electrons are drained towards the co-catalyst, whereas the photogenerated holes will not cross the interface region. This leads to a spatial separation between electrons and holes and thus prevents their recombination and increases the quantum efficiency (i.e. the ratio between incident photons and generated hydrogen molecules) of the photocatalyst.

2.2.2 “All-carbon” heterojunction composites

In principle, all three types of heterojunctions could be achieved by combinations of carbon or carbon/nitrogen compounds, as with different members of this materials “family” a broad range of band-structures is covered.

An “all-carbon” heterojunction would combine several advantages: Carbon compounds are non-toxic, they can be derived from cheap and naturally abundant materials and they are of good chemical and thermal stability. And furthermore, with a composite made from similar materials, the problem of the lattice-mismatch is minimized, which for a composite between different materials leads to a performance-lowering contact resistance.

For a heterojunction which can be applied in photocatalysis, two components are needed: A photoactive material with a band structure fitting to the occuring redox processes, and a co-catalyst which allows electronic contact and thus a heterojunction band alignment. Due to a suitable band structure and a good stability, the carbon/nitrogen compound which is usually applied as active compound in photocatalytic reactions, is g-C_3N_4 (see chapter 2.1.2 on carbon nitride). However, as with many photocatalyst, also g-C_3N_4 is characterized by a relatively high charge carrier recombination rate, resulting in a low quantum efficiency. To prevent this, there are already various reports on the construction of a type II heterojunction of g-C_3N_4 with various inorganic semiconductors (including TiO_2,[72] Ag_2CO_3,[73] Ag_3PO_4,[74] AgBr,[75] AgI,[75] CdS,[76] and several others[77]), which finally significantly increased the photocatalytic performance in water splitting or dye degradation. However, applying transition metal based co-catalysts destroys the metal-free character of the g-C_3N_4 system. Hence, a metal-free "all-carbon" heterojunction between g-C_3N_4 and another carbon or carbon/nitrogen compound would be highly desirable.

First attempts towards an "all-carbon" heterojunction for photocatalytic water splitting were made in 2011 by Jaroniec et al., who prepared a composite of g-C_3N_4 and graphene.[78] The obtained increased photocatalytic activity was attributed to a charge carrier separation at the graphene/g-C_3N_4 interface, as well as to an increased optical absorption of the composite. However, the exact underlying mechanisms were not completely resolved. In a following study by Smith et al., DFT calculations revealed that at the graphene/g-C_3N_4- interface electronic coupling occurs, which leads to the opening of a small band gap of 70 meV in the graphene.[79]

Also g-C_3N_4/g-C_3N_4- composites have been reported, where between g-C_3N_4 and sulfur-doped g-C_3N_4 a type II heterojunction is formed.[80,81]

Very recently, the preparation of a composite of mesoporous g-C_3N_4 nanofibers coated with nitrogen-doped carbon has been reported.[82] When tested for photocatalytic water splitting, the obtained material was capable of an extremely high rate of hydrogen production from water (18.3 times higher than pure g-C_3N_4, even without platinum as co-catalyst). The authors attributed the increased photocatalytic efficiency to an improved optical absorption and an efficient charge carrier separation due to the nitrogen-rich carbon.

There are several other reports on the preparation of "all-carbon" composites, however not for photocatalysis, but as electrode material for electrochemical water splitting[83-85] or fuel cell applications.[86-88]

As stated before, the recently discovered C_2N possesses properties which are complementary to form an efficient photocatalyst with g-C_3N_4. It possesses a smaller band gap than g-C_3N_4 (1.96 eV[70] vs. 2.7 eV for g-C_3N_4[56]) and a high charge carrier mobility (see chapter 2.1.2),[70] which makes it likely that in a heterojunction between the two components the transport of photogenerated electrons from g-C_3N_4 to C_2N is facilitated. In respect to g-C_3N_4, the optical absorption of C_2N is shifted further towards the visible light range.[70] As the low optical absorption of g-C_3N_4 in the visible light range is one of the major drawbacks for the use of g-C_3N_4 in photocatalytic applications, a composite with C_2N can be a way to achieve a better light harvesting.

Indeed, in a recently published study which was motivated from the previous discovery of the synthesis of C_2N, it was calculated with DFT that the g-C_3N_4/C_2N- interface is a type II heterojunction, with a valence band offset (difference in the potentials of the valence band edges) of 0.1 eV and a conduction band offset (difference in the potentials of the conduction band edges) of 0.4 eV, respectively.[89] The potentials for the splitting of water (reduction of H^+ to H_2 and oxidation of H_2O to O_2) are located inside the calculated band gap of the g-C_3N_4/C_2N- composite, which makes it a potential candidate for photocatalytic water splitting. It was also calculated that compared to the pure materials, the band gaps for the respective materials in the composite are slighty widened (3.01 eV for g-C_3N_4 in the composite vs. 2.7 eV[56] for pure g-C_3N_4 and 2.7 eV for C_2N in the composite vs. 1.96 eV[70] for pure C_2N).[89] A scheme for the aligned band structures of the g-C_3N_4/ C_2N- heterojunction as calculated in ref. 89, is shown in **Scheme 2.5**. The conduction- and valence band edge of C_2N in the composite are located at lower energies compared to g-C_3N_4: This facilitates the transport of photogenerated electrons in g-C_3N_4 across the interface into C_2N (blue arrow in **Scheme 2.5**), while photogenerated holes remain on the g-C_3N_4– side (red arrow in **Scheme 2.5**). Vice versa, photogenerated electrons in the C_2N remain on this side, whereas the migration of holes across the interface into g-C_3N_4 is favored. In combination with the experimentally obtained fast charge carrier transport in C_2N, for the g-C_3N_4/C_2N composite an efficient separation of the photogenerated charge carriers can be expected.

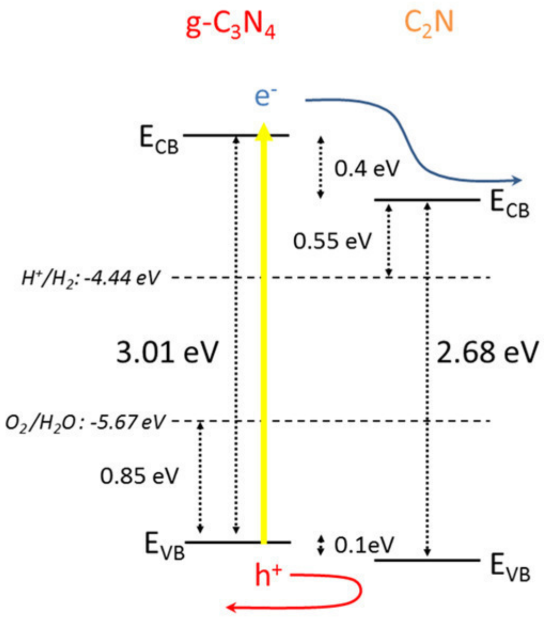

Scheme 2.5. Schematic plot of the band alignment for the g-C_3N_4/C_2N heterojunction as calculated in ref. 89, with the relative positions of the conduction band edges (E_{CB}) and valences band edges (E_{VB}) and the reduction potential of H^+/H_2 (-4.44 eV) and the oxidation potential of O_2/H_2O (-5.67 eV). Blue and red arrow indicate the separation of photogenerated electrons/ holes at the interface.

It was also calculated that the g-C_3N_4/C_2N composite has a broad absorption in the visible- and UV-light region, with a high absorption coefficient of 10^4 cm^{-1}.[89] Thus, a composite with C_2N would also increase the low optical absorption of g-C_3N_4 in the visible light region. Taking together the increased optical absorption and an enhanced separation of the charge carriers, it can be expected that making a composite with C_2N would significantly increase the photocatalytic activity of g-C_3N_4. Furthermore, the DFT calculations presented in ref. 89 predicted that the formation of the g-C_3N_4/ C_2N interface from the single components is exothermic.

However, even though C_2N was independently two times discovered synthetically before theoretical calculations to the composite were made, up to now a g-C_3N_4/C_2N- composite has not been synthesized yet. It is therefore the main objective of this work to synthesize an "all-carbon" heterojunction from g-C_3N_4 and C_2N for photocatalytic applications. This includes the research on the synthesis and appropriate structuring methods for each carbon material, as up to now this remains challenging.

2.3 “Rational design” of C_xN_y materials

Carbon materials are usually obtained by carbonization, i.e. the heating of organic precursors under inert atmosphere.

However, the problem with carbonization reactions is that processes occurring at high temperatures are not easy to control, which makes carbonization reactions some sort of “black box process”. Additionally, most organic molecules decompose at higher temperatures into low-molecular weight volatile fragments (e.g. CO, CO_2, water, ammonia, H_2S), leaving behind not much of a residue.

Hence, the quest for suitable precursors and structuring methods for a desired carbon material are not a trivial task. This problem becomes even more complicated, when carbons with special properties are needed, such as carbon/nitrogen compounds with the nitrogen being in a desired bonding state (graphitic, pyrazinic, etc.). For the material chemist who targets a specially designed carbon for a particular application, a precursor has to be found which upon heat treatment reacts towards a carbon with desired structural motifs.

An attempt towards this is the idea of pre-organizing the desired motifs of the final carbon material already on the stage of the precursor.[12] This can be achieved by applying precursors which contain fragments of the desired carbon motifs, which are stable and already give a guide-line for a potential reaction path, leading to the desired motif in the final carbon. Such potential reaction paths can be organic reactions like condensation, cyclization, Diels-Alder reactions or defined elimination schemes. With the idea of the pre-organized precursors, the rather randomly occurring carbonization process is in an ideal case replaced by a controlled condensation of neighbored molecular entities.

Pre-organization can be achieved with several precursor systems, like polymers or other large molecules.[12] They are not volatile and can contain molecular motifs of high thermal stability, which means that they can be transferred into carbon materials in high yields and with preservation of their certain structural motifs. Here, interaction forces like hydrogen bonds and electrostatic interactions become the main prerequisites for the formation of pre-organized precursors. Eventually, suitable substances have to fulfill these criteria.

This work is focused on supramolecular assemblies as precursors. In supramolecular assemblies, molecules as building blocks are assembled by non-covalent, reversible interactions (e.g. hydrogen-bonding, van der Waals-interactions, π-π-interactions, etc.) into larger, highly ordered assemblies.[13] The supramolecular assemblies applied in this work include 2D hydrogen-bridged supramolecular complexes, liquid crystalline precursors and organic crystals.

2.3.1 Supramolecular chemistry

Supramolecular chemistry is the field of chemical systems, in which molecules as building blocks assemble to larger superstructures, the supramolecules (supramolecular complexes, supramolecualr assemblies), by non-covalent, reversible interactions. Examples for supramolecular systems include bio-molecules like DNA, enzyme-interactions, micelles, organic crystals or liquid crystalline systems. Using an analogy made in 1988 by one of the pioneers of modern supramolecular chemistry, Jean-Marie Lehn, "supermolecules are to molecules and the intermolecular bond what molecules are to atoms and the covalent bond."[13] Such "intermolecular bonds" are weak, reversible interactions like hydrogen bonding, hydrophobic forces, metal-coordination, π-π-interactions, electrostatic effects, or van der Waals-forces.

Supramolecular assemblies are interesting for carbon synthesis in that sense, as they provide highly organized precursor complexes, in which adjacent molecular entities can contain pre-formed units of the final carbon material and thus pre-determine certain reaction pathways. With a broad variety of organic molecules as potential building blocks, various combinations of suitable molecules into supramolecular assemblies allows for the targeted synthesis of carbon materials with desired structural motifs.

The synthesis of organic supramolecular complexes with desired structural motifs is the field of organic crystal engineering. Supramolecular assemblies and organic crystals can be formed by self-assembly of suitable molecules via molecular recognition: Due to specific, directed interactions like hydrogen bonding, under the right reaction conditions suitable molecules can "recognize" each other and arrange in ordered patterns. It is one of the main tasks of organic crystal engineering, to build desired larger structural units in a supramolecular complex by the assembly of suitable molecules.[90] For the relation between those larger structural units and the molecules they are assembled of, Desiraju, one of the pioneers of organic crystal engineering, introduced the term "supramolecular synthon", which he defined as the structural units in a supramolecular complex that can be formed by intermolecular interactions by a known synthetic procedure.[90]

Of special interest for the preparation of supramolecular assemblies are molecules which can assemble due to hydrogen bonding. Hydrogen bonds are strong but reversible interactions.

They are directed, which allows for geometrical considerations for the design of hydrogen bonded supramolecular complexes. The supramolecular assemblies applied as precursors for the synthesis of carbons in this work, are based on hydrogen bonding. In the next chapter a hydrogen-bonded supramolecular precursor complex for the synthesis of g-C_3N_4 is presented, which is applied in this work.

2.3.2 The cyanuric acid/melamine complex as precursor for g-C_3N_4

In **Scheme 2.1** in chapter 2.1.2, the condensation cascade of melamine into g-C_3N_4 is shown. For this process, not only melamine but also molecules that decompose during heating into melamine (like cyanamide or dicyanamide) can be applied. However, the quality of the obtained g-C_3N_4 in degree of condensation and crystallinity greatly depends on the applied precursor. For instance, it has been shown that for applying pure melamine as precursor, to a certain degree the condensation process does not proceed further than to the stage of the polymeric melon (structure (6) in **Scheme 2.1**).[91] Another problem of applying melamine as precursor is the easy sublimation of this compound.

A precursor system to g-C_3N_4 which overcomes the problems of incomplete condensation and precursor sublimation is the supramolecular complex between melamine and cyanuric acid (in this work denoted as CM-complex, **Scheme 2.6**). In this complex, which was first described by Whitesides et al. in 1991,[92,93] melamine ((1) in **Scheme 2.6**) and cyanuric acid ((2) in **Scheme 2.6**) self-assemble into a planar 2D complex ((3) in **Scheme 2.6**) by three hydrogen bonds per molecule. The hydrogen bonding pairs are formed between the melamine NH_2-groups and the cyanuric acid carbonyl-groups, and between the melamine triazine-nitrogens and the cyanuric acid NH-groups (see **Scheme 2.6**). The complex can be prepared by shaking equimolar amounts of cyanuric acid and melamine in a solvent (e.g. water,[92,93] ethanol,[94] dimethylsulfoxide (DMSO),[95] chloroform[94]), which leads due to self-assembly of the respective components to the precipitation of the solid complex.

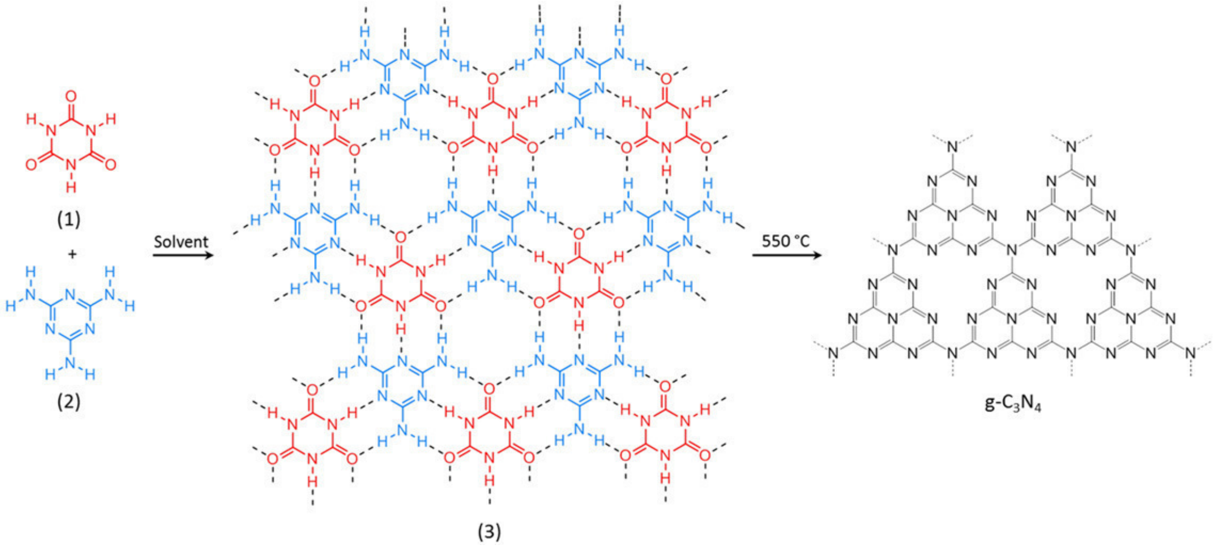

Scheme 2.6. Formation of the hydrogen-bonded cyanuric acid/melamine complex (CM complex) (3) from cyanuric acid (1) and melamine (2). Dashed lines indicate hydrogen bonds. When carbonized at 550 °C, the CM complex can be transformed into g-C_3N_4.[95,96]

The first report on applying this complex as precursor to g-C_3N_4, was given by Thomas et al. in 2013, who obtained g-C_3N_4 by heating the solid complex to 550 °C under nitrogen atmosphere.[95,96] The formation of g-C_3N_4 from the precursor complex occurs due to the reaction of cyanuric acid with ammonia (which is released from the condensation of melamine) at temperatures above 325 °C into melamine, which then condensates into g-C_3N_4. The CM complex as precursor to g-C_3N_4 can serve as a perfect example for the above described concept of gaining more control over the carbonization process by pre-organization and fixation of precursor molecules: In contrast to the rather randomly and poor controllable condensation of single molecule precursors (like melamine) to g-C_3N_4, for the supramolecular CM precursor complex the carbonization process is directed by the pre-organization of molecular entities. In the CM complex, the triazine-units of the final carbon nitride are already pre-aligned in the form of the hydrogen- bonded melamine and cyanuric acid molecules. This spatial proximity facilitates complete condensation and the hydrogen bonds prevent the sublimation of melamine. Furthermore, it is known from other heteroatom-containing precursors for g-C_3N_4 (like urea, thiourea or trithiocyanuric acid) that additional heteroatoms like oxygen or sulfur provide further leaving groups, which facilitate the condensation process and lead to more condensed g-C_3N_4-structures.[97,98] The higher degree of condensation for the g-C_3N_4 obtained from the CM-complex when compared to g-C_3N_4 prepared from melamine or dicyandiamide, is reflected in a lower distance between the tri-s-triazine- layers.[95]

The CM precursor complex not only leads to higher quality g-C_3N_4, but also allows for additional opportunities to process carbon nitride. Processing of carbon nitride, e.g. coating of electrodes for electrochemical applications (like water electrolysis, fuel cells or solar cells) is not an easy task, as carbon nitride is insoluble and the carbon nitride prepared from the most precursors has a large particle size. For deposition methods like spin coating and screen printing, this leads to a poor coverage and low adhesion of g-C_3N_4 on the most substrates. Thus, methods for processing g-C_3N_4 on conductive substrates are highly desired. Here, applying the CM complex offers a solution, as the precursor complex contains free hydroxy- and amino-groups, which allow for attachment on different substrates. Shalom et al. showed that the CM-complex can be deposited on glass, as well as on conducting materials like fluorine-doped tin oxide (FTO) and porous metal oxide electrodes (TiO_2, ZnO), due to interactions between the substrate and the hydroxyl- and amino-groups of the CM-complex.[99] After carbonization, the resulting g-C_3N_4 was still tightly bound to the substrate. The carbon nitride coated on a FTO-electrode, revealed a high activity for the electrochemical hydrogen evolution from water. Another possibility to process carbon nitride can be achieved with a slightly modified precursor complex: If melamine in the CM complex is replaced by a melamine-derivative with a phenyl-group at the C6-position (2,4-diamino-6-phenyl-1,3,5-triazine), a hydrogen-bonded precursor complex is obtained which turns to liquid at temperatures above 350 °C and also leads to the formation of g-C_3N_4 upon carbonization.[100] Hence, this precursor complex (here denoted as CMp-complex) can as well be applied for the coating of substrates.

A strength of the CM-complex as precursor system is the opportunity to address desired changes in the carbon nitride properties (e.g morphology, electronic properties) by targeted variations of the structure of the precursor complex. This can be done as illustrated above for the CMp-complex by using derivatives of the precursor molecules, or by adding a third component which as well can fit by hydrogen bonding into the precursor complex. For instance, it is known that if dicyandiamide is co-condensated with small amounts of barbituric acid, the resulting g-C_3N_4 has an enhanced optical absorption.[101] The explanation for this is that for every incorporated barbituric acid molecule, in the resulting g-C_3N_4 a nitrogen atom is replaced by a carbon atom, which alters the electronic structure. Barbituric acid can be also incorporated into the CM-complex by hydrogen bonding:[102] After carbonization, a carbon nitride material with domains of different C/N-ratios is obtained. As the C/N-ratio affects the electronic properties, the obtained material obtains local differences in the electronic structure. At the interfaces of these domains, heterojunctions are formed. Thus, the incorporation of barbituric acid leads to the formation of in-situ heterojunctions. It could be shown, that the carbon nitride obtained from the barbituric acid- doped CM-complex obtains an increased activity in photocatalytic water splitting. This was attributed to the higher optical absorption and to the *in-situ* formation of the heterojunctions, which favor the separation of photogenerated charge carriers. Furthermore, by addition of barbituric acid also the optical properties of carbon nitride derived from the CMp precursor can be tuned. In combination of both concepts, Shalom et al. succeded in fabricating an organic solar cell by coating barbituric acid- doped CMp- carbon nitride on a TiO_2/ITO substrate.[100] This proof-of-concept solar cell revealed an open circuit voltage of more than 1 V, which is a record value for organic systems.

In chapter 4.1, another possibility to tune the photocatalytic activity of g-C_3N_4 by adding a third compound to the CM precursor complex will be presented.

2.3.3 The hexaketocyclohexane/urea eutectic as precursor for C_2N

Another supramolecular precursor system which is applied in this work is the hexaketocyclohexane octahydrate/ urea precursor for the synthesis of C_2N.

As described in chapter 2.1.2, a mixture between hexaketocyclohexane octahydrate and urea in the molar ratio 1:3 forms a deep eutectic, which melts at 68 °C and shows liquid crystalline behavior.[69] For the material obtained from carbonizing this precursor complex at 800 °C, a defective C_2N structure as presented in **Scheme 2.3** (see chapter 2.1.2) was confirmed.

This precursor complex is a further example for the concept of gaining more control over the carbonization process by pre-organizing desired motifs of the carbon material already on the stage of the precursor, which substitutes the rather randomly carbonization process by the controlled condensation of adjacent molecular entities. This allows for the preparation of carbons in high yields, with the retention of nitrogen atoms at desired atomic positions.

Due to its low melting point, the hexaketocyclohexane/ urea eutectic allows for several processing possibilities.[69] The melt can be used for coating on substrates or molding into macroscopic shapes. Furthermore, templating techniques can be applied. With SBA-15, a mesoporous silica template, nanostructured C_2N can be obtained. Another approach to get nanostructured materials which can be applied to the hexaketocyclohexane/ urea eutectic, is the so-called salt-templating.[31] Here, inorganic salts are dissolved in a liquid precursor. When carbonizing this mixture, the salt phase can act as a “molecular template”, by forming ion-pairs or small salt clusters in the precursor phase. The salt can be washed out after the carbonization process is completed, leaving behind the porous carbon material. This templating method has several advantages: The dissolved salt as a template is homogenously distributed in the liquid precursor phase, leading to homogenously distributed pores. Furthermore, with the nature and the concentration of the salt, the pore size can be tuned. However, this method requires precursors which are liquid at one point of the synthesis, to achieve homogenous distribution of the applied salt. For the synthesis of porous carbon materials, ionic liquids are suitable precursors.[31] However, due to the liquid nature of the hexaketocyclohexane/ urea deep eutectic, also this precursor system can be processed by salt-templating. With $ZnCl_2$ as salt-template, microporous nanolayers of C_2N carbon with a specific BET surface are of 1512 m^2g^{-1} were obtained.[69]

In chapter 4.2.1, another possibility for processing the hexaketocyclohexane/ urea precursor will be presented.

3 Outline

This work targets the synthesis of a heterojunction solely from carbon-based materials, i.e. an "all-carbon heterojunction". Here, the difference in electronic properties of the two components is achieved by the introduction of different nitrogen motives into the carbon lattice. For the two components, the semiconductor g-C_3N_4 and the recently described less nitrogen containing C_2N will be used.

As described in chapter 2.2.2, a g-C_3N_4/C_2N composite is a promising material for photocatalytic applications, like photocatalytic water splitting or -dye degradation. The smaller band-gap of C_2N extends the optical absorption of the composite further into the visible light range. At the interface, band-alignment to a type II heterojunction is predicted, which promotes the separation of photo-generated charge carriers and thus leads to an increased quantum efficiency for the composite.[89] Efficient charge-carrier separation will also be supported by the high charge-carrier mobility observed for C_2N.[70] It has furthermore been calculated, that the interface formation between C_2N and g-C_3N_4 is exothermic.[89]

With the central aim of constructing a g-C_3N_4/C_2N "all-carbon composite" for photocatalytic water splitting, this work is divided into three parts. An overview to the chapters in the discussion part of this work, are depicted in **Scheme 3**.

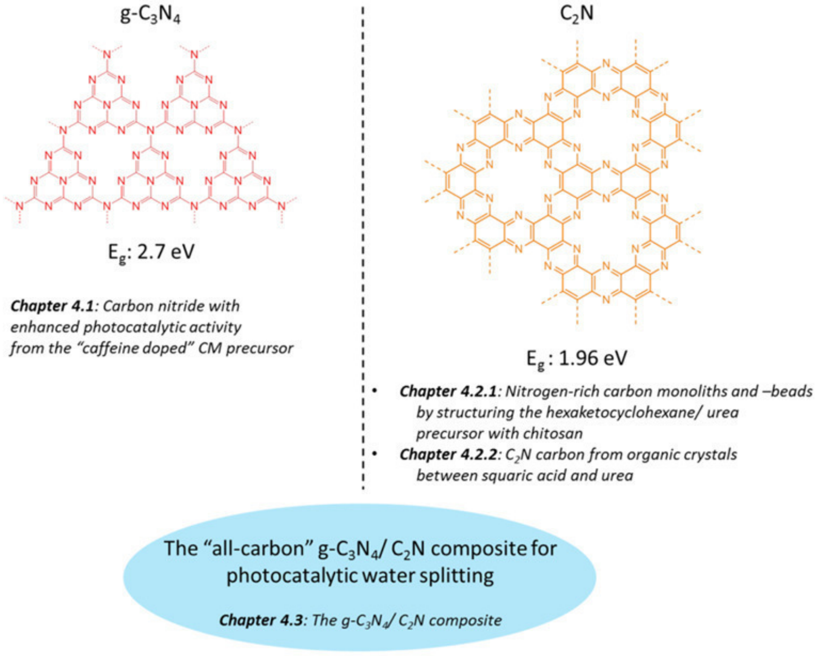

Scheme 3. Overview to the chapters in the discussion part. Band gap energies E_g for g-C_3N_4 and C_2N were taken from ref. 56 and ref. 70, respectively.

In the first part (chapter 4.1), component one of the desired composite is in the focus, which is the photoactive semiconductor g-C_3N_4. Here it is demonstrated how with pre-organizing precursor molecules in a supramolecular complex, targeted variations in the properties of g-C_3N_4 can be addressed. By introducing caffeine as “growth-stopper” molecule into the supramolecular cyanuric acid/melamine precursor complex, defects in the final g-C_3N_4 are induced, which lead to an increased photocatalytic activity of the obtained material.

The second part (chapter 4.2) is focused on C_2N as the second component of the desired composite. As C_2N is an only recently described compound, the composite preparation comprises the inherent difficulty that there is not much known yet about processing C_2N, or how to obtain it from different precursors. Hence, this chapter presents attempts towards the processing of a known C_2N precursor, which is the hexaketocyclohexane/urea eutectic, as well as the exploration of a novel precursor system for C_2N. In chapter 4.2.1, attempts towards structuring the hexaketocyclohexane/urea precursor with the biopolymer chitosan are presented. Guided by the concept of pre-organization on the precursor stage, in chapter 4.2.2 attempts towards the preparation of C_2N from an organic crystalline precursor from squaric acid and urea are presented.

Finally, in the third part (chapter 4.3), first attempts towards combining g-C_3N_4 and C_2N into a composite material are presented. Here, attempts towards the self-assembly of exfoliated nanolayers of g-C_3N_4 and C_2N carbon are presented. The preparation of nanolayers should be achieved by sonicating dispersions of the respective components. As components, g-C_3N_4 from the CMp-precursor and the material obtained from the squaric acid/urea precursor are applied. The obtained composites are then tested for their activity in photocatalytic water splitting.

4 Results and Discussion

4.1 g-C_3N_4 with enhanced photocatalytic activity from a "caffeine doped" CM precursor

In chapter 2.1.2, it was described that g-C_3N_4 is a promising material for metal-free photocatalysis. It has a band gap and band structure suitable for photocatalytic water splitting (see **Scheme 2.2**), is insoluble in water and the most solvents, highly stable in most chemical environments and against photocorrosion and it can be synthesized from cheap and non-toxic precursors. However, challenges for the use of g-C_3N_4 are the low optical absorption in the visible light range and the relatively high rate of photogenerated charge carrier recombination. Central aim of this work is it to overcome these problems by preparing a composite with C_2N. In this work, the components of this composite are prepared from pre-organized precursors, where desired motifs in the carbon/nitrogen materials are already pre-organized on the precursor stage. This concept will be presented in this chapter, by attempts towards increasing the photocatalytic activity of g-C_3N_4 by applying specially designed precursor complexes.

It has been observed in heterogeneous catalysis, that materials which have a certain degree of defects or are rich in surface terminations (like edges), are superior in their catalytic activity when compared to their more crystalline counterparts.[40,41] For heterogenous catalysis, defects and surface terminations are regarded as the catalytic active sites. In photocatalysis, defects or surface terminations can lead to an increased photocatalytic activity, however, too high concentrations of these sites can also have the contrary effect.[103-105] Defects or surface terminations are the interface between the crystalline material and the vacuum or amorphous domains. At this interface, the electronic band structure of the bulk material changes, which leads to the creation of new electronic states, the so called defect- or surface states. For semiconductors, defect- or surface states are usually located in the band gap right below the conduction band.[106-108] In Photocatalysis, these states can "trap" photogenerated charge carriers, which prevents them from their recombination and thus leads to an increased photocatalytic activity.[103-105]

In this chapter, the approach is presented to enhance the photocatalytic activity of g-C_3N_4 by the targeted introduction of defects or surface terminations. This is done by applying a modified supramolecular cyanuric acid/ melamine complex as g-C_3N_4 precursor.*

---

* The results of this approach are published by the author of this thesis as: T. Jordan, N. Fechler, J. Xu, T. J. K. Brenner, M. Antonietti, M. Shalom: "Caffeine Doping" of Carbon/Nitrogen-Based Organic Catalysts: Caffeine as a Supramolecular Edge Modifier for the Synthesis of Photoactive Carbon Nitride Tubes, *ChemCatChem* **2015**, *7*, 2826–2830 (ref. 68).

As presented in chapter 2.3.2, cyanuric acid and melamine can assemble into a supramolecular complex by hydrogen bonding, which can be applied as precursor for g-C_3N_4 (see **Scheme 2.6**). Given enough supply from the monomers cyanuric acid and melamine, the precursor complex can potentially grow endlessly. However, here the idea is it to integrate a "growth-stopping" molecule into the CM precursor complex, which blocks the growth of the precursor complex at certain sites and this way induces structural vacancies in the precursor complex, which can be preserved as defects or surface terminations in the g-C_3N_4 after carbonization. As defects or surface terminations are regarded to increase the (photo)catalytic activity, integrating a "growth stopper" molecule into the precursor complex can be a way to increase the photocatalytic activity.

As a "growth-stopper", caffeine was chosen. Like cyanuric acid, the caffeine molecule obtains two carbonyl groups in a 120° angle, which potentially allows it to integrate into the CM complex by two hydrogen bonds (see **Scheme 4.1.1**). However, at the sides of assimilated caffeine molecules, further growth of the CM complex is blocked in one direction, as the caffeine molecule does not provide further sides for hydrogen bonding. Consequently, the caffeine might induce vacancies in the 2D CM complex. The supramolecular precursor complexes are then transformed into g-C_3N_4 by heating to 500 °C under nitrogen atmosphere. During this process, structural vacancies in the CM complex might be preserved as defects or surface terminations in the final g-C_3N_4 materials, leading to an improved photocatalytical performance. This way, "caffeine-doping" of the CM precursor would provide an easy route to enhance the photocatalytic activity of g-C_3N_4.

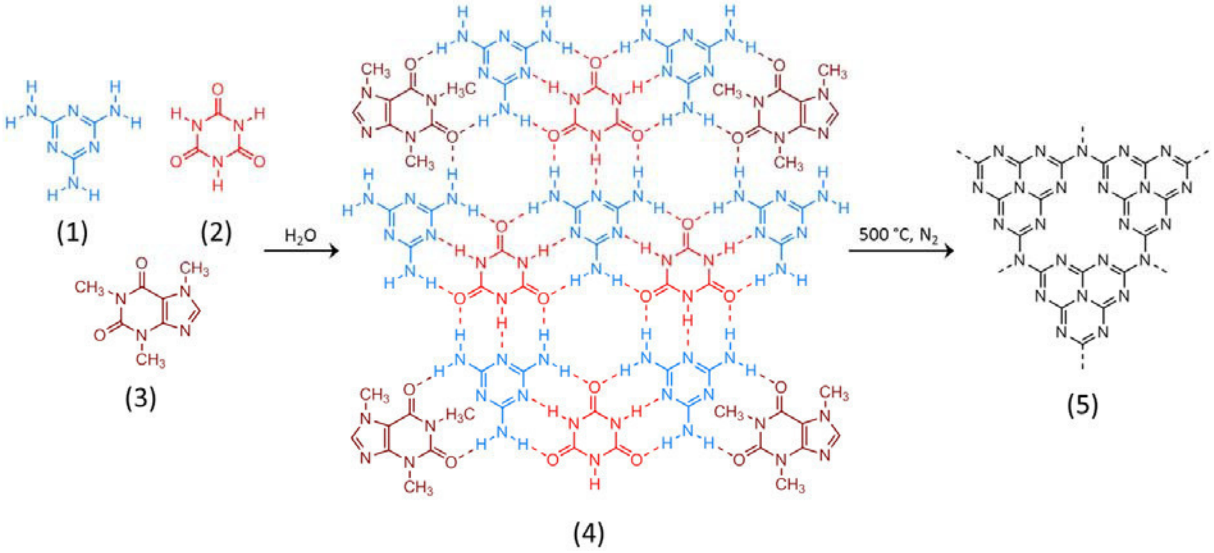

Scheme 4.1.1. Proposed reaction scheme for the preparation of g-C_3N_4 from "caffeine doped" cyanuric acid/melamine precursor complexes. In the first step, melamine (1), cyanuric acid (2) and caffeine (3) form a supramolecular precursor complex (4) by hydrogen bonding. In a second step, this complex is condensed to g-C_3N_4 (5) at 500 °C. Dashed lines indicate hydrogen bonds.

4.1.1 The "caffeine doped" CM precursor complex

The "caffeine-doped" CM complexes were prepared by shaking equimolar amounts of melamine and cyanuric acid with small amounts of caffeine (5 mol-%, 7.5 mol-% and 10 mol-% in relation to the molar amount of melamine/cyanuric acid) in water, to allow the formation of the supramolecular precursor complex.[68]

The precursor complexes are denoted as CM for the CM complex prepared without caffeine addition, and CM-*x*C for the CM complexes prepared with the addition of 5 mol% ($x = 5$), 7.5 mol% ($x = 5$) and 10 mol% ($x = 10$) caffeine.

The precursor complexes are obtained as white powders. For all samples, the formation of a hydrogen bonded CM complex is confirmed by fourier-transformed infrared (FT-IR) spectroscopy (**Figure SI-4.1.1** (a)).

Due to hydrogen bonding, the ν(C=O) stretching vibrations of cyanuric acid are shifted to higher wavenumbers (from 1691 cm^{-1} and 1753 cm^{-1} for cyanuric acid to 1713 cm^{-1} and 1777 cm^{-1} in the prepared complexes), whereas the triazine ring vibration of melamine is shifted to lower wavenumbers (from 815 cm^{-1} in melamine to 805 cm^{-1} in the prepared complexes).[109] No distinct differences can be observed between the samples prepared with different amounts of caffeine.

The high crystallinity of the precursor complexes is confirmed by powder x-ray diffractometry (PXRD) (**Figure SI-4.1.1** (b)). The diffraction patterns for all samples reveal sharp peaks, with the typical in-plane diffraction peaks for CM complexes at $2\theta = 10.7°$ ((100)-peak), $2\theta = 19.8°$ ((110)-peak) and $2\theta = 21.75°$ ((200)-peak).[95] Similar to the FT-IR data, no distinct differences can be observed between the different samples.

As observed by scanning electron microscopy (SEM), the caffeine does not affect the morphology of the precursor complexes. Regardless of the amount of caffeine added, for all the samples a roll-like morphology can be observed (**Figure SI-4.1.2**). This morphology is typical for CM complexes obtained in water.[94,95,99,102]

As neither the binding motifs of the CM complex nor the crystal structure or the morphology are affected by the caffeine addition, it is assumed that the caffeine is not incorporated into the bulk supramolecular structure, but is instead found at the edges of the 2D complex.

4.1.2 g-C_3N_4 from "caffeine doped" CM precursor complexes

The g-C_3N_4 materials are prepared by heating the precursor complexes for 4h at 500 °C under nitrogen atmosphere. The obtained materials are denoted as CM-500 (obtained from the precursor CM) and CM-*x*C-500 (obtained from the caffeine containing precursors CM-*x*C, with $x = 5$, 7.5 and 10; see chapter 4.1.1).

The formation of g-C_3N_4 is confirmed by elemental analysis, FT-IR and PXRD. With elemental combustion analysis, a molar C/N ratio of approximately 0.6 is determined for all samples (**Table SI-4.1.1**). This is close to the theoretical C/N ratio for g-C_3N_4 of 0.75, and typical for g-C_3N_4 prepared from CM precursor complexes.[94,95,99,102] The hydrogen content is less than 3 wt% for all samples, which indicates that most of the amino groups reacted during the condensation. Furthermore, the total weight of all elements indicates less than 5 wt% oxygen for all samples, which implies the elimination of most of the carbonyl groups from cyanuric acid. Apparently, the amount of caffeine added to the precursor mixture does not affect the elemental composition of the obtained g-C_3N_4 in an experimentally detectable fashion. When only caffeine is heated to 500 °C under nitrogen atmosphere, almost no residue is obtained, which indicates that caffeine nearly completely decomposes at the applied carbonization temperature. Hence, it can be assumed that most of the caffeine molecules which are bound at the edges of the 2D CM precursor complex decompose during the carbonization process, which explains why the elemental composition of the carbonized samples is not affected by the addition of caffeine.

The FT-IR spectra of the obtained samples show the characteristic vibrations for g-C_3N_4, i.e. the breathing modes of the triazine units at 800 cm^{-1} and the stretching modes for CN heterocycles between 1200 cm^{-1} and 1600 cm^{-1} (**Figure 4.1.1** (a)).[110] Between the samples prepared with different amounts of caffeine, no differences can be observed. The PXRD data show three diffraction peaks, at $2\theta = 13.1°$, 27.3° and 43° (**Figure 4.1.1** (b)). These reflections are attributed to the interplanar aromatic stacking peak of g-C_3N_4 ($2\theta = 27.3°$, (002)-peak) and the inner-plane peaks for graphitic materials ((100)-peak at $2\theta = 13.1°$ and (101)-peak at $2\theta = 43°$).[56] As already observed for the FT-IR data, no differences in the diffraction pattern between the samples prepared with different amounts of caffeine can be observed. This indicates that the caffeine addition does not affect the binding motifs and crystal structure of the obtained g-C_3N_4s. Taking together with the observation that also the elemental composition of the obtained g-C_3N_4s is not influenced by the caffeine addition, this further supports the assumption that caffeine is located at the edges of the 2D CM precursor complex and decomposes during carbonization.

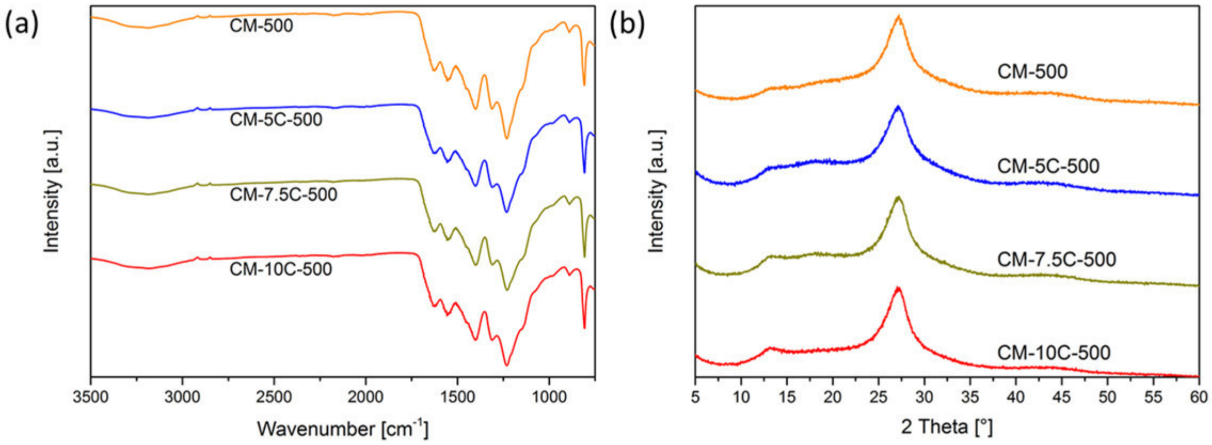

Figure 4.1.1. (a) FT-IR spectra and (b) PXRD pattern of the g-C_3N_4 materials obtained by carbonization (500 °C) of the CM complex (CM-500, orange) and by carbonization of the CM complex with addition of 5 mol-% caffeine (CM-5C-500, blue), 7.5 mol-% caffeine (CM-7.5C-500, yellow) and 10 mol-% caffeine (CM-10C-500, red).

However, one effect of the caffeine addition becomes apparent when examining the morphology by SEM (**Figure 4.1.2**). Without caffeine addition, mainly the typical plate like morphology for g-C_3N_4 from supramolecular CM complexes is observed.[102] Indeed, the addition of only 5 mol% caffeine to the CM complex leads to g-C_3N_4 materials with a primarily tubular morphology, which becomes more pronounced with increasing amount of caffeine. The observed tubes are of hexagonal shape, hollow and partially twisted. They are up to several µm in length, with a thickness between ≈ 100-500 nm (see also **Figure SI-4.1.3**). However, it is important to note, that single tubes can also be observed for the g-C_3N_4 prepared without the addition of caffeine, but only in small amounts. With caffeine in the precursor mixture, the obtained g-C_3N_4 is predominantly of tubular morphology and the tubes get significantly longer with increasing caffeine content.

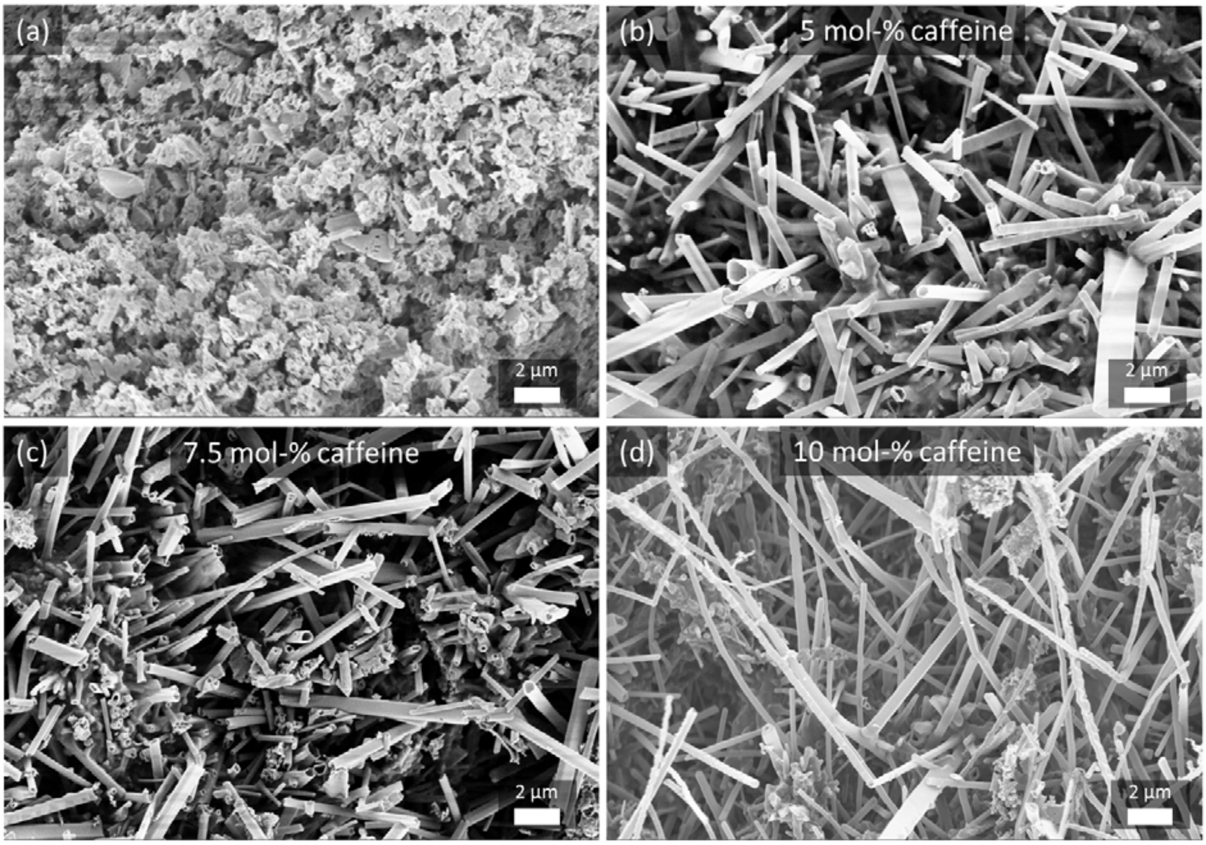

Figure 4.1.2. SEM images of the g-C_3N_4 materials obtained by carbonization (500 °C) of (a) the CM complex (CM-500), (b) the CM complex with addition of 5 mol-% caffeine (CM-5C-500), (c) the CM complex with addition of 7.5 mol-% caffeine (CM-7.5C-500) and (d) the CM complex with addition of 10 mol-% caffeine (CM-10C-500).

As measured by nitrogen physisorption, the obtained samples have only a negligible inner surface area. BET surface areas between 20 m^2/g and 41 m^2/g are determined, which are typical values for bulk g-C_3N_4 prepared from the CM precursor (**Table SI-4.1.1**, **Figure SI-4.1.4**).[102]

The mechanism for the formation of the observed tubular morphology is not resolved yet. However, there are already several literature reports on the formation of g-C_3N_4 nanotubes[111-114] or microfibers.[115,116] Nevertheless, for none of the reported tubular structures a formation mechanism could be confirmed. Gracia et al., who presented ab initio DFT calculations for the folding of g-C_3N_4 layers into tubes of different diameters, claimed that compared to pure carbon nanostructures, the folding energies for g-C_3N_4 are significantly reduced.[117] The reduced folding energy is attributed to the presence of vacancies, which are peculiar to the g-C_3N_4 structure of linked tri-s-triazine units, as well as to the corrugated character of this structure. It can be assumed that the addition of caffeine to the CM complex leads after carbonization to a g-C_3N_4 structure, in which those structural characteristics, i.e. the vacancies and the corrugated character of the structure, are even more pronounced: Due to the restricted possibilities of hydrogen bonding, incorporated caffeine molecules are supposed to induce large structural vacancies in the CM precursor complex (and potentially in the condensed g-C_3N_4 structure, see **Scheme 4.1.1**). Additionally, the steric effect of the methyl group in the caffeine can be expected to lead to a corrugated structure of the CM precursor complex, which in turn might lead to a more corrugated character of the tri-s-triazine structure in the g-C_3N_4 after condensation. On the basis of these considerations, it can be assumed that the folding energy for the resulting condensed g-C_3N_4 layers is even further decreased. Hence, the tube formation might start with the folding of single condensed g-C_3N_4 layers, which then induce the growth of further layers on top, to assemble into the observed microtubes. The hollow character of the tubes is probably due to the evaporation of gaseous products during carbonization.[115] The hexagonal shape is expectable, as both the supramolecular CM complex[92,93,118] and g-C_3N_4 have a hexagonal unit cell.[119] However, to gain further insights on the mechanism of the tube formation, electron backscatter diffraction in high resolution scanning (or transmission) electron microscopy (EBSD with HR-SEM or HR-TEM) would be useful analytical techniques. Here, the crystallinity and the orientation of the carbon nitride layers can be determined. For the proposed mechanism of the folding of carbon nitride layers, the tubes should be aligned along the a-axis (in-plane axis) of the g-C_3N_4 structure.

The caffeine was added with the purpose to act as "growth stopper" for the CM complex, which is supposed to lead to the introduction of defect sites or surface terminations in the resulting g-C_3N_4 and thus affect the photocatalytic properties. A potential influence on the photophysical properties can already be seen from the color of the obtained products. While the material obtained from the CM precursor without addition (CM-500) are of the yellowish color typical for g-C_3N_4, with increasing amount of caffeine the color of the obtained materials turns darker (**Figure SI-4.1.5**). The sample prepared with the addition of 10 mol% caffeine (CM-10C-500) is of brown color.

With UV/Vis diffusive reflectance spectroscopy, for all materials an absorption edge at ≈ 460 nm can be observed (**Figure 4.1.3** (a)). This absorption edge is typical for the semiconductor g-C_3N_4, and is due to an electronic transition between the valence band and the conduction band, corresponding to the band gap energy of g-C_3N_4 of ≈ 2.7 eV.[56] No considerably shift of the absorption edge can be observed between the differently prepared samples, which means that the band gap energy remains nearly constant. However, with increasing amount of caffeine, for the obtained g-C_3N_4 samples the optical density in the wavelength region right below the absorption edge (≈ 460- 600 nm) increases. An optical absorption tail at wavelengths right below the absorption edge can be attributed to the so-called Urbach absorption edge. The Urbach absorption edge is described for disordered semiconductor solids, and is the optical absorption due to defect- or surface states.[106-108] As these states are located in the band gap right below the conduction band, an increased optical absorption tail at wavelengths right below the absorption edge can be observed. Thus, the increased optical absorption indicates the formation of defects or surface terminations due to the caffeine addition. Electronic transitions to defect- or surface states are also reflected in the brown color of the samples prepared with caffeine.

In addition, also the photoluminescence spectra of the obtained samples show characteristics, which point towards the formation of defects or surface terminations. Upon excitation at 405 nm, for all samples an emission at ≈ 470- 480 nm can be observed (**Figure 4.1.3** (b)). The emission wavelength remains nearly constant, only a small redshift ($\Delta\nu \approx 10$ nm) can be observed for the samples prepared with caffeine. However, with increasing amount of caffeine, the emission intensity significantly decreases. The same trend applies for the emission lifetime, which decreases from 10 ns for the non-doped sample (CM-500), to 5.7 ns for the sample prepared with 5 mol% caffeine (CM-10C-500) and to 5.1 ns for the sample prepared with 10 mol% caffeine (CM-10C-500) (see inlet in **Figure 4.1.3** (b)).

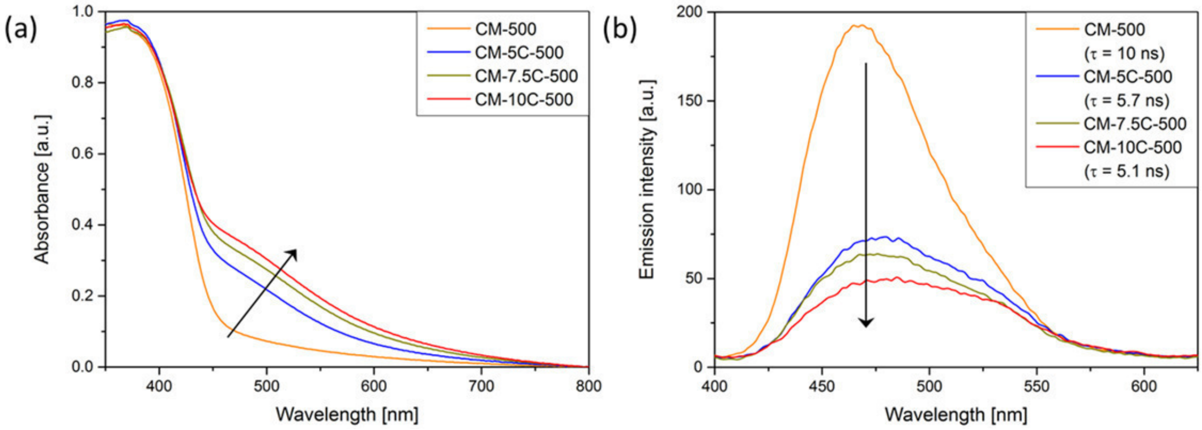

Figure 4.1.3. (a) UV/Vis diffusive reflectance spectra and (b) emission spectra ($\lambda_{exc} = 405$ nm) and emission lifetime τ for the $g\text{-}C_3N_4$ materials obtained by carbonization (500 °C) of the CM complex (CM-500, orange) and by carbonization of the CM complex with addition of 5 mol-% caffeine (CM-5C-500, blue), 7.5 mol-% caffeine (CM-7.5C-500, yellow) and 10 mol-% caffeine (CM-10C-500, red).

The decreased photoluminescence intensity and lifetime can be attributed to a quenching of the fluorescence by alternative non-radiative charge-transfer paths to defect- or surface states. Thus, photoluminescence spectroscopy gives another indication, that caffeine addition induces the formation of defects or surface terminations in the g-C_3N_4.

4.1.3 Effect of "caffeine doping" on the photocatalytic properties

Defect or surface states can trap photogenerated charge carriers and prevent them from their recombination, which will result in an increased photocatalytic activity.[103] To test the effect of the caffeine addition on the photocatalytic activity of the g-C_3N_4, the obtained materials were tested for photocatalytic dye degradation. As organic dye, Rhodamin B (RhB) was chosen. The photodegradation experiments were carried out by measuring the RhB concentration in solution during time while stirring with the respective samples (CM-5C-500, CM-10C-500 and CM-500 as reference sample) under white light irradiation.

The RhB concentration is calculated from the optical absorption at the absorption maximum (554 nm) by applying the Lambert-Beer law. The time-dependent decrease of the relative RhB concentration and the RhB absorption spectra are shown in **Figure 4.1.4**.

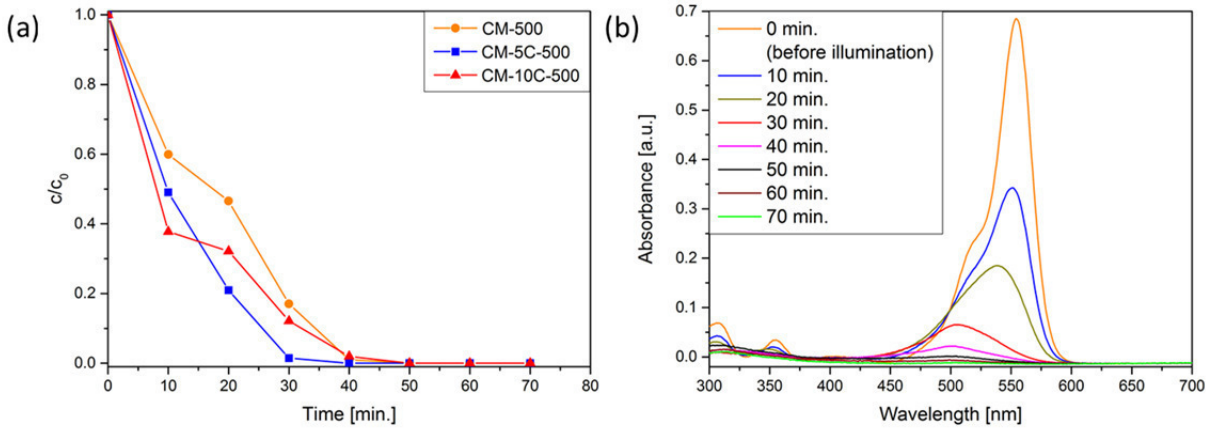

Figure 4.1.4. (a) Decrease of the relative RhB concentration as a function of illumination time for the photodegradation assay with the catalysts CM-500 (orange), CM-5C-500 (blue) and CM-10C-500 (red). (b) Absorption spectra of the RhB solution after different illumination times with addition of the photocatalyst CM-5C-500.

It can be seen that the RhB photodegradation is faster for the samples prepared with caffeine. The sample prepared with the addition of 5 mol% caffeine (CM-5C-500) demonstrates the highest photocatalytic activity and after 30 min. the RhB dye is completely degraded (50 min.

for the reference sample CM-500 which was prepared without caffeine addition). The degradation mechanism can be determined from the RhB optical absorption spectra. During irradiation, the RhB absorption maximum shifts gradually from 554 nm to 499 nm, which is the absorption maximum of Rhodamine, a compound obtained by N-deethylation of RhB (**Figure 4.1.4** (b)). Thus, degradation occurs via N-deethylation of Rhodamine B.[120]

To explain the increased photocatalytic activity of the samples which were prepared with caffeine, different factors which contribute to the activity of a photocatalytic system have to be considered. These are mainly the overall light absorption, the life time of the photogenerated charge carrier and the surface area of the photocatalyst.[103] Regarding the surface area, the most active sample (CM-5C-500) is also the one with the highest surface area (BET surface area of 41 m^2/g, see **Figure SI-4.1.4**). However, the sample with the lowest surface area (CM-10C-500, BET surface area of 20 m^2/g, see **Figure SI-4.1.4**) is still more active than the reference sample prepared without caffeine (CM-500, BET surface area of 31 m^2/g, see **Figure SI-4.1.4**). Furthermore, all obtained surface areas are low, and the differences are small. This makes it likely, that the superior photocatalytic activity is not mainly due to the surface area. Considering the obtained UV/Vis absorption and emission data, it is more likely to attribute the superior photocatalytic activity of the samples prepared with caffeine either to a better light harvesting, or to a decreased recombination rate of the photogenerated charge carrier. However, an increased optical absorption of the samples prepared with caffeine cannot be the only factor contributing to its superior photoactivity, as the sample CM-10C-500 reveals a lower photodegradation rate than CM-5C-500 (despite increased optical absorption). Indeed, the quenched photoluminescence intensity and lifetime for the more photoactive samples prepared with caffeine indicate that a decreased recombination rate is the primary factor. It is known from other semiconductor photocatalysts that a decreased recombination rate can be due to defects or surface terminations, which provide trapping sites for the photogenerated charge carriers.[104,105] Hence, the obtained results point to the interpretation that the increased photocatalytic activity of the g-C_3N_4 prepared with caffeine is due to the creation of defects or surface terminations, which lead to defect- or surface states in the electronic band structure of the obtained g-C_3N_4. The defect- or surface states can "trap" the charge carrier, prevent them from recombination and provide them for redox-processes at the catalyst surface.

However, defect- or surface states can also trap charge carrier in that way, that they are prevented from further migrating to the active sites and instead recombine.[103] That means that an increased defect concentration alone not necessarily correlates with an increased photodegradation rate, which could explain the inferior photocatalytic activity of the sample prepared with the higher amount of caffeine (CM-10C-500).

To test the stability of the photocatalytic performance, sequential degradation cycles were performed for the photocatalyst CM-5C-500. In three degradation cycles, the photodegradation rate remains unaffected, which means that no photocorrosion occurs. The materials stability during photocatalysis is confirmed by PXRD and FT-IR measurement of the photocatalyst CM-5C-500 after the third photodegradation cycle (**Figure SI-4.1.6**). When comparing the obtained data to the samples before the photodegradation testing, no changes can be observed, which proves that the material remains stable during photocatalysis.

In summary, this chapter showed how the morphology, electronic structure and photophysical properties of g-C_3N_4 can be modified by applying a "caffeine-doped" precursor complex. The obtained results suggest that the caffeine molecules act as a "growth-stopper" for the cyanuric acid/melamine complex, which introduces structural vacancies in the precursor complex that are preserved as defects or surface terminations in the g-C_3N_4 after carbonization. The defects or surface terminations lead to the formation of defect- or surface states in the electronic band structure of the obtained g-C_3N_4s, which can lead to a decreased rate of recombination of photogenerated charge carriers, and thus to an increased photocatalytic performance.

This chapter is meant to demonstrate the concept of the pre-organized precursor complexes, where desired properties of the g-C_3N_4- or carbon-material are addressed by the choice of appropriate precursor molecules. A further example for this concept is presented in chapter 4.2.2, where organic crystals between squaric acid and urea are applied as pre-organized precursor for C_2N carbon.

4.2 C_2N carbon

A further addition to the family of nitrogen containing carbon materials is C_2N, a compound which was very recently described for the first time. In chapter 2.1.2, the synthesis of C_2N from eutectic mixtures of hexaketocyclohexane octahydrate and urea is described.[69] Shortly after, the existence of C_2N was further confirmed by Baek et al., who succeeded to prepare this material from hexaketocyclohexane and hexaaminobenzene in NMP.[70,71] To the best of our knowledge, these are the only reports given on this novel carbon/ nitrogen compound so far.

However, as for any new material, a lot of basic knowledge regarding preparation and properties of C_2N still has to be collected. Nevertheless, the findings gathered so far suggest very interesting structural and electronic properties, like a pyrazinic structure, a semiconductive behavior and the fast charge carrier mobility. As described in chapter 2.2.2, these properties make C_2N a promising material as composite component with g-C_3N_4 for photocatalysis, as this potentially provides a way to increase the optical absorption of g-C_3N_4 and decrease the rate of charge carrier recombination.

However, as the preparation of nanocomposites is not a trivial task, it is highly beneficial to have certain opportunities of processing the single components. This includes the availability of different precursor systems. For C_2N, only two different precursor systems have been explored so far, which both apply the same component (hexaketocyclohexane octahydrate). Regarding the processing, the eutectic hexaketocyclohexane/urea precursor allows due to its liquid nature for interesting opportunities, like molding, and hard- or salt- templating (see chapter 2.3.3).[69] For the precursor system developed by Baek et al., the fabrication of a thin C_2N-film by solution casting is described.[70]

In this chapter on C_2N, a further approach towards processing the hexaketocyclohexane/urea precursor is presented, as well as the exploration of a novel precursor system for C_2N.

In chapter 4.2.1, the hexaketocyclohexane/urea precursor is structured with the biopolymer chitosan, resulting in mesoporous nitrogen-doped carbon monoliths and –beads. Although the composition of the obtained materials on the atomic scale still has to be further resolved, the applied methods depicts an interesting way to obtain a free-standing nitrogen-doped carbon monolith, without the use of additional binders. In chapter 4.2.2, the preparation of C_2N from a novel precursor system is approached. Following the concept of the pre-organized precursor systems, here supramolecular assemblies between urea and the cyclic oxocarbon squaric acid are applied as precursor. From these two compounds, organic crystals are prepared, from which upon carbonization materials with an unusual sheet-like morphology and a composition of C_2N are obtained.

4.2.1 Nitrogen-doped carbon monoliths and –beads by structuring the hexaketocyclohexane/urea precursor with chitosan

The two monomers hexaketocyclohexane and urea form a liquid mixture upon gentle heating at 90 °C, from which upon carbonization C_2N is obtained.[69] In chapter 2.3.3, it was described how the liquid nature of the eutectic C_2N precursor enables several processing opportunities: The molten precursor can be molded into desired shapes, and hard-templating (with SBA-15) or salt-templating (with $ZnCl_2$) can be applied to obtain porous C_2N.[69] More potential opportunities for processing are given by the observation that the eutectic hexaketocyclohexane/ urea precursor at 90 ° is miscible with water, which holds the potential of being structured by water-soluble structuring agents. In this chapter, attempts to structure the hexaketocyclohexane/ urea precursor in solution by interaction with the biopolymer chitosan (CTS) are presented.

In the early stage of the condensation, the 90 °C melt of the monomer mixture of urea and hexaketocyclohexane is miscible with water. As confirmed by FT-IR spectroscopy, it contains a high density of ketone groups, which offers the possibility of interacting and being structured by other functional molecules.[69]

On that purpose, an interesting option is the use of polymers from biomass as structuring agents. Biopolymers like natural polypeptides, polyaromatics or polysaccharides offer structural and functional diversity and can be obtained easily in large quantities from renewable resources.[121] By interactions between the biopolymer functional groups and certain materials, the natural structure of the biopolymer can be replicated. This concept is especially suitable for the directed growth of inorganic materials like metals and metal oxides.[122-125] However, this concept as well opens a route to structure carbon materials when applying it to compounds which can be further processed by carbonization.[126,127] Here, structuring of the hexaketocyclohexane/urea precursor with the polysaccharide CTS is demonstrated. This leads to gel formation, which can be transferred to mesoporous nitrogen rich carbon by drying and subsequent carbonization.

CTS is a biopolymer obtained by the deacetylation of the natural polysaccharide chitin. The degree of deacetylation can vary, so it can be regarded as a random copolymer of 2-Acetamido-2-desoxy-β-D-glucopyranose units and its deacetylated form (**Figure 4.2.1**).

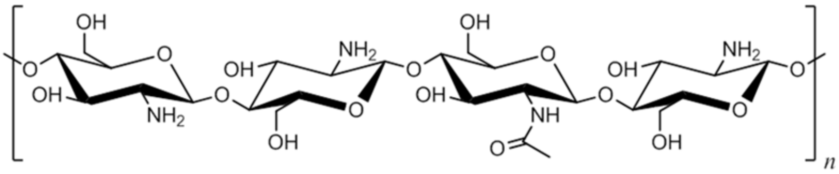

Figure 4.2.1. Representative repeating unit of chitosan.

Since chitin is the main compound of the exoskeleton of crustaceans (e.g. crabs, lobsters and shrimps), chitosan can be produced from natural resources and is completely biodegradable and biocompatible.

Properties of the CTS polymer like solubility or conformation are mainly influenced by the interplay between the hydrophobic polysaccharide backbone and the hydrophilic NH_2-groups. In acidic media, the amine groups can be protonated and CTS dissolves as a polycation.[128] CTS dissolved in diluted acetic acid, is obtained as highly viscous solution. When compounds with functional groups which allow for interactions with the protonated NH_2- groups (e.g. by hydrogen bonding) are mixed with the CTS solution, the CTS chains can be crosslinked, which results in gel formation.[129,130] When molding the gel into monolithic shape, after drying a monolithic polymer can be obtained.

When drops of an acidic CTS solution are introduced into alkaline environment, the hydrophobic interactions of the now deprotonated CTS-chains become pivotal and coagulation leads to the formation of gel beads.[129] Thus, the properties of the CTS-network can be easily tuned by varying the pH-value. Also for the gel beads, suitable compounds can be mixed with the gel and by specific interactions induce the crosslinking of the CTS-chains.[131]

Three types of functional groups are available for the crosslinking: The amino-group and both primary and secondary OH-groups at the C-2, C-3 and C-6 position. Crosslinking can occur non-covalent (reversible, e.g. by hydrogen bonding or complexation) and by covalent bonding (e.g. by Schiff Base reaction between the amino groups and aldehydes).[132] Typical crosslinking agents are ionic compounds (charged metal ions[133-135], oxidic compounds like silica[134-136], titania[131,135] or other metal oxides[137]), polymers (e.g. PEG,[138] PVP,[139] PVA,[140] PAA[141]) and molecules with appropriate functionalities (carboxylic acids,[142] epoxides[143 65], aldehydes[144,145]).

The use of CTS as structuring agent provides the inherent advantage, that in the gel stage the CTS based materials can be shaped into monolithic form or into the form of beads. Due to its unique properties, the shaping of carbon materials into a monolithic macromorphology is highly desired and subject of intensive research. Materials of monolithic shape are especially suitable for various practical applications like as column materials for adsorption (water purification,[146] CO_2 adsorption,[147-149] dye adsorption[150-152]) or as a structured support material, be it as catalyst support[153] or as electrode material in electrochemical devices.[154-156] Here, direct shaping of the required materials into the monolithic form is highly advantageous, as the use of additional binders for powders or grain particles affects the material properties and morphological features (e.g. the porosity).[155] Generally, there are several routes to the synthesis of carbon monoliths: The infiltration of monolithic materials (e.g. silica, PMMA spheres) by organic compounds and subsequent carbonization,[155-159] the carbonization of polymers (e.g. phenolic resins),[147,154,159,160] the activation of mesophase pitch[161] or the solvothermal treatment of biopolymers.[148]

With the use of CTS, the hexaketocyclohexane/ urea precursor can be structured according to **Scheme 4.2.1**. CTS ((1) in **Scheme 4.2.1**) is dissolved in acidic media ((2) in **Scheme 4.2.1**) and mixed with a solution of the eutectic intermediate ((3) in **Scheme 4.2.1**) obtained from hexaketocyclohexane and urea (in the following discussion denoted as HkU precursor), which acts as crosslinker. The crosslinking is completed at hydrothermal conditions (12 h at 100 °C in an autoclave). After drying of the obtained gel monolith, carbonization finally leads to a nitrogen containing carbon monolith (Route (a) in **Scheme 4.2.1**).

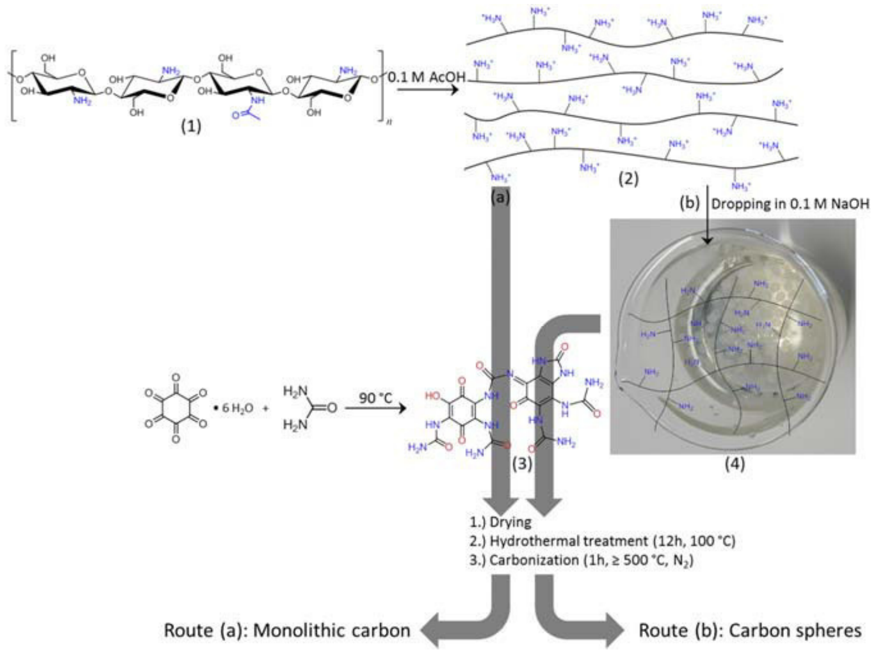

Scheme 4.2.1. Preparation of the nitrogen-doped carbon monolith (Route (a)) and -beads (Route (b)).

With a variation of this process, the nitrogen containing carbon can be also shaped into the form of spheres (beads) with tunable diameter. Here, the solution of the protonated CTS ((2) in **Scheme 4.2.1**) is dropped with a syringe into aqueous alkaline media. When in contact, deprotonation of the CTS amino groups occurs. This affects the solubility of the CTS chains, the hydrophobic interactions of the carbohydrate backbone become pivotal and lead to coagulation of the CTS polymer. The coagulation process is apparent as a direct transformation of the CTS solution drops into gel spheres ((4) in **Scheme 4.2.1**), which also means that the diameter of the CTS solution drops determines the diameter of the obtained gel beads. After washing the gel beads to neutral pH, they can be soaked into an aqueous solution of the hexaketocyclohexane/urea precursor ((3) in **Scheme 4.2.1**), which penetrates into the CTS network and leads to crosslinking. This process can again be completed at hydrothermal conditions. Finally, drying and carbonization of the obtained gel spheres lead to nitrogen containing carbon beads (Route (b) in **Scheme 4.2.1**).

In the following discussion, the prepared composite samples are denoted as *x*-CTS/HkU-*y* for the dried gels before carbonization and *x*-CTS/HkU-*y*-500 for the materials carbonized at 500 °C, with:

x = m for monolithic samples and *x* = b for bead- samples,

y = f for freeze-dried samples and *y* = sc for supercritical dried samples.

As references, samples were prepared without adding the HkU precursor. These samples are denoted as *x*-CTS-*y* for the dried gels before carbonization and *x*-CTS-*y*-500 for the materials carbonized at 500 °C, with the indications for *x* and *y* as given above. The freeze dried reference samples which were prepared with the addition of only urea or hexaketocyclohexane octahydrate are denoted as m-CTS/U-f and m-CTS/Hk-f, respectively.

A summary to all important data obtained (EA, carbonization yield, physisorption data) is given in **Table SI-4.2.1**.

4.2.1.1 Preparation and characterization of the CTS/HkU precursor gels

The different stages of the carbon monolith and carbon spheres preparation are depicted in **Figure 4.2.2** and **Figure 4.2.3**, respectively.

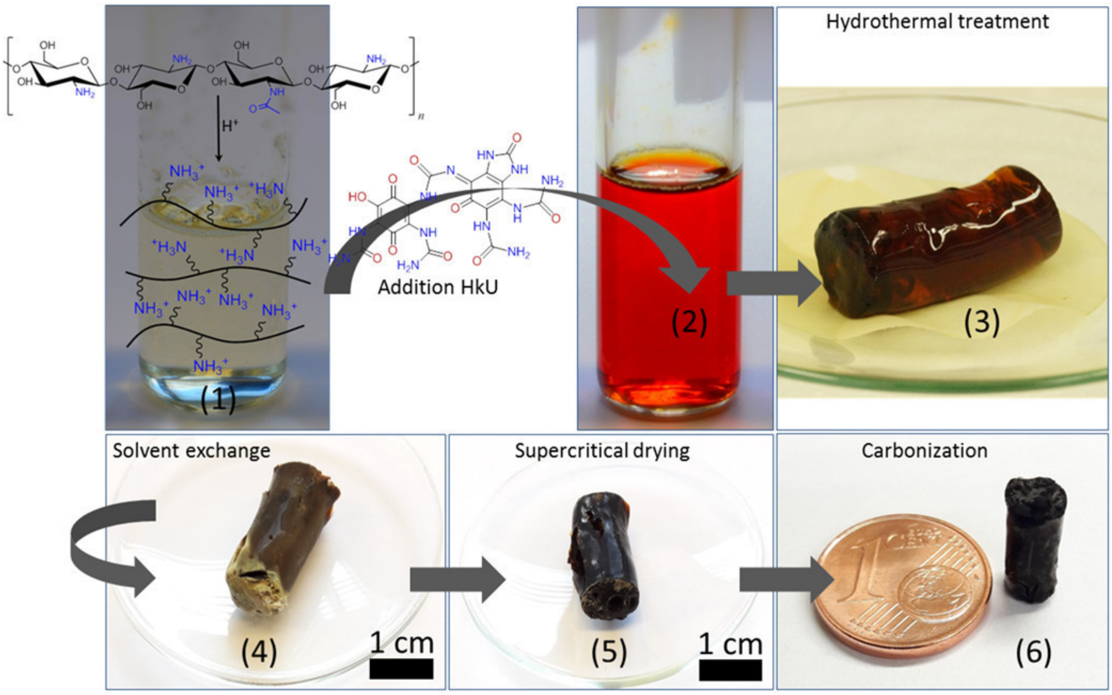

Figure 4.2.2. Photographs of different stages of the nitrogen-doped carbon monolith synthesis. (1) CTS dissolved in acid. (2) CTS solution after addition of the HkU precursor. (3) Polymer monolith after hydrothermal treatment. (4) Polymer monolith after the solvent exchange step. (5) Polymer monolith after supercritical drying (sample m-CTS/HkU-sc). (6) Monolith after carbonization at 500 °C (sample m-CTS/HkU-sc-500).

The addition of the dissolved HkU precursor to the acidic solution of the protonated CTS ((1) in **Figure 4.2.2**) goes along with a color change to deep red and viscosity increases ((2) in **Figure 4.2.2**). After the hydrothermal treatment of the obtained mixture for 12 h at 100 °C in a steel autoclave, a deep red gel monolith is obtained ((3) in **Figure 4.2.2**). It should be noted that the described changes only occur for the addition of the HkU precursor and cannot be observed when performing the synthesis with the addition of only urea or hexaketocyclohexane or none of these components. The addition of only urea leads to yellowish gel flakes after the hydrothermal step, whereas the same procedure with the addition of only hexaketocyclohexane results in small, black gel flakes. When performing the hydrothermal step with only the solution of the protonated CTS, no gelation at all can be observed (**Figure SI-4.2.1**). Hence, the observation that gelation to a one piece monolith only occurs for the addition of the HkU precursor, already points to its ability to crosslink the CTS chains.

When the CTS gel beads, which are obtained after dropping dissolved CTS into aqueous alkaline media, are soaked in a solution of the HkU precursor, the former colorless gel spheres ((1) in **Figure 4.2.3**) turn their color to deep red and a significant swelling of the gel beads can be observed ((2) in **Figure 4.2.3**). It should be noted that if the gel beads are mixed with more concentrated solutions of the HkU precursor, swelling of the gel beads is more pronounced and can even lead to bursting of the beads. It can be assumed that the swelling is due to changes in the osmotic pressure, which occur when the HkU precursor penetrates into the gel beads and thus induces a concentration gradient between the inside of the gel beads and the surrounding solution. After hydrothermal treatment (12 h at 100 °C in a steel autoclave), brown gel beads are obtained ((3) in **Figure 4.2.2**). For comparison, photographs of the CTS gel beads prepared without the addition of the HkU precursor are shown in **Figure SI-4.2.1**.

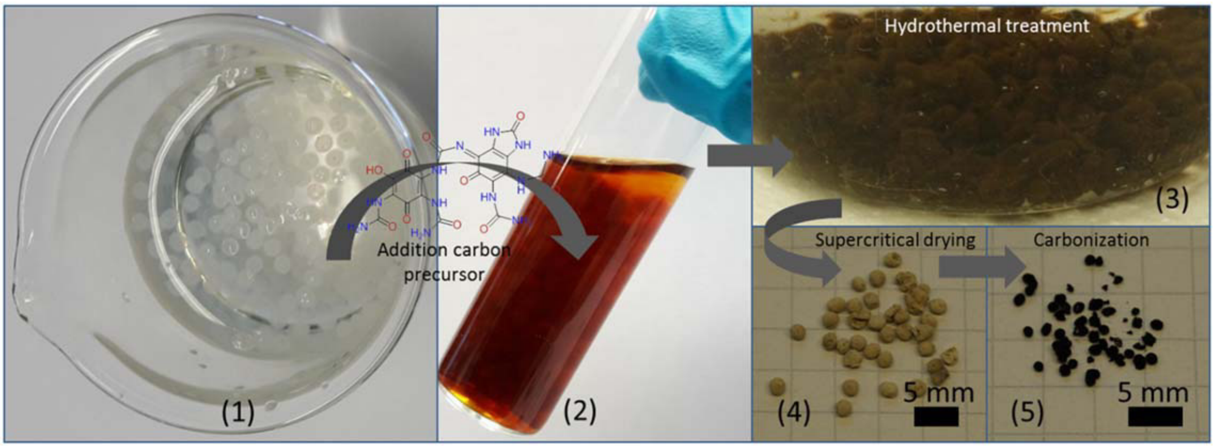

Figure 4.2.3. Photographs of different stages of the nitrogen-doped carbon beads preparation. (1) CTS beads before and (2) after soaking in a solution of the HkU precursor. (3) Gel beads after hydrothermal treatment. (4) Polymer beads after the solvent exchange and supercritical drying (sample b-CTS/HkU-sc). (5) Beads after carbonization at 500 °C (sample b-CTS/HkU-sc-500).

To gain maximum retention of the original gel microstructure, an appropriate drying method has to be chosen. Freeze drying or simple drying at reduced pressure bears the risk of a collapsing pore structure due to capillary forces at the occurring gas/ liquid interface. This problem can be avoided when drying with supercritical liquids, e.g. with supercritical CO_2.[129] For both, the gel- monolith and the gel- beads, it turns out that the more complex method of supercritical drying is essential when the gel microstructure should be retained.

The more simple method of freeze drying leads to golden shimmering monoliths or beads, but as determined by electron microscopy (SEM), no microstructure can be observed (**Figure SI-4.2.2**). With nitrogen physisorption measurements, no apparent surface area can be detected for the freeze dried samples (**Table SI-4.2.1**). It can be assumed that the golden color of the freeze-dried samples is due to thin layers of the dried HkU- precursor at the outer surface of the materials, as thin crystals of the solid HkU- complex reveal this color.

When drying the gel monolith or gel beads with supercritical CO_2, the obtained monolith or bead samples are of matt brown appearance. Photographs of the supercritical dried monolith and bead samples are shown in **Figure 4.2.2** (5) and **Figure 4.2.3** (4), respectively. Prior to the supercritical drying, the water of the gels has to be exchanged against acetone, which has a better miscibility with liquid CO_2. This step is necessary to achieve a complete exchange of the gel solvent against CO_2. It can be expected that during the solvent-exchange step a certain amount of the HkU-precursor gets washed out. This assumption is further supported by differences in the elemental composition between the freeze-dried- and supercritical dried samples, which will be discussed in more detail below.

Compared to the freeze dried materials, the supercritical dried monolith and beads are reduced in size (compare **Figure SI-4.2.2** and **Figure 4.2.2/ 3**, all materials obtained from the same sized gel monolith or beads). This shrinking not only occurs during the supercritical drying, but already during the solvent exchange step.

With SEM, for the supercritical dried samples a mesoporous structure can be observed (**Figure 4.2.4**). While the monolithic material reveals the structure of a porous network with pores in the range of ≈ 10- 20 nm, for the structure of the beads interconnected spheres with sizes ≈ 20 nm can be observed. The different structures indicate different degrees of crosslinking for the monolith- and beads- sample. This is due to differences in the preparation process: For the preparation of the monoliths, the protonated CTS-chains are dissolved and thus distributed over the whole solution, which means that crosslinking is likely to occur between single CTS chains. However, for the CTS-beads before the addition of the HkU precursor, hydrophobic interactions of the CTS-backbone lead to a much denser network, where all of the CTS-chains are assembled in a few bead- particles (see **Scheme 4.2.1**): This is expected to exacerbate the penetration of the carbon precursor into the CTS-network. Here it can be assumed that the HkU precursor does not fully penetrate into the CTS network, but crosslinks at different positions at the surface of domains of assembled CTS- chains. Hence, this process can be better described as coating of small spherical CTS domains by the HkU precursor. After drying, the coated CTS domains remain as interconnected spheres.

It can be assumed that the matt brown appearance for the supercritical dried materials (in contrast to the golden glossy appearance for the freeze dried samples), is due to multiple reflections at the rough, nanostructured surface.

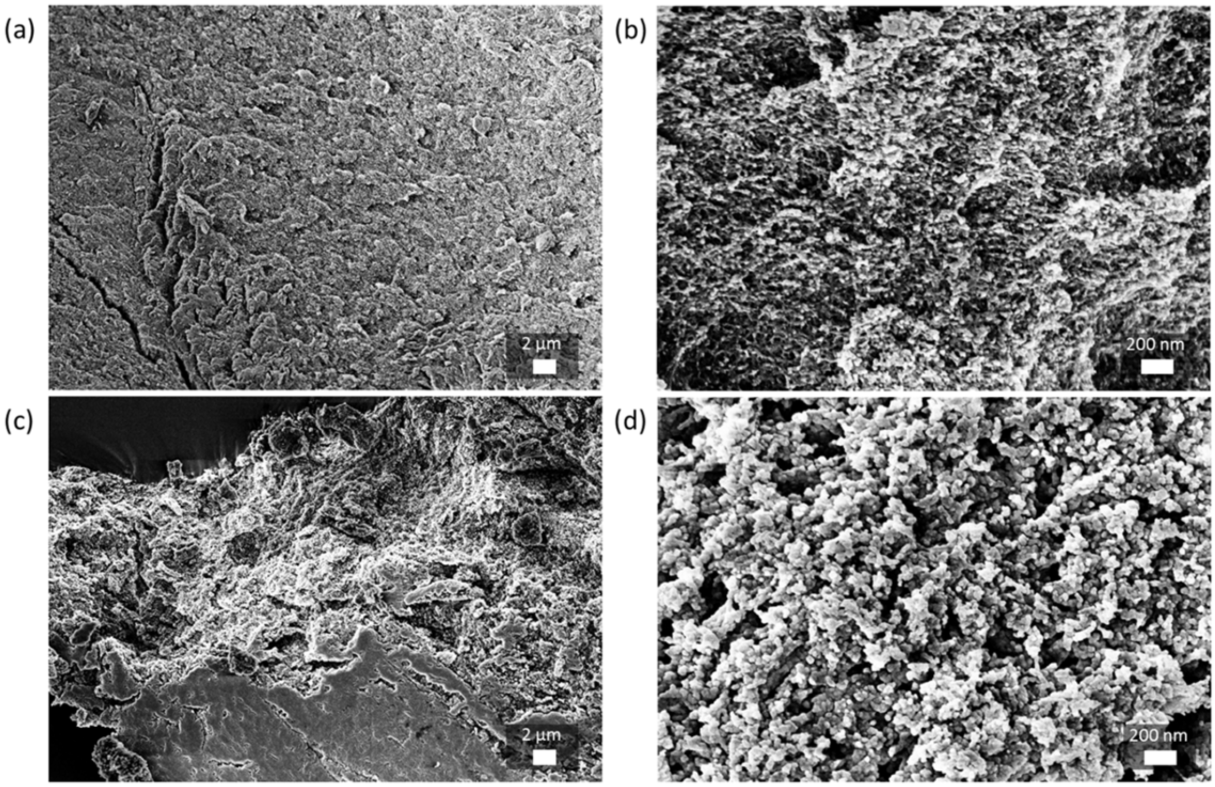

Figure 4.2.4. SEM images of the supercritically dried CTS/HkU gels. (a,b) CTS/HkU polymer monolith (sample m-CTS/HkU-sc) and (c,d) CTS/HkU polymer beads (sample b-CTS/HkU-sc).

With nitrogen physisorption, the mesoporous character of the supercritically dried monolith- and beads- samples can be confirmed (**Figure 4.2.5**, **Table SI-4.2.1**). For the supercritical dried polymer monolith an apparent BET surface area of 76 m^2/g can be detected. The sample reveals a mainly mesoporous pore-size distribution, with an average pore size of 12 nm and a mesopore- volume of 0.17 cc/g (total pore volume: 0.21 cc/g). The supercritically dried beads reveal an apparent BET surface area of 168 m^2/g and also a mainly mesoporous pore-size distribution. Here the average pore-size is 16 nm and the mesopore- volume is 0.8 cc/g (total pore volume: 0.87 cc/g).

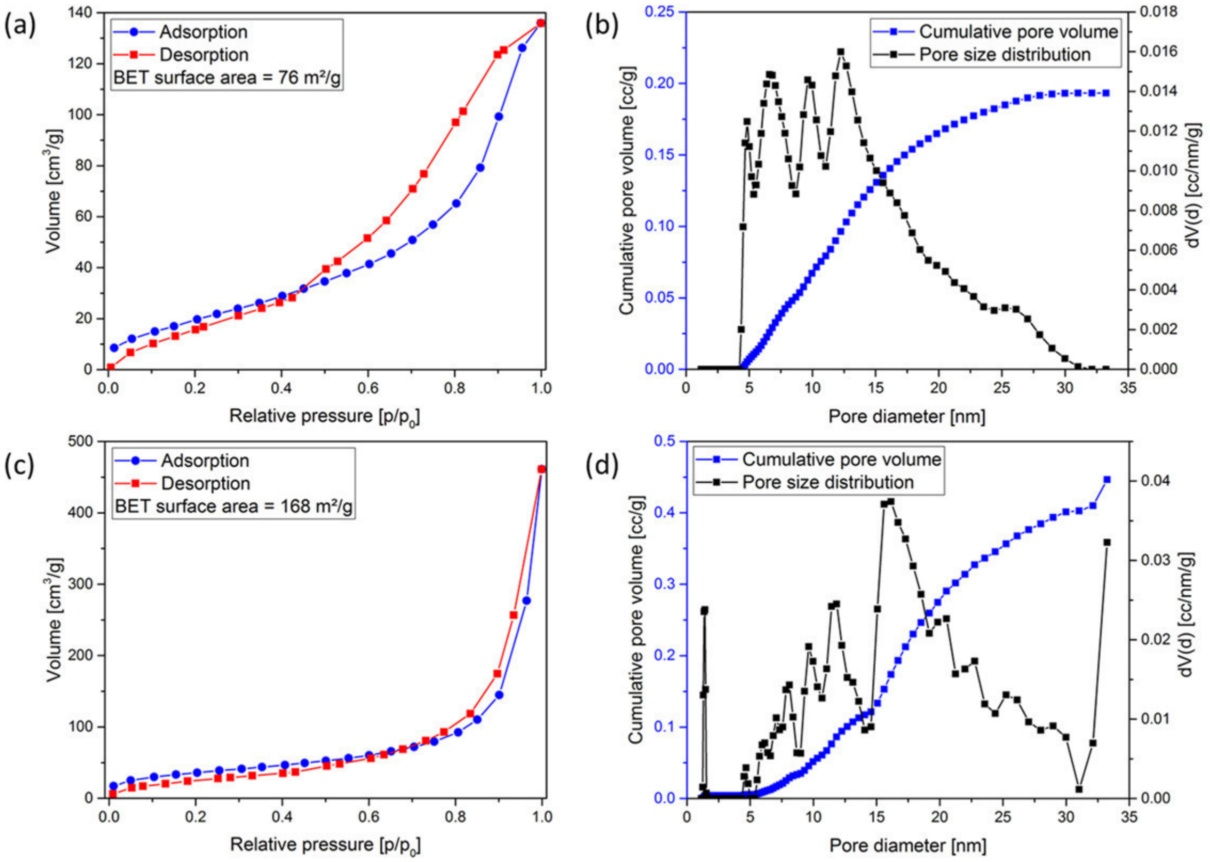

Figure 4.2.5. (a) Nitrogen sorption isotherms and BET surface area and (b) cumulative pore volume and pore size distribution of the supercritical dried CTS/HkU precursor gel monolith (sample m-CTS/HkU-sc). (c) Nitrogen sorption isotherms and BET surface area and (d) cumulative pore volume and pore size distribution of the supercritical dried CTS/HkU precursor gel beads (sample b-CTS/HkU-sc). Cumulative pore volume and pore size distribution were calculated applying the QSDFT model for slit/ cylindrical pores applied on the adsorption isotherm.

For the supercritical dried beads which were prepared without the HkU precursor (sample b-CTS-sc), only a low surface area can be detected (BET area of 39 m^2/g, see **Figure SI-4.2.3**). This huge influence of the HkU precursor on the porosity of the beads indicates its ability to interact with and stabilize the CTS network.

The elemental composition of the dried gel monolith- and beads- samples was determined with elemental combustion analysis and is listed in **Table SI-4.2.1**. Both, the freeze dried and supercritical dried polymer monolith which were prepared with addition of the HkU precursor (samples m-CTS/HkU-f and m-CTS/HkU-sc) reveal a higher nitrogen content than the reference sample m-CTS-f which was prepared without the HkU-precursor (nitrogen contents of 8.8 wt% for m-CTS/HkU-f and 8.3 wt% for m-CTS/HkU-sc vs. 6.1 wt% for m-CTS-f). As all materials were prepared with the same amount of chitosan, the higher nitrogen content indicates the successful incorporation of the HkU- precursor into the monolithic samples. The same trend applies for the bead- samples, with nitrogen contents of 8.3 wt% for the freeze-dried sample (b-CTS/HkU-f) and 7.9 wt% for the supercritically dried sample (b-CTS/HkU-sc), vs. 7.4 wt% and 7.5 wt% for the freeze-dried (b-CTS-f) and supercritical dried (b-CTS-sc) reference samples. However, taking into account the nitrogen content of the HkU precursor (22 wt%, see ref. 69) and the nitrogen content of the dried CTS-gels (≈ 7 wt%, see **Table SI-4.2.1**), from the initial CTS/HkU ratio applied for the synthesis (200 mg CTS and 328 mg HkU precursor) a theoretical nitrogen content of 16 wt% could be estimated for the CTS/HkU composites. Compared to that, the lower obtained nitrogen contents indicate that not the whole amount of the applied HkU precursor is incorporated into the CTS network. This was already indicated during the washing procedure and the solvent exchange, where a brown coloration of the applied solvents after washing indicated a leaking of a certain amount of non-bound HkU precursor. Presumably, also some urea which is not covalently linked in the HkU precursor is staying molecularly dissolved in water.

Attempts to increase the amount of the incorporated HkU precursor by applying higher initial HkU/CTS ratios for the synthesis did not result in stable gel monoliths or beads. For the monolithic samples, with higher HkU/CTS ratios small gel-flakes were obtained after the hydrothermal treatment: It can be assumed that above a certain concentration of the crosslinking HkU precursor the contact between the CTS chains in the network is disrupted, which prevents the formation of a one-piece monolith. As stated above, attempts to prepare the beads with higher concentrations of the HkU precursor leads to bursting of the beads due to an increased osmotic pressure. Hence, the applied concentration of the HkU precursor (328 mg HkU precursor plus 200 mg CTS) is the highest possible to obtain a one-piece monolith or beads.

Furthermore, for both the monolith- and the beads- samples, the nitrogen content for the supercritically dried samples is slightly lower than for the freeze-dried samples. As stated above, this indicates that a certain amount of the HkU precursor or urea gets washed out during the solvent exchange and the drying with liquid CO_2. It can also be observed that the nitrogen content for the HkU- containing beads- samples is lower than for the HKU-containing monolithic samples, which indicates that for the beads a lower amount of the HkU precursor is incorporated. As already stated above for the discussion of the different microstructures between monolith- and bead- samples (see **Figure 4.2.4**), this is due to the more difficult penetration of the HkU precursor into the denser network of the beads.

To further determine the interaction between the HkU precursor and the CTS-network, FT-IR spectra of the samples m-CTS/HkU-sc and b-CTS/HkU-sc were compared with the FT-IR spectra of the reference sample m-CTS-f (freeze dried CTS gel without additives) and the pure HkU precursor (**Figure 4.2.6**).

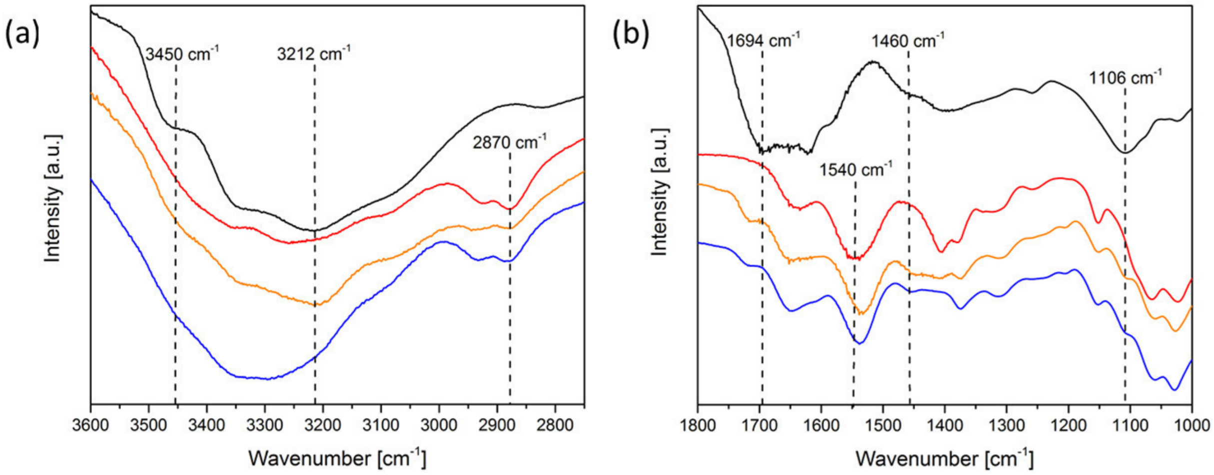

Figure 4.2.6. FT-IR spectra of the HkU precursor (black) and the samples m-CTS-f (CTS reference sample, red), m-CTS/HkU-sc (orange) and b-CTS/HkU-sc (blue), in the (a) 3600 cm^{-1} -2750 cm^{-1} range and (b) 1800 cm^{-1} -1000 cm^{-1} range.

Characteristic vibrations for the HkU precursor are amine vibrations at 1106 cm^{-1}, 1694 cm^{-1}, 3212 cm^{-1}, and 3450 cm^{-1}.[69] They can be traced back to the $\rho(NH_2)$- and $\delta(NH_2)$-vibrations of urea at 1150 cm^{-1} and 1674 cm^{-1} as well as the $\nu(NH_2)$-vibrations of urea at 3257 cm^{-1} and 3427 cm^{-1}, which are shifted during the condensation with hexaketocyclohexane to the HkU precursor.[162,163] Additionally, the ν(CN)-vibration of urea at 1460 cm^{-1} is still present in the HkU precursor.[162,163] All the characteristic vibrations of the HkU precursor appear for the HkU containing samples m-CTS/HkU-sc and b-CTS/HkU-sc, but cannot be observed for the reference sample prepared without additives (m-CTS-f). This indicates that the HkU precursor is incorporated into the CTS-network.

The signals at 2870 cm^{-1} can be assigned to vibrations of the aliphatic CH_2 groups of the CTS backbone, the signals at 1640 cm^{-1} and 1540 cm^{-1} are due to NH_2-vibrations of the CTS-backbone.[164,165] The signal at 1540 cm^{-1} (Amide II vibration) appears for solid CTS powders around 1580 cm^{-1}, the shift to 1540 cm^{-1} usually occurs due to protonation of the amide group.[166] A shift of the Amide II vibration to even lower wavenumbers can occur due to gradual disruption of present hydrogen bonding between the CTS chains.[133,167,168] This way, the shift of the Amide II vibration can be considered as an indication for an increased distcance between the CTS chains. Compared to the CTS reference sample (m-CTS-f), the HkU containing monolith and bead samples (m-CTS/HkU-f, m-CTS/HkU-sc, b-CTS/HkU-f and b-CTS/HkU-sc) reveal a distinct shift of the 1540 cm^{-1} vibration to lower wavenumbers (1432 cm^{-1}). This can be taken as another evidence for the incorporation of the HkU precursor into the CTS network.

4.2.1.2 Nitrogen-doped carbon monoliths and -beads

The dried monoliths (m-CTS/HkU-f, m-CTS/HkU-sc) and beads (b-CTS/HkU-f, b-CTS/HkU-sc) were carbonized by heating for 1h at 500 °C under nitrogen atmosphere. While the carbon materials derived from the freeze dried monolith and beads are obtained as silver glossy materials (m-CTS/HkU-f-500, b-CTS/HkU-f-500, photographs in **Figure SI-4.2.4**), the carbonized supercritical dried materials are of matt black appearance (m-CTS/HkU-sc-500, b-CTS/HkU-sc-500, photographs in **Figure 4.2.2** (6) and **Figure 4.2.3** (5)). This is in accordance to the golden color of the freeze-dried HkU containing polymers, which was attributed to thin layers of the HkU precursor on the surface of the respective samples (see **Figure SI-4.2.2**). As the C_2N carbon obtained from the carbonization of the pure HkU precursor at 500 °C has a metallic shine (see chapter 2.3.3 and ref. 69), the silver glossy appaerance of the carbonized freeze-dried monolith can be indicative towards the formation of C_2N layers on the materials surface. Contrary to the freeze-dried samples, the supercritically dried polymer samples were of matt brown appearance, which was attributed to the nanostructured surface of the supercritical dried samples. The matt black appearance of the carbonized supercritical dried samples indicates that the surface roughness is preserved during the carbonization.

The monolith samples prepared with the HkU precursor are obtained in slightly higher yields for the carbonization step than the m-CTS-f-500 reference sample (35 % yield for m-CTS/HkU-sc-500 and 38 % for m-CTS/HkU-f-500 vs. 28 % for m-CTS-f-500, see **Table SI-4.2.1**). The same observations can be made for the carbon beads prepared with the HkU precursor, which are obtained in yields of 34 % for b-CTS/HkU-sc-500 and 35 % for b-CTS/HkU-f-500 vs. 30 % carbonization yield for the reference sample b-CTS-sc-500 and 33 % for b-CTS-f-500 (see **Table SI-4.2.1**). This indicates that the HkU precursor is incorporated and stabilizes the CTS network. The higher carbonization yield for the monolithic samples when compared to the bead- samples is in accordance to the lower nitrogen content of the beads, which indicated that less amount of the HkU precursor or urea is incorporated into the beads. As already stated above, this was attributed to an inhibited penetration of the HkU precursor into the denser network structure of the beads sample.

The carbonization step goes along with a reduction in the monolith size or beads diameter. However, the monolithic shape or bead shape is completely retained during the carbonization process.

To determine whether the porous structure of the monolith- or beads- samples is retained after the carbonization process, SEM was applied. During carbonization, the network structure of the supercritical dried monolith polymer is transformed into a much denser structure of interconnected spheres with sizes around 20 nm (**Figure 4.2.7 (a,b)**). It can be assumed that this structural transformation is due to a melting of the HkU precursor during the carbonization, leading to spherical particles. However, as the precursor is linked to the stabilizing CTS network, the overall monolithic shape is retained. For the carbonized beads, a network of interconnected spheres with sizes ≈ 10 nm can be observed (**Figure 4.2.7 (c,d)**). However, compared to the monolithic sample and the beads- sample before carbonization, the density of the spheres-network is much lower. It was assumed for the microstructure of the beads, that CTS-rich domains are coated by the HkU precursor: From the lower yield for the carbonization of the CTS reference sample, it can be expected that the CTS domains decompose first during carbonization, which could explain the less dense microstructure of the beads-samples.

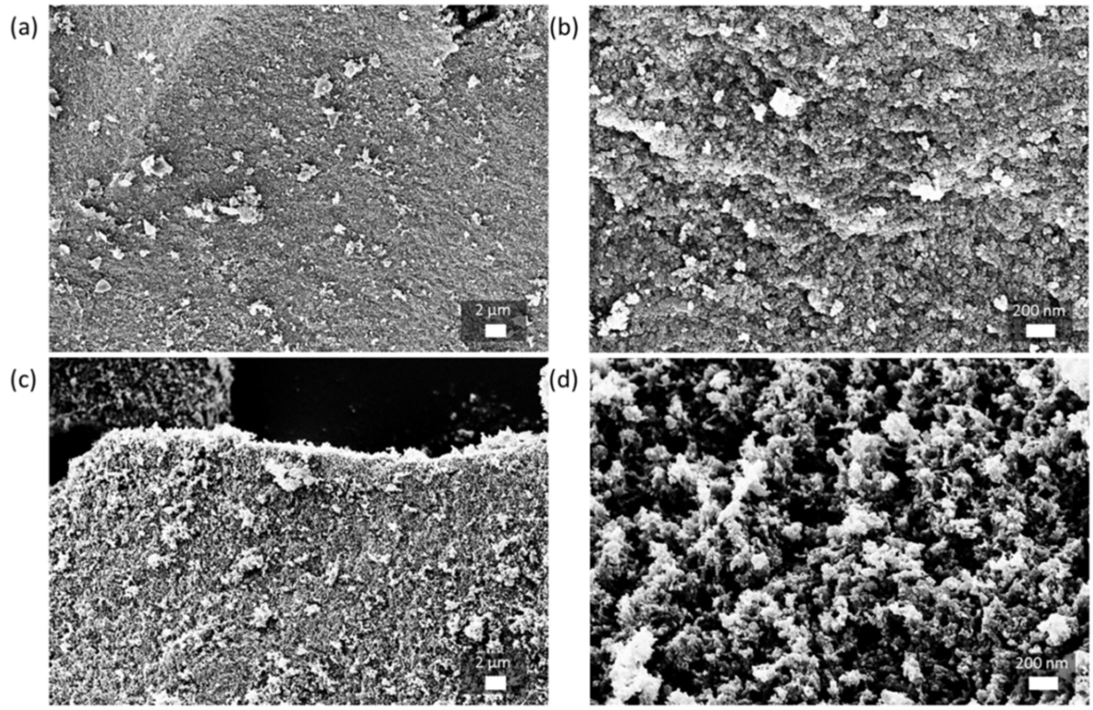

Figure 4.2.7. SEM images of the supercritically dried and carbonized (500 °C) monolith and bead samples. (a,b) Carbonized monolith (sample m-CTS/HkU-sc-500) (c,d) Carbonized beads (sample b-CTS/HkU-sc-500).

The porous structure of the carbonized monolith and –beads is confirmed by nitrogen physisorption (**Figure 4.2.8**, **Table SI-4.2.1**). For the monolithic sample, an apparent BET surface area of 348 m^2/g can be determined. The pore size distribution reveals pores with sizes mainly in the mesopore range. However, compared to the sample before carbonization, also some micropores can be detected, which is also reflected in a decreased average pore size of 8.2 nm. For the carbonized beads, an apparent surface area of 445 m^2/g can be detected. The pore size distribution is mainly mesoporous, but also here after the carbonization some micropores can be detected. This is reflected in a decreased average pore size of 5.2 nm. Thus, for the monolith and the beads, during the carbonization process the inner surface area increased significantly, also the amount of micropores, which is attributed to the decomposition of a certain amount of the material during carbonization.

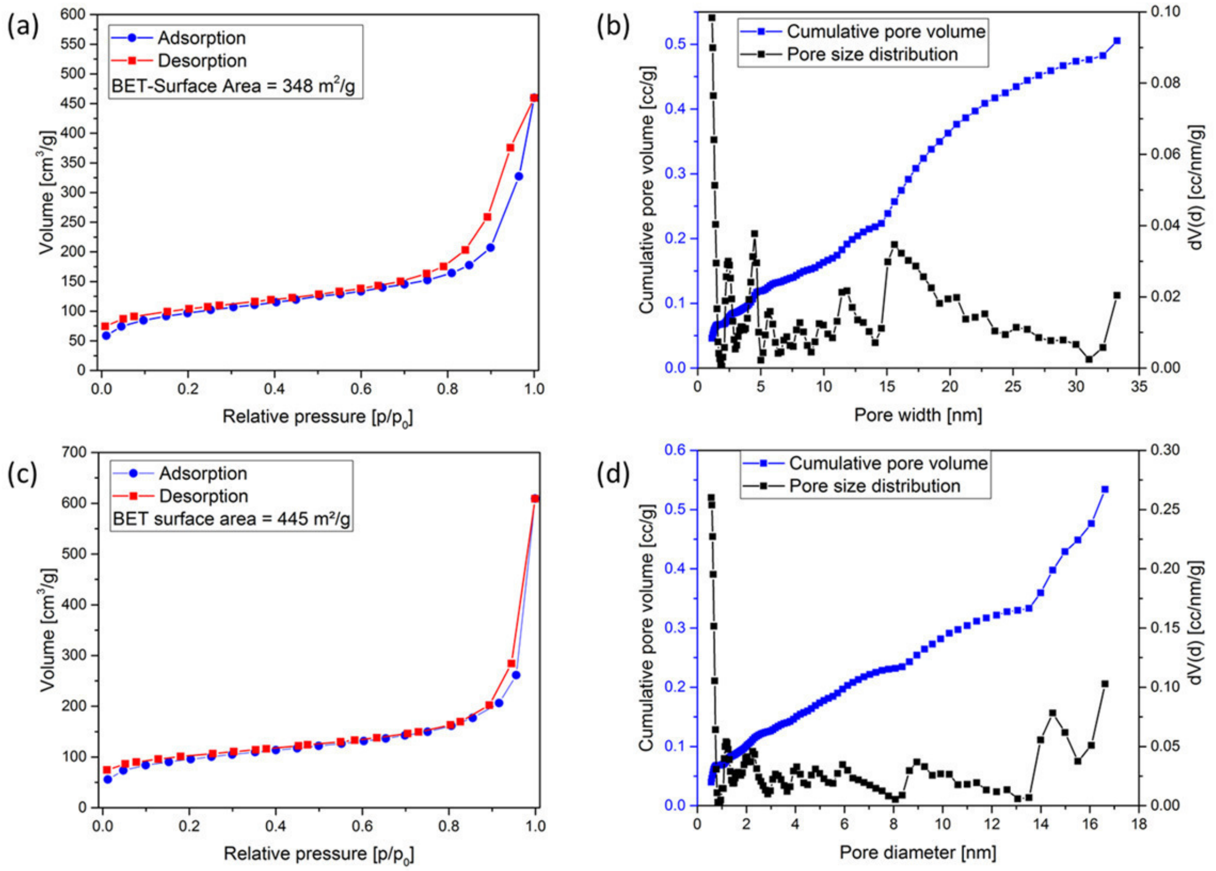

Figure 4.2.8. (a) Nitrogen sorption isotherms and BET surface area and (b) cumulative pore volume and pore size distribution of the supercritically dried and carbonized monolith (sample m-CTS/HkU-sc-500). (c) Nitrogen sorption isotherms and BET surface area and (d) cumulative pore volume and pore size distribution of the supercritically dried and carbonized gel beads (sample b-CTS/HkU-sc-500). Cumulative pore volume and pore size distribution were calculated applying the QSDFT model for slit/ cylindrical pores applied on the adsorption isotherm.

Expectedly, for the freeze dried carbonized samples (m-CTS/HkU-f-500, b-CTS/HkU-f-500) no considerable inner surface area can be detected by nitrogen physisorption (**Table SI-4.2.1**). Also with SEM, no microstructure is observed (**Figure SI-4.2.4**). This is to be expected, as already the freeze-dried samples revealed no porosity.

To determine the elemental composition of the obtained samples, elemental combustion analysis was performed. The monolithic carbons reveal nitrogen contents of 12 wt% (both for the supercritical dried and the freeze dried monolith) and C/N-ratios of 5.2 (m-CTS/HkU-sc-500) and 5.8 (m-CTS/HkU-f-500), respectively (**Table SI-4.2.1**). This is slightly higher than the nitrogen content obtained for the reference sample m-CTS-f-500 (nitrogen content of 10.4 wt% and a C/N-ratio of 6.0, see **Table SI-4.2.1**), which was prepared without addition of the HkU precursor. The same observations can be made for the carbon beads, which reveal a higher nitrogen content than the reference materials (nitrogen content of 10.8 wt% N and a C/N-ratio of 6.8 for b-CTS/HkU-sc-500; nitrogen content of 10.5 wt% and a C/N-ratio of 7.1 for the reference sample b-CTS-sc-500; The same trend applies for the freeze-dried bead samples, see **Table SI-4.2.1**). The higher nitrogen contents for the samples prepared with the HkU precursor are in accordance to the higher carbonization yields of those samples and indicate the successful incorporation of the HkU precursor into the CTS network. As already indicated from the carbonization yield, also the nitrogen content of the beads samples is lower than for the monolithic samples, which gives further indication that for the beads- samples a lower amount of the HkU precursor is incorporated.

It is known that the HkU precursor at 500 °C leads to a material with a nitrogen content of 36 wt% and a carbonization yield of ≈ 30 wt%.[69] Taking into account the yield and nitrogen content of the dried CTS gels after carbonization at 500 °C (≈ 10 wt% nitrogen and yield of ≈ 30wt% see **Table SI-4.2.1**), and combining this with the initial CTS/HkU ratio applied for the synthesis (200 mg CTS and 328 mg HkU precursor), a theoretical nitrogen content of 26 wt% could be estimated for the carbonized CTS/HkU composites. This value is distinctly higher than the experimentally obtained nitrogen contents. However, already the elemental analysis of the monolith- and beads- samples before carbonization indicated that only a small amount of the applied HkU precursor is really incorporated into the CTS network.

From the overall nitrogen content determined by elemental combustion analysis, the obtained materials can be classified as nitrogen-doped carbons (and will be denoted as nitrogen-doped carbons in the following discussion). However, the composition determined by elemental combustion analysis is an average value over the whole material, while the composition on a molecular scale is still not resolved yet. To explain the extra nitrogen found in the composite materials, two options can be discussed. The additional nitrogen can be due to C_2N domains, resulting from the carbonized crosslinking HkU precursor, beeing in a composite with nitrogen-doped carbon domains resulting from the carbonized CTS support. However, it can also be that due to the applied synthetic conditions the reaction cascade of the HkU precursor into C_2N is intermitted. Furthermore, contrary to the C_2N synthesis from the solid HkU precursor as described in ref. 69, here the HkU precursor is applied in a dissolved state, Here, not covalently bound urea might be dissolved out during the preparation process, inhibiting the condensation of the precursor into C_2N.

To furthermore resolve the question of the atomic composition of the carbonized CTS/HkU composites, further analytical techniques with a high spatial resolution (like high resolution TEM or STM) would be necessary.

In summary, mesoporous nitrogen doped carbon monoliths and beads can be prepared in a simple fashion by scaffolding the hexaketocyclohexane/urea eutectic with the biopolymer chitosan, followed by carbonization. Although the hexaketocyclohexane/urea eutectic is known to be a precursor to C_2N carbon, the local atomic composition of the obtained composites still has to be resolved. However, assuming that the obtained CTS/HkU composites contain C_2N- (from the HkU precursor) and nitrogen- doped carbon domains (from the carbonized CTS) in contact, the interfaces between these domains of different nitrogen content can be regarded as heterojunctions. For such a material with many local heterojunctions on a small scale, which even resembles to the vision of a "checkerboard doped" material as described in the introduction, interesting electronic properties can be expected.

Apart from that, mesoporous and binder-free materials of monolithic shape are especially suitable for various practical applications. However, this requires the accessibility to the pore system. To obtain more information regarding accessibility and potential surface functionalities of the monolithic pore system, carbon dioxide- and dye- adsorption experiments were performed with the carbonized monolith (sample m-CTS/HkU-sc-500).

4.2.1.3 The monolithic nitrogen-doped carbon for CO_2- and dye-adsorption

In this chapter, the accessibility of larger molecules to the monolithic pore system is presented, as well as the role of nitrogen functionalities on the pore surface as favored surface adsorption sites. The obtained results indicate interesting potential for applications of the monolith in the fields of CO_2- capture or dye- removal.

Due to its additional valence electron, the structural incorporation of nitrogen into the carbon framework increases the Lewis basicity of the carbon material,[37] which can be expected to improve the interaction of the framework with the Lewis acid CO_2. However, comparative studies which clearly reveal the influence of nitrogen incorporation into the carbon framework on the CO_2 adsorption are difficult to perform, as many parameters (surface area, pore architecture, presence of oxygen functionalities) contribute to the adsorption process. Nevertheless, the recent publications agree in the findings, that most important for CO_2 adsorption is the surface area and pore architecture, but in addition to that, incorporated nitrogen significantly improves the CO_2 heat of adsorption and thus the selectivity for CO_2 adsorption.[169-172] This is also supported by theoretical studies.[173]

A parameter which describes the strength of the interaction between the porous carbon material and the adsorbent CO_2, is the isosteric heat of adsorption (Q_{St}). As the gas adsorption on a solid surface is an exothermic process, this thermodynamic value is the standard enthalpy for the adsorption at a fixed surface coverage. It can be calculated from the sorption isotherms obtained at different temperatures by applying the Clausius-Clapeyron equation.[174] The CO_2 sorption isotherms recorded at 273 K, 284 K and 302 K are shown in **Figure 4.2.9 (a)**. The Q_{St} values calculated for the CO_2 adsorption at different CO_2 loadings are displayed in **Figure 4.2.9 (b)**.

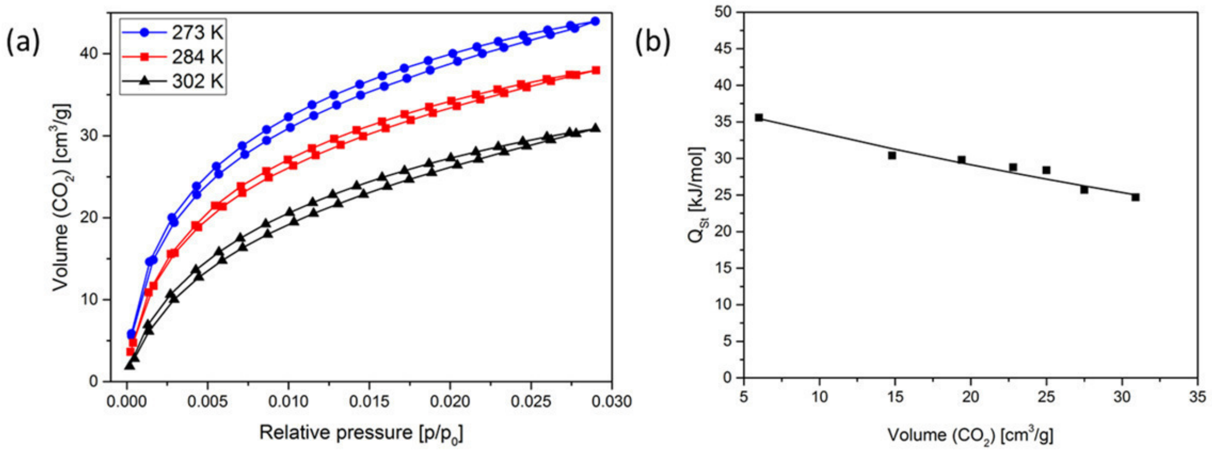

Figure 4.2.9. (a) Carbon dioxide physisorption isotherms for the carbon monolith (sample m-CTS/HkU-sc-500) at various temperatures (273 K (blue), 284 K (red) and 302 K (black)). (b) Calculated isosteric heat of adsoption (Q_{St}) for the CO_2 adsorption branch for the sample m-CTS/HkU-sc-500.

For the monolithic carbon, the isosteric heat of adsorption decreases with an increasing CO_2 loading. This decrease is typical for porous heteroatom doped carbons, and can be explained by different adsorption sites at different CO_2 loadings. At a low CO_2 coverage, specific sites like nitrogen functionalities lead to an increased CO_2 uptake, while at a higher CO_2 loading unspecific sites at the carbon surface are the determining factor.[175,176] Thus, the decreasing of Q_{St} reflects an inhomogenous surface in terms of adsorption energy, probably due to the nitrogen functionalities.

At a low CO_2 loading (6 cm^3 CO_2 per g, see **Figure 4.2.9 (b)**), the monolithic material shows an isosteric heat of adsorption of 36 kJ/mol. This is a significantly higher Q_{St} value than the average Q_{St} values reported for microporous carbons without nitrogen content, which are around 20-25 kJ/mol.[175,177] The high Q_{St} value indicates the presence of strong adsorption sites. This, and the onlyslightly decrease of Q_{St} with increasing CO_2 loadings, point to the presence of nitrogen functionalities at the pore surface as favored CO_2 adsorption sites.

Recently published DFT calculations on the effect of nitrogen functional groups in carbon materials for the adsorption of CO_2, revealed that pyridone and pyridine groups have a much higher energy for CO_2 adsorption than amine or quaternary nitrogen groups or pristine carbon.[178] This was attributed to Lewis acid- base interactions between the electron lone pair at the pyridinic nitrogen and the Lewis-acid CO_2. It is known from the carbonization of the pure HkU precursor, that the resulting material has a high content of pyridinic/ pyrazinic nitrogen (see chapter 2.2.2).[69] Hence, the high Q_{St} values for the carbonized

CTS/HkU monolith can be indicative for pyridinic or pyrazinic nitrogen from the carbonized HkU precursor.

Applications for materials with good CO_2- adsorbing properties are capturing-, storing- or converting carbon dioxide. In times of global warming, this is a field of intensive research, as it opens ways to tackle the emission of the greenhouse gas CO_2. Requirements on appropriate materials regard the CO_2- adsorption capacitiy and – selectivity, as well as opportunities to again release captured CO_2 from the sorbent material. The opportunity to easily release the captured CO_2 is important for practical applications, as this allows for a re-cycling process. However, as a high CO_2 adsorption energy goes along with a high energy for the desorption process, it is still challenging to find materials with good adsorption capacities and the opportunity to easily release the captured CO_2. However, a very interesting approach in this regard, is the idea of electrocatalytically switchable CO_2 capture:[179-181] The idea here is it, to reversibly alter the structure of the sorbent by charging, which affects the character of the interaction with CO_2. For instance, it was recently proposed for nitrogen-doped carbon nanotubes with pyridinic nitrogen, that injecting electrons significantly and reversible alters the strength of interaction with CO_2.[180] Thus, CO_2 adsorption and desorption can be switched electronically. This requires conducting materials with a high electron mobility and good CO_2 adsorption properties. Promising materials in this regard are carbon/nitrogen compounds, as here the nitrogen atoms are at the same time the adsorption sites for CO_2 and sites for charge accumulation. Recently published DFT calculations also proposed g-C_3N_4 nanosheets as material suitable for that.[181] However, here the low conductivity can be expected to be problematic for practical applications. For C_2N, a good conductivity and high electron mobility have been confirmed (see chapter 2.2.2) and it contains pyridinic/ pyrazinic nitrogen, which in ref. 180 have been proposed to be switchable charge accumulation/ sorption sites.[69,70] As shown in this chapter, the HkU precursor can be processed into monoliths with good CO_2 adsorption properties. Although the composition of the obtained monolith still has to be further resolved, it is therefore a promising material to be tested for the electrocatalytic switching of CO_2 capture.

To demonstrate the accessibility of the monolith pore network also to larger molecules, additionally dye adsorption experiments have been performed. As organic dye, Rhodamine B was applied. The time dependent RhB uptake was calculated from the RhB optical absorption maximum at 554 nm and is shown in **Figure 4.2.10 (a)**. It can be seen, that the monolithic material is capable of a very fast dye adsorption, after only 10 min. adsorption almost reaches saturation. To determine the maximum adsorption capacity, a RhB solution of higher concentration (200 mg/l) was applied. With the concentrated solution, after 48 h an adsorption capacity of 63 mg/g is reached. This is in the range of adsorption capacity values typically obtained for mesoporous carbon materials (for RhB adsorption) and thus proves the efficient transport of the dye molecule into the monolith pore system.[182,183]

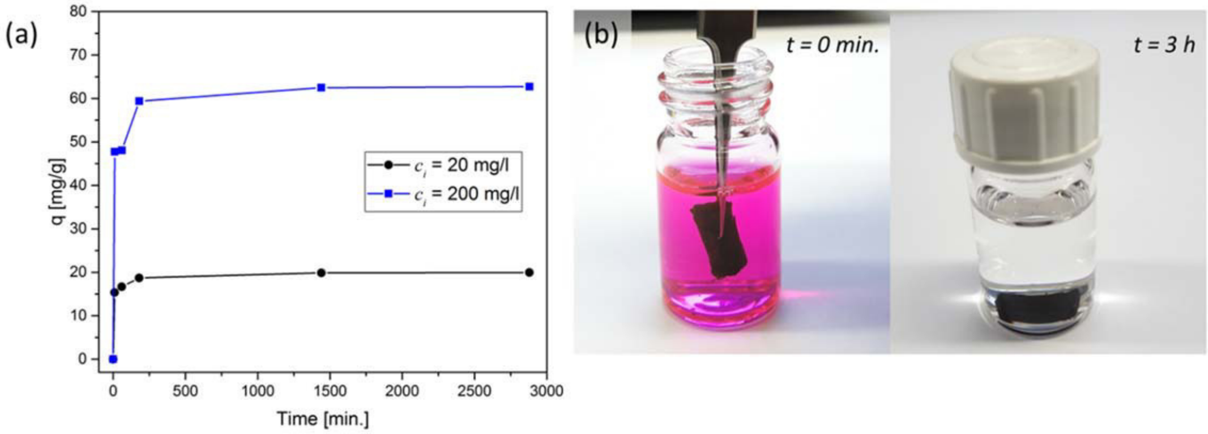

Figure 4.2.10. (a) Time dependent dye adsorption capacity q of the sample m-CTS/HkU-sc-500 as powder, with initial RhB concentrations c_i of 20 mg/l (black) and 200 mg/l (blue). (b) Decolourization of a RhB solution (initial concentration: 20 mg/l) after 3 h by the macroscopic monolith sample m-CTS/HkU-sc-500.

With regard to a final application as adsorbate material, the adsorption abilities of the macroscopic monolith are demonstrated in **Figure 4.2.10 (b)**. After only 3 h, the monolith is capable of completely decolorizing a RhB solution. This proves that the inner pore system is accessible to larger molecules not only for the monolithic material as powder, but also for the as-obtained one-piece monolith after carbonization.

4.2.2 C_2N carbon from organic crystals between squaric acid and urea

In this chapter, attempts towards the preparation of C_2N from another supramolecular precursor system are presented.

Here, a precursor system related to the hexaketocyclohexane/urea system is applied, but with the substitution of hexaketocyclohexane by another cyclic oxocarbon, i.e. squaric acid.

In general, cyclic oxocarbons like deltic acid, squaric acid, croconic acid or rhodizonic acid are interesting candidates as compounds for supramolecular precursors for carbon/nitrogen materials. This is for several reasons: They possess aromaticity or tend to condensation reactions to gain aromaticity.[69,70,184] They do not possess C-H-bonds, which hinder later thermal elimination and this way dimish sp^3 sites within the carbon.[12] And finally, they possess carbonyl-groups, which allow for the formation of hydrogen bonds or salt-formation with organic amines.

An interesting cyclic oxocarbon with an unusual molecular structure is squaric acid (3,4-Dihydroxycyclobut-3-ene-1,2-dione, **Figure 4.2.11**). It is a strong organic acid, has approximately the structure of a square and possesses non-classical aromaticity.[185-189] Squaric acid and its deprotonated form, the squarate- and disquarate- anions, are known to form layered supramolecular complexes by hydrogen-bonding with several organic amines, which assemble to stacked layers by van-der-Waals-, ionic- or π-π-interactions.[189-193] Furthermore, as described in chapter 2.3.3, it has been revealed that urea can crosslink with acidic OH-groups in organic molecules, like it was observed for the crosslinking of urea with hexaketocyclohexane octahydrate.[69]

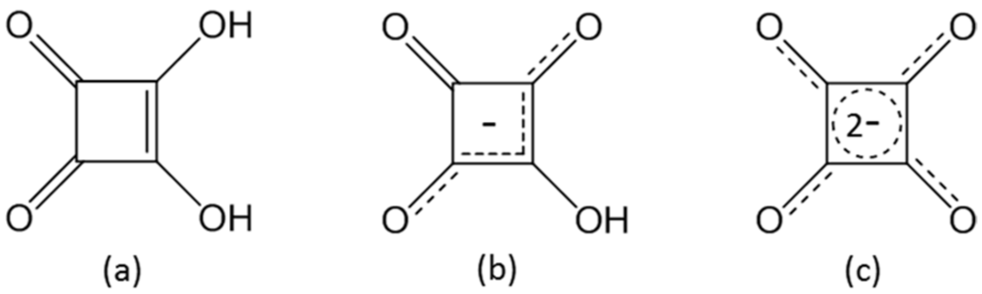

Figure 4.2.11. (a) Squaric acid and the (b) squarate- and (c) di-squarate- anion.

In this chapter, supramolecular complexes between squaric acid and urea were investigated as potential precursor for C_2N.[†] The choice of these monomers was based on the concept of pre-organization as described in chapter 2.3: Squaric acid, which is known for the formation of layered, stacked supramolecular assemblies, is meant to induce the structural information, i.e. the structure of stacked 2D layers which is also the basis for graphitic materials. Furthermore, the delocalized π-electron system of squarate anions allows for the formation of aromatic units. On the other hand, urea is meant to serve as bridging agents to the squaric acid units and as nitrogen source.

4.2.2.1 The squaric acid/urea precursor crystals

The precursor crystals were prepared by the crystallization of mixtures of squaric acid and urea dissolved in water.[194]

Suspensions of squaric acid and urea (molar ratios: 1:1 and 1:2) in water were dissolved by heating to 90 °C. When cooling down, crystallization of colorless needles (molar ratio squaric acid : urea = 1:1, denoted as SaU-1) or smaller white crystals (molar ratio squaric acid : urea = 1:2, denoted as SaU-2) can be observed (inlets in **Figure 4.2.12**). Both samples are obtained in a yield of 68 wt% each.

Optical microscopy images of the obtained crystals reveal a plate like morphology for the 1:1-crystals (SaU-1) and flower-like bundles for the 1:2-crystals (SaU-2) (**Figure SI-4.2.5**). Both observed crystal morphologies are different from the respective morphologies of the educts squaric acid (cubes) and urea (needles, see **Figure SI-4.2.5**). This already indicates the formation of new crystalline species during the preparation, and not just co-crystallization of the educts. In the optical microscope, both samples are birefringent.

More information on the crystal morphology are obtained by electron microscopy (**Figure 4.2.12**). SEM images of the SaU-1 crystals reveal stacked sheets with a thickness of ≈ 0.5 µm. For the sample prepared with the 1:2 molar ratio (SaU-2), rhombohedral crystals of irregular geometry and a thickness of several µm can be observed.

[†] The results presented in this chapter are published by the author of this thesis as: T. Jordan, M. Shalom, M. Antonietti, N. Fechler: Carbon Nanoarchitectures by Design: Preorganizing Squaric Acid with Urea, *Asia-Pac. J. Chem. Eng.* **2016**, *11*, 866-873, (ref. 194).

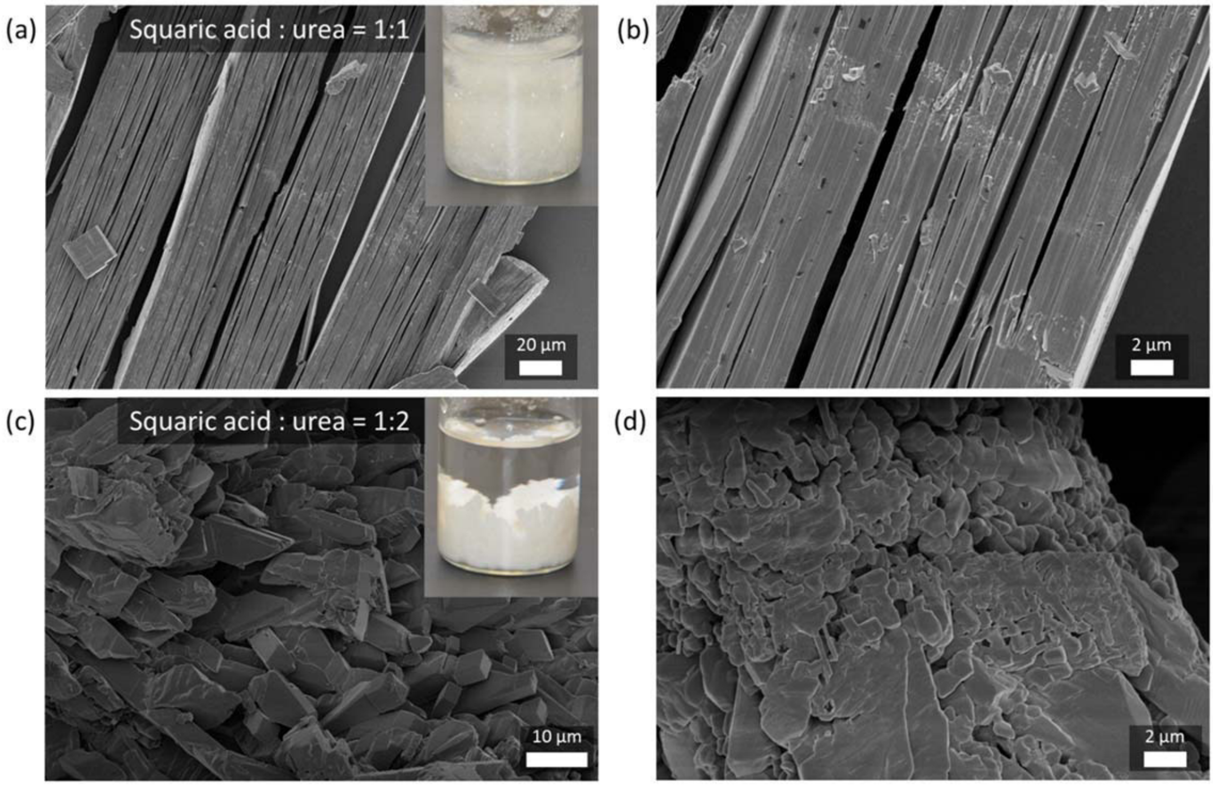

Figure 4.2.12. SEM images of the precipitated crystals of the (a,b) 1:1 squaric acid/urea crystals (sample SaU-1) and (c,d) the 1:2 squaric acid/ urea crystals (sample SaU-2). Inserts show photographs of the respective samples after precipitation.

PXRD analysis of the samples SaU-1 and SaU-2 reveals sharp and defined peaks, which indicates high a degree of crystallinity (**Figure 4.2.13**). The obtained diffraction pattern differ from the educts urea and squaric acid, as well as from each other. This indicates that the applied preparation method leads to the formation of new compounds with own crystal structures and not just to co-cyrstals of the educts.

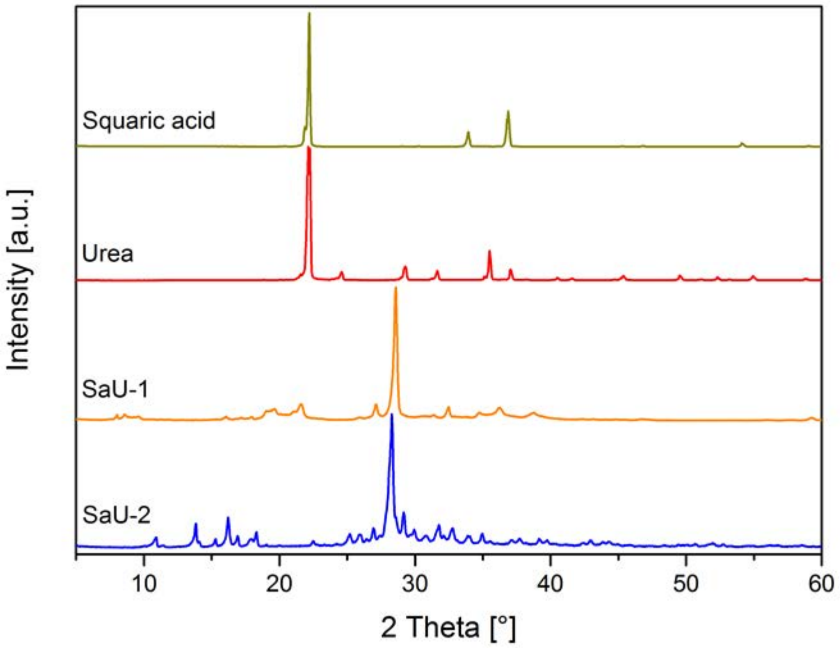

Figure 4.2.13. PXRD pattern of re-crystallized squaric acid (yellow), urea (red), and the SaU-1 crystals (orange) and SaU-2 crystals (blue).

In both samples, a new intense diffraction peak at 2θ = 28.3° appears, corresponding to a lattice distance of 0.31 nm. This is in the size range of the interlayer distance in graphitic materials.[195] With regard to the layered morphology observed by SEM for the SaU-1 crystals (see **Figure 4.2.12 (a,b)**), this diffraction peak suggests a structure of stacked 2D sheets. This would be in accordance to reports on the formation of stacked 2D-complexes between squaric acid with several organic amines (e.g. with 4,4-bipyridine,[191] imidazole,[192] histidine,[192] 2-aminopyridine,[192,193] 4-aminopyridine,[192,193] or several alkylamines[190]), which are stacked by π-π-, VdW-, or ionic interactions. It can be also observed that the diffraction pattern of the SaU-2 crystals reveals more and less defined peaks than SaU-1. Along with its irregular morphology (as observed by SEM, see **Figure 4.2.12 (c,d)**), this suggests that the sample SaU-2 consists of a mix of several structures.

The elemental composition of both samples was determined by elemental combustion analysis (**Table SI-4.2.2**). For both samples, the composition is almost identical with the calculated theoretical composition when assuming stochiometric incorporation of all educts, which means that the whole amount of the applied educts is consumed in the respective SaU- crystals or corresponding mixtures.

More information on the binding motifs of the SaU-crystals were obtained by FT-IR spectroscopy. Compared to the educts squaric acid and urea, in the infrared spectra of the obtained complexes significant changes can be observed (**Figure 4.2.14**).[162,196] In general, infrared spectroscopy gives indications for hydrogen bonding between squaric acid and urea, as well as for a proton transfer from squaric acid to urea. This is in accordance to the above described reported supramolecular complexes between squaric acid and several organic amines (see ref. 190-193), which are formed by hydrogen bonds between squarate anions and the protonated amine. As these complexes were also prepared by crystallizing dissolved mixtures of squaric acid and the respective amine from water, it is likely that complex formation between squaric acid and urea occurs in the same manner.

Indications for hydrogen bonds at the urea amine groups are given by the shifts of the urea δ$(NH)_2$-vibrations from 1674 cm^{-1} to 1690 cm^{-1}, and of the ν$(NH)_2$-vibrations from 3426 cm^{-1} to 3464 cm^{-1} (**Figure 4.2.14**).[162,163,197]

Furthermore, evidence for the protonation of urea is given by the appearance of two new peaks for the SaU complexes: A strong peak at 3156 cm^{-1} (SaU-1) and 3144 cm^{-1} (SaU-2), and a broad weak peak at 2780 cm^{-1} (SaU-1) and 2764 cm^{-1} (SaU-2). Both peaks are attributed to stretching modes of the (NH_3^+)-group in protonated urea.[198] The occurrence of these peaks is reported for several supramolecular complexes between squaric acid and organic amines, indicating an intermolecular proton transfer of the acidic squaric acid OH-groups to urea.[197,198] This is further supported by the shift of the urea ρ(NH_2)-vibrations from 1150 cm^{-1} to 1144 cm^{-1} in SaU-1 and 1129 cm^{-1} in SaU-2, which is as well reported for protonated urea.[198] Strong evidence for urea protonation is also given by the shift of the ν(C=O)-vibration from 1590 cm^{-1} to 1627 cm^{-1} (both SaU-complexes) and of the ν(CN)-vibration from 1460 cm^{-1} in urea to 1465 cm^{-1} in SaU-1 (for SaU-2, this vibration is overlayed by aromatic signals, see below), as protonation alters the bonding multiplicity of these atomic bonds.[198] It should be noted that the mentioned changes in the infrared spectra are much more pronounced for SaU-2, which gives indication for a higher degree of urea protonation in SaU-2. This is to be expected, as this sample was prepared with the double amount of urea.

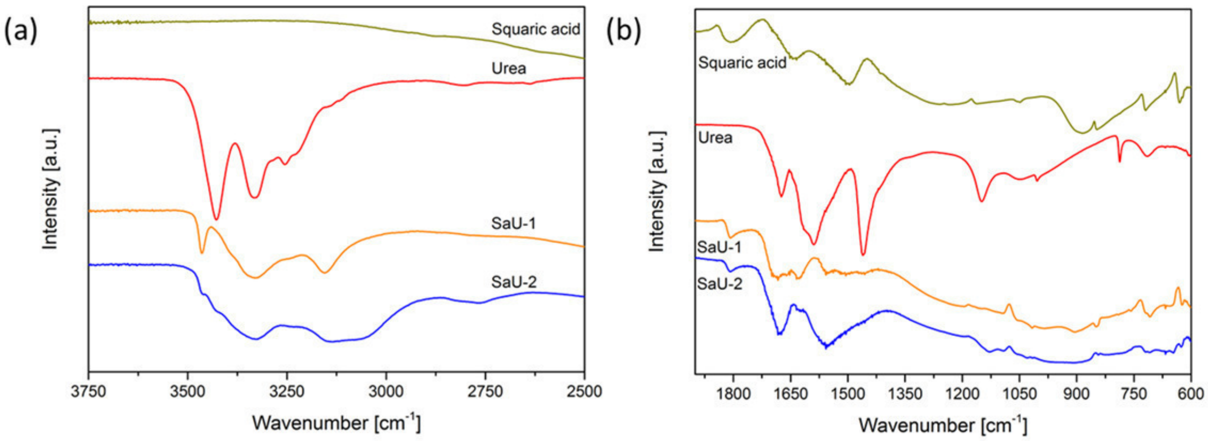

Figure 4.2.14. FT-IR spectra of squaric acid (yellow), urea (red) and the SaU-1 crystals (orange) and the SaU-2 crystals (blue) in the (a) 3750 cm^{-1} – 2500 cm^{-1} range and the (b) 1950 cm^{-1} -600 cm^{-1} range.

Evidence for hydrogen bonding and proton transfer are also reflected in the signals assigned to the vibrations of squaric acid. The vibrations at 1804 cm^{-1} and 1643 cm^{-1}, which are attributed to ν(C=O)-vibrations of squaric acid, are shifted in the SaU complexes to 1810 cm^{-1} (SaU-1) and 1634 cm^{-1} (SaU-2).[196] This indicates changes in the environment of the squaric acid carbonyl group, e.g. by hydrogen bonding.[199,200] Obvious indications on the assumed proton transfer can be gained from examining the aromatic region in the infrared spectra of squaric acid (around 1500 cm^{-1}). For pure squaric acid, in this region only the (C=C)-vibration at 1497 cm^{-1} appears.[196] However, with increasing electronic delocalization in the oxocarbon ring, the (C=C)-vibration disappears and is replaced by weak and broad aromatic signals.[201] This can be seen in the infrared spectra of the SaU-complexes, which reveal weak and poor defined peaks at 1505 cm^{-1}, 1511 cm^{-1} and 1560 cm^{-1} (SaU-1) or a very broad peak centered at 1560 cm^{-1} (SaU-2). It is reported, that the degree of electronic delocalization also affects the intensity of the ν(C=O) vibration, which gets less intense with an increased aromaticity of the oxocarbon ring.[201,202] For both complexes, the ν(C=O) vibration is significantly weaker than in pure squaric acid, and less intense for SaU-2 compared to SaU-1. For squaric acid, the degree of electronic delocalization increases with the degree of deprotonation. Thus, the aromatic signals support the assumption of a (partially) deprotonated squaric acid core, with a presumably higher degree of deprotonation in the SaU-2 complex.

4.2.2.2 The carbonized squaric acid/urea-crystals

To obtain carbon materials, the SaU crystals were carbonized at 550 °C under nitrogen atmosphere.

After carbonization, a matt-black (starting from the 1:1 crystals and denoted as SaU-1-550) or a metallic (graphitic gloss) black powder (starting from the 1:2 crystals and denoted as SaU-2-550) are obtained in yields of 31 wt% and 24 wt%, respectively. It should be noted, that the metallic gloss for carbons prepared below 800 °C is very unusual and gives a first indication towards the formation of a conjugated 2D network.

Despite the distinct appearance and carbonization yield, both samples reveal nearly the same elemental composition (SaU-1-550: 62 wt% C, 26 wt% N, 2 wt% H, 10 wt% O; SaU-2-550: 61 wt% C, 27 wt% N, 2 wt% H, 10 wt% O), with a C/N-ratio of 2.3 (**Table SI-4.2.2**). This is equivalent to an atomic composition of $C_5N_2H_2O_{0.6}$. The elemental composition is almost identical to that of the C_2N carbon obtained from hexaketocyclohexane octahydrate and urea at 800 °C (63 wt% C, 28 wt% N, 1.3 wt% H; C/N ratio: 2.2; see ref. 69), and regarding the C/N-ratio identical to the C_2N carbon reported by Baek et al. (see ref. 70).

The formation of graphitic domains is confirmed by PXRD. The diffraction pattern for both samples reveal the characteristic aromatic stacking peak for graphitic structures at $2\theta = 26°$ ((002)-peak) (**Figure 4.2.15**).[195] This corresponds to an interlayer distance of 0.34 nm between the graphitic sheets, which is slightly larger than in graphite (0.335 nm).[203] This is in contrast to the smaller interlayer distance (compared to graphite) for the C_2N carbon reported by Baek et al. (0.328 nm).[70] However, the stacking distance of the C_2N like carbon derived from the hexaketocyclohexane/urea system is also slightly larger than in graphite (0.338 nm for the materials obtained at 550 °C and 800 °C, as calculated from the (002)-peak at $2\theta = 26.3°$; **Figure SI-4.2.6**). In our cases, the increased interlayer distance can be due to a more defectous structure. A further indication for the existence of graphitic domains is a broad peak of low intensity at $2\theta = 43°$, which is the inner-plane peak ((101)-peak) for graphitic materials.[204] Interestingly, for both samples an additional peak at $2\theta = 11°$ can be observed, corresponding to a lattice distance of 0.8 nm. This is in the same range as the inner-plane peak at $2\theta = 13.1°$ for g-C_3N_4, which for g-C_3N_4 is attributed to the interhole-distance between the nitride pores (see chapter 4.1.2 on the carbon nitride from “caffeine doped” CM complexes).[48] For the C_2N obtained from the hexaketocyclohexane/urea precursor, these peaks (here: at $2\theta = 13°$, corresponding to a lattice distance of 0.68 nm; see **Figure SI-4.2.6**) can be also observed.[69] As the C_2N structure has periodically arrayed pores which are flanked by the pyrazinic nitrogen, the peaks around 2θ = 11° for the SaU- carbons and at 2θ = 13° for the C_2N carbon derived from the HkU precursor might be attributed to the interhole distance between these pores. For the C_2N synthesized from hexaaminobenzene and hexaketocyclohexane by Baek et al., with STM a interhole- distance of 0.83 nm between the pyrazinic pores was determined.[70] This is in the same range than the observed periodic pattern in the PXRD data for the SaU- and HkU- carbons. Thus, also PXRD gives evidence towards the formation of C_2N domains from the squaric acid/urea complexes.

However, it should be noticed that the obtained PXRD peaks for both SaU- carbons are rather broad, which indicates small crystal sizes of the domains with the graphitic structure and no long-range order.

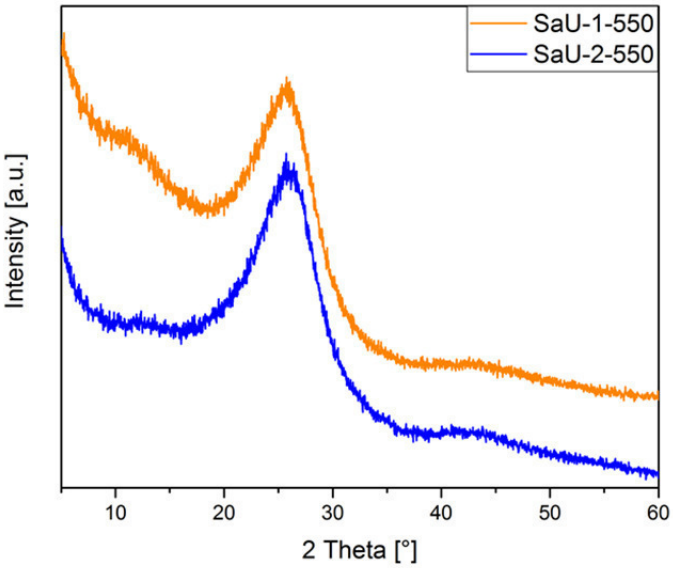

Figure 4.2.15. PXRD pattern of the carbonized 1:1 complex (sample SaU-1-550, orange) and 1:2 complex (sample SaU-2-550, blue).

Further indication for the formation of a conjugated, graphitic-like carbon network can be obtained from solid state ^{13}C nuclear magnetic resonance spectroscopy (cross-polarization magic angle spinning (CP MAS) ^{13}C-NMR) of the carbonized 1:1 crystals (SaU-1-550). Here, only one signal at δ = 137 ppm can be observed (**Figure SI-4.2.7**). This is in the δ = 100- 150 ppm region of chemical shifts typically observed for aromatic, graphitic-like carbons.[27] However, compared to the characteristic carbon signal at δ = 129 ppm for not heteroatom- containing graphene or aromatic carbons,[205] the signal observed for SaU-1-550 is de-shielded, which indicates less electron density at the carbon atoms. In aromatic carbons, de-shielding of the carbon atoms can be attributed to the presence of adjacent incorporated oxygen- or nitrogen-atoms. For aromatic carbons with nitrogen atoms in quaternary or pyridinic positions, shifts in the δ = 150- 170 ppm range can be observed.[91,206] As for the obtained materials a high nitrogen-content was determined by elemental analysis, the de-shielded aromatic carbon signal can be attributed to the presence of nitrogen atoms incorporated into the aromatic carbon framework. The absence of additional signals (or peak shoulders) in the 150 ppm- to 190 ppm-range, which would be due to carbonyl or amine carbons, indicates that no significant amounts of residual carbonyl- or amine-functionalities are left in the carbon material.[27]

For the squaric acid/urea 1:1 crystals (SaU-1), a layered sheet-like morphology can be observed. Interestingly, this morphology can be preserved during the carbonization process: As can be seen by SEM, the carbonized SaU-1 complex (SaU-1-550) reveals the structure of stacked sheets (**Figure 4.2.16 (a,b)**). In contrast to that, the carbonized 1:2 crystals (SaU-2-550) reveals a hollow tubular morphology (**Figure 4.2.16 (c,d)**). The retention of the sheet-like structure of the 1:1 complex shows that condensation occurs without a melting process. Along with the high carbonization yields, the retention of the morphology from the crystals to the carbon shows that no significant re-arrangements in the original structure of the complex occurs, which proves that the idea of pre-organization was successfully applied.

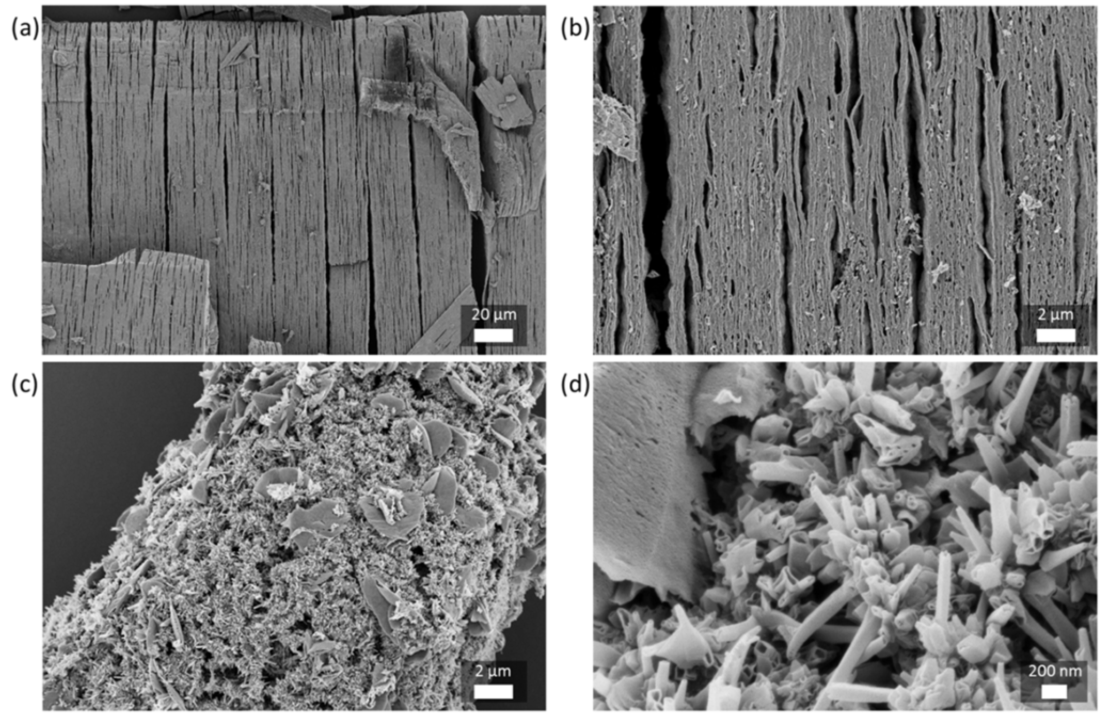

Figure 4.2.16. SEM images of (a,b) the 1:1 squaric acid/urea crystals carbonized at 550 °C (sample SaU-1-550) and (c,d) the 1:2 squaric acid/urea crystals carbonized at 550 °C (sample SaU-2-550).

Both, the layered morphology of the 1:1 crystals and the tubular morphology of the 1:2 crystals can be preserved even at a temperature of 900 °C (**Figure SI-4.2.8**). However, with increasing temperature, the sheet-like structure gets more buckled and porous, due to the evaporation of gaseous decomposition products at elevated temperatures.

For the SaU-1-550 carbon, no considerable BET surface area can be detected by means of nitrogen physisorption. For SaU-2-550, an apparent BET surface area of 79 m^2/g can be detected, going well with its tubular structure (**Figure SI-4.2.9**).

To obtain more information on the formation-process of the carbon materials, thermogravimetric analysis coupled with mass spectrometry (TGA-MS) was performed. Additionally, samples obtained after heating the SaU-complexes for 2 h under nitrogen atmosphere at 200 °C (and 235 °C, respectively), were analyzed by UV/Vis-spectroscopy, FT-IR-spectroscopy and elemental analysis.

According to TGA, the condensation of SaU-1 into the carbon/nitrogen material occurs in three major reaction steps (at 170 °C, 230 °C and 270 °C, **Figure 4.2.17 (a)**). For the condensation of SaU-2, four major reaction steps can be distinguished, with the first three steps (at 165 °C, 215 °C and 270 °C) occurring at nearly the same temperature than for SaU-1 and one additional reaction step at 335 °C (**Figure 4.2.17 (b)**). With coupled mass spectrometry, the evolution of CO_2, H_2O and NH_3 can be identified. The release of H_2O and CO_2 (m/z = 17, 18, 44 g/mol) occurs mainly in the first two reaction steps (170 °C and 230 °C). Additionally, for the SaU-2 complex the release of CO_2 (m/z = 44 g/mol) and NH_3 (m/z = 16 g/mol) at temperatures above 335 °C can be observed. Furthermore, FT-IR spectroscopy of the samples obtained at 200 °C and 235 °C reveals the development of characteristic aromatic vibrations in the 1400- 1700 cm^{-1} range, indicating the formation of aromatic species (**Figure 4.2.17 (c)**).[201] The formation of oligomeric species is further supported by a color change during the carbonization process, from colorless for the SaU-crystals to yellow (200 °C), dark brown (235 °C) and finally black (550 °C) (**Figure SI-4.2.10**). With UV/Vis diffusive reflectance spectroscopy, this can be seen as an increasing absorption at higher wavelengths with increasing temperature (**Figure 4.2.17 (d)**).

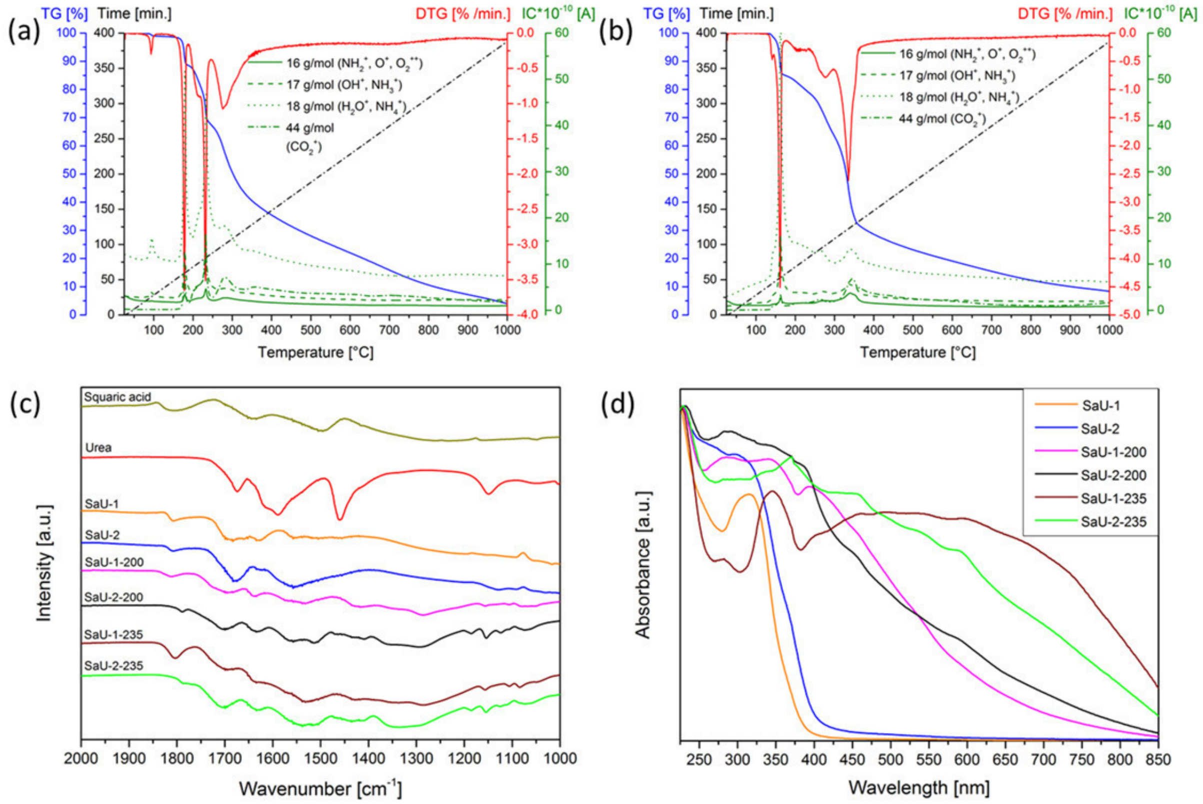

Figure 4.2.17. TGA-MS data for the samples (a) SaU-1 and (b) SaU-2. (c) FT-IR spectra (1000- 2000 cm^{-1}- range) of the samples SaU-1 (orange), SaU-2 (blue), SaU-1-200 (magenta), SaU-2-200 (black), SaU-1-235 (brown), SaU-2-235 (green) and squaric acid (yellow) and urea (red). (d) UV/Vis diffusive reflectance spectra of the respective samples SaU-1, SaU-2, SaU-1-200, SaU-2-200, SaU-1-235 and SaU-2-235.

On the basis of these results, the reaction of squaric acid and urea to the carbon/nitrogen material could proceed along the mechanism proposed in **Scheme 4.2.2**. In the initial reaction step, the preparation of the SaU crystals, supramolecular hydrogen bonded assemblies of protonated urea and squarate (or disquarate) anions are formed ((1) in **Scheme 4.2.2**). When heating the complexes, the urea could react with squaric acid by transamidation to a squaramide ((2) in **Scheme 4.2.2**), under the release of H_2O and CO_2. This reaction can be attributed to the first reaction step at 170 °C. Further heating could result in the reaction of several squaramide-units to conjugated, N-heterocyclic intermediates. This is represented by the structure (3) (in **Scheme 4.2.2**), which contains a pyrazine unit (highlighted in red in **Scheme 4.2.2**), and can be obtained formally by the condensation of the squaramide (2) with an additional squaric acid unit. The oligomerization could be attributed to the reaction steps at 230 °C and 270 °C, supported by the increase of the aromatic FT-IR signals and the rapid color changes at temperatures above 200 °C. Finally, further condensation leads to a conjugated, N-heterocyclic carbon network. In (4) in **Scheme 4.2.2**, the structure of a C_2N network with pyrazinic units (highlighted in red) is displayed, which could be obtained formally by further condensation of the pyrazinic intermediate (3).

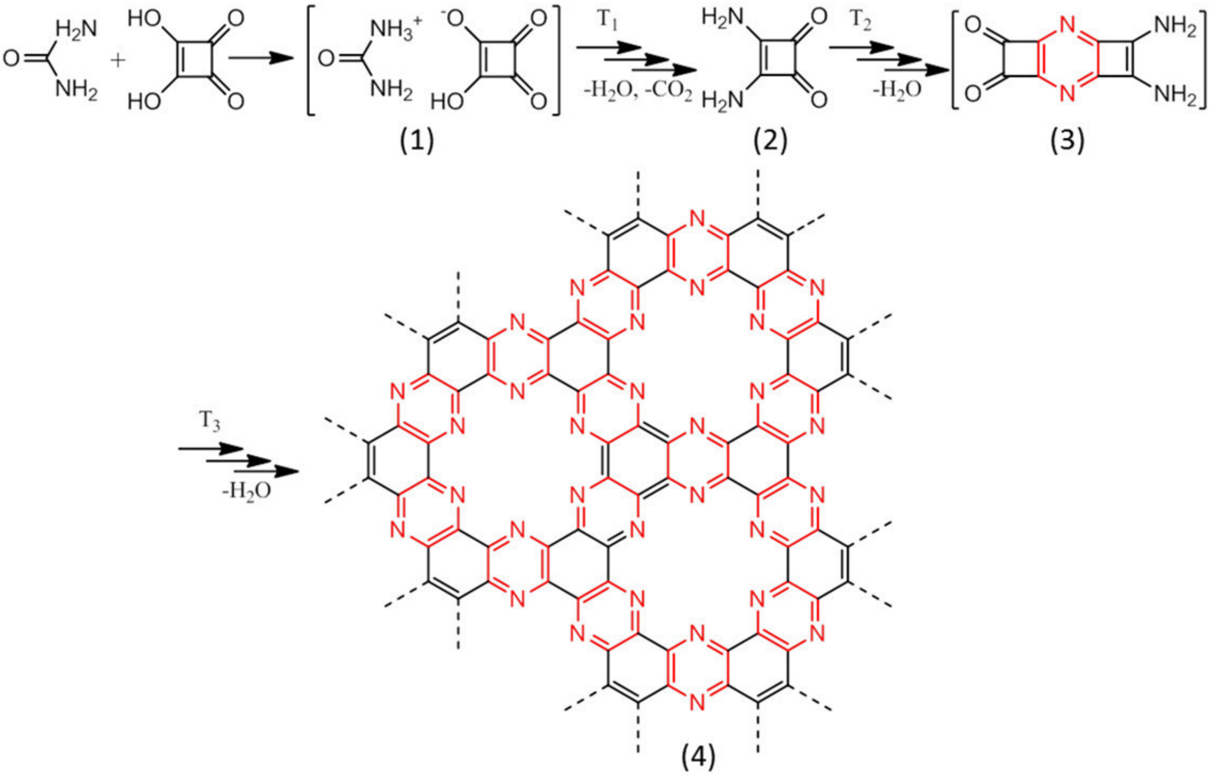

Scheme 4.2.2. Proposed reaction pathway towards the nitrogen containing carbon from the squaric acid/urea crystals. Dotted lines for the C_2N structure in (4) indicate connection to the carbon lattice.

However, this is an idealized reaction scheme. To confirm the proposed reaction pathway and intermediates, further analytical techniques are necessary. Of special interest would be a temperature-resolved solid state NMR- or XPS-analysis, which could confirm the existence of the proposed pyrazinic C_2N structure motifs, like it is observed for the carbon derived from the hexaketocyclohexane/urea- system.[69]

At temperatures above 550 °C, some nitrogen gets expelled from the structure. The C/N-ratio shifts towards a value of 4 at 800 °C and 900 °C (**Table SI-4.2.2**). This indicates that the nitrogen is less stable incorporated than in the materials obtained from the hexaketocyclohexane/urea system (C/N-ratio of 2.2 at 800 °C, see ref. 69).

It is interesting to note, that the SaU-1- and SaU-2-carbons are different in morphology, but reveal the same elemental composition. However, convergence of the elemental composition between the two samples cannot be observed until temperatures of 235 °C. Until this temperature, the C/N-ratio of the SaU-2 materials remains nearly constant at values around 1.4, which is, due to the double amount of the nitrogen-source urea in the precursor, lower than for the SaU-1 materials (see **Table SI-4.2.2**). An increase of the C/N-ratio, which is equivalent with a loss of nitrogen, can be observed between the samples obtained at 235 °C and 550 °C. At 550 °C, both SaU-carbons reveal nearly the same C/N-ratio (2.4 for SaU-1-550 and 2.3 for SaU-2-550, see **Table SI-4.2.2**). In the same temperature range appears the TGA-signal at 335 °C for the SaU-2 material, which cannot be observed for the SaU-1 material (see **Figure 4.2.17 (b)**). This signal is attributed to the release of H_2O, CO_2 and NH_3 (m/z = 16, 17, 18 and 44 g/mol). Combined with the lower carbonization yield for the SaU-2 samples, it is likely to attribute the additional TGA signal and the sudden increase of the C/N-ratio to a decomposition process occurring for SaU-2 around 335 °C. This leads to the assumption that the SaU-2 complex consists of a mixture of several crystalline structures with different thermal stability, with the less thermally stable structures decomposing around 335 °C, leaving behind the same carbon compound as obtained for SaU-1. The assumption of SaU-2 as a mixture of crystalline structures is also supported by its irregular morphology and (in comparison to SaU-1) more complex PXRD pattern (see **Figure 4.2.12** and **Figure 4.2.13**). The decomposition of less stable structures can as well be responsible for the formation of the hollow, tubular SaU-2-550 morphology. It is assumed that the decomposition of structurally integrated, but thermally unstable domains leads to structural defects, which in turn lead to buckling or rolling up of otherwise planar, conjugated carbon networks. Evaporation of gaseous decomposition products might then lead to the observed hollow morphology. A similar effect (void or tube formation), based on a related mechanism as the proposed one, can be observed for some metal alloys (Kirkendall-effect).[207,208] If the contact of two different metals (or metal alloys) is heated, it can result in the expansion of one metal phase accompanied by shrinking of the other one, leading to the formation of voids or tubes. The reason for this behavior is the difference in the diffusion rates of the two metals. This principle might be adapted to the SaU-2 system. If in a system of stacked layers, one layer develops structural defects (due to decomposition of thermally less stable domains), bending of the stacked layer system can occur.

In summary, by carbonization of organic crystals between squaric acid and urea, carbon/nitrogen materials with a composition of $C_5N_2H_2O_{0.6}$ were obtained. The data obtained so far, point towards the formation of domains with C_2N- motifs as depicted in **Scheme 4.2.2** (4), however without long-range order. To further prove the existence of the

C_2N domains, analytical techniques with a high spatial resolution like HR-TEM or STM are required. However, for a simple and large-scale solid-state synthesis like it was applied here, the formation of defect-free materials cannot be expected. As it is well-known for carbon nitride, which until now as well could not have been prepared in sufficient amounts as single-crystalline defect-free material, a long-range order of the material is not really important for most applications. To the contrary, for many applications the presence of defects is highly beneficial (see chapter 4.1).[40,41] If C_2N motifs for the material prepared here can be proven by the techniques mentioned above, the applied synthetic procedure is due to its simplicity and cheap educts highly advantageous to that developed by Baek et al., who applied complex preparation methods resulting in low amounts of C_2N.[70,71]

In any case, the applied precursor system shows an interesting example for the idea of the pre-organized precursor complexes, as here the carbonization reactions occur in such a well- arranged manner, that the morphology of the precursor crystals is completely retained after carbonization. This shows the potential of a template-free route towards structured carbon materials, by applying organic crystals of special morphology as precursors.

4.2.2.3 Porous SaU-carbons by templating with $ZnCl_2$

Due to its liquidity, the eutectic hexaketocyclohexane/urea precursor holds inherent advantages for processing, e.g. hard-templating with SBA-15 or salt- templating with $ZnCl_2$ (see chapter 2.3.3), which allows for the facile synthesis of microporous C_2N.[69] This is highly beneficial in regard to applications which depend on the surface area of the active material, like adsorption, catalysis or electrochemistry. But also with respect to the construction of a composite material, an increase in surface area correlates with an increased interfacial area.

However, contrary to the eutectic hexaketocyclohexane/urea precursor, templating of the squaric acid/urea precursor is more difficult, as here a solid, crystalline precursor is applied. This precursor does not melt during the synthesis, which makes it difficult to achieve a homogenous mixture with hard- or salt-templating agents. Furthermore, adding the salt-template before precipitation of the crystals could affect the structure of the crystals. However, with variations in the synthetic procedure, also homogenous mixtures between squaric acid, urea and $ZnCl_2$ can be obtained: It is known, that urea forms deep eutectics by complexation with the Lewis-acid $ZnCl_2$.[209,210] As it has been revealed for the squaric acid/urea- precursor system, that the amount of urea in the precursor does not affect the composition of the material after carbonization, an excess of urea in the precursor mixture can be used as eutectic solvent, allowing for the homogenization with the $ZnCl_2$.

Taking advantage on this, microporous carbon with a C_2N composition were obtained from 1:2 mixtures of squaric acid and urea (molar ratio), mixed with $ZnCl_2$ in the weight-ratio 1:1, after carbonization at 550 °C (sample denoted as SaU-2-550-Zn). The obtained material reveals a specific BET surface area of 865 m^2/g, a total pore volume of 0.4126 cc/g, and a micropore volume of 0.3217 cc/g (**Figure 4.2.18** (**a**)). The pore size-distribution, which is obtained from the physisorption data and reveals microporosity, is shown in **Figure 4.2.18** (**b**). The average pore size is 2 nm, confirming the microporous character of the SaU-2-550 sample. With electron microscopy, additional macropores can be detected (**Figure 4.2.18** (**c**)).

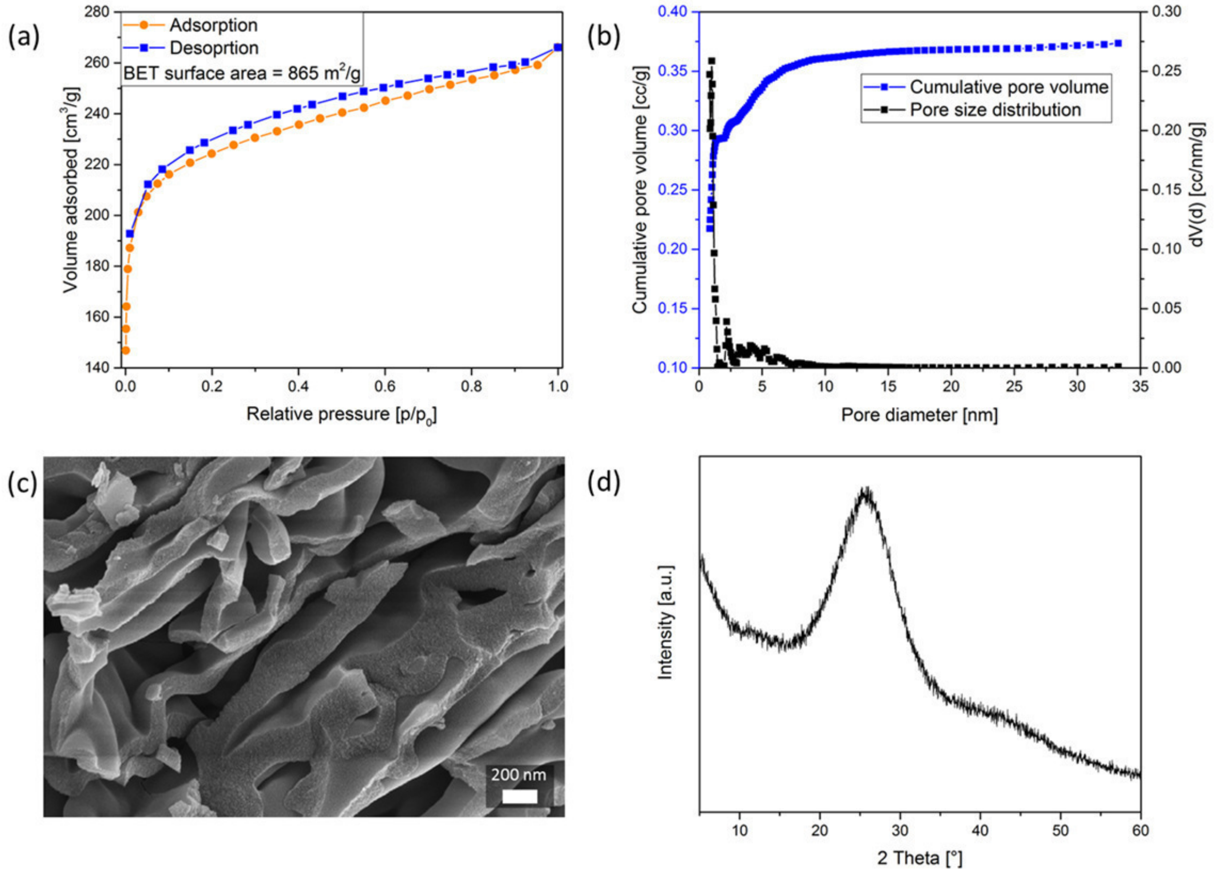

Figure 4.2.18. (a) Nitrogen sorption isotherms and BET surface area, (b) pore size distribution (c) SEM image and (d) PXRD pattern of the sample SaU-2-Zn-550. Cumulative pore volume and pore size distribution were calculated applying the QSDFT model for slit/ cylindrical pores applied on the adsorption isotherm.

As determined by elemental combustion analysis, the obtained material reveals a C/N- ratio of 2, with a nitrogen content of 22.3 wt% and a carbon content of 43.5 wt% (see **Table SI-4.2.2**).

However, when compared to the pristine SaU-carbon, the material prepared with $ZnCl_2$ reveals significantly higher oxygen content (20.9 wt% oxygen for SaU-2-550-Zn and 9.9 wt% oxygen for SaU-2-550, see **Table SI-4.2.2**). It is known, that the deep eutectic between urea and $ZnCl_2$ is built by complexation of the Zn-atom and the urea carbonyl group.[209] During carbonization, the additional urea which is bound to the $ZnCl_2$ and does not get incorporated into the resulting carbon/nitrogen material, will decompose into CO_2, ammonia and lead to the formation of ZnO. To remove the resulting ZnO or residual $ZnCl_2$, the material obtained after carbonization is washed with 0.1 M hydrochloric acid. However, it can be assumed that despite the washing step, a certain amount of residual ZnO will remain in the micropores. In the PXRD pattern of the obtained material, no peaks for residual Zn-spezies can be observed (**Figure 4.2.18 (d)**). But as the sample still can contain residual amorphous Zn-spezies which do not appear in the PXRD pattern, other analytical methods (e.g. Inductively coupled plasma mass spectrometry, ICP-MS) are required to detect residual metal spezies. From the PXRD pattern it can be also seen that the addition of $ZnCl_2$ does not affect the structure of the obtained carbon/nitrogen material, as the same refelections at $2\theta = 11°$, 26° and 42 ° as for the pristine SaU-2-550 carbon can be observed.

Indication towards the role of urea as deep-eutectic with $ZnCl_2$ are given by the elemental composition of the material which is obtained under the same conditions but with applying a squaric acid/urea 1:1 molar mixture: Here, the material obtained at 550 °C (denoted as SaU-1-550-Zn) has a lower nitrogen content when compared to SaU-2-550-Zn (nitrogen content of 17.7 wt%, carbon content of 45.4 wt% and C/N- ratio of 2.6, see **Table SI-4.2.2**). The lower nitrogen content can be attributed to a smaller amount of urea available for the reaction with squaric acid to the carbon/nitrogen material, as a certain amount of urea is complexed by $ZnCl_2$.

4.3 The g-C_3N_4/C_2N composite

In chapter 2.2.2, it was described how the inherent limitations for the use of g-C_3N_4 as photocatalyst, which are the low optical absorption in the visible light part of the spectrum and the relatively high rate of charge carrier recombination, can potentially be overcomed by making a nanocomposite with the recently described C_2N. DFT calculations predicted an increased optical absorption in the visible light part of the spectrum and the formation of a type II heterojunction for this composite.[89] The band alignment at the heterojunction will lead to the separation of photogenerated electrons and holes, which prevents them from recombination and this way leads to an increased photocatalytic activity (see **Scheme 2.5** in chapter 2.2.2). Furthermore, it was calculated that the composite has a negative interface adhesion energy, which means that the interface formation is exothermic.[89]

Recently, the preparation of a g-C_3N_4/nitrogen-rich carbon composite was reported, which showed an extremely high rate of hydrogen evolution in photocatalytic water splitting (18.3 times higher compared to pure g-C_3N_4).[82] In this reference, a 3D network of g-C_3N_4 fibers was prepared by the hydrothermal treatment of a dicyandiamide solution, followed by freeze-drying. The framework was afterwards treated with pyrrole, which is a well-known precursor for N-doped carbons.[211] After carbonization at 600 °C, a fiber-network of g-C_3N_4 coated with nitrogen containing carbon was obtained, which had a BET surface area of 372 m^2/g and an overall C/N ratio of 0.86.[82] In accordance to the theoretical predictions in ref. 89, the increased photocatalytic activity of the obtained composite was attributed to its increased light harvesting and a decreased electron/hole recombination rate, which is due to a charge transfer of the photogenerated electrons into the nitrogen-rich carbon.

However, up to now, a nanocomposite between carbon nitride and C_2N has not been synthesized. In this chapter, first attempts towards the preparation of a composite of g-C_3N_4 and C_2N carbon are presented.

For materials with a layered graphitic structure, nanocomposites are described in which layers of different 2D materials are stacked onto each other by van der Waals interactions, the so-called van der Waals heterostructures.[212] There are already reports on van der Waals heterostructures of g-C_3N_4 and other 2D materials like graphene or N-doped graphene, which were applied as efficient electrocatalysts for the hydrogen evolution reaction.[83-85] These nanocomposites can be prepared in two steps: In the first step, 2D nanosheets of the respective materials are prepared. This is done by de-stacking of the bulk material, which can be achieved by chemical methods, e.g. via thermal oxidation etching, or by liquid exfoliation.

For thermal oxidation etching, attractive forces between the stacked 2D layers are disturbed by oxidation of the material.[213] A more simple method is liquid exfoliation: Here, dispersions of the respective materials are treated by sonication, which leads to the exfoliation of 2D nanosheets or even single layers from the bulk material.[214] To achieve exfoliation, the surface energy of the 2D layers has to be matched by the surface energy of the applied solvent, which means that the choice of the solvent plays a crucial role to achieve exfoliation. For the preparation of the nanohybrids, dispersions of the exfoliated nanosheets of the respective materials are mixed, which can lead to the formation of the heterostructures by self-assembly of the nanosheets.[83-85] For conjugated carbons like graphene, g-C_3N_4 or N-doped carbons, self-assembly can occur due to van der Waals- interactions or π-π stacking of the conjugated 2D layers.[83] Furthermore, the surface charge of the 2D layers can be affected by chemical methods, e.g. by protonation.[215,216] If dispersions of exfoliated nanosheets with different surface charges are mixed, self-assembly can also occur due to electrostatic interactions.[83]

In this chapter, attempts towards the preparation of a composite of g-C_3N_4 and the C_2N-carbon by the self-assembly of exfoliated g-C_3N_4- and C_2N-nanosheets are presented. To achieve exfoliation, dispersions of the respective components are treated in a sonication bath. For the single components, g-C_3N_4 from the CMp-precursor (a supramolecular precursor complex between cyanuric acid and a phenyl-modified melamine-derivative, see chapter 2.3.2) and the C_2N carbon obtained from the squaric acid/urea crystals are applied. In chapter 4.3.1, the preparation of nanosheets by the sonication method is presented, as well as attempts to obtain g-C_3N_4 nanosheets with a positive surface charge by protonation. In chapter 4.3.2, the obtained composites are tested for their activity in photocatalytic water splitting.

4.3.1 Preparation of g-C_3N_4 and C_2N nanosheets by liquid exfoliation

Recently, the preparation of carbon nitride nanosheets by sonicating dispersions of the g-C_3N_4 obtained from the CMp precursor was reported.[217] This procedure has been repeated here to obtain dispersed nanosheets of g-C_3N_4. For this purpose, dispersions of the CMp-g-C_3N_4 (prepared by carbonization of the CMp precursor complex at 450 °C, denoted as CMp-450)[100,217] were treated by sonication for 10 h (concentration of the dispersion: 0.5 mg/ml). After centrifugation (30 min. at 5000 rpm to remove bigger particles and aggregates) of the resulting dispersion, pale colloidal dispersions were obtained (**Figure SI-4.3.1 (a,b)**). As measured by dynamic light scattering (DLS), the obtained dispersion contains particles with a broad size distribution, with two main species centered at 246 nm and 4771 nm (with the bigger particles not sufficiently removed by centrifugation) (**Figure SI-4.3.1 (c)**). The colloid particles are negatively charged, with a surface zeta potential of -29 mV (**Figure SI-4.3.1 (d)**). This is in good agreement with earlier published values for the surface zeta potential of colloidal g-C_3N_4 and indicates a stable colloidal dispersion.[217,218]

For the composite material, the dispersed g-C_3N_4 nanosheets should be mixed with dispersed nanosheets of the C_2N carbon. For the C_2N carbon, the material obtained from the carbonization of the squaric/urea 1:1 crystals at 550 °C (sample SaU-1-550, see chapter 4.2.2.2) was applied. Therefore, attempts were made to obtain SaU-1-550 nanosheets by sonication. After 10 h of sonicating a dispersion of SaU-1-550 in water (concentration of the dispersion: 0.5 mg/ml), followed by centrifugation, a brown, clear dispersion is obtained (**Figure 4.3.1 (a)**). According to DLS measurements, the dispersion contains species with particle sizes around 95 nm, 416 nm and 9420 nm (**Figure 4.3.1 (c)**). Thus, nanoparticles of the SaU-1-550 material can be prepared by sonication of the dispersion in water. Sheet-particles with lateral dimensions around 100 nm can be also observed by transmission electron microscopy (TEM, **Figure SI-4.3.2**).

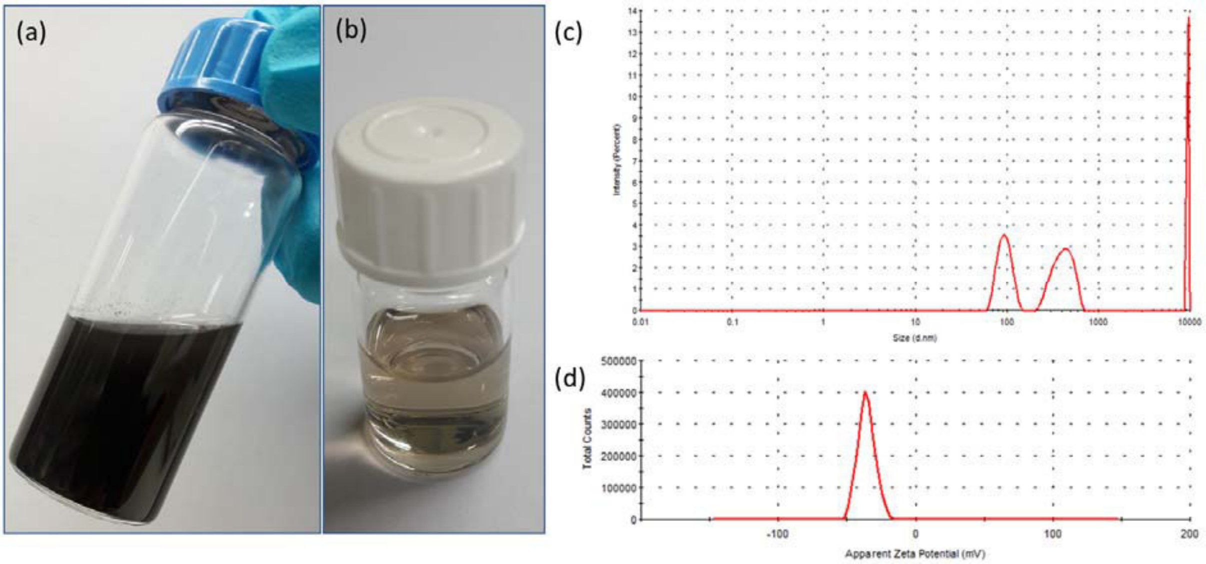

Figure 4.3.1. Photographs of the SaU-1-550 dispersion after sonication (a) before and (b) after centrifugation. (c) Size distribution of the dispersed SaU-1-550 particles after sonication and centrifugation as determined by DLS. (d) Surface zeta potential of the dispersed SaU-1-550 particles after sonication and centrifugation.

The surface zeta potential of the dispersed particles was measured as -36 mV (**Figure 4.3.1 (d)**). This indicates a stable colloidal dispersion of negatively charged particles. However, after two days, already a precipitate of aggregated particles can be observed, which indicates no long-term stability of the obtained dispersion. To determine the concentration of the colloidal dispersion, the dispersion was freeze-dried after centrifugation and the mass of the obtained residue weighted. With this method, the concentration of the colloidal dispersion was determined to be ≈ 0.05 mg/ml, which corresponds to a yield of ≈ 10 wt% of dispersed particles.

As determined by the zeta potential measurements, both the CMp-450 nanoparticles and the SaU-1-550 nanosheets have a negative surface charge. However, for the self-assembly experiments, it would be appropriate to have particles with different surface charges, as then attractive forces between the different materials can be increased by electrostatic interactions. It is known for g-C_3N_4, that the surface charge can be changed by protonation with concentrated hydrochloric acid, without destroying the graphite-like structure.[215,216] For this purpose, CMp-450 powder was stirred overnight in concentrated hydrochloric acid and subsequently washed with water. The obtained product (denoted as CMp-450-prot) can be dispersed in water by sonication, resulting in pale dispersions (**Figure 4.3.2 (a,b)**). The dispersed particles exhibit a surface zeta potential of +44 mV, indicating highly positive charged particles (**Figure 4.3.2 (c)**). Thus, protonation can switch the surface charge of the CMp-450 particles.

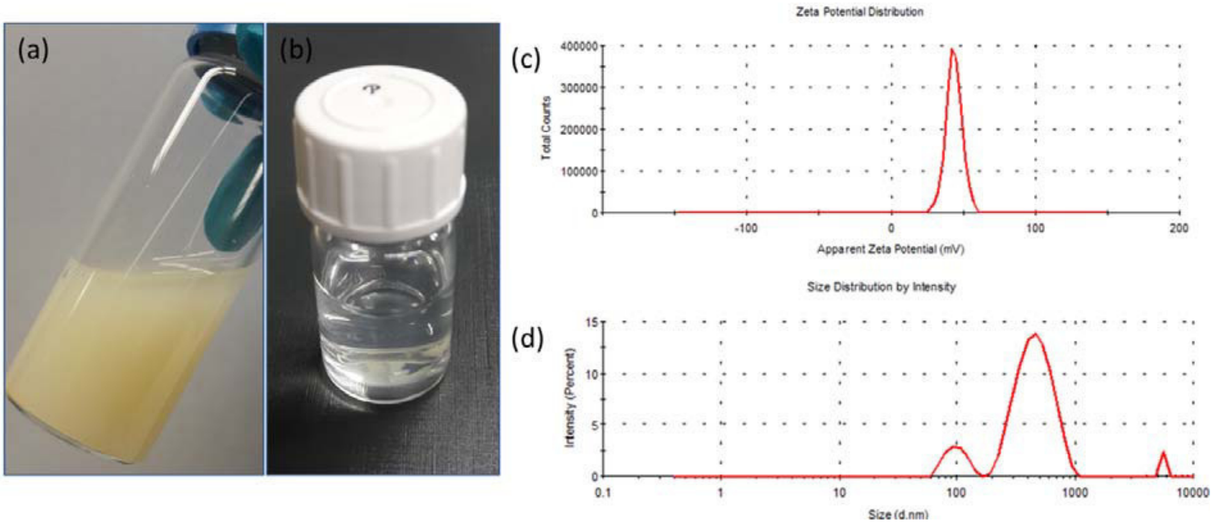

Figure 4.3.2. Photographs of the CMp-450-prot dispersion after sonication (a) before and (b) after centrifugation. (c) Surface zeta potential of the dispersed CMp-450-prot particles after sonication and centrifugation. (d) Size distribution of the dispersed CMp-450-prot particles after sonication and centrifugation as determined by DLS.

With DLS, particles with sizes around 98 nm, 470 nm and 5560 nm can be determined (**Figure 4.3.2 (d)**). Compared to the CMp-450 nanosheets obtained after sonication, the protonated CMp-450-prot nanosheets are of smaller particle size when sonicated for the same time. This indicates that exfoliation of the protonated CMp carbon nitride requires less energy. This observation is also reported for protonated carbon nitride derived from other precursors and is attributed to a disruption of the attractive forces (hydrogen bonding, van der Waals forces) between the single carbon nitride layers due to their protonation.[215,216]

PXRD of the protonated sample (without sonication) shows the typical peaks for g-C_3N_4 at 2θ = 13.9° (in-plane (100)-peak), 2θ = 27.7° ((002) stacking-peak) and 2θ = 43° ((101)-peak) (**Figure 4.3.3 (a)**).[56] With FT-IR, the signals for the breathing modes of the triazine units at 800 cm^{-1} and the stretching modes for CN heterocycles between 1200 cm^{-1} and 1600 cm^{-1} can be observed (**Figure 4.3.3 (b)**).[110] Hence, PXRD and FT-IR indicate that protonation does not affect the structure of the g-C_3N_4 sample.

However, for the protonated sample CMp-450-prot, the optical absorption is blue-shifted in respect to the pristine sample CMp-450 and the protonated sample reveals a much brighter, nearly white color (**Figure 4.3.3 (c,d)**). This is also reported for protonated g-C_3N_4 derived from other precursors and indicates a widening of the band gap.[215,216] As protonation disrupts the attractive forces between the g-C_3N_4-layers, the band gap widening might indicate a partial delamination of the g-C_3N_4 layers, even without sonication.

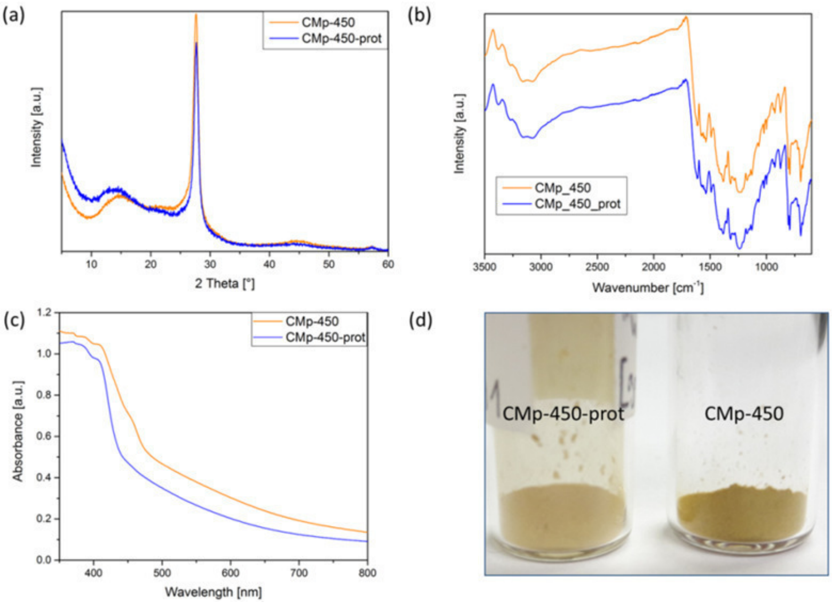

Figure 4.3.3. (a) PXRD pattern, (b) FT-IR infrared spectra, (c) UV-Vis diffusive reflectance spectra and (d) photographs of the samples CMp-450 and the protonated sample CMp-450-prot.

The C/N-ratio of the protonated sample is slightly decreased (C/N-ratio of 0.89 for CMp-450-prot vs. 0.95 for CMp-450), whereas the hydrogen- and oxygen-content are significantly increased (3.4 wt% hydrogen and 10.9 wt% oxygen for CMp-450-prot vs. 2.7 wt% hydrogen and 5.4 wt% oxygen for CMp-450, see **Table SI-4.3.1**). In summary, these findings indicate that protonation of CMp carbon nitride does not lead to destruction of its chemical structure, but changes its surface charge and facilitates exfoliation.

4.3.2 The g-C_3N_4/C_2N composites for photocatalytic water splitting

The g-C_3N_4/C_2N composites were prepared in two steps. In the first step, a colloidal dispersion of SaU-1-550 is prepared by sonicating a dispersion of SaU-1-550 in water (0.5 mg/ml), followed by centrifugation (30 min. at 5000 rpm, to remove bigger aggregates). In the second step, an excess of CMp-g-C_3N_4 (2 mg/ml) was dispersed in the SaU-1-550 colloidal dispersion, followed by ultrasonication, to exfoliate the g-C_3N_4. After 10 h of sonication, the dispersions were put overnight in a drying oven (100 °C), to evaporate the water and potentially allow for the nanocomposite- formation due to self-assembly of the nanosheets. Subsequently, the composites were tested for photocatalytic water splitting under white light irradiation. Two different composites were prepared, a composite between CMp-450 and SaU-1-550 (denoted as CMp-450-SaU) and a composite between the positive charged, protonated CMp-450-prot and SaU-1-550 (denoted as CMp-450-prot-SaU). For fair comparison, the described procedure was carried out only with CMp-450 or CMp-450-prot, without adding it to the SaU-1-550-dispersion. The reference materials are denoted as colloidal CMp-450 and colloidal CMp-450-prot.

The obtained composites are homogenous, dark-yellowish (CMp-450-SaU) or grey (CMp-450-prot-SaU) powders (inserts in **Figure 4.3.4**). Indication towards the formation of a composite material is given by elemental analysis, which reveals a small increased C/N ratio for the composites when compared to the pristine CMp-450 carbon nitride (C/N-ratio of 0.97 for CMp-450-SaU vs. 0.95 for CMp-450 and 0.91 for CMp-450-prot-SaU vs. 0.89 for CMp-450-prot, see **Table SI-4.3.1**). However, the fraction of the SaU-1-550 material in the composite is expected to be very small, as the concentration of dispersed SaU-1-550 nanosheets after sonication was determined to be only ≈ 0.05 mg/ml (see above). Thus, the maximum concentration of SaU-1-550 in the composite is ≈ 2.5 wt%.

UV-Vis spectroscopy shows an increased optical absorption for the composites (**Figure 4.3.4**). However, from the UV-Vis spectra and elemental analysis data, it cannot be decided if the composite materials are just mixtures of CMp carbon nitride and SaU-1-550, or if they consist of assembled layers of g-C_3N_4 and the C_2N carbon.

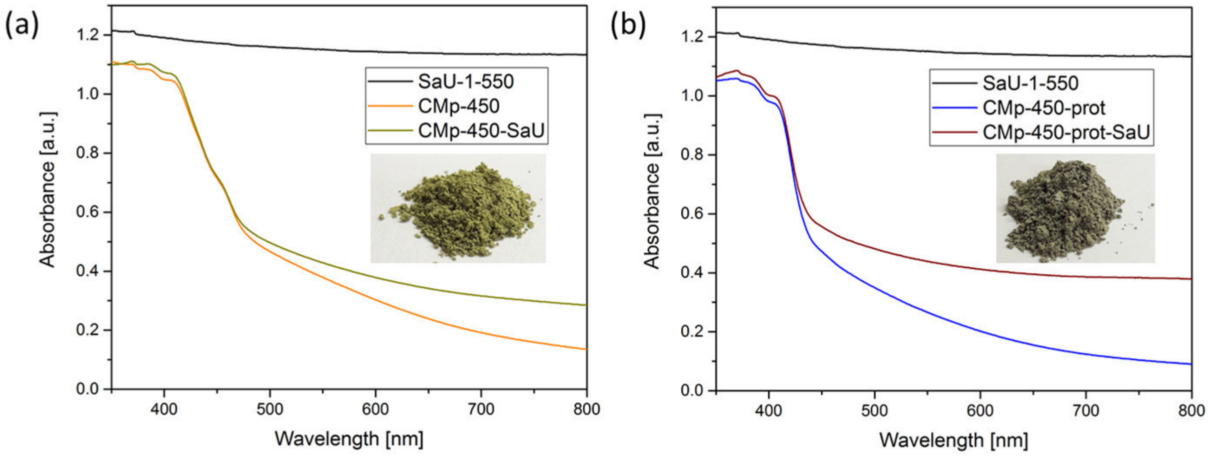

Figure 4.3.4. UV/Vis diffusive reflectance absorbance spectra of (a) SaU-1-550, CMp-450 and CMp-450-SaU and (b) SaU-1-550, CMp-450-prot and CMp-450-prot-SaU. Inserts show photographs of the composite samples CMp-450-SaU (in (a)) and CMp-450-prot-SaU (in (b)).

The activity of the composite samples for the photocatalytic water splitting was tested with the addition of Pt as co-catalyst and triethanolamine as sacrificial agent.[56] The time dependent hydrogen evolution under white light irradiation is shown in **Figure 4.3.5**. With the composite samples, hydrogen evolution rates of 388 µmol $h^{-1}g^{-1}$ for CMp-450-SaU (**Figure 4.3.5 (a)**) and 360 µmol $h^{-1}g^{-1}$ for CMp-450-prot-SaU are measured (**Figure 4.3.5 (c)**). For g-C_3N_4 materials, the obtained rates in hydrogen evolution are rather high. Compared to CMp-450 as bulk material, this is a two-fold increase in the hydrogen evolution rate (180 µmol $h^{-1}g^{-1}$ for CMp-450, see **Figure SI-4.3.3**). However, compared to the reference samples which were also prepared by sonication (colloidal CMp-450 and colloidal CMp-450-prot), the composite samples show no significant superior photocatalytic activity. Both reference samples are in the same range regarding the hydrogen evolution rate, with rates of 344 µmol $h^{-1}g^{-1}$ for the colloidal CMp-450 (**Figure 4.3.5 (b)**) and of 341 µmol $h^{-1}g^{-1}$ for the colloidal CMp-450-prot (**Figure 4.3.5 (d)**). The slightly higher hydrogen evolution rates for the composites are within the experimental error of this method and do not allow for further conclusions. Thus, the high hydrogen evolution rate of the composites seems to be primary an effect of their increased surface area due to the sonication, rather than due to their composition. Without the co-catalyst Pt, for none of the samples the evolution of hydrogen can be observed.

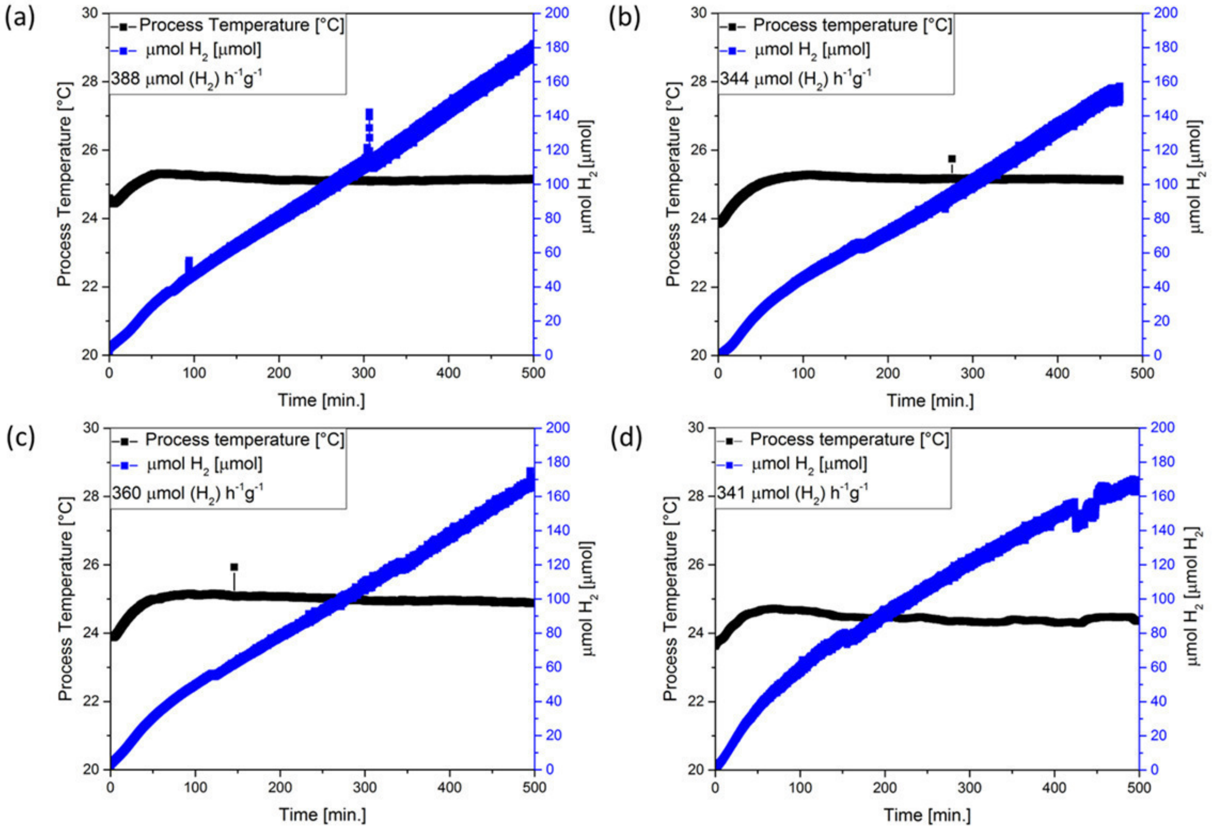

Figure 4.3.5. Rate of hydrogen evolution for the photocatalytic splitting of water with the materials (a) CMp-450-SaU, (b) colloidal CMp-450, (c) CMp-450-prot-SaU and (d) colloidal CMp-450-prot tested as photocatalyst.

Hence, the testing for photocatalytic water splitting does not give clear evidence for the formation of a g-C_3N_4/C_2N nanocomposite with increased photocatalytic activity.

An important parameter for the activity of a photocatalytic system is the mass ratio between the photocatalyst and the co-catalyst. For the g-C_3N_4/C_2N system, C_2N is supposed to take the part of the co-catalyst, which leads to an enhanced optical absorption of the photocatalytic system and decreases the charge carrier recombination rate. The maximum performance of a photocatalytic system is achieved only for a certain mass ratio between photocatalyst and co-catalyst. At too high loadings of the co-catalyst, the co-catalyst particles shield the active sites of the photocatalyst and decrease the intensity of light which penetrates into the reaction solution.[219] At too low concentrations of the co-catalyst, only a small amount of the photocatalyst particles is in contact with the co-catalyst. For the above introduced photocatalytic system of g-C_3N_4 and N-doped carbon from polypyrrole (ref. 82), a co-catalyst loading (which is the N-doped carbon) below and above 8.6 wt% lead to a tremendous decrease in the hydrogen evolution rate.[82] The loading of the potential co-catalyst SaU-1-550 in the composites presented here, is estimated to be ≈ 2.5 wt%. Thus, it can be assumed that the loading of SaU-1-550 in the composites is too low to significantly increase the catalytic performance of g-C_3N_4. Thus, the composite preparation via aqueous colloidal dispersions is technically limited, since exfoliation in aqueous dispersions is accompanied by too low yields. This however is a consequence of a certain mismatch in the surface energies of water and the C_2N carbon.

A commonly used solvent for the exfoliation of carbon materials is N-Methyl-2-pyrrolidone (NMP). It has a surface tension of 40.1 mJ/m^2, which is equivalent to a surface energy of ≈ 70 mJ/m^2, matching well to that of graphite (70- 80 mJ/m^2).[214,220,221] Compared to the aqueous dispersions, the dispersions obtained when sonicating SaU-1-550 in NMP are much more stable (**Figure 4.3.6 (a)**). For the centrifuged dispersions of SaU-1-550 in NMP, even after several months no aggregation can be observed, whereas in the case of the aqueous dispersions aggregation can be observed after a few days. Also CMp-450 carbon nitride can be dispersed in NMP (**Figure 4.3.6 (b)**).

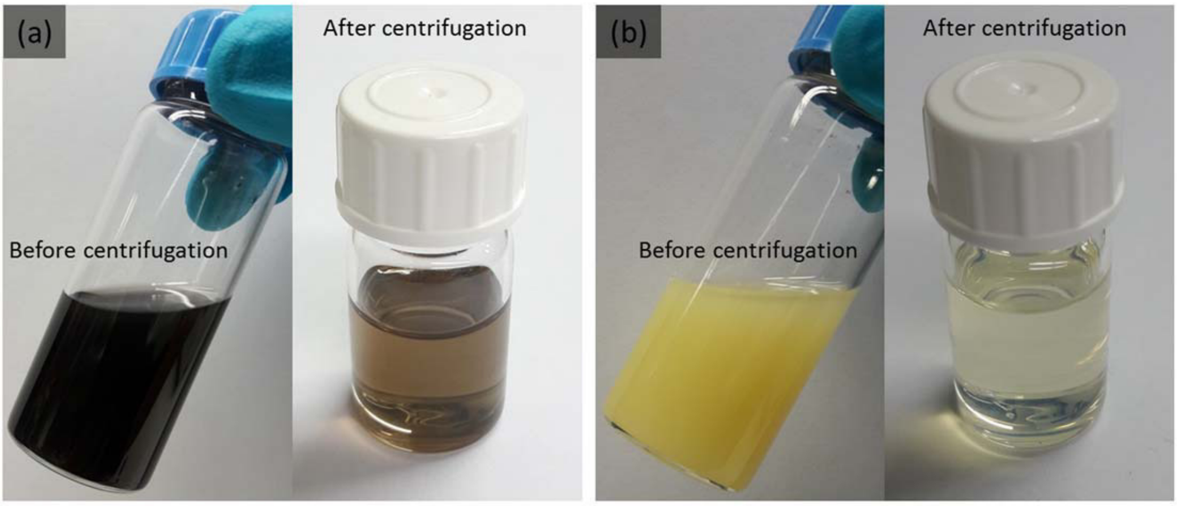

Figure 4.3.6. Photographs of colloidal dispersion obtained after sonication of dispersions of (a) SaU-1-550 and (b) CMp-450 in NMP, before and after centrifugation.

Hence, the preparation of the CMp-450/SaU-1-550 composites in NMP could be a way to overcome the problem of the low SaU-1-550 loading. However, due to the high boiling point of NMP (b.p. = 204 °C), the challenge here is the removal of the solvent to obtain the composites as powders. A way to circumvent this problem can be a solvent-exchange step by dialysis.

For future attempts to prepare the composites by the self-assembly of nanosheets, it would be also interesting trying to allow more time for the self-assembly process. For instance, self-assembly of the mixed dispersed nanosheets can be attempted by aging the mixture at elevated temperatures in an autoclave, as reported by Quiao et al. for the successful self-assembly of g-C_3N_4 nanosheets and carbon nanotubes.[83] Another interesting approach would it be to mix the dispersed SaU-1-550 nanosheets with the water soluble g-C_3N_4 precursor dicyandiamide. A similar approach was reported by Quiao et al., who prepared a nanohybrid of g-C_3N_4 and N-doped graphene by mixing dicyandiamide with aqueous dispersions of exfoliated graphene oxide.[85] Here, the positively charged dicyandiamide deposited on the negatively charged surface of the graphene oxide nanosheets. After lyophilization and carbonizing, g-C_3N_4 layers were grown in-situ on the graphene oxide surface.

5 Summary and Conclusion

The central aim of this thesis on hand was the preparation of an “all-carbon” heterojunction composite solely based from carbon materials, where differences in electronic properties of the single components are achieved by the introduction of different nitrogen motifs into the carbon lattice. For such a composite, the combination of the advantages of its single components as well as synergistic behavior like the formation of electronic heterojunctions can be expected.

The realization of such a material was motivated by the quest for appropriate catalysts for the photocatalytic spitting of water. In the context of global warming and dwindling fossil resources, photocatalytic water splitting provides an interesting way to obtain hydrogen from water and sunlight. Here, the organic semiconductor g-C_3N_4 is a promising candidate as metal-free photocatalyst, which combines a suitable band structure with the advantages of high chemical stability, high stability against photocorrosion, insolubility and the opportunity to be prepared from cheap and non-toxic precursors. However, inherent limitations for this material are a low optical absorption in the visible light part of the spectrum and a relatively high rate of charge carrier recombination. It was the approach of this work, to overcome these limitations by making a composite between g-C_3N_4 and another carbon/nitrogen compound, which was the recently described semiconductor C_2N. For a g-C_3N_4/C_2N composite, it was predicted that at the interface a type II heterojunction is formed, which decreases the rate of charge carrier recombination and thus leads to an increased quantum efficiency.[89] It was furthermore predicted that the composite has an increased optical absorption in the visible light part of the spectrum and that the composite formation from the single components is exothermic.[89]

However, as C_2N is an only recently described compound, special emphasis was given on processing this material, which includes finding a potential new precursor system. From a synthetic viewpoint, this work was focused on applying pre-organized precursors, which allow for the targeted modification of the carbon properties already on the stage of the precursor.

The practical application of this concept was introduced in chapter 4.1., which was focused on g-C_3N_4 as component one of the composite. Here, it was the idea to increase the photocatalytic activity of g-C_3N_4 by the introduction of defects or surface terminations. This was done by applying a supramolecular hydrogen-bonded precursor complex from cyanuric acid and melamine, where caffeine as "growth stopper" molecule was meant to induce structural vacancies in the 2D complex. After carbonization at 500 °C, these vacancies should be preserved as defects or surface terminations in the obtained g-C_3N_4, which are known to increase the (photo)catalytic activity.[103-105] It was found that caffeine addition does not affect the chemical composition and binding motifs of the obtained g-C_3N_4s, but greatly affects the morphology. With caffeine addition, hollow g-C_3N_4 tubes with a length of several µm were obtained. Also the electronic properties of the obtained g-C_3N_4s were influenced by the caffeine addition. UV-Vis spectroscopy and photoluminescence measurements indicated the formation of defect- or surface states in the electronic band structure of the g-C_3N_4s prepared with caffeine. When tested for the photocatalytic degradation of the organic dye Rhodamin B, the samples prepared with caffeine showed an increased activity. This was attributed to the defect- or surface states, which can decrease the rate of charge carrier recombination and thus enhance the photocatalytic activity. Hence, the obtained results indicate that caffeine as "growth stopper" for the CM complex induces structural vacancies, which are preserved as defects or surface terminations in the obtained g-C_3N_4 and lead to an increased photocatalytic activity. Thus, this chapter showed how with applying pre-organized supramolecular complexes as precursors, desired properties of the carbon/nitrogen materials can be addressed already on the precursor stage.

After introducing the concept of "pre-organization on the precursor-stage" with the example of the "caffeine-doped" g-C_3N_4, in the second part of this work the focus was shifted to the other component of the composite, which is the just very recently discovered C_2N. In chapter 4.2.1, another opportunity for processing a C_2N precursor, which is the eutectic between hexaketocyclohexane and urea, was presented. It was shown that the eutectic crosslinks with the polysaccharide chitosan, which leads to gel monoliths or beads. After drying the gels with supercritical CO_2, mesoporous polymer monoliths or –beads were obtained, with apparent BET surface areas of 76 m^2/g and 168 m^2/g, respectively. The polymer monolith and –beads could then be transformed into nitrogen-doped carbon monoliths or –beads by carbonization at 500 °C. As determined by elemental combustion analysis, the obtained samples revealed nitrogen contents of 12 wt% and 11 wt%, respectively. The porosity of the gels could be retained during carbonization. The carbonized monolith and beads are mesoporous materials with apparent surface areas of 348 m^2/g for the monolith and 445 m^2/g for the beads. However, the local atomic composition of the obtained materials is not resolved yet and it can be only speculated if the materials contain C_2N domains. To resolve this question, further analytical techniques with a high spatial resolution (like HR-TEM or STM) would be highly interesting. From a synthetic viewpoint, the applied preparation method is an interesting route towards mesoporous nitrogen-doped carbon in monolithic shape: Contrary to the usually applied routes towards monolithic carbons, it does neither require toxic chemicals like phenolic resins, nor hard-templates, binders or additional steps like activation. An interesting application for the monolithic carbon is indicated from the CO_2 adsorption behavior. As calculated from CO_2 adsorption isotherms by applying the Clausius-Clapeyron equation, the monolithic carbon has a high isosteric heat Q_{St} for CO_2 adsorption of 36 KJ/mol. It has been recently proposed that nitrogen containing carbons with good CO_2 adsorption properties are promising materials for electrocatalytically switchable CO_2 capture.[179-181] As revealed by DFT calculations, pyridinic/ pyrazinic nitrogens in carbon/nitrogen compounds can be applied as electronically switchable CO_2 adsorption sites.[180] The material derived from the hexaketocyclohexane/urea precursor is rich in pyrazinic nitrogen,[69] which makes the obtained monolithic material an interesting candidate for the first practical experiments on electrocatalytic switchable CO_2 capture.

With dye absorption experiments, it was furthermore shown that the monolithic pore system is also accessible to larger molecules.

In chapter 4.2.2, another precursor system for C_2N carbon was explored. Following the concept of pre-organization on the precursor stage, squaric acid and urea were chosen as compounds for a potential C_2N precursor. Squaric acid, which is known for the formation of layered 2D complexes with several organic amines, was chosen as structure-directing compound, since 2D layers are the basis for graphitic materials.[189-193] Urea was chosen as bridging agent to the squaric acid units and as nitrogen source. From 1:1 mixtures of squaric acid and urea, hydrogen-bonded organic crystals with a layered morphology were formed by proton-transfer from squaric acid to urea. After carbonization at 550 °C, materials with a composition of "$C_5N_2H_2O_{0.6}$" were obtained, which is the same elemental composition as obtained for the C_2N materials from Fechler et al. and Baek et al.[69,70,71] The formation of a material with a graphitic structure was confirmed by PXRD and CP MAS ^{13}C NMR. From the diffraction pattern, an in-plane periodicity with a distance of 8 Å was observed, which is in the same range as the distance between the pyrazinic pores in C_2N (8.3 Å).[70] However, PXRD also indicated a rather defective material without long-range order. The position of the aromatic signal in CP MAS ^{13}C NMR indicated the incorporation of nitrogen atoms in the carbon lattice. The layered morphology of the precursor crystals was retained after carbonization and is retained even until temperatures of up to 900 °C. With variations in the ratio of squaric acid: urea in the precursor, after carbonization a material with the same elemental composition, but a tube-like morphology was obtained. TGA- measurements and temperature-resolved FT-IR- and UV-Vis-measurements indicated that from the squaric acid/urea crystals at temperatures > 170 °C squaramides are formed by trans-amidation, which around 230 °C condensate into conjugated, N-heterocyclic intermediates. Further condensation could then lead to a C_2N structure. However, to confirm the existence of C_2N motifs in the obtained materials, further analytical techniques like XPS, STM or HR-TEM still have to be applied.

It was also demonstrated, that the squaric acid/urea crystals as potential C_2N precursor can be processed by salt-templating. Here, it was taken advantage on the ability of urea to form deep eutectics with $ZnCl_2$.[209,210] As it has been revealed that an excess of urea in the precursor mixture does not affect the materials composition after carbonization, from precursor mixtures with additional urea and $ZnCl_2$ microporous materials with a specific BET surface area of 865 m^2/g were obtained after carbonization.

Finally, in chapter 4.3, first attempts towards the preparation of a g-C_3N_4/C_2N-composite were made. Here, the composite formation was attempted by the self-assembly of exfoliated nanosheets of g-C_3N_4 and C_2N carbon. Exfoliation should be achieved by sonicating aqueous dispersions of the respective materials. As g-C_3N_4 component for the composite, the material obtained from carbonizing the CMp precursor at 450 °C was applied. It is already known, that by sonicating aqueous dispersion of this material, nanosheets can be obtained.[217] For the C_2N component, the material obtained from carbonizing the squaric acid/urea precursor at 550 °C was applied (sample SaU-1-550). It was demonstrated, that also for this material nanosheets with sizes around 95 nm can be prepared by sonication. However, the dispersions of the SaU-1-550 nanosheets were obtained in low concentrations of ≈ 0.05 mg/ml. For the colloidal dispersions of both materials, negative surface zeta potentials of -29 mV (for the g-C_3N_4 nanoparticles) and -36 mV (for the C_2N nanosheets) were determined. However, with the idea to enable self-assembly of the nanosheets also by ionic interactions, attempts towards changing the surface charge of the g-C_3N_4 nanoparticles were made. This was achieved by protonation with concentrated hydrochloric acid, from which after sonication g-C_3N_4 nanoparticles with sizes around 100 nm and a positive surface zeta potential of 44 mV were obtained. For the preparation of the composites, g-C_3N_4 from the CMp precursor was sonicated in the dispersion of the SaU-1-550 nanosheets, followed by water evaporation at

100 °C. The same procedure was applied for composites between the protonated g-C_3N_4 and the C_2N carbon. Both obtained composites showed an increased optical absorption when compared to the pure g-C_3N_4s. When tested for photocatalytic water splitting, the composites showed high rates of hydrogen evolution, with a two-fold increased rate when compared to bulk- g-C_3N_4. However, when compared to nanosheets of solely g-C_3N_4, the composites revealed only slightly increased rates of hydrogen production, which led to the conclusion that the high rates of hydrogen production for the composites were an effect primary due to their increased surface area, rather than to their composition. It was assumed, that for a composite with a significantly increased photocatalytic activity, a higher concentration of the SaU-1-550 nanosheets as co-catalyst has to be applied. This might be achieved with colloidal dispersions of SaU-1-550 in NMP, for which a higher matching in surface energies and thus a higher degree of exfoliation can be expected.[214,220,221]

Even if in this final project the formation of a g-C_3N_4/C_2N heterojunction with significantly increased photocatalytic activity was not observed, the performed experiments showed that nanosheets of the C_2N carbon from the squaric acid/urea crystals can be prepared by liquid exfoliation. As future experiments, the self-assembly under hydrothermal conditions was suggested. Another approach towards the composite material would be a co-synthesis approach, i.e. the in-situ synthesis of one or both carbon/nitrogen compounds in the composite instead of mixing the final carbon/nitrogen materials. For the materials applied here, an interesting co-synthesis approach would be the mixing of dispersed SaU-1-550 nanosheets with the water-soluble g-C_3N_4 precursor dicyandiamide, followed by solvent-evaporation and carbonization, to allow the in-situ formation of g-C_3N_4 on the C_2N nanosheets.

In conclusion, this thesis provided precious synthetic contributions to the class of carbon/nitrogen materials.

This regards the processing into materials of desired shape and morphology, as it was shown for the preparation of binder-free mesoporous nitrogen-doped carbon monoliths and –beads without the use of hard-templates or additional activation steps.

As an approach to achieve more control over the carbonization process without additional agents but solely from the choice of the precursor molecules, the concept of pre-organization on the precursor stage was shown. This can be realized with hydrogen-bonded supramolecular precursor complexes, as it was shown for the "caffeine-induced" surface terminations, or with highly ordered organic crystals, as it was shown for the C_2N carbon obtained from the squaric acid/urea crystals.

Furthermore, with the squaric acid/urea crystals another precursor system for the novel carbon/nitrogen compound C_2N has been found. However, here further analytics to clarify the local atomic composition still have to be done.

6 References

[1] U.S. Energy Information Administration, Center for Strategic and International Studies, "International Energy Outlook 2016."

[2] United Nations, Department of Economic and Social Affairs, Population Division, "World Population Prospects: The 2015 Revision."

[3] International Energy Agency, “Key World Energy Statistics 2015”.

[4] World Energy Assessment: Energy and the Challenge of Sustainability, United Nations Development Programme, New York **2000**.

[5] W. Cao, J. Xue: Recent progress in organic photovoltaics: device, architecture and optical design, *Energy Environ. Sci.* **2014**, *7*, 2123-2144.

[6] O. A. Abdulrazzaq, V. Saini, S. Bourdo, E. Dervishi, A. S. Biris: Organic Solar Cells: A Review of Materials, Limitations, and Possibilities for Improvement, *Particulate Science and Technology*, **2013**, *31*, 427–442.

[7] M. A. Green, K. Emery, Y. Hishikawa, W. Warta, E. D. Dunlop: Solar cell efficiency tables, *Prog. Photovolt. Res. Appl.* **2013**, *21*, 1–11.

[8] M. Batzill: Fundamental aspects of surface engineering of transition metal oxide photocatalysts, *Energy Environ. Sci.* **2011**, *4*, 3275-3286.

[9] J. Ran, J. Zhang, J. Yu, M. Jaroniec, S. Z. Qiao: Earth-abundant cocatalysts for semiconductor-based photocatalytic water splitting, *Chem. Soc. Rev.* **2014**, *43*, 7787-7812.

[10] H. Yana, J. Yanga, G. Maa, G. Wua, X. Zonga, Z. Leia, J. Shia, C. Lia: Visible-light-driven hydrogen production with extremely high quantum efficiency on Pt–PdS/CdS photocatalyst, *J. Catal.* **2009**, *266*, 165-168.

[11] A. Kudo, Y. Misekia: Heterogeneous photocatalyst materials for water splitting, *Chem. Soc. Rev.* **2009**, *38*, 253-278.

[12] N. Fechler, M. Antonietti: Domino games: Controlling structure and patterns of carbon nanomaterials in 2D & 3D, *Nano Today* **2015**, *10*, 593-614.

[13] J.-M. Lehn: Supramolecular Chemistry -Scope and Perspectives; Molecules, Supermolecules, and Molecular Devices (Nobel Lecture), *Angew. Chem. Int. Ed. Engl.* **1988**, *27*, 89-112.

[14] E. Wiberg, N. Wiberg: Inorganic Chemistry, Academic Press **2001**.

[15] A. A. Balandin, S. Ghosh, W. Bao, I. Calizo, D. Teweldebrhan, F. Miao, C. N. Lau: Superior Thermal Conductivity of Single-Layer Graphene, *Nano Lett.* **2008**, *8*, 902-907.

[16] M. D. Stoller, S. Park, Y. Zhu, J. An, R. S. Ruoff: Graphene-Based Ultracapacitors, *Nano Lett.* **2008**, *8*, 3498-3502.

[17] C. Lee, X. Wei, J. W. Kysar, J. Hone: Measurement of the Elastic Properties and Intrinsic Strength of Monolayer Graphene, *Science* **2008**, *321*, 385-388.

[18] E. Quesnel, F. Roux, F. Emieux, P. Faucherand, E. Kymakis, G. Volonakis, F. Giustino, B. Martín-García, I. Moreels, S. A. Gürsel, A. B. Yurtcan, V. Di Noto, A. Talyzin, I. Baburin, D. Tranca, G. Seifert, L. Crema, G. Speranza, V. Tozzini, P. Bondavalli, G. Pognon, C. Botas, D. Carriazo, G. Singh, T. Rojo, G. Kim, W. Yu, C. P Grey, V. Pellegrini: Graphene-based technologies for energy applications, challenges and perspectives, *2D Mater.* **2015**, *2*, 030204.

[19] P. F. Fulvio, J. S. Lee, R. T. Mayes, X. Wang, S. M. Mahurin, S. Dai: Boron and nitrogen-rich carbons from ionic liquid precursors with tailorable surface properties, *Phys. Chem. Chem. Phys.* **2011**,*13*, 13486-13491.

[20] X. Zhu, P. C. Hillesheim, S. M. Mahurin, C. Wang, C. Tian, S. Brown, H. Luo, G. M. Veith, K. S. Han, E. W. Hagaman, H. Liu, S. Dai: Efficient CO_2 Capture by Porous, Nitrogen-Doped Carbonaceous Adsorbents Derived from Task-Specific Ionic Liquids, *ChemSusChem* **2012**, *5*, 1912–1917.

[21] N. Fechler, T.-P. Fellinger, M. Antonietti: One-pot synthesis of nitrogen–sulfur-co-doped carbons with tunable composition using a simple isothiocyanate ionic liquid, *J. Mater. Chem. A* **2013**, *1*, 14097-14102.

[22] J. P. Paraknowitsch, Y. Zhang, B. Wienerta, A. Thomas: Nitrogen- and phosphorus-co-doped carbons with tunable enhanced surface areas promoted by the doping additives, *Chem. Commun.* **2013**, *49*, 1208.

[23] J. P. Paraknowitsch, J. Zhang, D. Su, A. Thomas, M. Antonietti: Ionic Liquids as Precursors for Nitrogen-Doped Graphitic Carbon, *Adv. Mater.* **2010**, *22*, 87–92.

[24] E. G. Gillan: Synthesis of Nitrogen-Rich Carbon Nitride Networks from an Energetic Molecular Azide Precursor, *Chem. Mater.* **2000**, *12*, 3906-3912.

[25] W. Quanhong, A. Tomita, T. Kyotani: Double Coaxial Structure and Dual Physicochemical Properties of Carbon Nanotubes Composed of Stacked Nitrogen-Doped and Undoped Multiwalls, *Chem. Mater.* **2005**, *17*, 2940–2945.

[26] J. Wei, D. Zhou, Z. Sun, Y. Deng, Y. Xia, D. Zhao: A Controllable Synthesis of Rich Nitrogen-Doped Ordered Mesoporous Carbon for CO_2 Capture and Supercapacitors, *Adv. Funct. Mater.* **2013**, *23*, 2322–2328.

[27] L. Zhao, N. Baccile, S. Gross, Y. Zhang, W. Wei, Y. Sun, M. Antonietti, M.-M. Titirici: Sustainable nitrogen-doped carbonaceous materials from biomass derivatives, *Carbon*, **2010**, *48*, 3778-3787.

[28] M. Graglia, J. Pampel, T. Hantke, T.-P. Fellinger, D. Esposito: Nitro Lignin-Derived Nitrogen-Doped Carbon as an Efficient and Sustainable Electrocatalyst for Oxygen Reduction, *ACS Nano* **2016**, *10*, 4364-4371.

[29] J. P. Paraknowitsch, A. Thomas, M. Antonietti: A detailed view on the polycondensation of ionic liquid monomers towards nitrogen doped carbon materials, *J. Mater. Chem.* **2010**, *20*, 6746-6758.

[30] J. S. Lee , X. Wang , H. Luo , G. A. Baker , S. Dai: Facile Ionothermal Synthesis of Microporous and Mesoporous Carbons from Task Specific Ionic Liquids, *J. Am. Chem. Soc.* **2009**, *131*, 4596-4597.

[31] N. Fechler, T.-P. Fellinger, M. Antonietti: “Salt Templating”: A Simple and Sustainable Pathway toward Highly Porous Functional Carbons from Ionic Liquids, *Adv. Mater.* **2013**, *25*, 75–79.

[32] P. Zhang, J. Yuan, T.-P. Fellinger, M. Antonietti, H. Li, Y. Wang: Improving Hydrothermal Carbonization by Using Poly(ionic liquid)s, *Angew. Chem. Int. Ed.* **2013**, *52*, 6028-6032.

[33] D. Esposito, S. Kirchhecker, M. Antonietti: A Sustainable Route towards Imidazolium Building Blocks Based on Biomass Molecules, *Chem. Eur. J.* **2013**, *19*, 15097-15100.

[34 183] H. Wang, T. Maiyalagan, X. Wang: Review on Recent Progress in Nitrogen-Doped Graphene: Synthesis, Characterization, and Its Potential Applications, *J. Appl. Catal. B* **2008**, *79*, 89-99.

[35] P. H. Matter, L. Zhang, U. S. Ozkan: The role of nanostructure in nitrogen-containing carbon catalysts for the oxygen reduction reaction, *J. Catal.* **2006**, *239*, 83–96.

[36] S. Zhang, S. Tsuzuki, K. Ueno, K. Dokko, M. Watanabe: Upper Limit of Nitrogen Content in Carbon Materials, *Angew. Chem. Int. Ed.* **2014**, *53*, 1-6.

[37] S. Maldonado, K. J. Stevenson: Influence of Nitrogen Doping on Oxygen Reduction Electrocatalysis at Carbon Nanofiber Electrodes, *J. Phys. Chem. B* **2005**, *109*, 4707-4716.

[38] H. Kim, K. Lee, S. I. Woo, Y. Jung: On the mechanism of enhanced oxygen reduction reaction in nitrogen-doped graphene nanoribbons, *Phys. Chem. Chem. Phys.* **2011**, *13*, 17505-17510.

[39] J. D. Wiggins-Camacho, K. J. Stevenson: Effect of Nitrogen Concentration on Capacitance, Density of States, Electronic Conductivity, and Morphology of N-Doped Carbon Nanotube Electrodes, *J. Phys. Chem. C* **2009**, *113*, 19082-19090.

[40] N. Keller, N. I. Maksimova, V. V. Roddatis, M. Schur, G. Mestl, Y. V. Butenko, V. L. Kuznetsov, R. Schlögl: The Catalytic Use of Onion-Like Carbon Materials for Styrene Synthesis by Oxidative Dehydrogenation of Ethylbenzene, *Angew. Chem. Int. Ed.* **2002**, *41*, 1885-1888.

[41] Y. Wang, X. Wang, M. Antonietti: Polymeric graphitic carbon nitride as a heterogeneous organocatalyst: from photochemistry to multipurpose catalysis to sustainable chemistry, *Angew. Chem. Int. Ed.* **2012**, *51*, 68–89.

[42] J. Suntivich, K. J. May, H. A. Gasteiger, J. B. Goodenough, Y. Shao-Horn: A Perovskite Oxide Optimized for Oxygen Evolution Catalysis from Molecular Orbital Principles, *Science*, **2011**, *334*, 1383-1385.

[43] Y. Lee, J. Suntivich, K. J. May, E. E. Perry, Y. Shao-Horn: Synthesis and Activities of Rutile IrO_2 and RuO_2 Nanoparticles for Oxygen Evolution in Acid and Alkaline Solutions, *J. Phys. Chem. Lett.* **2012**, *3*, 399–404.

[44] Y. Zhao, R. Nakamura, K. Kamiya, S. Nakanishi, K. Hashimoto: Nitrogen-doped carbon nanomaterials as non-metal electrocatalysts for water oxidation, *Nat. Commun.* **2013**, *4*, 2390-2397.

[45] A. Y. Liu, M. L. Cohen: Prediction of New Low Compressibility Solids, *Science* **1989**, *245*, 841-842.

[46] A. Y. Liu, M. L. Cohen: Structural properties and electronic structure of low-compressibility materials: β-Si_3N_4 and hypothetical β-C_3N_4, *Phys. Rev. B* **1990**, *41*, 10727-10734.

[47] C. Niu, Y. Z. Lu, C. M. Lieber: Experimental Realization of the Covalent Solid Carbon Nitride, *Science* **1993**, *261*, 334-33.

[48] A. Thomas, A. Fischer, F. Goettmann, M. Antonietti, J.-O. Müller, R. Schlögl, J.M. Carlsson: Graphitic carbon nitride materials: variation of structure and morphology and their use as metal-free catalysts, *J. Mater. Chem.* **2008**, *18*, 4893-4908.

[49] S. Matsumoto, E.-Q. Xie, F. Izumi: On the validity of the formation of crystalline carbon nitrides, C_3N_4, *Diamond Relat. Mater.* **1999**, *8*, 1175–1182

[50] A. V. Semencha, L. N. Blinov: Theoretical Prerequisites, Problems, and Practical Approaches to the Preparation of Carbon Nitride: A Review, *Glass Phys. Chem.* **2010**, 36, 199–208.

[51] T. Komatsu, T. Nakamura: Polycondensation/pyrolysis of tris-s-triazine derivatives leading to graphite-like carbon nitrides, *J. Mater. Chem.* **2001**, *11*, 474-478.

[52] M. Groenewolt, M. Antonietti: Synthesis of g-C_3N_4 Nanoparticles in Mesoporous Silica Host Matrices, *Adv. Mater.* **2005**, *17*, 1789-1792.

[53] X. Li, J. Zhang, L. Shen, Y. Ma, W. Lei, Q. Cui, G. Zou: Preparation and characterization of graphitic carbon nitride through pyrolysis of melamine, *Appl. Phys. A* **2009**, *94*, 387–392.

[54] T. Tyborski, C. Merschjann, S. Orthmann, F. Yang, M.-C. Lux-Steiner, T. Schedel-Niedrig: Crystal structure of polymeric carbon nitride and the determination of its process temperature-induced modifications, *J. Phys.: Condens. Matter* **2013**, 25, 395402-395409.

[55] F. Fina, S. K. Callear, G. M. Carins, J. T. S. Irvine: Structural Investigation of Graphitic Carbon Nitride via XRD and Neutron Diffraction, *Chem. Mater.* **2015**, *27*, 2612−2618.

[56] X. Wang, K. Maeda, A. Thomas, K. Takanabe, G. Xin, J. M. Carlsson, K. Domen, M. Antonietti: A metal-free polymeric photocatalyst for hydrogen production from water under visible light, *Nat. Mater.* **2009**, *8*, 76-80.

[57] J. V. Liebig, Ann. Pharm. **1834**, *10*, 10.

[58] C. E. Redemann, H. J. Lucas: Some Derivatives of Cyameluric Acid and Probable Structures of Melam, Melem and Melon, *J. Am. Chem. Soc.* **1940**, *62*, 842–846.

[59] L. Shi, L. Liang, F. Wang, M. Liu, K. Chen, K. Sun, N. Zhang, J. Sun: Higher Yield Urea-Derived Polymeric Graphitic Carbon Nitride with Mesoporous Structure and Superior Visible-Light-Responsive Activity, *ACS Sustainable Chem. Eng.* **2015**, *3*, 3412−3419.

[60] B. V. Lotsch, W. Schnick: New Light on an Old Story: Formation of Melam during Thermal Condensation of Melamine, *Chem.-Eur. J.* **2007**, *13*, 4956-4968.

[61] Q. Bao, K. P. Loh: Graphene photonics, plasmonics, and broadband optoelectronic devices, *ACS Nano* **2012**, 3677-3694.

[62] J. Wirth, R. Neumann, M. Antonietti, P. Saalfrank: Adsorption and photocatalytic splitting of water on graphitic carbon nitride: a combined first principles and semiempirical study, *Phys.Chem.Chem.Phys.* **2014**, *16*, 15917-15926.

[63] Y. Zheng, J. Liu, J. Liang, M. Jaroniec, S.Z. Qiao: Graphitic carbon nitride materials: controllable synthesis and applications in fuel cells and photocatalysis, *Energy Environ. Sci.* **2012**, *5*, 6717-6731.

[64] X. Chen, S. Shen, L. Guo, S. S. Mao: Semiconductor-based photocatalytic Hydrogen Generation, *Chem. Rev.* **2010**, *110*, 6503-6570.

[65] J. Zhuang, W. Dai, Q. Tian, Z. Li, L. Xie, J. Wang, P. Liu: Photocatalytic Degradation of RhB over TiO_2 Bilayer Films: Effect of Defects and their Location, *Langmuir* **2010**, *26*, 9686-9694.

[66] B. Choudhurya, P. K. Giri: Isotype heterostructure of bulk and nanosheets of graphitic carbon nitride for efficient visible light photodegradation of methylene blue, *RSC Adv.* **2016**, *6*, 24976-24984.

[67] S. Gu, J. Xieb, C. M. Li: Hierarchically porous graphitic carbon nitride: large-scale facile synthesis and its application toward photocatalytic dye degradation, *RSC Adv.* **2014**, *4*, 59436-59439.

[68] T. Jordan, N. Fechler, J. Xu, T. J. K. Brenner, M. Antonietti, M. Shalom: "Caffeine Doping" of Carbon/Nitrogen-Based Organic Catalysts: Caffeine as a Supramolecular Edge Modifier for the Synthesis of Photoactive Carbon Nitride Tubes, *ChemCatChem* **2015**, *7*, 2826– 2830.

[69] N. Fechler, N.P. Zussblatt, R. Rothe, R. Schlögl, M.-G. Willinger, B.F. Chmelka, M. Antonietti: Eutectic Syntheses of Graphitic Carbon with High Pyrazinic Nitrogen Content, *Adv. Mater.* **2016**, *28*, 1287-1294.

[70] J. Mahmood, E.K. Lee, M. Jung, D. Shin, I.-Y. Jeon, S.-M. Jung, H.-J. Choi, J.-M. Seo, S.Y. Bae, S.-D. Sohn, N. Park, J.H. Oh, H.-J. Shin, J.-B. Baek: Nitrogenated holey two-dimensional structures, *Nat. Commun.* **2015**, *6*, 6486-6492.

[71] J. Mahmood, S.-M. Jung, S.-J. Kim, J. Park, J.-W. Yoo, J.-B. Baek: Cobalt Oxide Encapsulated in C_2N-h*2*D Network Polymer as a Catalyst for Hydrogen Evolution, *Chem. Mater.* **2015**, *27*, 4860-4864.

[72] Y. Li, J. Wang, Y. Yang, Y. Zhang, D. He, Q. An, G. Cao: Seed-Induced Growing Various TiO_2 Nanostructures on g-C_3N_4 Nanosheets with Much Enhanced Photocatalytic Activity under Visible Light, *J. Hazard. Mater.* **2015**, *292*, 79−89.

[73] Y. Li, L. Fang, R. Jin, Y. Yang, X. Fang, Y. Xing, S. Song: Preparation and Enhanced Visible Light Photocatalytic Activity ofNovel g-C_3N_4 Nanosheets Loaded with Ag_2CO_3 Nanoparticles, *Nanoscale* **2015**, *7*, 758−764.

[74] D. Jiang, J. Zhu, M. Chen, J. Xie: Highly Efficient Heterojunction Photocatalyst Based on Nanoporous g-C_3N_4 Sheets Modified by Ag_3PO_4 Nanoparticles: Synthesis and Enhanced Photocatalytic Activity, *J. Colloid Interface Sci.* **2014**, *417*, 115−120.

[75] H. Xu, J. Yan, Y. Xu, Y. Song, H. Li, J. Xia, C. Huang, H. Wan: Novel Visible-Light-Driven AgX/Graphite-Like C_3N_4 (X = Br, I) Hybrid Materials with Synergistic Photocatalytic Activity, *Appl. Catal. B* **2013**, *129*, 182−193.

[76] J. Zhang, Y. Wang, J. Jin, J. Zhang, Z. Lin, F. Huang, J. Yu: Efficient Visible-Light Photocatalytic Hydrogen Evolution and Enhanced Photostability of Core/Shell CdS/g-C_3N_4 Nanowires. *ACS Appl. Mater. Interfaces* **2013**, *5*, 10317−10324.

[77] W.-J. Ong, L.-L. Tan, Y. H. Ng, S.-T. Yong, S.-P. Chai: Graphitic Carbon Nitride (g-C_3N_4)-Based Photocatalysts for Artificial Photosynthesis and Environmental Remediation: Are We a Step Closer To Achieving Sustainability?, *Chem. Rev.* **2016**, *116*, 7159−7329.

[78] Q. Xiang, J. Yu, M. Jaroniec: Preparation and Enhanced Visible-Light Photocatalytic H_2-Production Activity of Graphene/C_3N_4 Composites, *J. Phys. Chem. C* **2011**, *115*, 7355-7363.

[79] A. Du, S. Sanvito, Z. Li, D. Wang, Y. Jiao, T. Liao, Q. Sun, Y. H. Ng, Z. Zhu, R. Amal, S. C. Smith: Hybrid Graphene and Graphitic Carbon Nitride Nanocomposite: Gap Opening, Electron−Hole Puddle, Interfacial Charge Transfer, and Enhanced Visible Light Response, *J. Am. Chem. Soc.* **2012**, *134*, 4393−4397.

[80] J. Zhang, M. Zhang, R.-Q. Sun, X. Wang: A Facile Band Alignment of Polymeric Carbon Nitride Semiconductors to Construct Isotype Heterojunctions, *Angew. Chem. Int. Ed.* **2012**, *51*, 10145–10149.

[81] F. Dong, Z. Zhao, T. Xiong, Z. Ni, W. Zhang, Y. Sun, W.-K. Ho: In Situ Construction of g-C_3N_4/g-C_3N_4 Metal-Free Heterojunction for Enhanced Visible-Light Photocatalysis, *ACS Appl. Mater. Interfaces* **2013**, *5*, 11392−11401.

[82] Q. Han, B. Wang, J. Gao, L. Qu: Graphitic Carbon Nitride/Nitrogen-Rich Carbon Nanofibers: Highly Efficient Photocatalytic Hydrogen Evolution without Cocatalysts, *Angew. Chem.* **2016**, *128*, 11007-11011.

[83] T. Y. Ma, S. Dai, M. Jaroniec, S. Z. Qiao: Graphitic Carbon Nitride Nanosheet-Carbon Nanotube Three-Dimensional Porous Composites as High-Performance Oxygen Evolution Electrocatalysts, *Angew. Chem. Int. Ed.* **2014**, *53*, 7281-7285.

[84] J. Duan, S. Chen, M. Jaroniec, S. Z. Qiao: Porous C_3N_4 Nanolayers@N-Graphene Films as Catalyst Electrodes for Highly Efficient Hydrogen Evolution, *ACS Nano* **2015**, *9*, 931-940.

[85] Y. Zheng, Y. Jiao1, Y. Zhu, L. Hua, Y. Han, Y. Chen, A. Du, M. Jaroniec, S. Z. Qiao: Hydrogen evolution by a metal-free electrocatalyst, *Nat. Commun.* **2014**, *5*, 3783- 3789.

[86] J. Liang, Y. Zheng, J. Chen, J. Liu, D. Hulicova-Jurcakova, M. Jaroniec, S.Z. Qiao: Facile Oxygen Reduction on a Three-Dimensionally Ordered Macroporous Graphitic C_3N_4/Carbon Composite Electrocatalyst, *Angew. Chem. Int. Ed.* **2012**, *51*, 3892-3896.

[87] Y. Zheng, Y. Jiao, J. Chen, J. Liu, J. Liang, A. Du, W. Zhang, Z. Zhu, S. C. Smith, M. Jaroniec, G. Q. Lu, S. Z. Qiao: Nanoporous Graphitic-C_3N_4@Carbon Metal-Free Electrocatalysts for Highly Efficient Oxygen Reduction, *J. Am. Chem. Soc.* **2011**, *133*, 20116-20119.

[88] J. Liang, X. Du, C. Gibson, X. W. Du, S. Z. Qiao: N-Doped Graphene Natively Grown on Hierarchical Ordered Porous Carbon for Enhanced Oxygen Reduction, *Adv. Mater.* **2013**, *25*, 6226–6231.

[89] H. Wang, X. Li, J. Yang: The g-C_3N_4/C_2N Nanocomposite: A g-C_3N_4-Based Water-Splitting Photocatalyst with Enhanced Energy Efficiency, *ChemPhysChem* **2016**, *17*, 2100- 2104.

[90] G. R. Desiraju: Supramolecular Synthons in Crystal Engineering- A New Organic Synthesis, *Angew. Chem. Int. Ed. Engl.* **1995**, *34*, 2311- 2327.

[91] B. V. Lotsch, M. Döblinger, J. Sehnert, L. Seyfarth, J. Senker, O. Oeckler, W Schnick: Unmasking Melon by a Complementary Approach Employing Electron Diffraction, Solid-State NMR Spectroscopy, and Theoretical Calculations—Structural Characterization of a Carbon Nitride Polymer, *Chem. Eur. J.* **2007**, *13*, 4969– 4980.

[92] G. M. Whitesides, J. P. Mathias, C. T. Seto: Molecular Self-Assembly and Nanochemistry: A Chemical Strategy for the Synthesis of Nanostructures, *Science* **1991**, *254*, 1312-1319.

[93] G. M. Whitesides, E. E. Simanek, J. P. Mathias, C. T. Seto, D. N. Chin, M. Mammen, D. M. Gordon: Noncovalent Synthesis: Using Physical-Organic Chemistry To Make Aggregates, *Acc. Chem. Res.* **1995**, *28*, 37-44.

[94] M. Shalom, S. Inal, C. Fettkenhauer, D. Neher, M. Antonietti: Improving Carbon Nitride Photocatalysis by Supramolecular Preorganization of Monomers, *J. Am. Chem. Soc.* **2013**, *135*, 7118-7121.

[95] Y.S. Jun, E.Z. Lee, X. Wang, W.H. Hong, G.D. Stucky, A. Thomas: From Melamine-Cyanuric Acid Supramolecular Aggregates to Carbon nitride Hollow Spheres, *Adv. Funct. Mater.* **2013**, *23*, 3661-3667.

[96] Y.-S. Jun, J. Park, S.U. Lee, A. Thomas, W.H. Hong, G.D. Stucky: Three-Dimensional Macroscopic Assemblies of Low-Dimensional Carbon Nitrides for Enhanced Hydrogen Evolution, *Angew. Chem. Int. Ed.* **2013**, *52*, 11083-11087.

[97] J. Zhang, J. Sun, K. Maeda, K. Domen, P. Liu, M. Antonietti, X. Fua, X. Wang: Sulfur-mediated synthesis of carbon nitride: Band-gap engineering and improved functions for photocatalysis, *Energy Environ. Sci.* **2011**, *4*, 675–678.

[98] G. Zhang, J. Zhang, M. Zhang, X. Wang: Polycondensation of thiourea into carbon nitride semiconductors as visible light photocatalysts, *J. Mater. Chem.* **2012**, *22*, 8083-8091.

[99] M. Shalom, S. Gimenez, F. Schipper, I. Herraiz-Cardona, J. Bisquert, M. Antonietti: Controlled Carbon Nitride Growth on Surfaces for Hydrogen Evolution Electrodes, *Angew. Chem. Int. Ed.* **2014**, *53*, 3654-3658.

[100] J. Xu, T. J. K. Brenner, L. Chabanne, D. Neher, M. Antonietti, M. Shalom: Liquid-Based Growth of Polymeric Carbon Nitride Layers and Their Use in a Mesostructured Polymer Solar Cell with V_{oc} Exceeding 1 V, *J. Am. Chem. Soc.* **2014**, *136*, 13486-13489.

[101] J. Zhang, X. Chen , K. Takanabe, K. Maeda, K. Domen, J. D. Epping, X. Fu, M. Antonietti, X. Wang: Synthesis of a Carbon Nitride Structure for Visible-Light Catalysis by Copolymerization, *Angew. Chem. Int. Ed.* **2010**, *49*, 441 –444.

[102] M. Shalom, M. Guttentag, C. Fettkenhauer, S. Inal, D. Neher, A. Llobet, M. Antonietti: *In Situ* Formation of Heterojunctions in Modified Graphitic Carbon Nitride: Synthesis and Noble Metal Free Photocatalysis, *Chem. Mater.* **2014**, *26*, 5812-5818.

[103] M. R. Hoffmann, S. T. Martin, W. Choi, D. W. Bahnemann: Environmental Applications of Semiconductor Photocatalysis, *Chem. Rev.* **1995**, *95*, 69-96.

[104] R. I. Bickley, T. Gonzalez-Carreno, J. S. Lee, L. Palmisano, R. J. D. Tilley: A Structural Investigation of Titanium Dioxide Photocatalysts, *J. Solid State Chem.* **1991**, *92*, 178-190.

[105] C. M. Janet, S. Navaladian, B. Viswanathan, T. K. Varadarajan, and R. P. Viswanath: Heterogeneous Wet Chemical Synthesis of Superlattice-Type Hierarchical ZnO Architectures for Concurrent H_2 Production and N_2 Reduction, *J. Phys. Chem. C* **2010**, *114*, 2622-2632.

[106] F. Urbach: The Long-Wavelength Edge of Photographic Sensitivity and of the Electronic Absorption of Solids, *Phys. Rev.* **1953**, *92*, 1324.

[107] M. V. Kurik: Urbach Rule, *Phys. Status Solidi (a)* **1971**, *8*, 9-45.

[108] S. John, C. Soukoulis, M. H. Cohen, E. N. Economou: Theory of Electron Band Tails and the Urbach Optical-Absorption Edge, *Phys. Rev. Lett.* **1986**, *57*, 1777-1780.

[109] G. Arrachart, C. Garcel, P. Trens, J. J. E. Moreau, M. W. C. Man: Silylated Melamine and Cyanuric Acid as Precursors for Imprinted and Hybrid Silica Materials with Molecular Recognition Properties, *Chem. Eur. J.* **2009**, *15*, 6279-6288.

[110] B. Jürgens, E. Irran, J. Senker, P. Kroll, H. Müller, W. Schnick: Melem (2,5,8-Triamino-tris-s-triazine), an Important Intermediate During Condensation of Melamine Rings to Graphitic Carbon Nitride: Synthesis, Structure Determination by X-ray Powder Diffractometry, Solid State NMR, and Theoretical Studies, *J. Am. Chem. Soc.* **2003**, *125*, 10288-10300.

[111] Q. Guo, Y. Xie, X. Wang, S. Zhang, T. Hou, S. Lv: Synthesis of carbon nitride nanotubes with the C_3N_4 stoichiometry via a benzene-thermal process at low temperatures, *Chem. Commun*. **2004**, 26-27.

[112] J. Li, C. Cao, J. Hao, H. Qiu, Y. Xu, H. Zhu, Self-assembled one-dimensional carbon nitride architectures, *Diam. Relat. Mater.* **2006**, *15*, 1593–1600.

[113] T. Oku, M. Kawaguchi: Microstructure analysis of CN-based nanocage materials by high-resolution electron microscopy, *Diamond and Related Materials* **2000**, *9*, 906-910.

[114] J. Li, C. Cao, H. Zhu: Synthesis and characterization of graphite-like carbon nitride nanobelts and nanotubes, *Nanotechnol.* **2007**, *18*, 115605.

[115 90] S. Guo, Z. Deng, M. Li, B. Jiang, C. Tian, Q. Pan, H. Fu: Phosphorus-Doped Carbon Nitride Tubes with a Layered Micronanostructure for Enhanced Visible-Light Photocatalytic Hydrogen Evolution, *Angew. Chem. Int. Ed.* **2016**, *55*, 1830-1834.

[116] Y. Zhao, Z. Liu, W. Chu, L. Song, Z. Zhang, D. Yu, Y. Tian, S. Xie, L. Sun: Large-Scale Synthesis of Nitrogen-Rich Carbon Nitride Microfibers by Using Graphitic Carbon Nitride as Precursor, *Adv. Mater.* **2008**, *9999*, 1-5.

[117] J. Gracia, P. Kroll: First principles study of C_3N_4 carbon nitride nanotubes, *J. Mater. Chem*. **2009**, *19*, 3020-3026.

[118] A. Ranganathan, V. R. Pedireddi, C. N. R. Rao: Hydrothermal Synthesis of Organic Channel Structures: 1:1 Hydrogen-Bonded Adducts of Melamine with Cyanuric and Trithiocyanuric Acids, *J. Am. Chem. Soc.* **1999**, *121*, 1752-1753.

[119] F. Fina, S. K. Callear, G. M. Carins, J. T. S. Irvine: Structural Investigation of Graphitic Carbon Nitride via XRD and Neutron Diffraction, *Chem. Mater.* **2015**, *27*, 2612-2618.

[120] T. Watanabe, T. Takizawa, K. Honda: Photocatalysis through excitation of adsorbates. 1. Highly efficient N-deethylation of rhodamine B adsorbed to cadmium sulfide, *J. Phys. Chem.* **1977**, *81*, 1845-1851.

[121] Z. Schnepp: Biopolymers as a Flexible Resource for Nanochemistry, *Angew. Chem. Int. Ed.* **2013**, *52*, 1096-1108.

[122] J. Huang, T. Kunitake: Nano-Precision Replication of Natural Cellulosic Substances by Metal Oxides, *J. Am. Chem. Soc.* **2003**, *125*, 11834–11835.

[123] Z. Schnepp, S. R. Hall, M. J. Hollambya, S. Mann: A flexible one-pot route to metal/metal oxide nanocomposites, *Green. Chem.* **2011**, *13*, 272-275.

[124] S. R. Hall, V. M. Swinerd, F. N. Newby, A. M. Collins, S. Mann: Fabrication of Porous Titania (Brookite) Microparticles with Complex Morphology by Sol-Gel Replication of Pollen Grains, *Chem. Mater*, **2006**, *18*, 598-600.

[125] D. Walsh, L. Arcelli, T. Ikoma, J. Tanaka, S. Mann: Dextran templating for the synthesis of metallic and metal oxide sponges, *Nat. Mater.* **2003**, *2*, 386-390.

[126] Z. Schnepp, W. Yang, M. Antonietti, C. Giordano: Biotemplating of Metal Carbide Microstructures: The Magnetic Leaf, *Angew. Chem. Int. Ed.* **2010**, *49*, 6564-6566.

[127] Z. Schnepp, Y. Zhang, M. Hollamby, B.R. Pauw, M. Tanaka, Y. Matsushita, Y. Sakka: Doped-carbon electrocatalysts with trimodal porosity from a homogeneous polypeptide gel, *J. Mater. Chem. A* **2013**, *1*, 13576-13581.

[128] M. Rinaudo, G. Pavlov, J. Desbrières: Influence of acetic acid concentration on the solubilization of chitosan, *Polymer*, **1999**, *40*, 7029-7032.

[129] A.E. Kadib, M. Bousmina: Chitosan Bio-Based Organic–Inorganic Hybrid Aerogel Microspheres, *Chem. Eur. J.* **2012**, *18*, 8264-8277.

[130] Z.-L. Yu, Z.-Y. Wu, S. Xin, C. Quiao, Z.-Y. Yu, H.P. Cong, S.-H. Yu: General and Straightforward Synthetic Route to Phenolic Resin Gels Templated by Chitosan Networks, *Chem. Mater.* **2014**, *26*, 6915-6918.

[131] A. El Kadib, K. Molvinger, C. Guimon, F. Quignard, D. Brunel: Design of Stable Nanoporous Hybrid Chitosan/Titania as Cooperative Bifunctional Catalysts, *Chem. Mater.* **2008**, *20*, 2198-2204.

[132] J. Berger, M. Reist, J.M. Mayer, O. Felt, N.A. Peppas, R. Gurny: Structure and interactions in covalently and ionically crosslinked chitosan hydrogels for biomedical applications, *Eur. J. Pharm. Biopharm.* **2004**, *57*, 19-34.

[133] A. Primo, F. Quignard: Chitosan as efficient porous support for dispersion of highly active gold nanoparticles: design of hybrid catalyst for carbon-carbon bond formation, *Chem. Commun.* **2010**, *46*, 5593-5595.

[134] F. Liu, L. D. Carlos, R. A. S. Ferreira, J. Rocha, M. C. Ferro, A. Tourrette, F. Quignard, M. Robitzer: Synthesis, Texture, and Photoluminescence of Lanthanide-Containing Chitosan-Silica Hybrids, *J. Phys. Chem. B* **2010**, *114*, 77-83.

[135] A. E. Kadib, K. Molvinger, M. Bousmina, D. Brunel: Decoration of chitosan microspheres with inorganic oxide clusters: Rational design of hierarchically porous, stable and cooperative acid–base nanoreactors, *J. Catal.* **2010**, *273*, 147-155.

[136] K. Molvinger, F. Quignard, D. Brunel, M. Boissière, J.-M. Devoisselle: Porous Chitosan-Silica Hybrid Microspheres as a Potential Catalyst, *Chem. Mater.* **2004**, *16*, 3367-3372.

[137] A. El Kadib, A. Primo, K. Molvinger, M. Bousmina, D. Brunel: Nanosized Vanadium, Tungsten and Molybdenum Oxide Clusters Grown in Porous Chitosan Microspheres as Promising Hybrid Materials for Selective Alcohol Oxidation, *Chem. Eur. J.* **2011**, *17*, 7940-7946.

[138] A. Dal Pozzoa, L. Vaninia, M. Fagnonia, M. Guerrinia, A. De Benedittis, R. A. A. Muzzarelli: Preparation and characterization of poly(ethylene glycol)-crosslinked reacetylated chitosans, *Carbohydr. Polym.* **2000**, *42*, 201-206.

[139] M. V. Risbud, A. A. Hardikar, S. V. Bhat, R. R. Bhonde: pH-sensitive freeze-dried chitosan-polyvinyl pyrrolidone hydrogels as controlled release system for antibiotic delivery, *J. Controlled Release* **2000**, *68*, 23-30.

[140] V. Crescenzi, G. Paradossi, P. Desideri, M. Dentini, F. Cavalieri, E. Amici, R. Lisi: New hydrogels based on carbohydrate and on carbohydrate-synthetic polymer networks, *Polym. Gels and Netw.* **1997**, *5*, 225-239.

[141] H. Wang, W. Li, Y. Lu, Z. Wang, Studies on chitosan and poly(acrylic acid) interpolymer complex. I. Preparation, structure, pH-sensitivity and salt sensitivity of complex-forming poly(acrylic acid): chitosan semi-interpenetrating polymer network, *J. Appl. Polym. Sci.* **1997**, *65*, 1445-1450.

[142] S. Hirano, R. Yamaguchi, N. Fukui, M. Iwata: A chitosan oxalate gel: its conversion to an N-acetylchitosan gel via a chitosan gel, *Carbohydr. Res.* **1990**, *201*, 145-149.

[143] M. Sahin, N. Kocak, G. Arslan, H. I. Ucan: Synthesis of Crosslinked Chitosan with Epichlorohydrin Possessing Two Novel Polymeric Ligands and Its Use in Metal Removal, *J. Inorg. Organomet. Polym.* **2011**, *21*, 69-80.

[144] F.-L. Mia, C.-Y. Kuanb, S.-S. Shyub, S.-T. Leea, S.-F. Chang: The study of gelation kinetics and chain-relaxation properties of glutaraldehyde-cross-linked chitosan gel and their effects on microspheres preparation and drug release, *Carbohydr. Polym.* **2000**, *41*, 389-396.

[145] O.A.C. Monteiro Jr., C. Airoldi: Some studies of crosslinking chitosan–glutaraldehyde interaction in a homogeneous system, *Int. J. Biol. Macromol.* **1999**, *26*, 119-128.

[146] L. Chen, H. Wang, H. Wei, Z. Guo, M. A. Khan, D. P. Young, J. Zhu: Carbon monolith with embedded mesopores and nanoparticles as a novel adsorbent for water treatment, *RSC Adv.* **2015**, *5*, 42540-42547.

[147] G.-P. Hao, W.-C. Li, D. Qian, A.-H. Lu: Rapid Synthesis of Nitrogen-Doped Porous Carbon Monolith for CO_2 Capture, *Adv. Mater.* **2010**, *22*, 853–857.

[148] X. Ma, B. Zou, M. Cao, S.-L. Chen, C. Hu: Nitrogen-doped porous carbon monolith as a highly efficient catalyst for CO_2 conversion, *J. Mater. Chem. A* **2014**, *2*, 18360-18366.

[149] Z. Geng, Q. Xiao, H. Lv, B. Li, H. Wu, Y. Lu, C. Zhang: One-Step Synthesis of Microporous Carbon Monoliths Derived from Biomass with High Nitrogen Doping Content for Highly Selective CO_2 Capture, *Sci. Rep.* **2016**, DOI: 10.1038/srep30049.

[150] X. He, K. B. Male, P. N. Nesterenko, D. Brabazon, B. Paull, J. H. T. Luong: Adsorption and Desorption of Methylene Blue on Porous Carbon Monoliths and Nanocrystalline Cellulose, *ACS Appl. Mater. Interfaces* **2013**, *5*, 8796-8804.

[151] S.-M. Alatalo, E. Mäkilä, E. Repo, M. Heinonen, J. Salonen, E. Kukk, M. Sillanpääa, M.-M. Titirici: Meso- and microporous soft templated hydrothermal carbons for dye removal from water, *Green. Chem.* **2016**, *18*, 1137-1146.

[152] M. R. Malekbala, M. A. Khan, S. Hosseini, L. C. Abdullah, T. S. Y. Choong: Adsorption/desorption of cationic dye on surfactant modified mesoporous carbon coated monolith: Equilibrium, kinetic and thermodynamic studies, *J. Ind. Eng. Chem.* **2015**, *21*, 369-377.

[153] A.F. Pérez-Cadenas, S. Morales-Torres, F. Kapteijn, F.J. Maldonado-Hódar, F. Carrasco-Marín, C. Moreno-Castilla, J.A. Moulijn: Carbon-based monolithic supports for palladium catalysts: The role of the porosity in the gas-phase total combustion of m-xylene, *Appl. Catal. B* **2008**, *77*, 272-277.

[154] D.-W. Wang, F. Li, L.-C. Yin, X. Lu, Z.-G. Chen, I. R. Gentle, G. Q. M. Lu, H.-M. Cheng: Nitrogen-Doped Carbon Monolith for Alkaline Supercapacitors and Understanding Nitrogen-Induced Redox Transitions, *Chem. Eur. J.* **2012**, *18*, 5345-5351.

[155] Y.-S. Hu, P. Adelhelm, B. M. Smarsly, S. Hore, M. Antonietti, J. Maier: Synthesis of Hierarchically Porous Carbon Monoliths with Highly Ordered Microstructure and Their Application in Rechargeable Lithium Batteries with High-Rate Capability, *Adv. Funct. Mater.* **2007**, *17*, 1873-1878.

[156] K. T. Lee, J. C. Lytle, N. S. Ergang, S. M. Oh, A. Stein: Synthesis and Rate Performance of Monolithic Macroporous Carbon Electrodes for Lithium-Ion Secondary Batteries, *Adv. Funct. Mater.* **2005**, *15*, 547-556.

[157] A. Taguchi, J. H. Smatt, M. Linder: Carbon Monoliths Possessing a Hierarchical, Fully Interconnected Porosity, *Adv. Mater.* **2003**, *15*, 1209-1211.

[158] A. H. Lu, J. H. Smatt, S. Backlund, M. Linder: Easy and flexible preparation of nanocasted carbon monoliths exhibiting a multimodal hierarchical porosity, *Microporous Mesoporous Mater.* **2004**, *72*, 59-65.

[159] Z. Wang, F. Li, N. S. Ergang, A. Stein: Effects of Hierarchical Architecture on Electronic and Mechanical Properties of Nanocast Monolithic Porous Carbons and Carbon-Carbon Nanocomposites, *Chem. Mater.* **2006**, *18*, 5543-5553.

[160] W. C. Li, A. H. Lu, F. Schüth: Preparation of Monolithic Carbon Aerogels and Investigation of Their Pore Interconnectivity by a Nanocasting Pathway, *Chem. Mater.* **2005**, *17*, 3620-3626.

[161] J. M. Ramos-Fernández, M. Martinez-Escandell, F. Rodriguez-Reinoso: Production of binderless activated carbon monoliths by KOH activation of carbon mesophase materials, *Carbon* **2008**, *46*, 384-386.

[162] E. Stewart: Infrared Absorption Spectra of Urea, Thiourea, and Some Thiourea-Alkali Halide Complexes, *J. Chem. Phys.* **1957**, *26*, 248-254.

[163] R. Keuleers, H.O. Desseyn, B. Rousseau, C. Van Alsenoy: Vibrational Analysis of Urea, *J. Phys. Chem. A* **1999**, *103*, 4621-4630.

[164] P. Kolhe, R.N. Kannan: Improvement in Ductility of Chitosan through Blending and Copolymerization with PEG: FTIR Investigation of Molecular Interactions, *Biomacromolecules* **2003**, *4*, 173-180.

[165] M. Mucha, J. Piekielna, A. Wieczorek: Characterisation and morphology of biodegradable chitosan/ synthetic polymer blends, *Macromol. Symp.* **1999**, *144*, 391-412.

[166] A. Wrzyszczynski, X. Qu, L. Szosland, E. Adamczak, L.A. Linden, J.F. Rabek: Blends of poly(ethylene oxide) with chitosane acetate salt and with dibuturylchitin: Structure and morphology, *Polym. Bull.* **1995**, *34*, 493-500.

[167] J. G. Domszya, G. A. F. Roberts: Evaluation of infrared spectroscopic techniques for analyzing chitosan, *Makromol. Chem.* **1985**, *186*, 1671-1677.

[168] D G. K. Moore, G. A. F. Roberts: Determination of the degree of N-acetylation of chitosan, *Int. J. Biol. Macromol.* **1980**, *2*, 115-116.

[169] B. Ashourirad, A. K. Sekizkardes, S. Altarawneh, H. M. El-Kaderi: Exceptional Gas Adsorption Properties by Nitrogen-Doped Porous Carbons Derived from Benzimidazole-Linked Polymers, *Chem. Mater.* **2015**, **27**, 1349-1358.

[170] L. Wang, R. T. Yang: Significantly Increased CO_2 Adsorption Performance of Nanostructured Templated Carbon by Tuning Surface Area and Nitrogen Doping, *J. Phys. Chem. C* **2012**, *116*, 1099-1106.

[171] B. Zhu, K. Li, J. Liu, H. Liu, C. Sun, C. E. Snape, Z. Guo: Nitrogen-enriched and hierarchically porous carbon macro-spheres – ideal for large-scale CO_2 capture, *J. Mater. Chem. A* **2014**, *2*, 5481-5489.

[172] J. Fujiki, K. Yogo: The increased CO_2 adsorption performance of chitosan-derived activated carbons with nitrogen-doping, *Chem. Commun.* **2016**, *52*, 186-189.

[173] K. V. Kumar, K. Preuss, L. Lu, Z. X. Guo, M. M. Titirici: Effect of Nitrogen Doping on the CO_2 Adsorption Behavior in Nanoporous Carbon Structures: A Molecular Simulation Study, *J. Phys. Chem. C* **2015**, *119*, 22310-22321.

[174] A. A. Alhwaige, T. Agag, H. Ishidab, S. Qutubuddin: Biobased chitosan hybrid aerogels with superior adsorption: Role of graphene oxide in CO_2 capture, *RSC Adv.* **2013**, *3*, 16011-16020.

[175] C. F. Martin, E. Stockel, R. Clowes, D. J. Adams, A. I. Cooper, J. J. Pis, F. Rubiera, C. Pevida: Hypercrosslinked organic polymer networks as potential adsorbents for pre-combustion CO_2 capture, *J. Mater. Chem.* **2011**, *21*, 5475-5483.

[176] M. C. Gutierrez, D. Carriazo, C. O. Ania, J. B. Parra, M. L. Ferrer, F. del Monte: Deep eutectic solvents as both precursors and structure directing agents in the synthesis of nitrogen doped hierarchical carbons highly suitable for CO_2 capture, *Energy Environ. Sci.* **2011**, *4*, 3535-3544.

[177] G.-P. Hao, W.-C. Li, D. Qian, G.-H. Wang, W.-P. Zhang, T. Zhang, A.-Q. Wang, F. Schüth, H.-J. Bongard, A.-H. Lu: Structurally Designed Synthesis of Mechanically Stable Poly(benzoxazine-co-resol)-Based Porous Carbon Monoliths and Their Application as High-Performance CO_2 Capture Sorbents, *J. Am. Chem. Soc.* **2011**, *133*, 11378-11388.

[178] G. Lim, K. B. Lee, H. C. Ham: Effect of N‑Containing Functional Groups on CO_2 Adsorption of Carbonaceous Materials: A Density Functional Theory Approach, *J. Phys. Chem. C* **2016**, *120*, 8087−8095.

[179] Q. Sun, Z. Li, D. J. Searles, Y. Chen, G. M. Lu, A. Du: Charge-Controlled Switchable CO_2 Capture on Boron Nitride Nanomaterials, *J. Am. Chem. Soc.* **2013**, *135*, 8246–8253.

[180] Y. Jiao,Y. Zheng, S. C. Smith, A. Du, Z. Zhu: Electrocatalytically Switchable CO_2 Capture: First Principle Computational Exploration of Carbon Nanotubes with Pyridinic Nitrogen, *ChemSusChem* **2014**, *7*, 435–441.

[181] X. Tan, L. Kou, H. A. Tahini, S. C. Smith: Conductive Graphitic Carbon Nitride as an Ideal Material for Electrocatalytically Switchable CO_2 Capture, *Sci. Rep.* **2015**, *5*, DOI: 10.1038/srep17636.

[182] S. J. Yang, M. Antonietti, N. Fechler: Self-Assembly of Metal Phenolic Mesocrystals and Morphosynthetic Transformation toward Hierarchically Porous Carbons, *J. Am. Chem. Soc.* **2015**, *137*, 8269−8273.

[183] L. Sun, C. Tian, L. Wang, J. Zou, G. Mu, H. Fu: Magnetically separable porous graphitic carbon with large surface area as excellent adsorbents for metal ions and dye, *J. Mater. Chem.* **2011**, *21*, 7232-7239.

[184] G. Seitz, P. Imming: Oxocarbons and Pseudooxocarbons, *Chem. Rev.* **1992**, *92*, 1227-1260.

[185] R. West, H.-Y. Niu, D. L. Powell, M. V. Evans: Symmetrical resonance stabilized anions, C_nO_{n-2}, *J. Am. Chem. Soc.* **1960**, *82*, 6204–6205.

[186] R. West, D. L. Powell: New Aromatic Anions. 111. Molecular Orbital Calculations on Oxygenated Anions, *J. Am. Chem. Soc.* **1963**, *85*, 2577-2579.

[187] D. Semmingsen: The structure of squaric acid (3,4-dihydroxy-3-cyclobutene-1,2-dione), *Tetrahedron Lett.* **1973**, *11*, 807–808.

[188] D. Semmingsen, J. Feder: A structural phase transition in squaric acid, *Solid State Commun.* **1974**, 15, 1369–1372.

[189] E. J. Samuelsen, D. Semmingsen: Squaric acid, a twodimensional hydrogen-bonded material with a phase transition, *Solid State Commun.* **1975**, *17*, 217–219.

[190] S. Mathewa, G. Paula, K. Shivasankara, A. Choudhurya, C. N. R. Rao, Supramolecular hydrogen-bonded structures in organic amine squarates, *J. Mol. Struct.* **2002**, *641*, 263–279.

[191] M. T. Reetz, S. Höger, K. Harms: Proton-Transfer-Dependent Reversible Phase Changes in the 4,4′-Bipyridinium Salt of Squaric Acid, *Angew. Chem Int. Ed.* **1994**, *33*, 181-183.

[192] I. L. Karle, D. Ranganathan, V. Haridas: A Persistent Preference for Layer Motifs in Self-Assemblies of Squarates and Hydrogen Squarates by Hydrogen Bonding [X−H···O; X = N, O, or C]: A Crystallographic Study of Five Organic Salts, *J. Am. Chem. Soc.* **1996**, *118*, 7128–7133.

[193] V. Bertolasi, P. Gilli, V. Ferrettia G. Gillia: General rules for the packing of hydrogen-bonded crystals as derived from the analysis of squaric acid anions: aminoaromatic nitrogen base co-crystals, *Acta Crystallogr.* **2001**, *B57*, 591-598.

[194] T. Jordan, M. Shalom, M. Antonietti, N. Fechler: Carbon Nanoarchitectures by Design: Preorganizing Squaric Acid with Urea, *Asia-Pac. J. Chem. Eng.* **2016**, 11, 866–873.

[195] K. P. Gierszal, M. Jaroniec, T.-W. Kim, R. Ryoo: High temperature treatment of ordered mesoporous carbons prepared by using various carbon precursors and ordered mesoporous silica templates, *New J. Chem.* **2008**, *32*, 981-993.

[196] F, G. Baglin, C. B. Rose: The infrared and Raman spectra of crystalline squaric acid, *Spectrochim. Acta* **1970**, *26A*, 2293-2304.

[197] O. Z. Yeşilel, M. Odabaşoğlu, O. Büyükgüngör: Supramolecular squarate and hydrogensquarate compounds with 4-amino-1,2,4-triazole, 2-aminothiazole and 2-aminobenzimidazole, *J. Mol. Struct.* **2008**, *874*, 151-158.

[198] E.Spinner: The vibration spectra and structures of the hydrochlorides of urea, thiourea and acetamide. The basic properties of amides and thioamides, *Spectrochim. Acta* **1959**, *15*, 95-109.

[199] N. Süleymanoğlu, R. Ustabaş, Y. B. Alpaslan, F. Eyduran, C. Özyürek, I. N. O. Nazan: Experimental (^{13}C NMR, ^{1}H NMR, FT-IR, single-crystal X-ray diffraction) and DFT studies on 3,4-bis(isopropylamino)cyclobut-3-ene-1,2-dione, *Spectrochim. Acta A* **2011**, *83*, 472-477.

[200] S. L. Georgopoulus, R. Diniz, M. I. Yoshida, N. L. Speziali, H. F. Dos Santos, G. M. A. Junqueira, L. F. C. de Oliveira: Vibrational spectroscopy and aromaticity investigation of squarate salts: a theoretical and experimental approach, *J. Mol. Struct.* **2006**, *794*, 63-70.

[201] J. Gauger, G. Manecke: Kondensationsprodukte der Quadratsäure mit primären und sekundären Aminen, I, *Chem. Ber.* **1970**, *103*, 2696-2706.

[202] G. Manecke, J. Gauger: Kondensationsprodukte der Quadratsäure mit primären und sekundären aromatischen Aminen, *Tetrahedron Lett.* **1967**, *36*, 3509-3515.

[203] H.-K. Jeong, Y. P. Lee, R. J. W. E. Lahaye, M.-H. Park, K. H. An, I. J. Kim, C.-W. Yang, C. Y. Park, R. S. Ruoff, Y. H. Lee: Evidence of Graphitic AB Stacking Order of Graphite Oxides, *J. Am. Chem. Soc.* **2008**, *130*, 1362-1366.

[204] R. Liu, D. Wu, X. Feng, K. Müllen: Nitrogen-Doped Ordered Mesoporous Graphitic Arrays with High Electrocatalytic Activity for Oxygen Reduction, *Angew. Chem. Int. Ed.* **2010**, *49*, 2565–2569.

[205] W. Cai, R. D. Piner, F. J. Stadermann, S. Park, M. A. Shaibat, Y. Ishii, D. Yang, A. Velamakanni, S. J. An, M. Stoller, J. An, D. Chen, R. S. Ruoff: Synthesis and Solid-State NMR Structural Characterization of ^{13}C-Labeled Graphite Oxide, *Science* **2008**, *321*, 1815-1817.

[206] B. Jürgens, E. Irran, J. Senker, P. Kroll, H. Müller, W. Schnick: Melem (2,5,8-Triamino-tri-s-triazine), an Important Intermediate during Condensation of Melamine Rings to Graphitic Carbon Nitride: Synthesis, Structure Determination by X-ray Powder Diffractometry, Solid-State-NMR, and Theoretical Studies, *J. Am. Chem. Soc.* **2003**, *125*, 10288-10300.

[207] E. O. Kirkendall: Diffusion of zinc in alpha brass, *Trans. Am. Inst. Min. Metall. Eng.* **1942**, 147, 104-109.

[208] A. D. Smigelskas, E.O. Kirkendall: Zinc Diffusion in Alpha Brass, *Trans. Am. Inst. Min. Metall. Eng.* **1947**, *171*, 130-141.

[209] H. Lian, S. Hong, A. Carranza, J. D. Mota-Morales, J. A. Pojman: Processing of lignin in urea–zinc chloride deep eutectic solvent and its use as a filler in a phenol formaldehyde resin, *RSC Adv.* **2015**, *5*, 28778–28785.

[210] Q. Wang, X. Yao, Y. Geng, Q. Zhou, X. Lu, S. Zhang: Deep eutectic solvents as highly active catalysts for the fast and mild glycolysis of poly(ethyleneterephthalate) (PET), *Green Chem.* **2015**, *17*, 2473- 2479.

[211] C.-M. Yang, C. Weidenthaler, B. Spliethoff, M. Mayanna, F. Schüth: Facile Template Synthesis of Ordered Mesoporous Carbon with Polypyrrole as Carbon Precursor, *Chem. Mater.* **2005**, *17*, 355-358.

[212] A. K. Geim, I. V. Grigorieva: Van der Waals heterostructures, *Nature* **2013**, *499*, 419-425.

[213] P. Niu, L. Zhang, G. Liu, H.-M. Cheng: Graphene-Like Carbon Nitride Nanosheets for Improved Photocatalytic Activities, *Adv. Funct. Mater.* **2012**, *22*, 4763– 4770.

[214] Y. Hernandez, V. Nicolosi, M. Lotya, F. M. Blighe, Z. Suni, S. De, I. T. McGovern, B. Holland, M. Byrne, Y. K. Gun'Ko, J. J. Boland, P. Niraj, G. Duesberg, S. Krishnamurthy, R. Goodhue, J. Hutchison, V. Scardaci, A. C. Ferrari, J. N. Coleman: High-yield production of graphene by liquid-phase exfoliation of graphite, *Nat. Nanotechnol.* **2008**, *3*, 563-568.

[215] T. Y. Ma, Y. Tang, S. Dai, S. Z. Qiao: Proton-Functionalized Two-Dimensional Graphitic Carbon Nitride Nanosheet: An Excellent Metal-/Label-Free Biosensing Platform, *Small* **2014**, *10*, 2382-2389.

[216] Y. Zhang, A. Thomas, M. Antonietti, X. Wang: Activation of Carbon Nitride Solids by Protonation: Morphology Changes, Enhanced Ionic Conductivity, and Photoconduction Experiments, *J. Am. Chem. Soc.* **2009**, *131*, 50-51.

[217] Q. Cui, J. Xu, X. Wang, L. Li, M. Antonietti, M. Shalom:Phenyl-Modified Carbon Nitride Quantum Dots with Distinct Photoluminescence Behavior, *Angew. Chem. Int. Ed.* **2016**, *55*, 3672-3676.

[218] B. Zhu, P. Xia, W. Ho, J. Yu: Isoelectric point and adsorption activity of porous g-C_3N_4, *Appl. Surf. Sci.* **2015**, *344*, 188–195.

[219] Q. Li, B. Guo, J. Yu, J. Ran, B. Zhang, H. Yan, J. R. Gong: Highly Efficient Visible-Light-Driven Photocatalytic Hydrogen Production of CdS-Cluster-Decorated Graphene Nanosheets, *J. Am. Chem. Soc.* **2011**, *133*, 10878–10884.

[220] J. N. Coleman: Liquid Exfoliation of Defect-Free Graphene, *Acc. Chem. Res.* **2013**, *46*, 14-22.

[221] J. Lyklema: The surface tension of pure liquids; Thermodynamic components and corresponding states, *Colloids Surf. A* **1999**, *156*, 413-421.

[222] G. Hölzer, M. Fritsch, M. Deutsch, J. Härtwig, E. Förster: $K_{\alpha 1,2}$ and $K_{\beta 1,3}$ x-ray emission lines of the 3*d* transition metals, *Phys. Rev. A* **1997**, *56*, 4554-4568.

[223] K. S. W. Sing, Reporting physisorption data for gas/solid systems with special reference to the determination of surface area and porosity, *Pure Appl. Chem.* **1985**, *57*, 603-619.

[224] M. Thommes, K. Kaneko, A. V. Neimark, J. P. Olivier, F. Rodriguez-Reinoso, J. Rouquerol, K. S. W. Sing: Physisorption of gases, with special reference to the evaluation of surface area and pore size distribution (IUPAC Technical Report), *Pure Appl. Chem.* **2015**, *87*, 1051–1069.

[225] I. Langmuir: The Constitution and fundamental Properties of Solids and Liquids. Part I. Solids, *J. Am. Chem. Soc.* **1916**, *38*, 2221–2295.

[226] S. Brunauer, P. H. Emmett, E. Teller: Adsorption of Gases in Multimolecular Layers, *J. Am. Chem. Soc.* **1938**, *60*, 309–319.

[227] E. P. Barrett, L. G. Joyner, P. P. Halenda: The Determination of Pore Volume and Area Distributions in Porous Substances. I. Computations from Nitrogen Isotherms, *J. Am. Chem. Soc.* **1951**, *73*, 373-380.

[228] A. V. Neimark, Y. Lina, P. I. Ravikovitch, M. Thommes: Quenched solid density functional theory and pore size analysis of micro-mesoporous carbons, *Carbon* **2009**, *47*, 1617-1628.

[229] J.-M. Wu, T.-W. Zhang: Photodegradation of rhodamine B in water assisted by titania films prepared through a novel procedure, *J. Photochem. Photobiol. A* **2004**, *162*, 171-177.

I Appendix

I.I Abbreviations

AcOH - Acetic acid
ATR – Attenuated total reflection
CB - Conduction band
CNT – Carbon nanotube
CTS - Chitosan
CV – Cyclic voltammetry
DFT – Density functional theory
DLS – Dynamic light scattering
DSC – Differential scanning calorimetry
EA – Elemental analysis
EDS - Energy-dispersive x-ray spectroscopy
EELS – Electron energy loss spectroscopy
FT-IR – Fourier transform infrared
FTO – Fluorine doped tin oxide
HER – Hydrogen evolution reaction
HR-TEM – High resolution
ICP-MS - Inductively coupled plasma mass spectrometry
IL - Ionic liquid
MS – Mass spectrometry
MWCNT – Multi-walled carbon nanotube
NaOH – Sodium hydroxide
NDC - Nitrogen doped carbon
NHE - Normal hydrogen electrode
NMP – N-methyl-2-pyrrolidone
NMR – Nuclear magnetic resonance
OER – Oxygen evolution reaction
PAA - Polyacrylamide
PEG – Polyethylene glycole
PIL - Poly-ionic liquid
PMMA – Poly(methyl methacrylate)
PVA – Polyvinyl acetate

PVP – Polyvinyl pyrrolidone

PXRD – Powder x-ray diffraction

QSDFT – Quenched solid density functional theory

RhB – Rhodamine B

SEM – Scanning electron microscopy

STM – Scanning tunneling microscopy

SWCNT – Single-walled carbon nanotube

TCSPC - Time-correlated single photon counting setup

TEM – Transmission electron microscopy

TEOA - Triethanolamine

TGA – Thermogravimetric analysis

VB - Valence band

VdW – Van der Waals

WAX – Wide angle x-ray diffraction

XPS – X-ray photoelectron spectroscopy

I.II Applied Methods

Fourier-transform infrared spectroscopy (FT-IR)

In infrared spectroscopy, molecular vibrations are initiated by excitation with infrared radiation. As different functional groups and molecular entities have specific energies for certain modes of vibration, specific wavelengths are absorbed for excitation. However, excitation by electromagnetic radiation is only possible for vibration modes which lead to a change in the electronic dipole moment of the respective molecular entity. For the measurement, the amount of absorbed photons as a function of the excitation wavelength is measured. This provides information about the molecular structure of the sample, e.g. about the existence of functional groups and changes in their chemical environment (e.g. due to protonation or hydrogen bonding).

For this thesis, infrared spectroscopy was performed with an attenuated total reflectance (ATR) setup. With this technique, the sample is placed on an internal reflection element, which totally reflects the incident infrared laser beam. Near the surface of this element, the reflected laser beam creates an evanescent wave, which can be absorbed by the sample due to the excitation processes. This leads to an attenuation of the reflected laser beam which is then detected. The main advantage of this configuration is that both powder and drop samples can be measured without further preparation.

FT-IR spectra were recorded on a Varian 1000 spectrometer with an attenuated total reflectance setup.

Powder x-ray diffraction (PXRD)

With x-ray diffraction, information about crystallinity, crystal structure, and unit cell parameters of a sample can be obtained. For crystalline materials, the periodic arrangement of the atoms can be described by lattice planes, which are characterized by their relative positions in regard to the unit cell. When an electromagnetic radiation with a wavelength similar to the distance between the lattice planes, i.e. x-rays, is shined on the crystal, diffraction patterns can be obtained. The condition for constructive interference for scattered x-rays at a certain lattice plane is given by the Bragg-equation (**Equation 2**), where θ is the incident angle, λ the wavelength of the x-rays, d the distance between the lattice planes and n the diffraction order:

$$2 \cdot d \cdot sin\theta = n \cdot \lambda \qquad \textbf{(Eq.2)}$$

In x-ray diffraction experiments, the intensity of the scattered x-rays is measured as a function of the incident angle θ. From the obtained diffraction pattern, the crystal structure and unit cell parameters of a crystalline sample can be determined. In powder x-ray diffraction (PXRD), a powdered bulk material of a crystalline solid, rather than a single crystal is examined. Here, also information about the size of crystalline domains in a certain crystallographic direction can be obtained. This is described by the Debye-Scherrer equation (**Equation 3**), where L is the length of a crystalline domain in a certain crystallographic direction, β the full width half maximum of the corresponding reflection, θ the angle of the reflection, λ the x-ray wavelength and K the shape factor (a constant):

$$L = \frac{K \cdot \lambda}{\beta \cdot cos\theta} \qquad \textbf{(Eq.3)}$$

For not purely crystalline materials, this also allows for estimating the amount of amorphous domains: The broader the reflections, the higher the amount of amorphous domains.

PXRD patterns were measured on a Bruker D8 Advance instrument with Cu-K_α radiation.
The lattice distance d was calculated from the position 2θ of the respective reflection in the obtained diffraction patterns using the Bragg-equation (see **Equation 2**), with the diffraction order $n = 1$ and the wavelength $\lambda = 1.540561$ Å for Cu-K_α radiation.[222]

Microscopy methods

In this work, three types of microscopy were applied: Optical microscopy, scanning electron microscopy (SEM) and transmission electron microscopy (TEM).

The resolution of an optical imaging technique is limited by the wavelength of the source of illumination. Electrons have a much smaller de Broglie wavelength than visible light, and less energy than electromagnetic radiation of the same wavelength. This means that by using electrons as an illumination source, a higher resolution than with optical light can be achieved, without inducing too destructive interactions with the most specimen materials. In scanning electron microscopy, an electron beam which is produced by a hot cathode at the top of the microscope is focused with electromagnetic lenses on the specimen. When the electron beam interferes with the specimen, electrons can be backscattered by elastic scattering or secondary electrons can be emitted. Both types of electrons can be detected. However, in the usual measuring mode, the image of the specimen is produced with detection of the secondary electrons. The amount of secondary electrons which reaches the detector depends on the topography of the sample, which allows for topography imaging with SEM.

To prevent too high charging of the specimen during measurement, non-conductive samples are usually sputtered with a thin film of a conducting metal (usually gold or platinum) before measuring.

In transmission electron microscopy, electrons which transmit the specimen are detected. This requires sufficiently thin samples (not more than a few hundred nanometers). On the way through the specimen material, the electron beam interacts with the material (backscattering, diffraction, absorption) and gets attenuated, which allows imaging the thickness of the sample by detecting the intensity of the transmitted electrons. However, this intensity not only depends on the thickness of the sample, but also on the sample composition.

Optical microscopy images were taken with an Olympus BX41 optical microscope.

SEM measurements were performed with a Gemini Leo-1550 electron microscope. Prior to the microscopy measurement, the samples were sputtered with platinum.

TEM measurements were perfomed on a Zeiss EM 912 microscope.

Elemental analysis

Elemental combustion analysis is a technique which allows for quantifying the elemental content of carbon, nitrogen, hydrogen and sulfur. A certain mass of the sample is quantitatively burned at high temperatures under an oxygen atmosphere and the characteristic combustion products (CO_2, N_2, H_2O, SO_2) are quantified using heat conductance detectors.

Elemental combustion analysis was performed with a Vario Micro device.

UV/Vis absorption-spectroscopy and emission-spectroscopy

Electronic transitions within a material can be achieved by excitation with visible and UV-light. In UV/Vis-spectroscopy (optical spectroscopy), the absorption of UV- and visible light by a sample due to electronic transitions is measured as a function of the excitation wavelength. This provides information about the electronic structure of the sample, e.g. about π-conjugated systems for molecules or about the structure of metal complexes. Optical spectroscopy on semiconductor solid state materials provides information about the band gap of the material or the existence of defects.

The attenuation of a light beam traveling through a solution of an optically absorbing material is described by the Lambert-Beer law (**Equation 4**):

$$log\left(\frac{I_0}{I}\right) = A = \varepsilon_\lambda \cdot c \cdot d \qquad \textbf{(Eq.4)}$$

Here, I_0 is the intensity of the incident light beam, I the intensity of the light beam after passing through the solution, A is the absorbance, ε_λ the molar decadic extinction coefficient for a given wavelength λ, c the concentration of the solution and d the distance which the light has to travel through the solution. In optical spectroscopy, usually the absorbance A is plotted as a function of the wavelength λ. Thus, by applying a literature reported ε_λ–value, UV/Vis-spectroscopy can be used to determine the concentration of a chromophore in a solution. In this thesis, this method is used to determine the concentration of the dye Rhodamine B in dye degradation and –adsorption experiments.

Since light cannot penetrate opaque solid powders, UV/Vis spectra for powered samples are obtained with a different setup. Here, the diffusive reflectance of a sample is measured. To achieve this, the powder sample is placed in an integrating sphere, which collects all the reflected light. By comparing the reflection intensity of the sample with the one of a non-absorbing reference sample, the relative amount of absorbed light can be determined.

UV/Vis absorption spectra were measured on a Varian Cary 50Conc UV/Vis spectrometer with neoLab semi-micro polystyrene cuvettes of 1 cm length.
UV/Vis diffusive reflectance spectra were measured on a Shimadzu UV2600 spectrophotometer with an integrating sphere.

In emission spectroscopy, the wavelength of the emission (photoluminescence) of electromagnetic radiation is measured. Emission is due to electronic transitions from higher energy states to states of lower energy, with the energy of emitted photons corresponding to the energy difference between the states. To achieve photoemission, electrons are excited to states of higher energy by absorbing light with an appropriate energy. In a photoluminescence measurement, electronic transitions are induced by laser irradiation and the intensity of emitted light is measured in respect to the emission wavelength. From the emission wavelengths, the structure of electronic states of the sample can be determined.

The emission spectra were measured on a LS-50B Perkin Elmer instrument.
The photoluminescence lifetime was determined with time-resolved fluorescence measurements using a time-correlated single photon counting setup (TCSPC) with a Becker & Hickl SPC-130 acquisition system and a multichannel PML-16-C-1 PMT detector. The excitation at λ = 405 nm was done with a PicoQuant PDL-800B CW laser with a repetition rate of 2 MHz and the emission was monitored at λ = 500 nm.

Nitrogen physisorption

Nitrogen physisorption is a method to determine the surface area, the pore volume and the pore size distribution of a porous sample. Here, the volume of the adsorbate (nitrogen) which is adsorbed by the adsorbent (the solid, porous sample) is measured in respect to the relative pressure (p/p_0) of the adsorbate. The measurement process is conducted at the boiling point of nitrogen (77 K) and under ambient pressure, to ensure equilibrium conditions. At these conditions, nitrogen is adsorbed only by weak interactions, i.e. van der Waals interactions, and multilayer-adsorption occurs. In a typical experiment, first the adsorption process is measured by detecting the adsorbed nitrogen volume with increasing the relative pressure until $p/p_0 \approx 1$. Then, the desorption process is measured by lowering the relative pressure. For both processes, the adsorbed volume is plotted as a function of the relative pressure, resulting in an adsorption- and a desorption isotherm. From the shape of the isotherms, information about the pore size and -shape can be obtained. Regarding their sizes, usually three types of pores are distinguished, i.e. micro-, meso- and macropores. According to the definition given by the IUPAC in 1985, pores with a diameter below 2 nm are classified as micropores, pores with diameters between 2 nm and 50 nm as mesopores and pores with diameters above 50 nm as macropores.[223] The IUPAC also classified six types of physisorption isotherms, which are shown in **Figure A1**.[224]

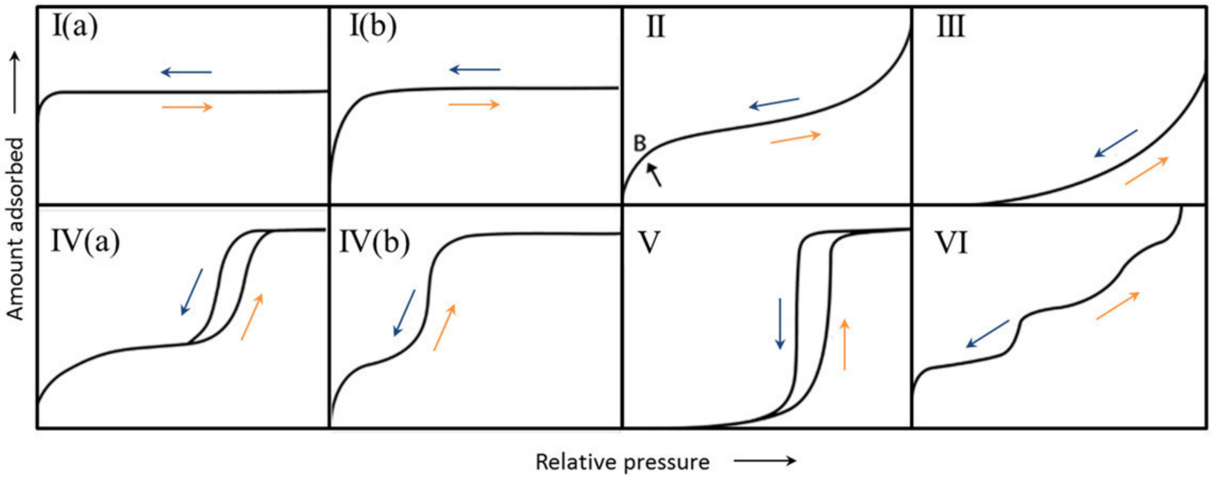

Figure A1. IUPAC classification of physisorption isotherms, according to ref. 224. Orange arrows indicate adsorption isotherms, blue arrows indicate desorption isotherm.

The reversible type I isotherm is typically observed for microporous solids with a small external surface. This isotherm type is characterized by a steep increase in the nitrogen uptake at low relative pressures, followed by the approach of a limited uptake value. The steep increase at low p/p_0 values is due to enhanced interactions between adsorbate and adsorbent in small micropores of molecular dimensions. If all micropores are filled, the limit in the uptake is reached. Type I(a) is the typical isotherm shape for materials with small micropores (with a width < 1nm) and a narrow pore size distribution. For microporous materials with a broader pore size distribution, type I(b) isotherms are obtained.

Reversible type II isotherms are typically observed for non-porous or macroporous solids. The physisorption process on these materials is characterized by unrestricted monolayer/ multilayer adsorption. The isotherm can display a sharp knee (point B in **Figure A1**), which marks the end of the monolayer adsorption and the beginning of multilayer adsorption.

For type III isotherms, no knee (as in type II isotherms) can be observed. This indicates relatively weak adsorbent/ adsorbate interactions, where no distinct monolayer formation occurs but molecules are clustered at favored adsorption sites of the non- or macroporous solid.

Type IV isotherms are observed for mesoporous solids. Here, adsorbent/ adsorbate interactions as well as interactions between adsorbate molecules in the condensed state determine the adsorption process, as here mono- and multilayer adsorption is followed by pore condensation. For type IV(a) isotherms, pore condensation leads to a hysteresis loop in the isotherms. For smaller mesopore widths, completely reversible type IV(b) isotherms can be observed.

Type V isotherms are typically observed for relatively weak adsorbent/ adsorbate interactions, where at higher relative pressures molecular clustering and then pore filling occurs.

Reversible, step-like type VI isotherms are observed for non-porous materials with a very homogenous surface, where adsorption occurs in a layer-by-layer fashion. Both, the type V and type VI isotherms are relatively uncommon and only observed for certain materials.

By relating the adsorbed volume to the thickness of the adsorbed mono-and multilayers, the area covered by the adsorbate can be calculated. This value, the specific surface area, represents the internal surface area of the porous material. For this relation, different theories have been developed. The first theory developed was the Langmuir theory, which assumes the formation of only monolayers and thus is not applicable for mesoporous materials.[225] A further development of this theory which also takes into account the formation of multilayers, is the commonly used BET theory (named after their developers Brunauer, Emmett and Teller).[226] In this thesis, this theory is used to determine the specific surface area from the physisorption isotherms. The BET equation is given in **Equation 5**, where p/p_0 is the relative pressure, V_{ads} the total adsorbed volume, V_{mono} the volume of a monolayer and C the adsorption constant.

$$\frac{p}{(p_0 - p) \cdot V_{ads}} = \frac{1}{C \cdot V_{Mono}} + \frac{C - 1}{C \cdot V_{Mono}} \cdot \frac{p}{p_0} \qquad \textbf{(Eq.5)}$$

If the term on the left side of the equation is plotted as a function of the relative pressure p/p_0, the volume of the adsorbed monolayer V_{mono} can be determined from the slope of the obtained line and the intersection with the y-axis after extrapolation. With V_{mono}, the specific BET surface area S (in m^2/g) can be calculated according to **Equation 6**, with N_A being the Avogadro constant, σ_{N_2} the surface area covered by a single N_2 molecule in dense package ($0.162\ nm^2$), V_{mol} the ideal gas volume and m_{Ads} the mass of the adsorbent:

$$S = \frac{N_A \cdot V_{Mono} \cdot \sigma_{N_2}}{V_{mol} \cdot m_{Ads}} \qquad \textbf{(Eq.6)}$$

With physisorption, also the pore size distribution of a porous sample can be determined. Here, different methods have been developed. Macroscopic, thermodynamic models like the BJH model (named after their developer Barrett, Joyner and Halenda)[227] are based on the Kelvin equation (**Equation 7**). This equation describes the relation between the relative pressure p/p_0 at which pore condensation occurs in a cylindrical pore and the radius r_{menisc} of the meniscus of the condensed liquid in the pore. Here, γ is the surface tension of the gas/fluid interface, V_{mol} the ideal gas volume, φ the wetting angle, R the ideal gas constant and T the temperature.

$$ln\frac{p}{p_0} = \frac{-2 \cdot \gamma \cdot V_{mol}}{r_{menisc} \cdot R \cdot T} \cdot cos\varphi \qquad \textbf{(Eq.7)}$$

From this equation it can be concluded, that pore condensation occurs at higher relative pressures in pores with a larger diameter (and thus a smaller curvature of the meniscus). However, this model is only applicable for cylindrical pores and pore diameters above 2.5 nm. In micropores with a smaller radius, interactions between the pore walls and the adsorbate become dominant, which are not considered for the Kelvin-equation. Further developments are microscopic methods, which are based on the density functional theory (DFT) and are applicable for meso- and micropores. For this thesis, the quenched solid density functional theory (QSDFT) method was chosen to determine the pore size distribution, as this method takes into account the surface heterogeneity of porous carbon and carbon/nitrogen materials.[228]

The nitrogen physisorption measurements were performed at 77 K on a Quantachrome Quadrasorb SI porosimeter. Prior to the physisorption measurements, the samples were degassed for 20 h at 150 °C under vacuum.

The apparent surface area was calculated with the BET model, which was applied on the isotherm data points of the adsorption branch for $p/p_0 < 0.3$. The pore volume was calculated from the physisorption data with the program QuadraWin (version 5.11), with the mesopore volume calculated by subtracting the micropore volume from the total pore volume. The pore size distribution was determined by the program QuadraWin (version 5.11) by using the QSDFT-theory for slit/cylindrical pores applied on the nitrogen adsorption isotherm.

Carbon dioxide physisorption

Besides nitrogen, carbon dioxide is a gas which is commonly used for the characterization of porous materials by physisorption. CO_2 physisorption measurements are usually carried out at temperatures of 273 K or 298 K and under ambient pressure. Due to the higher thermal energy of the adsorbate CO_2, adsorption occurs also in ultramicropores, which are micropores with a very small diameter (< 0.8 nm). This is an advantage in comparison to nitrogen physisorption, where the detection of very small micropores is not possible.

The strength of the interaction between the porous material and the adsorbent CO_2 is described by the isosteric heat of adsorption Q_{St}. It can be calculated from the sorption isotherms obtained at different temperatures by applying the Clausius-Clapeyron equation (**Equation 8**), where R is the ideal gas constant, P is the CO_2 partial pressure, T is the temperature and q_a is the CO_2 adsorption capacity (in mmol g^{-1}).

$$-\frac{Q_{St}}{R} = \left(\frac{\partial(\ln P)}{\partial(1/T)}\right)_{q_a} \qquad \textbf{(Eq.8)}$$

When for a constant CO_2 loading q_a the corresponding partial pressures P at different temperatures T are plotted as lnP against $1/T$, Q_{st} can be determined from the slope of the obtained straight line.[174]

The CO_2 physisorption measurements were performed at 273 K, 284 K and 302 K on a Quantachrome Quadrasorb SI porosimeter. Prior to the measurements, the samples were degassed for 20 h at 150 °C under vacuum.

The isosteric heat of CO_2 adsorption was calculated from the CO_2 physisorption isotherms obtained at different temperatures by applying the Clausius-Clapeyron equation (as described above, see **Equation 8**).

Nuclear magnetic resonance spectroscopy

Nuclear magnetic resonance (NMR) spectroscopy is a non-destructive technique, which gives information about the electronic environment of certain NMR-active isotopes and their interactions with neighbored atoms. Hence, NMR spectroscopy is a powerful method to characterize the structure of molecular and solid-state compounds. The technique is based on nuclear magnetic resonance, a physical phenomenon which describes the absorption and emission of electromagnetic radiation of certain nuclei in a magnetic field. The resonance frequency, which is in the radio frequency range, depends on the strength of the magnetic field and the magnetic properties of the isotopes. Therefore, the absorption frequency depends also on the electronic environment of the isotopes and coupling effects to adjacent isotopes can be observed. From the frequency shifts observed due to that, information on the structure of the sample can be obtained. Requirement for nuclear magnetic resonance is a nonzero nuclear spin. The most frequent examined isotopes in NMR-experiments are ^{1}H and ^{13}C, which makes NMR spectroscopy especially interesting for the structural elucidation of organic molecules.

NMR spectroscopy experiments are typically performed with dissolved samples, as in this case Brownian motion averages the orientation dependency of interactions between isotopes and their electronic environment. However, the anisotropy of these interactions is a problem for NMR spectroscopy on solid samples, and leads to broadened signals. This problem can be bypassed by spinning the sample with a high rotation speed in the so-called "magic angle", i.e. in an angle of 54.7 ° in respect to the external magnetic field, which leads to an averaging of the anisotropic isotope interactions (magic-angle spinning (MAS) NMR). However, there can still be a dipolar coupling between nuclear spins, which leads to broadened signals in solid state NMR despite the magic-angle spinning. A technique to obtain stronger signals in solid state NMR, is the cross-polarization (CP) NMR spectroscopy, where a magnetization transfer from more sensitive nuclei (e.g. ^{1}H) to less sensitive nuclei (e.g. ^{13}C) takes place.

^{13}C CP MAS NMR spectra were recorded on a Bruker Avance 400 spectrometer at 100.6 MHz with a 4 mm double resonance probe-head, operating at a spinning rate of 10 kHz.

Thermogravimetric analysis (TGA)

With thermogravimetric analysis, the mass change of a sample during heating is observed. A sample on a balance is heated with a certain heating rate and the mass of the sample is recorded as a function of temperature and time. This apparatus can be coupled with a mass spectrometer (TGA-MS), which allows for in-situ detection of evolving products. The obtained mass/temperature curves typically have the shape of steps, in which the single steps are related to decomposition or reaction processes (when heating a reaction mixture). With TGA-MS, the steps can be linked to the evolution of certain products, which allows for information regarding the sample composition or the reaction mechanism.

Thermogravimetric analysis coupled with mass spectrometry was performed on a Netsch thermogravimetry TG 209F1 Libra connected to a Pfeiffer Vacuum Omnistar gas analysis system with 194 cycles and with a M_w detection range from 10 Da to 195 Da under nitrogen atmosphere. The heating rate was 2.5 K/min.

Dynamic light scattering (DLS)

With dynamic light scattering, the hydrodynamic radius of dispersed or dissolved particles can be determined. When a laser beam is directed on particles which are much smaller than the wavelength of the laser, elastic scattering of the light in all directions occurs (Rayleigh scattering). For the light scattered by the different particles, interference occurs, which combined with the Brownian motion of the particles leads to fluctuations in the intensity of the scattered light. The diffusion coefficient D of the particles can be determined by analyzing the intensity fluctuations as a function of time. The diffusion coefficient D is related to the hydrodynamic radius r of the particles by the Stokes-Einstein equation (**Equation 9**).

$$D = \frac{k_B \cdot T}{6 \cdot \pi \cdot \eta \cdot r} \qquad \textbf{(Eq.9)}$$

Here, k_B is the Boltzmann-constant, T the temperature and η the viscosity of the dispersion medium.

Dynamic light scattering measurements were performed with a Malvern Zetasizer Nano ZS90.

Zeta-Potential measurement

The zeta potential is the electric potential difference between the stationary layer of an interfacial double layer around a charged particle and the dispersion medium. A high zeta potential indicates a high surface charge for the dispersed particles, which goes along with a high stability of the colloidal dispersion.

The zeta potential can be measured by electrophoresis. Here, an electrical field in the measurement cell forces the charged particles to move in a certain direction. The motion speed depends on the charge of the particles, and therefore correlates with their zeta potential. The velocity of the particles is usually measured with laser Doppler velocimetry, a technique which uses the Doppler shift of the scattered light of a moving object when illuminated with a laser beam.

Zeta potential measurements were performed with a Malvern Zetasizer Nano ZS90.

Photocatalytic dye degradation

The photocatalytic dye degradation experiments with the g-C_3N_4 from the “caffeine doped” CM precursor were carried out with the organic dye Rhodamine B.

For the photodegradation experiments, 10 mg of the respective g-C_3N_4 sample were dispersed by stirring in 10 ml of a RhB solution (20 mg/l) and illuminated with a white light emitting LED ($\lambda > 410$ nm, 50 W light output, OSA opto lights). Aliquots were taken before illumination and then every 10 min, to determine the RhB concentration with UV/Vis spectroscopy from the RhB maximum absorption wavelength ($\lambda = 554$ nm). Before taking the first aliquot, the dispersion was stirred for 1 h in the dark, to allow the adsorption of RhB on the catalyst surface. The degradation efficiency was determined by plotting the relative RhB concentration c/c_0 as a function of the time t, with c being the RhB concentration at a certain time t and c_0 the RhB concentration before illumination ($t = 0$). According to the Lambert Beer law (see **Equation 4**), it is $c/c_0 = A/A_0$ with A and A_0 being the optical absorbance of the RhB solution at the time t and $t = 0$, respectively, as determined by UV/Vis spectroscopy.

Dye adsorption

The dye adsorption experiments with the nitrogen-doped carbon monolith (sample m-CTS/HkU-sc-500) were carried out with Rhodamine B.

For the adsorption experiments, 5 mg of the powdered sample m-CTS/HkU-sc-500 were dispersed in 5 ml of a Rh B solution (20 mg/l and 200 mg/l) and placed inside a closed box (to prevent photodegradation) on an automatic shaker. To determine the RhB-concentration, aliquots (0.2 ml for the 20 mg/l solution and 25 µl for the 200 mg/l solution) were taken at $t = 0$ min. (before dispersing the sample in the RhB solution) and $t = 10$ min, 60 min, 180 min, 24 h and 48 h (after dispersing the sample in the RhB solution). The RhB concentration c_t at the time t was determined by UV/Vis-spectroscopy, by calculating the concentration from the absorbance A at the maximum absorption wavelength ($\lambda = 554$ nm) according to the Lambert-Beer equation (**Equation 4**). For the extinction coefficient at 554 nm, the literature reported value of $\varepsilon = 88000$ (cm mol/l)$^{-1}$ was used.[229] As the Lambert-Beer law is only valid for diluted solutions, the aliquots were diluted to achieve an absorbance $A < 1$. The RhB uptake q_t

at the time t was then calculated according to **Equation 10**, with the concentration c_t at the time t, the initial concentration c_0 at the time $t = 0$ (before addition of the sample), the volume V of the dispersion (5 ml) and the mass W of the sample m-CTS/HkU-sc-500 (5 mg):

$$q_t = \frac{(c_0 - c_t) \cdot V}{W} \qquad \textbf{(Eq.10)}$$

To subtract out factors which might contribute to a decrease in the RhB concentration besides the adsorption by the sample (e.g. adsorption at the glass surface, photodegradation), the RhB concentration of a reference sample which contains only RhB solution (20 mg/l or 200 mg/l) was determined in parallel. However, under the given experimental conditions, no changes in the concentration of the reference samples could be observed.

As maximum adsorption capacity, the adsorption capacity for the 200 mg/l RhB solution after 48 h was taken.

Photocatalytic water splitting

The testing for photocatalytic water splitting was performed in a tightly closed reaction chamber with a quartz-window for illumination and connection to a pressure measuring unit to detect the amount of evolved hydrogen (**Scheme A1**).

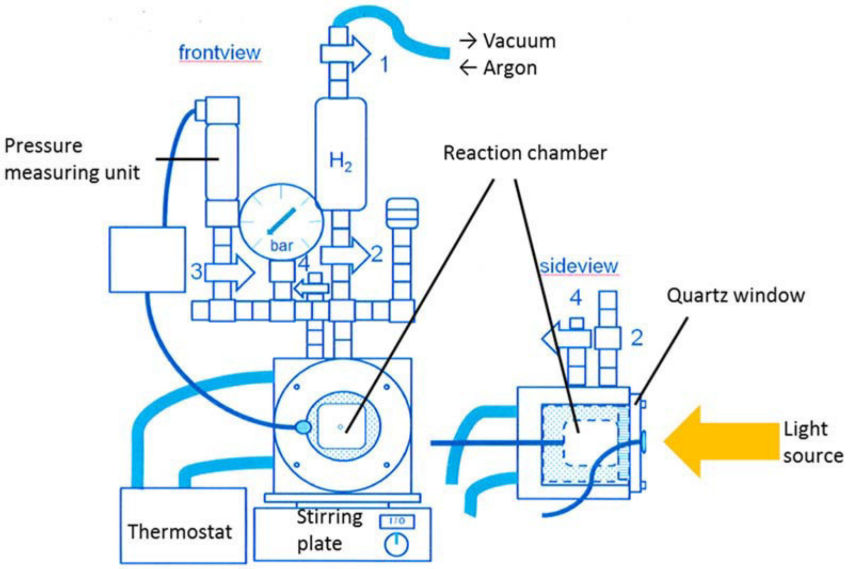

Scheme A1. Setup for the photocatalytic water splitting. Blue arrows indicate valves. During measurement, only valve 3 (connection to the pressure measuring unit) is opened. The chamber between valve 1 and valve 2 allows for enlarging the volume for collecting hydrogen.

For the measurement, 50 mg of the sample were dispersed in 34 ml water, with 3.8 ml triethanolamine (TEOA) and 39.4 µl H_2PtCl_6 (8 wt% aqueous solution). All reagents were degassed and purged with argon prior to the measurement. After purging the reaction chamber with argon, it was filled with the reaction mixture and under stirring and illumination with a LED-light (White light, 50 W light output, OSA opto lights) the pressure in the reaction chamber was recorded. The reaction chamber is connected with a thermostat, the experiments were performed at 25 °C.

The amount n of evolved hydrogen was calculated from the pressure p in the reaction chamber by applying the ideal gas law (**Equation 11**):

$$p \cdot V = n \cdot R \cdot T \qquad \textbf{(Eq.11)}$$

With the free volume V of the reaction chamber (i.e. excluding the volume of the liquid reaction mixture), the gas constant R = 8.3145 J mol^{-1} K^{-1} and the temperature T (here: 298 K). The hydrogen evolution rate (in µmol h^{-1}g^{-1}) was calculated as the amount of hydrogen evolved in a certain time per mass of the photocatalyst, for the time range in which the amount of evolved hydrogen increased linearly.

I.III Experimental Part

Chemicals

Table A.1. List of all chemicals applied

Substance	Chemical formula (CAS number)	Purity	Supplier
Acetic acid, 0.1 M	CH_3COOH (CAS: 64-19-7)	Titripur®	Sigma Aldrich
Acetone	CH_3COCH_3 (CAS: 67-64-1)	≥ 99.7 %	Sigma Aldrich
Caffeine	$C_8H_{10}N_4O_2$ (CAS: 58-08-2)	ReagentPlus®	Sigma Aldrich
Chitosan, medium molecular weight	(CAS: 9012-76-4)		Sigma Aldrich
Cyanuric acid	$C_3H_3N_3O_3$ (CAS: 108-80-5)	99 %	Alfa Aesar
2,4-diamino-6-phenyl-1,3,5-triazine	$C_9H_9N_5$ (CAS: 91-76-9)	97 %	Sigma Aldrich
Hexachloroplatinic acid (8 wt% aqueaous solution)	H_2PtCl_6 (CAS: 16941-12-1)		Sigma Aldrich
Hexaketocyclohexane octahydrate	$C_6O_6 \bullet 8\ H_2O$ (CAS: 527-31-1)	97 %	Sigma Aldrich
Hydrochloric acid, 37 %	HCl (CAS: 7647-01-0)	Reagent grade	Sigma Aldrich
Melamine	$C_3H_6N_6$ (CAS: 108-78-1)	99 %	Sigma Aldrich
NaOH solution, 0.1 M	NaOH (CAS: 1310-73-2)	Titripur®	Sigma Aldrich
N-Methyl-2-pyrrolidone (NMP)	C_5H_9NO (CAS: 872-50-4)	≥ 99 %	Alfa Aesar
Rhodamine B	$C_{28}H_{31}C_lN_2O_3$ (CAS: 81-88-9)	95 %	Sigma Aldrich

Table A.1 (Continuation). List of all chemicals applied

3,4-Dihydroxy-3-cyclobutene-1,2-dione (Squaric acid)	$(HO)_2C_4O_2$ (CAS: 2892-51-5)	≥ 99.7 %	Sigma Aldrich
Triethanolamine	$(HOCH_2CH_2)_3N$ (CAS: 102-71-6)	≥ 99.5 %	Sigma Aldrich
Urea	NH_2CONH_2 (CAS: 57-13-6)	BioReagent	Sigma Aldrich
Zinkchloride	$ZnCl_2$ (CAS: 7646-85-7)	≥ 99.995 %	Sigma Aldrich

Synthesis

Carbonization

All carbonization reactions were carried out in a chamber oven (Nabertherm N7/H chamber oven with a P300 temperature controller), under nitrogen flow and with a heating rate of 2.5 K/min. For that purpose, the respective precursors were placed in a lid-covered ceramic crucible and heated up to the respective carbonization temperature. This temperature was kept for a certain time (for the respective carbonization times: see below). Subsequently, the samples were kept in the oven under nitrogen flow until they equilibrated to room temperature.

4.1 g-C_3N_4 with enhanced photocatalytic activity from a "caffeine doped" CM precursor

Synthesis of the "caffeine doped" CM precursor complexes:

10 mmol cyanuric acid, 10 mmol melamine and x mmol caffeine (x = 0 for CM, x = 0.5 for CM-5C, x = 0.75 for CM-7.5C and x = 1 for CM-10C) were grinded together and then shaken in 50 ml of water for 12 h. The milky suspensions were then vacuum filtrated, washed with water and dried in a vacuum oven at 60 °C.

Synthesis of carbon nitride from the "caffeine doped" CM precursor complexes:

The carbon nitride materials were obtained from the respective precursor complexes by carbonization for 4 h at 500 °C.

4.2 C_2N carbon

4.2.1 Nitrogen-doped carbon monoliths and –beads by structuring the hexaketocyclohexane/ urea precursor with chitosan

Synthesis of the CTS/HkU precursor gels:

The HkU precursor was synthesized according to ref. 69.

208 mg hexaketocyclohexane octahydrate and 120 mg urea were mixed in a glass vial and molten in an oil bath at 90 °C (molar ratio hexaketocyclohexane octahydrate : urea = 1:3). After melting, the mixture turns to deep red and the evaporation of water and gases can be observed. When this process is completed, 3 ml water were added to dissolve the liquid deep eutectic. The solution is stirred for additional 5 min. in the oil bath, and then taken out to allow cooling down to room temperature.

The HkU precursor as reference sample (for the FT-IR measurements) was prepared as solid precursor, i.e. in the same way as described above but without addition of the water.

To prepare the CTS/HkU precursor gels, first a chitosan solution was prepared by dissolving 200 mg chitosan (CTS) in 10 ml water, followed by the addition of 50 µl 0.1 M acetic acid and sonication for 5 min.

For the preparation of the monolithic gels, the CTS solution was homogenously mixed with the solution of the HkU precursor (as described above) in an autoclave glass tube (diameter: 2 cm, height: 8.5 cm). The autoclave glass tube was placed in a tightly closed steel autoclave bomb (Parr instrument company, diameter: 4.5 cm, height: 13.5 cm, with Teflon-inlet) and put for 12 h in an oven at 100 °C. Afterwards, the obtained deep red gel monolith was carefully taken out and washed by repeatedly placing it in a beaker with 300 ml water (3 times for 10 min. each). Afterwards, drying with supercritical CO_2 or freeze drying was applied.

For the preparation of the gel beads, the CTS solution was dropped slowly with a syringe into a 0.1 M aqueous solution of NaOH. The obtained gel beads were washed with water until a neutral pH was reached and then put into the autoclave glass tube, followed by the addition of 6 ml water and the solution of the HkU precursor. Hydrothermal treatment (12h at 100 °C) and subsequent washing was carried out as described above for the monolithic gels.

Drying of the CTS/HkU precursor gels:

For freeze-drying, the respective gel samples (monolith or beads) were frozen in a freezer. After being completely frozen, the gels were dried with a freeze-drier (Lyotech LYO SG2-10) at -48 °C and 0.04 mbar.

For supercritical CO_2 drying, first the water in the gels was replaced by acetone. For that purpose, the respective gel samples were placed for 2 h each in erlenmayer flasks with water/acetone mixtures with an consecutively increased acetone content (starting with 5 vol% acetone, then 10 vol%, 30 vol%, 50 vol%, 70 vol%, 90 vol%, 96 vol% and then pure acetone). The gels were then dried by supercritical CO_2 with a Leica EM CPD300 supercritical drier, with 12 repetition cycles of exchanging CO_2 against acetone.

Carbonization of the dried CTS/HkU precursor gels:

The dried CTS/HkU precursor samples were carbonized for 1h at 500 °C.

The reference samples were prepared as described above, but without addition of the HkU precursor (samples *x*-CTS-*y* and *x*-CTS-*y*-500). The freeze dried reference samples m-CTS/U-f and m-CTS/Hk-f were also prepared as described above, but with the addition of dissolved urea (sample m-CTS/U-f) or dissolved hexaketocyclohexane octahydrate (sample m-CTS/Hk-f) instead of the HkU precursor.

4.2.2 C_2N carbon from organic crystals between squaric acid and urea

The squaric acid/urea crystals were prepared by suspending 1.14 g (10 mmol) squaric acid and urea (600 mg (10 mmol) for SaU-1, 1.2 g (20 mmol) for SaU-2) in 10 ml water, followed by heating up at 90 °C, to allow complete dissolution of the educts. Afterwards the solution was allowed to cool down to room temperature, which leads to the crystallization of the precursor complexes. The obtained crystals were filtrated, washed with small amount of cold water and dried in a vacuum oven at 60 °C.

To obtain the carbonized materials, the precursor crystals were carbonized for 1 h at the respective temperatures (200 °C for SaU-*x*-200, 235 °C for SaU-*x*-235, 550 °C for SaU-*x*-550, 800 °C for SaU-*x*-800 and 900 °C for SaU-*x*-900).

The $ZnCl_2$ templated sample SaU-2-550-Zn was prepared by grinding 1.14 g squaric acid and 1.2 g urea with 2.34 g $ZnCl_2$ and carbonizing this mixture for 1 h at 550 °C. To remove the Zn-species from the obtained carbon material, the sample was grinded and stirred in

1 M hydrochloric acid for 12 h. Afterwards, the sample was washed with water, then with ethanol and finally dried in a vacuum oven at 60 °C.

The $ZnCl_2$ templated sample SaU-1-550-Zn was prepared in the same way, but from 1.14 g squaric acid, 600 mg urea and 1.74 g $ZnCl_2$ as precursor mixture.

4.3 The g-C_3N_4/C_2N composites

Preparation of CMp-450 g-C_3N_4:

10 mmol cyanuric acid and 10 mmol 2,4-diamino-6-phenyl-1,3,5-triazine were grinded together and then shaken in 50 ml of water for 12 h. The milky suspensions were then vacuum filtrated, washed with water and dried in a vacuum oven at 60 °C.

The dried powder was then carbonized for 4 h at 450 °C.

Protonation of CMp-450 carbon nitride (sample CMp-450-prot):

For protonation, 100 mg of CMp-450 were stirred for 12 h in concentrated hydrochloric acid (37 %). Afterwards, the sample was centrifuged (10 min at 3000 rpm) and then three times washed with water by centrifugation (10 ml water each, centrifugation for 10 min. at 3000 rpm). The sample was then dried in a vacuum oven at 60 °C. Yield: 87 %.

Preparation of the SaU-1-550-, CMp-450- and CMp-450-prot- colloidal dispersions in water and NMP:

7.5 mg of the respective samples (SaU-1-550, CMp-450 or CMp-450-prot) were suspended in 15 ml of the respective dispersant (water or NMP) and sonicated for 10 h in a low-power ultrasonication bath. To remove bigger particles and aggregates, the obtained dispersions were afterwards centrifuged for 30 min. at 5000 rpm.

Preparation of the composite samples CMp-450-SaU and CMp-450-prot-SaU:

30 mg of the respective carbon nitride samples (CMp-450 for CMp-450-SaU and CMp-450-prot for CMp-450-prot-SaU) were dispersed in 15 ml of the SaU-1-550 dispersion (after centrifugation, prepared as described above) and sonicated for 10 h in a low-power ultrasonication bath. To obtain the composite as solid powder, the water from the obtained dispersions was evaporated by heating the dispersion for 12 h at 100 °C in a drying oven.

The reference samples (colloidal CMp-450 and colloidal CMp-450-prot) for the testing for photocatalytic water splitting were prepared as described above, but the respective samples (CMp-450 and CMp-450-prot) were suspended in water and not in the SaU-1-550 dispersion.

I.IV Supporting Figures and Tables

4.1 g-C_3N_4 with enhanced photocatalytic activity from a „caffeine doped“ CM precursor

Table SI-4.1.1. Elemental composition (as obtained by elemental combustion analysis), yields for the carbonization step and BET-surface area (as obtained by N_2 sorption measurement) for the caffeine doped CM and CMp complexes and the carbon nitride materials prepared out of them.

Sample	N [wt%]	C [wt%]	H [wt%]	Yield [wt%]	BET-surface area [m^2/g]
CM-500	58.8	34.1	2.2	19	31
CM-5C-500	58.8	34.0	2.2	19	41
CM-7.5C-500	58.9	34.2	2.2	21	21
CM-10C-500	58.9	34.1	2.2	22	20

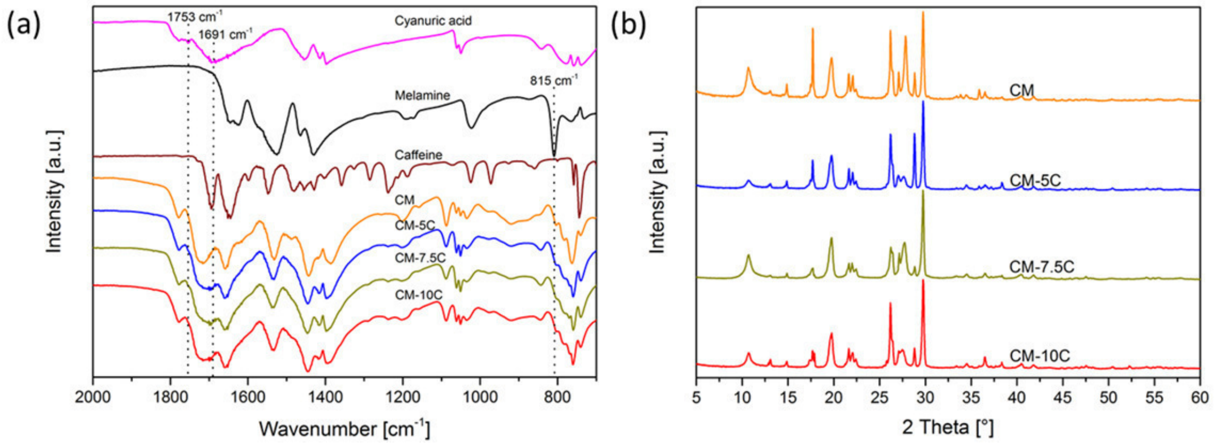

Figure SI-4.1.1. (a) FT-IR spectra and (b) X-ray diffraction patterns of the CM complex (orange) and the caffeine doped CM complexes CM-5C (blue), CM-7.5C (yellow), and CM-10C (red). For comparison, in (a) also the FT-IR spectra of cyanuric acid (magenta), melamine (black) and caffeine (brown) are shown.

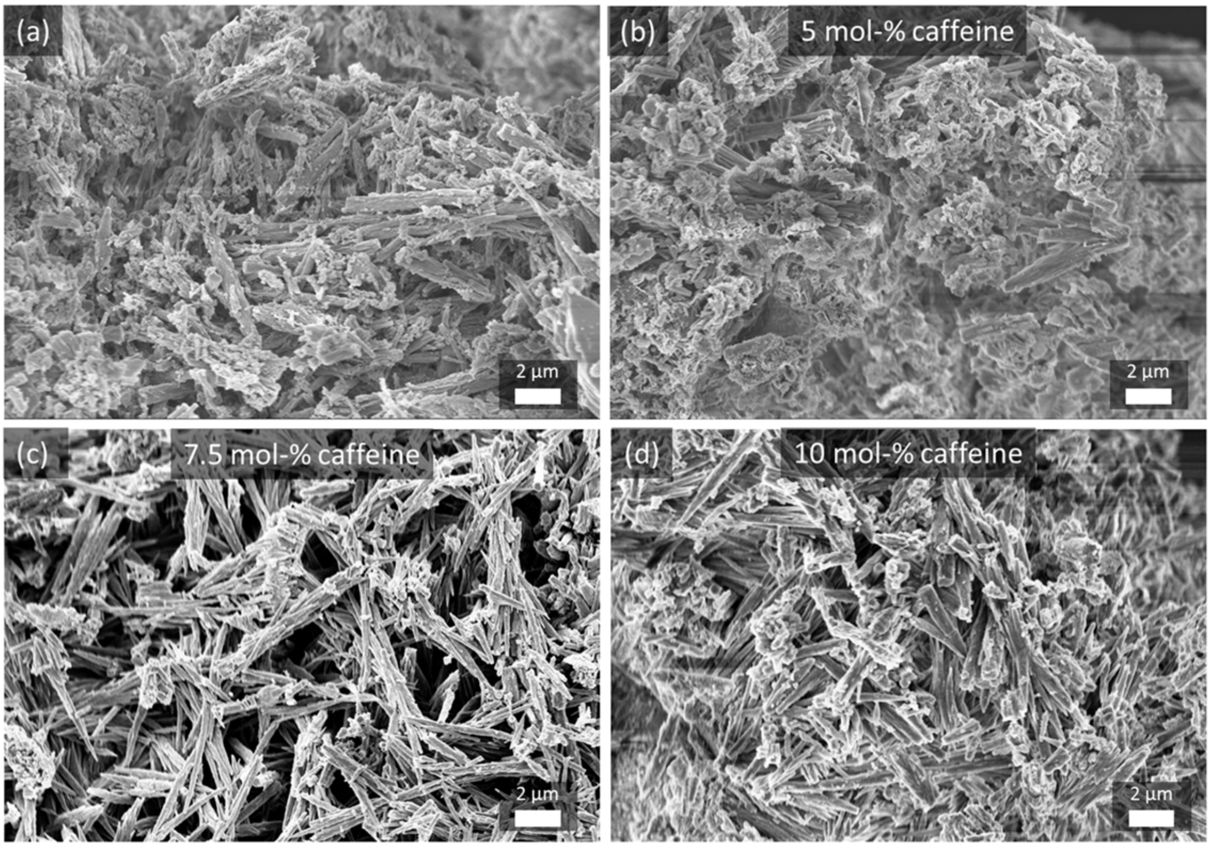

Figure SI-4.1.2. SEM images of the (a) CM complex (sample CM), and the CM complex with addition of (b) 5 mol-% caffeine (sample CM-5C), (c) 7.5 mol-% caffeine (sample CM-7.5C) and (d) 10 mol-% caffeine (sample CM-10C) before carbonization.

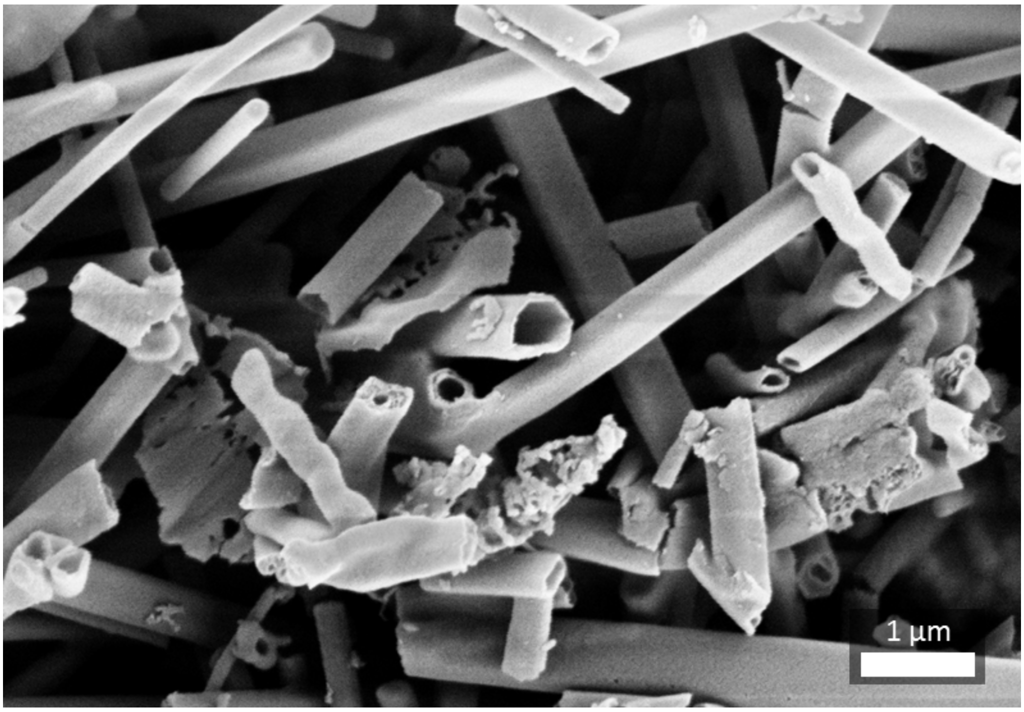

Figure SI-4.1.3. Higher magnification SEM image of the sample CM-7.5C-500.

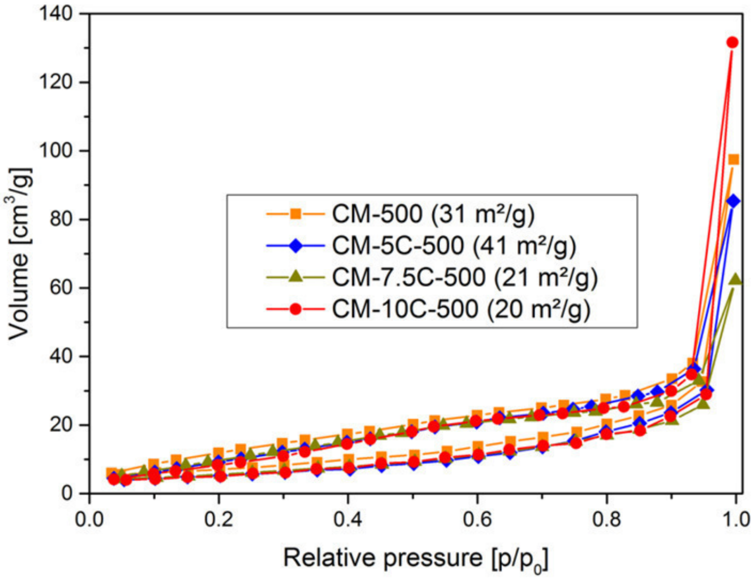

Figure SI-4.1.4. Nitrogen sorption isotherms and specific BET surface area of the samples CM-500 (orange), CM-5C-500 (blue), CM-7.5C-500 (yellow) and CM-10C-500 (red).

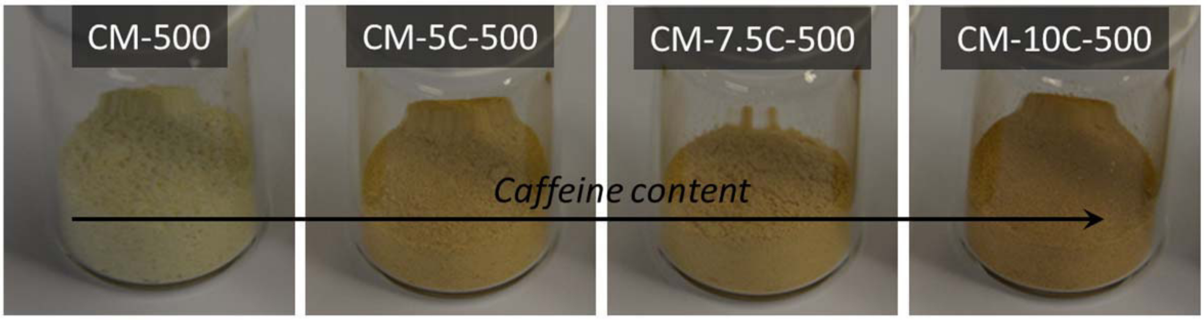

Figure SI-4.1.5. Photographs of the samples CM-500, CM-5C-500, CM-7.5C-500 and CM-10C-500 (from left to right).

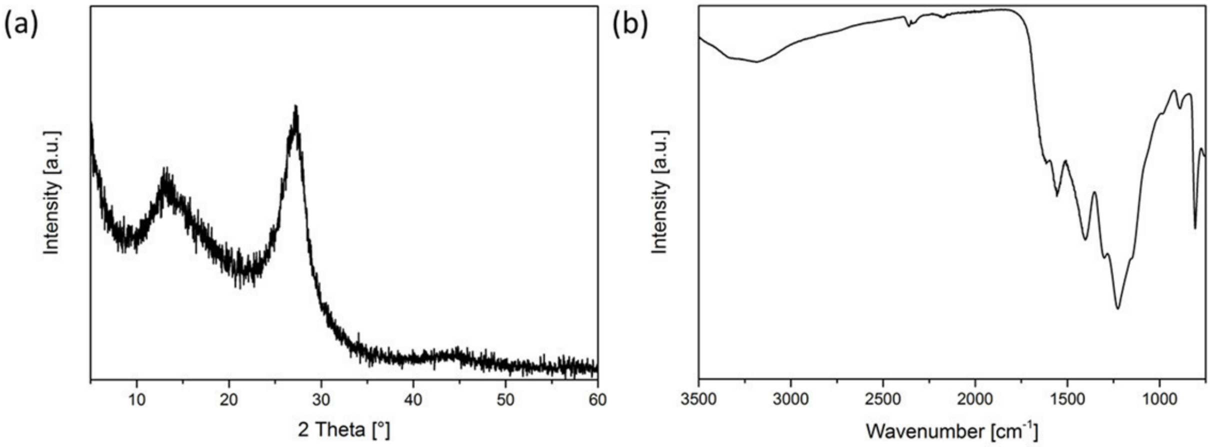

Figure SI-4.1.6. (a) PXRD pattern and (b) FT-IR spectra of the sample CM-5C-500 after the third RhB photodegradation cycle.

4.2 C_2N carbon

4.2.1 Nitrogen-doped carbon monoliths and –beads by structuring the hexaketocyclohexane/urea precursor with chitosan

Table SI-4.2.1. Elemental composition (as obtained by elemental combustion analysis), yields for the carbonization step, BET-surface area (as obtained by nitrogen pysisorption measurement), total pore volume and mesopore volume (as obtained by nitrogen physisorption measurement, with the mesopore volume calculated by subtracting the micropore volume from the total pore volume) for the CTS supported samples.

Sample	N [wt%]	C [wt%]	H [wt%]	C/N-ratio	Yield [wt%]	BET-surface area [m^2/g]	Total pore volume [cc/g]	Mesopore volume [cc/g]
m-CTS/HkU-f	8.8	38.3	6.0	3.7		-	-	-
m-CTS/HkU-sc	8.3	38.9	6.0	4.0		76	0.21	0.17
b-CTS/HkU-f	8.3	39.4	5.9	4.7		-	-	-
b-CTS/HkU-sc	7.9	38.8	5.7	4.9		168	0.87	0.80
m-CTS-f	6.1	39.0	6.3	5.5		-	-	-
b-CTS-f	7.4	41.5	5.9	5.6		-	-	-
b-CTS-sc	7.5	42.4	6.5	5.7		39	-	-
m-CTS/HkU-f-500	12.0	69.5	3.4	5.8	38	-	-	-
m-CTS/HkU-sc-500	12.0	73.0	3.1	5.2	35	348 m^2/g	0.71 cc/g	0.57 cc/g
b-CTS/HkU-f-500	12.1	70.9	3.4	5.9	35	-	-	-
b-CTS/HkU-sc-500	10.8	73.1	3.2	6.8	34	445 m^2/g	1.14 cc/g	0.97 cc/g
m-CTS-f-500	10.4	73.2	3.3	6.0	28	-	-	-
b-CTS-f-500	10.9	74.7	3.3	6.9	33	-	-	-
b-CTS-sc-500	10.5	75.1	3.3	7.1	30	-	-	-

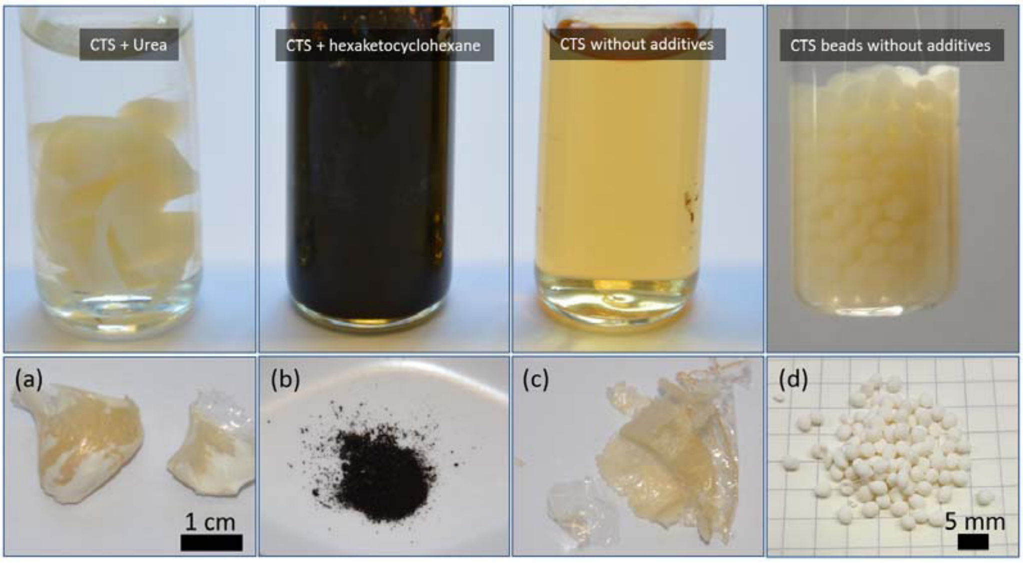

Figure SI-4.2.1. Photographs of the CTS reference samples prepared with the addition of only urea, only hexaketocyclohexane and without any additives, after the hydrothermal step (top row) and after drying (bottom row). The reference samples (a) m-CTS/U-f (prepared with addition of only urea), (b) m-CTS/Hk-f (prepared with addition of only hexaketocyclohexane) and (c) m-CTS-f (prepared without additives) are freeze dried. (d) Supercritical dried beads b-CTS-sc (prepared without additives).

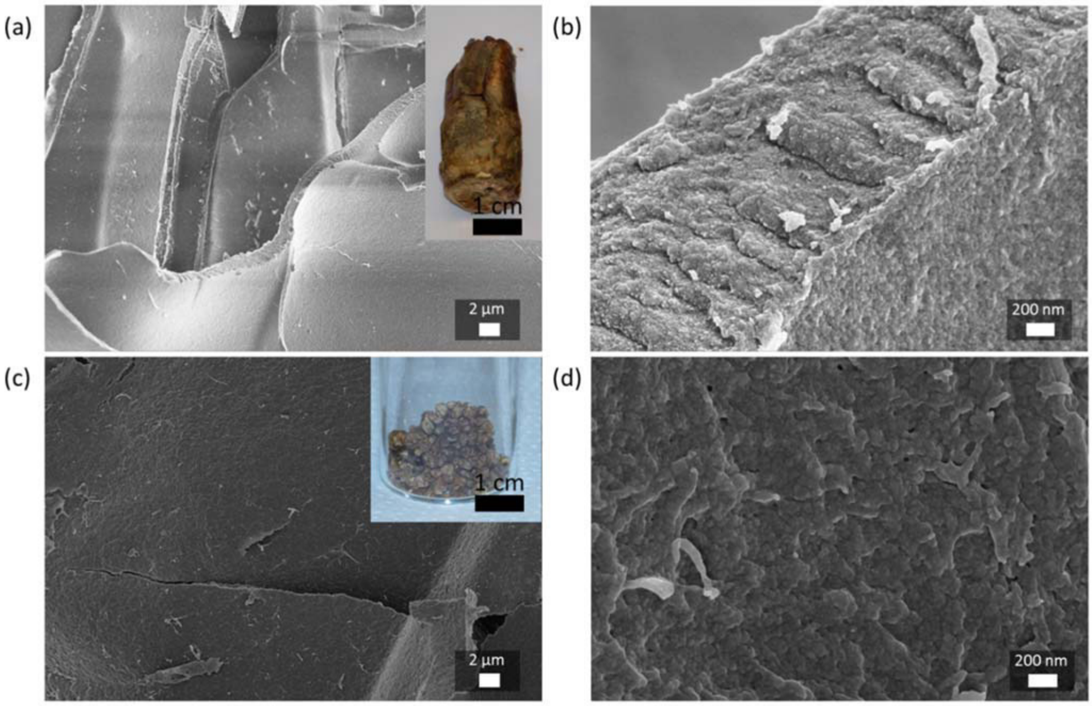

Figure SI-4.2.2. SEM images of the freeze dried (a,b) CTS/HkU precursor gel monolith (sample m-CTS/HkU-f) and (c,d) CTS/HkU precursor gel beads (sample b-CTS/HkU-f). Inlets show photographs of the respective samples.

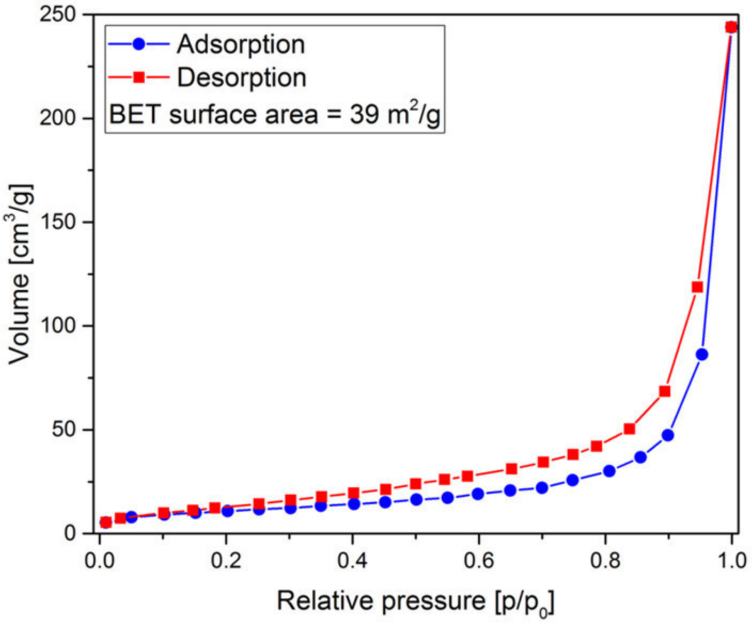

Figure SI-4.2.3. Nitrogen sorption isotherms and specific BET surface area of the supercritical dried CTS gel beads (sample b-CTS-sc).

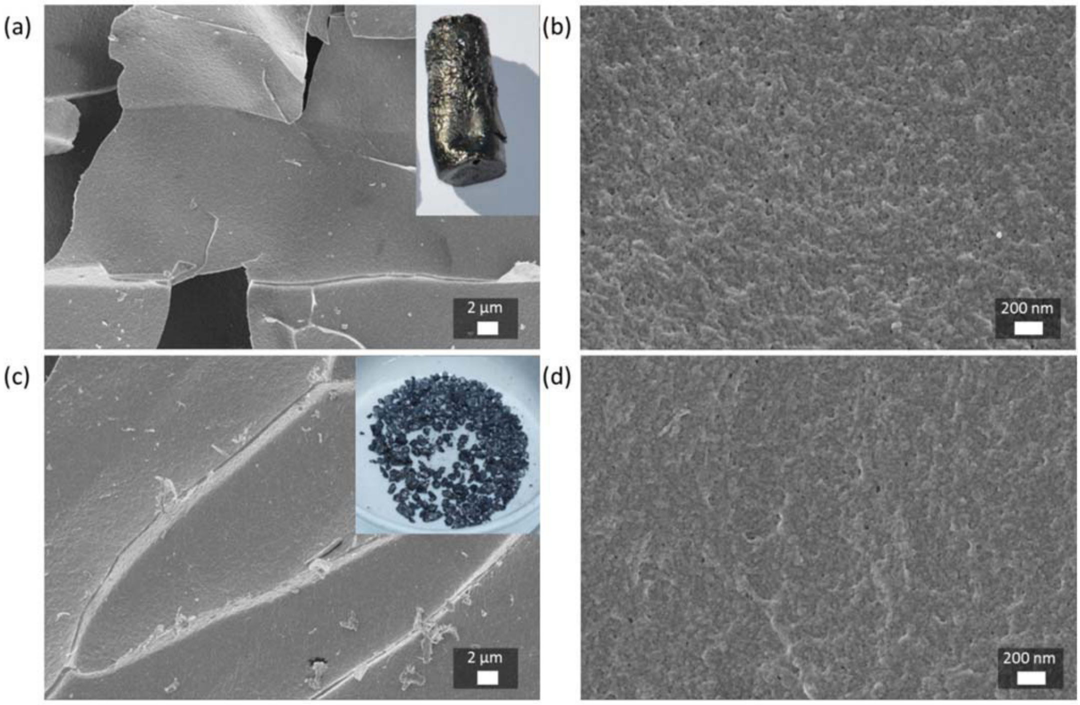

Figure SI-4.2.4. SEM images of the freeze dried and carbonized (a,b) monolith (sample m-CTS/HkU-f-500) and (c,d) beads (sample b-CTS/HkU-f-500). Inlets show photographs of the respective samples.

4.2.2 C_2N carbon from organic crystals between squaric acid and urea

Table SI-4.2.2. Elemental composition (as obtained by elemental combustion analysis), yields for the carbonization step and BET-surface area (as obtained by N_2 sorption measurement) for the SaU-samples.

Sample	N [wt%]	C [wt%]	H [wt%]	O [wt%]	C/N ratio
SaU-1	15.4	34.3	3.5	45.9	2.2
SaU-2	22.7	30.9	4.2	n.a.	1.4
SaU-1-200	16.8	37.2	3.2	n.a.	2.2
SaU-2-200	25.8	34.7	3.7	n.a.	1.3
SaU-1-235	20.2	41.5	3.1	n.a.	2.1
SaU-2-235	25.8	35.3	3.4	n.a.	1.4
SaU-1-550	25.9	61.50	2.3	9.9	2.4
SaU-2-550	26.6	60.7	2.3	9.9	2.3
SaU-1-800	20.7	75.4	1.1	10.0	3.6
SaU-2-800	20.6	74.7	1.1	n.a.	3.6
SaU-1-900	18.0	80.0	1.0	n.a.	4.4
SaU-2-900	17.1	81.0	1.0	n.a.	4.7
SaU-1-550-Zn	17.7	45.4	3.4	n.a.	2.6
SaU-2-550-Zn	22.3	43.5	3.6	20.9	2.0

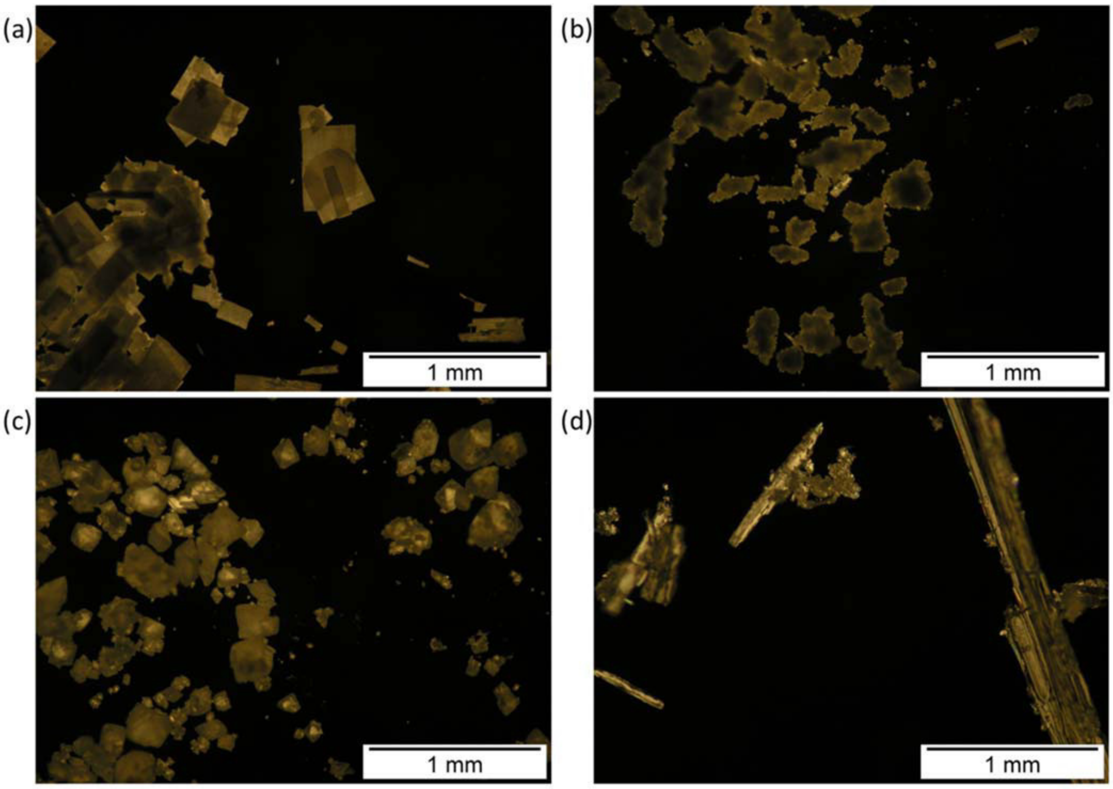

Figure SI-4.2.5. Optical microscopy images of the (a) 1:1 squaric acid/urea crystals (sample SaU-1), (b) 1:2 squaric acid/urea crystals (sample SaU-2), (c) re-crystallized squaric acid and (d) re-crystallized urea.

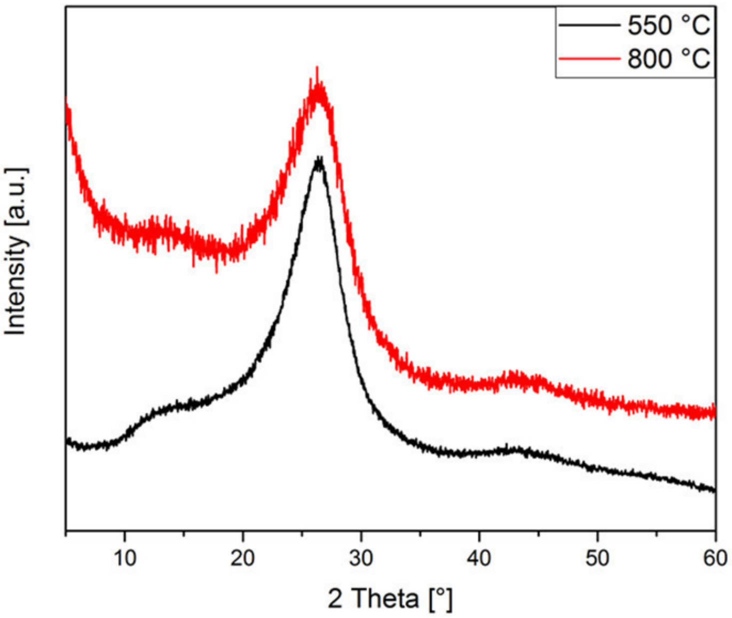

Figure SI-4.2.6. PXRD pattern of the eutectic hexaketocyclohexane/urea precursor carbonized at 550 °C (black) and 800 °C (red).

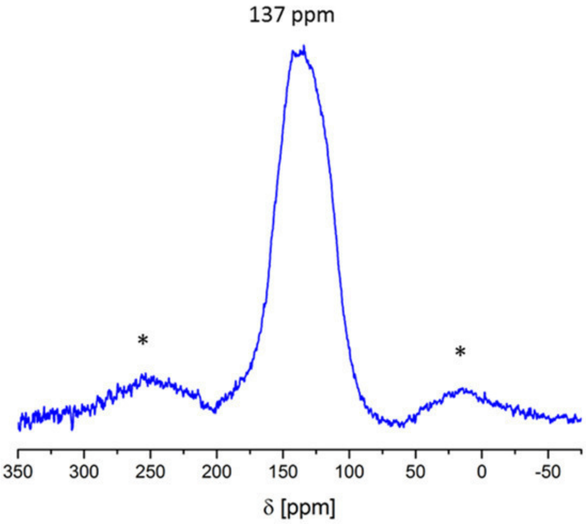

Figure SI-4.2.7. Solid state CP MAS ^{13}C NMR spectra of the 1:1 squaric acid/urea-crystals after carbonization at 550 °C (sample SaU-1-550). Spinning side bands are marked with asterisks.

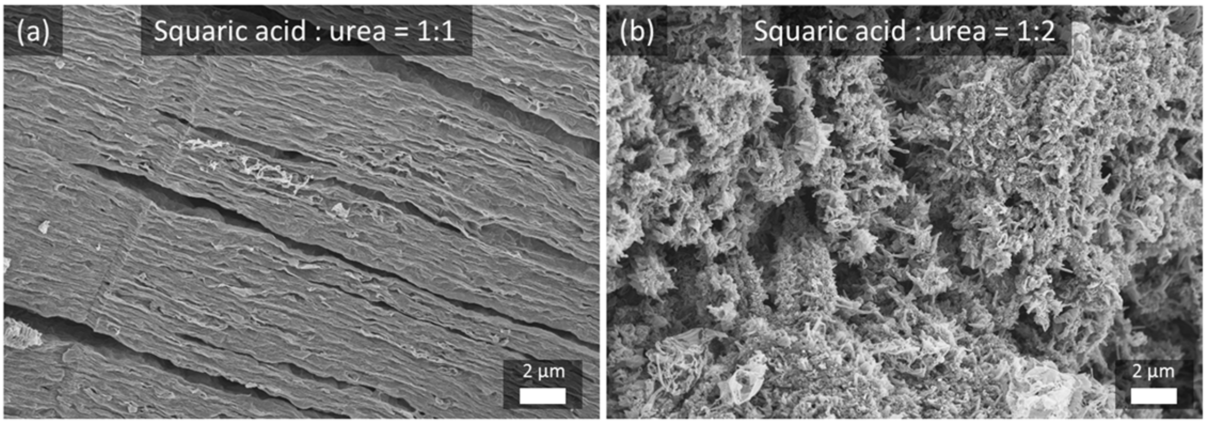

Figure SI-4.2.8. SEM images of the samples (a) SaU-1-900 and (b) SaU-2-900 obtained after carbonization at 900 °C.

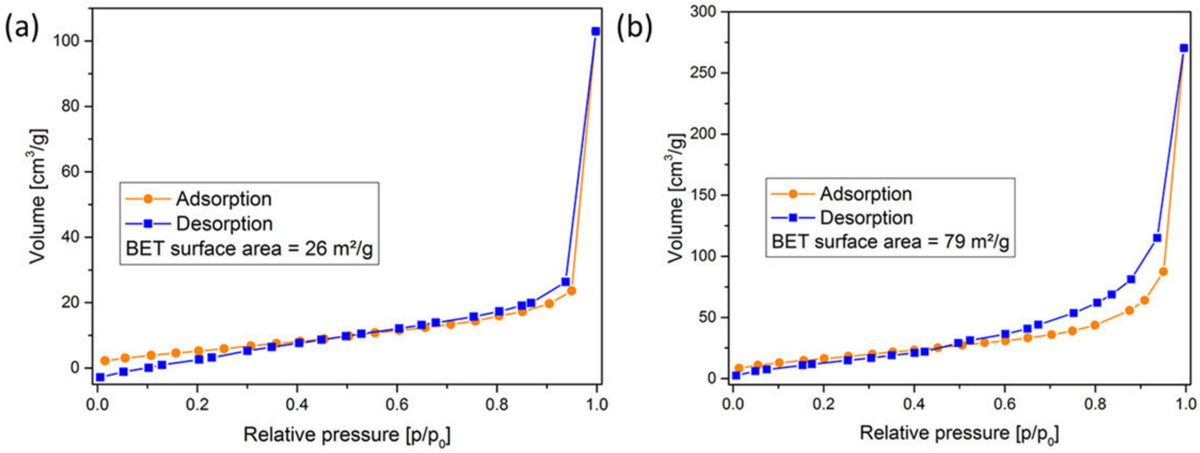

Figure SI-4.2.9. Nitrogen sorption isotherms and specific BET surface area of the samples (a) SaU-1-550 and (b) SaU-2-550.

Figure SI-4.2.10. Photographs of the SaU-1 crystals after thermal condensation for 2h at 200 °C (sample SaU-1-200, right), 235 °C (sample SaU-1-235, middle) and 550 °C (sample SaU-1-550, left).

4.3 The g-C_3N_4/C_2N composites

Table SI-4.3.1. Elemental composition (as obtained by elemental combustion analysis) for the samples CMp-450, CMp-450-prot, CMp-450-SaU and CMp-450-prot-SaU.

Sample	N [wt%]	C [wt%]	H [wt%]	O [wt%]	C/N ratio
CMp-450	47.3	45.0	2.7	5.4	0.95
CMp-450-prot	43.8	39.1	3.4	10.9	0.89
CMp-450-SaU	45.3	43.8	2.8	n.a.	0.97
CMp-450-prot-SaU	44.4	40.3	2.8	n.a.	0.91

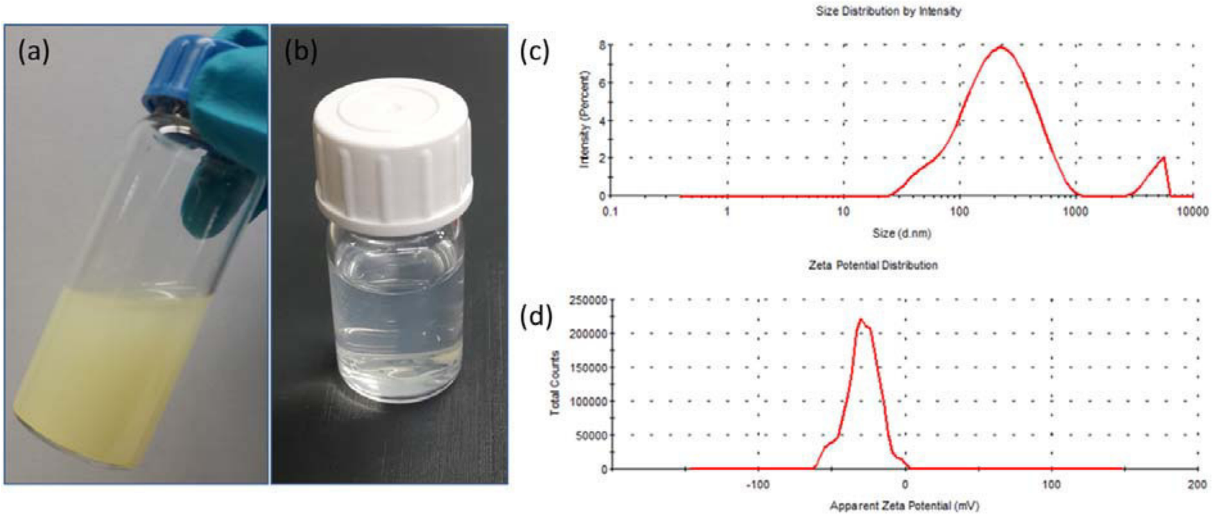

Figure SI-4.3.1. (a) Photograph of the CMp-450 dispersion after sonication and before centrifugation and (b) after centrifugation. (c) Size distribution of the CMp-450 dispersion after sonication and centrifugation, as determined by DLS. (d) Surface zeta potential of the CMp-450 dispersion after sonication and centrifugation.

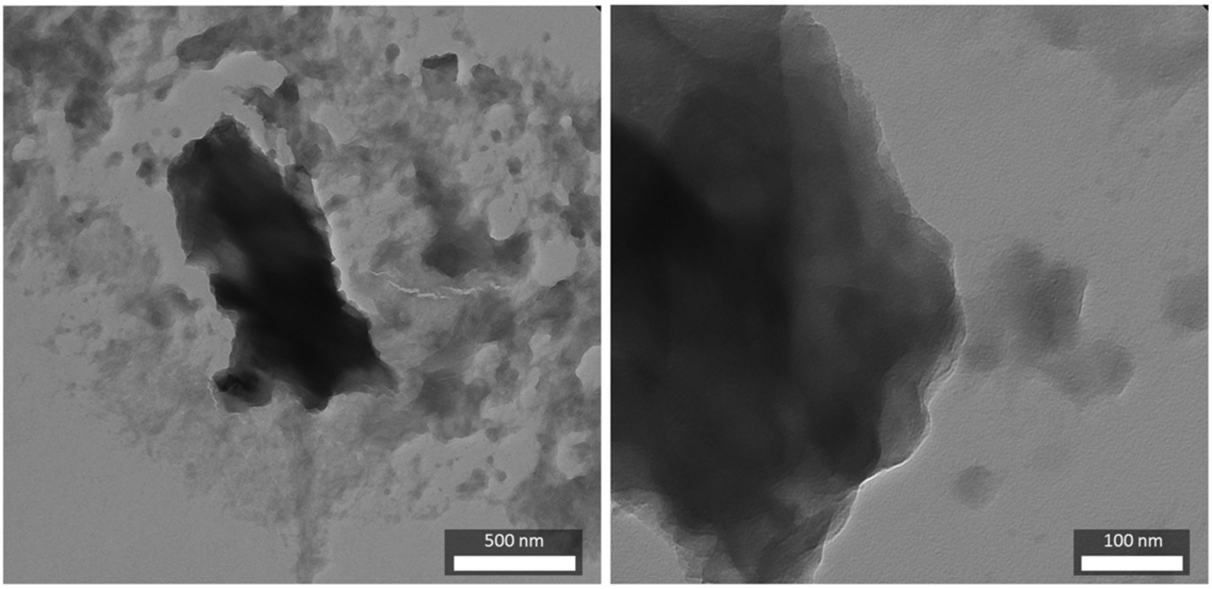

Figure SI-4.3.2. Transmission electron microscopy images of the SaU-1-550 dispersion after sonication and centrifugation.

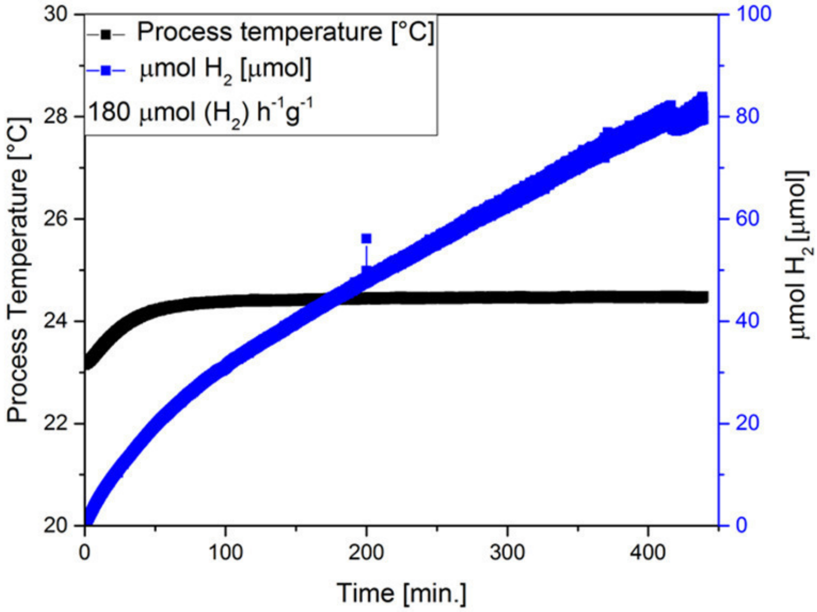

Figure SI-4.3.3. Hydrogen evolution rate for the photocatalytic water splitting with the material CMp-450 (as bulk material) as photocatalyst.

I.V List of publications

J. K. Berg, T. Jordan, Y. Binder, H. G. Börner, D. Gebauer: Mg^{2+} Tunes the Wettability of Liquid Precursors of $CaCO_3$: Toward Controlling Mineralization Sites in Hybrid Materials, *J. Am. Chem. Soc.* **2013**, *135*, 12512–12515.

T. Jordan, N. Fechler, J. Xu, T. J. K. Brenner, M. Antonietti, M. Shalom: “Caffeine Doping” of Carbon/Nitrogen-Based Organic Catalysts: Caffeine as a Supramolecular Edge Modifier for the Synthesis of Photoactive Carbon Nitride Tubes, *ChemCatChem* **2015**, *7*, 2826– 2830.

T. Jordan, M. Shalom, M. Antonietti, N. Fechler: Carbon Nanoarchitectures by Design: Preorganizing Squaric Acid with Urea, *Asia-Pac. J. Chem. Eng.* **2016**, 11, 866–873.

R. Nisticò, S. Tabasso, G. Magnacca, T. Jordan, M. Shalom, N. Fechler: The reactive hypersaline route: A one-pot synthesis of photoactive titania nanocomposites, **2016**, *submitted*.

I.VI Declaration

Die vorliegende Dissertation entstand im Zeitraum zwischen August 2014 und Januar 2017 am Max-Planck-Institut für Kolloid- und Grenzflächenforschung unter Betreuung von Prof. Dr. Dr. h.c. Markus Antonietti.

Hiermit erkläre ich, dass die vorliegende Arbeit selbstständig angefertigt wurde und keine anderen als die angegebenen Hilfsmittel und Quellen verwendet wurden.

The present work was carried out during the period from August, 2014 to January, 2017 at the Max Planck Institute of Colloids and Interfaces under supervision of Prof. Dr. Dr. h.c. Markus Antonietti.

I declare that I have written this work on my own and used no other than the named aids and references.

Thomas Jordan,

Potsdam 30.01.2017